Retrofitting CLT panels and Glulam beams subjected to static and dynamic loads

By
Bita Hosseinian Ahangarnazhad

Supervised by
Dr. Ghasan Doudak

Thesis submitted to the University of Ottawa
in partial Fulfillment of the requirements for the degree of

Doctor of Philosophy
in Civil Engineering

Department of Civil Engineering
Faculty of Engineering
University of Ottawa

Abstract

Mass timber products such as cross-laminated timber (CLT) and glued laminated timber (glulam) have become more common in contemporary structures, particularly mid- to high-rise ones, as a result of their development. Although engineered wood products are structurally efficient and reliable, their performance can deteriorate over time due to factors such as material deterioration, increased service demands, and exposure to extreme loading conditions. As a result, research on strengthening and rehabilitating timber members has gained significant attention in structural engineering. The current research aims to investigate the effect of CFRP in improving the structural performance of CLT panels and glulam beams under static and dynamic blast loads. Experiments were conducted at the University of Ottawa using a shock tube designed to replicate the high strain rates associated with blast loading. Different retrofit configurations were investigated, including confinement only and combined configurations with both unidirectional tension reinforcement and CFRP confinement. The confinement was applied in various configurations, including full length, localized (shear and moment regions), and U-shaped arrangements, using both unidirectional and bidirectional CFRP. According to the experimental results, CFRP fabrics significantly improved the resistance, stiffness, and ductility of the specimens. In the static tests, the retrofitted CLT specimens exhibited increases in peak resistance from 13% to 133%, while stiffness improvements reached up to 49%. The ductility ratio increased to a maximum of 1.67, indicating enhanced energy absorption. Under dynamic loading, peak resistance increased up to 166%, while stiffness improvement reached up to about 52%. In addition, the failure mode shifted from rolling shear in the unretrofitted CLT panel to predominantly flexural behavior in the retrofitted ones. For the glulam specimens, the retrofitting led to peak resistance and stiffness increases up to 46% and 13%, respectively, under static loading. Under dynamic loading, peak resistance increased by up to 123%, with the failure modes primarily governed by flexural behavior. A fiber section analytical model was developed to simulate the behaviour of the specimens up to peak resistance. The predictions showed good agreement with experimental data, accurately reflecting force response, stiffness, and displacement at peak resistance.

Acknowledgments

First and foremost, I would like to express my sincere gratitude to my thesis supervisor, Prof. Ghasan Doudak, for his continuous guidance, support, and encouragement throughout my PhD studies. His knowledge, patience, and valuable advice greatly contributed to the completion of this research and to my academic and professional growth.

I am sincerely grateful to my family for their unconditional love, encouragement, and support throughout this journey. Their patience, understanding, and belief in me gave me the strength and motivation to complete this work.

I would also like to thank Dr. Muslim Majeed and Dr. Gamal Elnabelsya for their assistance and support in the laboratory throughout the experimental program. Their technical expertise and help during testing were greatly appreciated.

Finally, I would like to thank all my colleagues, friends, and everyone who supported me during my graduate studies and contributed, directly or indirectly, to this research.

Table of Contents

List of Figures

List of Tables

Chapter 1 Introduction

1.1 Research needs

Advances in manufacturing techniques for engineered wood products (EWPs), such as cross-laminated timber (CLT) and glued-laminated timber (glulam), have enabled the use of timber in structural applications far beyond traditional low-rise light-frame construction. Among these products, particularly in recent years, CLT has experienced substantial growth, mainly due to its distinctive mechanical characteristics and structural versatility. CLT is an engineered wood product composed of layers of dimension lumber arranged in alternating orthogonal directions and bonded together with structural adhesives. This cross-laminated configuration enhances dimensional stability and provides two-way load-carrying capability, enabling CLT panels to act as structural wall, floor, and roof elements. Individual laminations are visually or machine stress-rated and may be finger-jointed to achieve longer panel lengths. CLT panels are manufactured in various thicknesses and layups, typically consisting of three to nine layers, allowing flexibility in structural design(Karacabeyli and Gagnon 2020). Although CLT exhibits high stiffness and strength relative to its weight, its orthotropic and layered nature results in complex stress distributions under bending. In flexural applications, structural behaviour is often governed by tensile rupture of the outer laminations and rolling shear failure in transverse layers, which may limit deformation capacity under high or dynamic loading conditions (Brandner et al. 2016; Hassanieh et al. 2017). Consequently, improving the flexural strength and post-peak behaviour of CLT members through external reinforcement techniques has become an important area of research.

Glulam is constructed by bonding multiple layers of dimensional lumber along the grain direction with a structural adhesive. Each lamination is stress-rated, providing control over the mechanical properties of the individual lamellae. This results in a structural component with greater uniformity and reliability compared to traditional sawn timber. To achieve greater lengths and larger cross-sectional dimensions, individual lumber pieces are connected with finger joints. Due to its versatility and enhanced strength-to-weight ratio, glulam is ideal for various structural applications, including beams, columns, and large-scale roof structures. Higher-grade laminations are strategically placed in regions of maximum stress, while lower-grade material is positioned near the neutral axis, resulting in an efficient structural member with predictable mechanical performance (Canadian Standards Association 2024).

Despite the structural efficiency and reliability of engineered timber products, their performance may be compromised over time due to material degradation, increased service demands, changes in design requirements, or exposure to extreme loading conditions. Consequently, strengthening and rehabilitation of timber members have become important research areas in structural engineering. Retrofitting, defined as the process of strengthening or upgrading existing structures to improve their performance and durability, has become increasingly important in extending the service life of timber members, particularly in aging structures and those subjected to increased loading demands (Corradi et al. 2017; Gentile et al. 2002). Recently, advancements in research have led to the development and growing use of fibre-reinforced polymers (FRP) for retrofitting wood members due to their high strength-to-weight ratio, corrosion resistance, and ease of application (Lacroix and Doudak 2019, 2020).

When externally bonded to timber elements, FRP has been shown to significantly enhance flexural strength, stiffness, and load-carrying capacity while adding minimal weight and causing little geometric alteration to the original member (Fiorelli and Dias 2003; Alam et al. 2009; Borri et al.

2013). In addition, FRP retrofitting allows for localized strengthening of critical regions such as tension zones and areas subjected to high bending or shear demands, making it an efficient solution for structural upgrading without the need for extensive demolition or replacement (Hay et al. 2006). As a result, FRP-based retrofitting techniques have emerged as a promising approach for improving the structural performance of both conventional timber and engineered wood products under a wide range of loading conditions

While much of the existing research has focused on strengthening timber members under conventional service and gravity loading, increasing attention has been directed toward their performance under extreme loading scenarios such as blast events. Structural members subjected to blast loading experience high strain rates due to the short duration and rapid increase in the applied pressure, which can significantly influence their mechanical response. The need for appropriate structural detailing to ensure adequate performance of elements and assemblies under blast loading has led to the development of various analytical and design guidelines (Office of the Deputy Prime Minister 2004; Unified Facilities Criteria Program 2008; PDC 2008; ASCE 2011; DHS 2011; CSA 2012). In addition, the demand for improved assessment of structural response under blast loads has increased as a result of the catastrophic damage observed in structures exposed to such extreme events.

Due to the relatively low density and limited ductility of wood, early research on the behaviour of timber structures under blast loading was limited. However, in recent years, significant progress has been made in understanding the response of timber structural elements subjected to blast loads, supported by advances in experimental methods and numerical modeling. These research efforts have included studies on glulam members (Lacroix and Doudak 2018b, 2018a), CLT panels

(Lopez-Molina and Doudak 2019; Poulin et al. 2018), timber structural assemblies incorporating connections and joints (Viau and Doudak 2019), and light-frame wood stud walls (Viau and Doudak 2016).

Although the Canadian blast design standard CSA S850 (CSA 2025) does not explicitly address retrofitting requirements for wood structural elements, but it does provide design guidance for the strengthening and retrofitting of reinforced concrete and masonry members using fiber-reinforced composite materials. This highlights a gap in current design provisions regarding the application of retrofitting strategies for timber structures subjected to blast loading.

Recent experimental and analytical studies have improved the understanding of timber structures subjected to blast loading, building upon established blast analysis and design methodologies and structural dynamics formulations. Research on glulam members exposed to blast and impulsive loading has shown that their response is typically governed by flexural behaviour and tensile rupture (Lacriox 2017; Lacroix and Doudak 2018c). Studies focusing on CLT panels have further highlighted the influence of orthotropic material behaviour and interlayer interaction on blast response (Lopez-Molina and Doudak 2019; Poulin et al. 2018).
Although these studies have significantly advanced the current understanding of timber response under blast loading, the available literature has largely focused on unretrofitted members and assemblies. In addition, limited research has investigated the behaviour of CFRP retrofitted CLT panels and glulam beams subjected to high strain rate blast loading, particularly using different retrofit configurations and combined experimental and analytical methods. Therefore, further investigation is required to evaluate the effectiveness of CFEP retrofitting techniques in improving the structural performance and blast resistance of timber elements under both static and dynamic

loading conditions. In addition, limited research has investigated the behaviour of CFRP-retrofitted CLT panels and glulam beams subjected to blast-induced high-strain-rate loading, particularly using different retrofit configurations and combined experimental and analytical approaches. Furthermore, the influence of CFRP confinement arrangements and tensile reinforcement on the post-peak behaviour, ductility, energy dissipation, and failure mechanisms of mass timber members under dynamic loading conditions has not been fully understood.

1.2 Research objectives

The main goal of this research study is to investigate reinforcement strategies and techniques to enhance the performance of CLT panels and glulam beams.

More specifically, the objectives are to:

1. Evaluate the effectiveness of new configurations using CFRP as reinforcement material for CLT panels and glulam beams.
2. Investigate the failure mechanisms of CFRP-reinforced CLT panels and glulam beams subjected to static and blast-simulated loads.
3. Assess the impact of retrofitting on the performance in the post-peak region and investigate configurations that would enhance the ductility and energy dissipation.
4. Provide recommendations, where relevant, regarding analysis and design approaches.

1.3 Methodology

The following is the methodology followed to accomplish the research goals:

- Conduct a comprehensive review of dynamic and blast analysis approaches, characteristics of blast shock waves, and recent design guidelines for wood structures subjected to blast loading.

- Conduct a literature review on the behaviour of timber elements subjected to static and simulated blast loads with a focus on those strengthened with CFRP fabrics.
- Undertake experimental investigation of retrofitted configurations with glulam beams and CLT panels under static loading and simulated blast loading, including their resistance curves and failure modes.
- Propose an analytical procedure that can capture the behaviour until peak loading and validate with experimental data.
- Provide recommendations, where appropriate, on design and analysis methods for CLT panels and glulam beams reinforced with CFRP.

1.4 Structure of Thesis

The structure of the thesis is organized as follows:

Chapter 1 introduces the research needs, research objectives, and overall methodology.

Chapter 2 presents a comprehensive literature review, including the behaviour of timber elements under dynamic loading, with emphasis on the effects of FRP used as reinforcement.

Chapter 3 describes the experimental research methodology, including detailed descriptions of the tested specimens and corresponding test setups.

Chapter 4 presents the results of the static and dynamic tests conducted on both retrofitted and unretrofitted CLT panels and glulam beams.

Chapter 5 presents the analytical model and results obtained for the unreinforced and reinforced elements.

Chapter 6 discusses and interprets the results from both the experimental and analytical investigations.

Chapter 7 summarizes key findings of the study and provides recommendations for future research.

Appendices A and B provide detailed test results for the unretrofitted and retrofitted CLT panels and glulam beams tested statically and dynamically, respectively.

Appendix C presents detailed outputs for fiber section analysis and SDOF models.

Chapter 2 Background and Literature Review

2.1 General

This chapter presents the background information required for the experimental and analytical investigation conducted in this thesis. It includes a review of the material properties and flexural behaviour of wood, the characteristics of FRP reinforcement, and the fundamental aspects of blast loading and structural response. In addition, previous studies related to timber elements subjected to static, dynamic, and blast loading are reviewed, with emphasis on strengthening and retrofitting applications relevant to CLT panels and glulam beams.

2.2 Wood as a construction material

Wood is widely used in structural applications due to its favorable strength-to-weight ratio, renewability, and versatility. However, as a natural material, its mechanical behaviour is influenced by growth characteristics, defects, grain orientation, moisture content, and loading conditions.

2.2.1 Properties of wood

Wood can be considered as an orthotropic material, as it has unique mechanical properties in the directions of three mutually perpendicular axes: longitudinal, radial, and tangential. The longitudinal axis, L, is parallel to the fiber (grain), the radial axis R is normal to the growth rings (perpendicular to the grain in the radial direction), and the tangential axis T is perpendicular to the grain but tangent to the growth rings. These axes are shown in Figure 2.1 (Ross 2010).

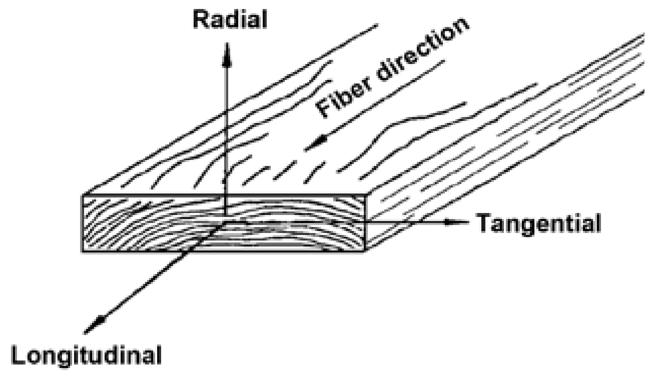

Figure 2.1 Three principal axes of wood concerning grain direction and growth rings (Ross 2010)

Flexural failure is categorized based on how the cracked surface appears and how the failure manifests itself. Figure 2.2 shows various static bending failure types. According to (ASTM (American Society for Testing and Materials) 2011) fractured surfaces can be categorized as "brash" and "fibrous", with "brash" denoting a sudden failure and "fibrous" denoting a fracture with splinters.

(a) Simple Tension (side-view)

(d) Brash tension (View of tension surface)

(b) Cross-grain tension (side-view)

(e) Compression (Side view)

(c) Splintering tension (View of tension surface)

(f) Horizontal shear (Side view)

Figure 2.2 Types of failures in static bending (ASTM (American Society for Testing and Materials) 2014)

In structural applications, wood members are typically loaded parallel to the grain in order to utilize the higher strength and stiffness available in the longitudinal direction. This is particularly relevant for flexural members such as glulam beams and the longitudinal laminations in CLT panels, where the structural response is governed primarily by the material properties parallel to the grain (Brandner et al. 2016; Lacroix and Doudak 2018c). Under short-duration loading conditions, such as those associated with blast events, timber members experience high strain rates that may alter their mechanical response compared to static loading conditions. Experimental studies on glulam beams subjected to simulated blast loads have shown that these high strain-rate effects influence both strength and deformation behaviour of timber elements (Lacroix and Doudak 2018b).

2.2.2 Flexural resistance of wood

In flexural applications, the behaviour of wood is governed primarily by the material properties parallel to the grain, particularly the tensile and compressive strengths in the longitudinal direction. Due to the orthotropic nature of wood and the presence of natural defects, the response of structural members under bending differs from that observed in clear wood specimens (Buchanan 1990). Bazan (1980) developed the stress-strain relationship for tension and compression of clear wood. Buchanan (1990) further developed the model to account for in-grade lumber. The stress-strain relationship used by Buchanan (1990) for in-grade lumber is shown in Figure 2.3.

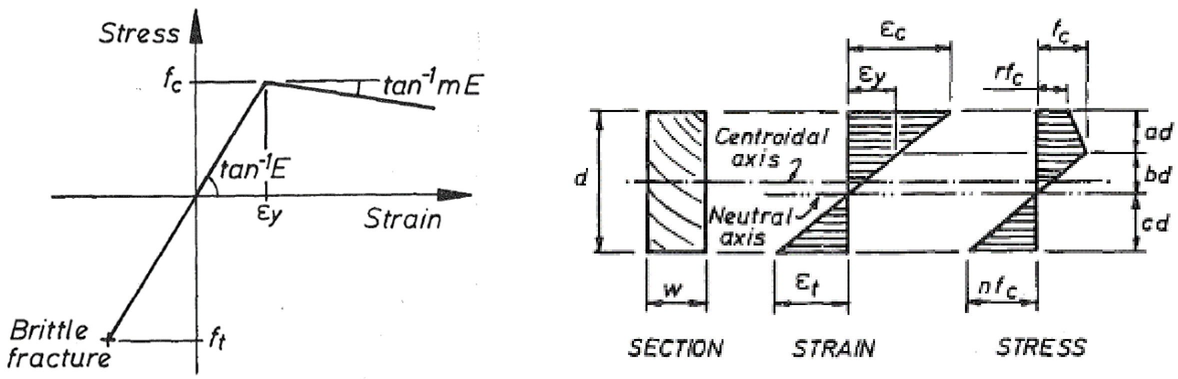

Figure 2.3 Model proposed by Buchanan (1990)

According to Figure 2.3, tension behaviour is assumed to be linearly elastic, with failure occurring at a stress f_t. In compression, a bilinear relationship is assumed, so that beyond the maximum compression stress f_c (and corresponding strain ε_y), the slope of the falling branch is a certain ratio, m, of the modulus of elasticity, E (Buchanan 1990).

2.3 FRP Reinforcement

Over the past decades, FRP composites have become widely adopted for strengthening and retro-fitting a variety of structures. FRP composites provide exceptional advantages, including high corrosion resistance, environmental durability, and an excellent stiffness-to-weight ratio. Additionally, their ease of application makes FRP highly appealing for civil infrastructure projects, particularly where constraints on weight, space, and time are significant considerations (Yi et al. 2010). The type of resin has a significant impact on the composites' failure mechanism and fracture toughness. In addition, there are numerous additional elements that affect how well FRP fabrics operate, such as fiber orientations, resin curing rate, manufacturing, and quality that have an impact on the performance of the FRP fabrics.

The most popular materials used to create FRP fabrics are typically glass, carbon, aramid, and basalt. FRP fabrics can be made with fibers that are unidirectional, bidirectional, triaxial, or quadriaxial (Figure 2.4). The fibers for bidirectional fabrics could be orientated at angles (±45) or right angles (0° / 90°). Also, there are two types of resin: thermoset and thermoplastic. Solid thermosetting resins, in contrast to thermoplastic resins, cannot be reshaped or returned to their initial liquid state after curing. Thermosetting resins such as epoxy resins, polyesters, and vinyl esters are used in the composite industry as the matrix. To improve and modify the properties of composite materials and to reduce costs, additives, and fillers can be implemented with resins. Epoxy resins offer a higher level of corrosion resistance and are less sensitive to heat and moisture than other polymeric substrates. The disadvantages are cost and longer curing cycles. Epoxy resins can be manufactured with various components or combined with other resins to produce specific qualities. Epoxy resins are compatible with glass, carbon, aramid, and basalt fibers and have great mechanical qualities, resistance to corrosive liquids and environments, and good performance at high temperatures.

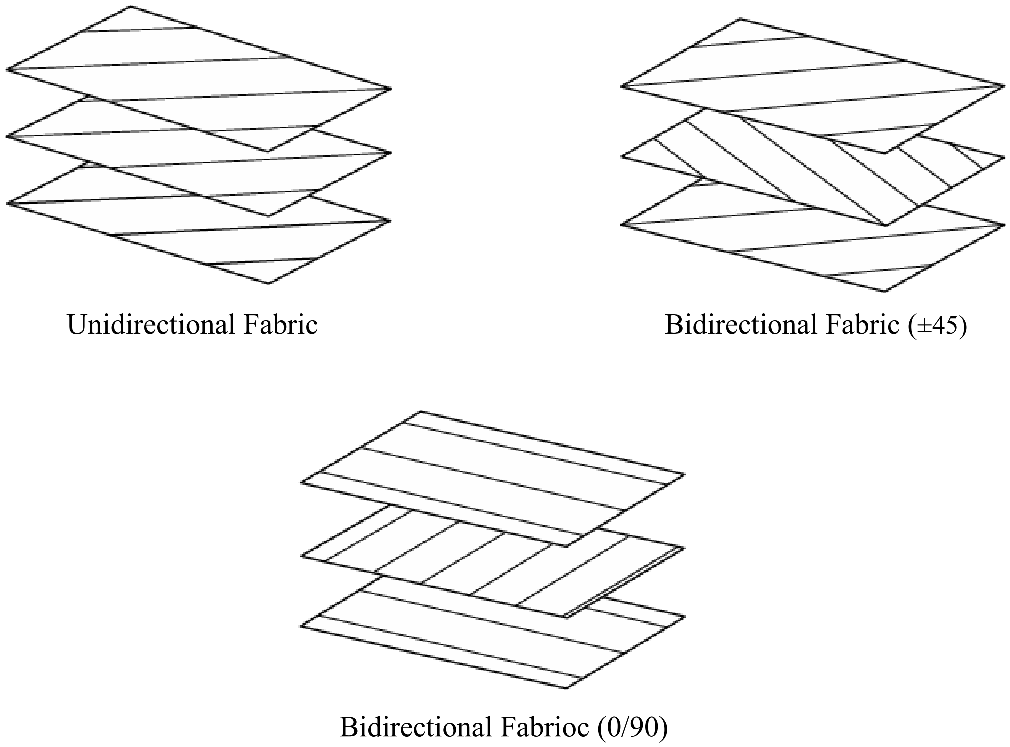

Figure 2.4 Unidirectional and bidirectional (0/90), FRP laminate configuration (Mallick 2007)

2.4 Blast wave characteristics and effects on the structures

2.4.1 Introduction

An explosion is a phenomenon associated with a sudden outward release of energy within a very short period. The energy is released in milliseconds and can be physical, chemical, or nuclear.

2.4.2 Source of blast

Deflagration and detonation are two groups of blasts involving chemical reactions according to their reaction rates. Deflagration is an oxidation reaction that spreads at a rate less than the speed of sound and the related blast wave is termed pressure (Figure 2.5).

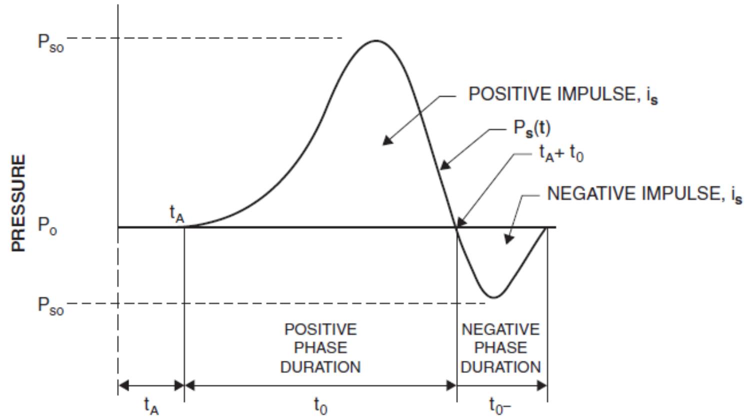

Figure 2.5 Pressure wave from deflagration (Dusenberry 2010)

In contrast, detonation propagates supersonically, and this blast wave is called a shock wave and has an immediate increase in pressure (Figure 2.6). Also, since pressure is related to reaction rate, the pressures produced by detonation are usually higher in comparison to deflagration pressures.

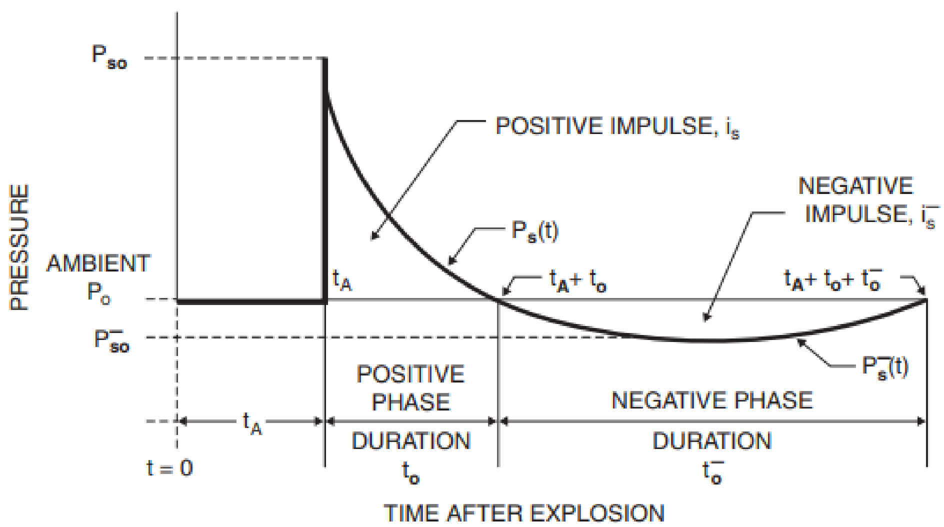

Figure 2.6 Shock wave from detonation (Dusenberry 2010)

High explosive materials detonate with supersonic reaction fronts. High-explosive materials are classified as primary, secondary, and territory explosives based on their sensitivity to initiation. Dynamite, TNT, and Semtex are examples of secondary high explosives. Tertiary explosives (e.g., ANFO) are much less sensitive to initiation in comparison to primary and secondary explosions and a powerful charge is required to initiate detonation. Low explosives such as solid and liquid rocket propellants, gun propellants, and black powder have relatively low reaction rates and therefore lead to low blast pressure output since they do not detonate, and they are used to create gas, sound, smoke, and flash or sound (Dusenberry 2010).

2.4.3 Blast wave parameters

When a high explosive detonates, the chemical reaction generates highly pressurized, hot gases. As these gases rapidly expand, they displace the surrounding air and force it outward from the volume they occupy. Consequently, a layer of compressed air termed shock or blast wave is produced in front of the expanding gas. As illustrated in Figure 2.7 the pressure created by the explosion increases the ambient pressure ($P_o = 101.3$ KPa) to a peak pressure P_{so} (also known as peak overpressure or side-on overpressure) at the arrival time t_A, when the shock front reaches that point. The peak pressure decreases at an exponential rate until reaching the ambient pressure at $t_A + t_o$ (t_o time-related to positive phase duration). The pressure wave reflects off a structure's surface when it interacts with it, creating what is known as reflected pressure. The side-on overpressure is often smaller than the reflected pressure.

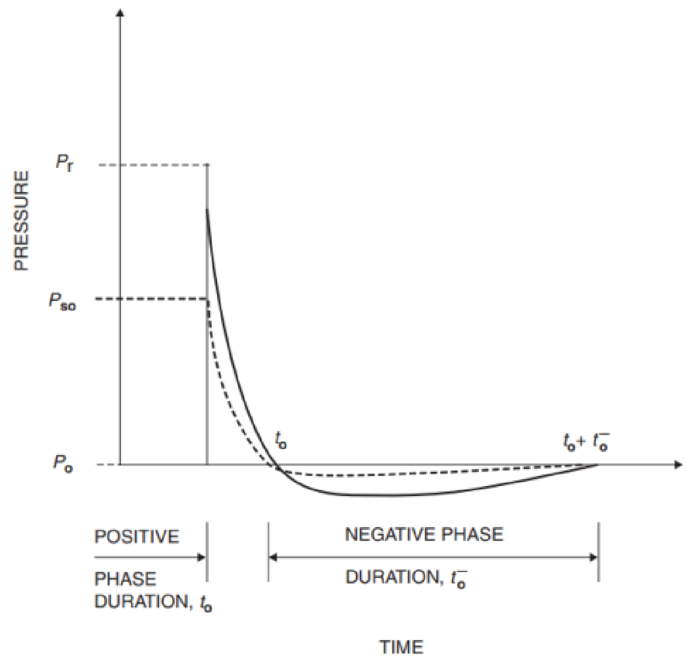

Figure 2.7 Reflected pressure vs. side-on overpressure (Cormie, et al. 2009)

The time-varying reflected pressure of any blast wave shown in Figure 2.7 can be approximated by the Friedlander exponential equation (Equation 2.1) (Cormie, et al. 2009). The positive and negative impulses $I^+$and I^-, representing the area under the pressure-time histories shown in Figure 2.7, can be determined using Equation2.2 and Equation 2.3, respectively.

$$\mathrm{P_r(t) = P_r\ e^{(-bt/t_d)}\left(1 - \frac{t}{t_d}\right)} \qquad \text{Equation 2.1}$$

$$\mathrm{I^+ = \int_{t_A}^{t_A+t_o} P_r(t)\, dt} \qquad \text{Equation 2.2}$$

$$\mathrm{I^- = \int_{t_A+t_o}^{t_A+t_o+t_o^-} P_r(t)\, dt} \qquad \text{Equation 2.3}$$

Where t is time, t_d is the idealized positive phase duration, P_r is the peak reflected pressure, and b is the decay coefficient of the waveform parameter.

2.4.4 Dynamic Analysis

2.4.4.1 Single-Degree-of-Freedom Analysis

The blast load has a short duration compared to static loads such as dead and live loads, and other dynamic loads like wind and earthquake. This requires that inertial forces and kinetic energy be accounted for in the analyses and design of structural elements. Studies have shown that the equivalent single degree of freedom (SDOF) analysis method is adequate in predicting the blast behaviour of various structural elements (Viau and Doudak 2016; Poulin et al. 2018; Ciornei 2012). Considering the SDOF system as shown in Figure 2.8, the closed-form solution of these systems is obtained by solving the equation of motion shown in Equation 2.4 (Biggs 1964; Chopra 2017).

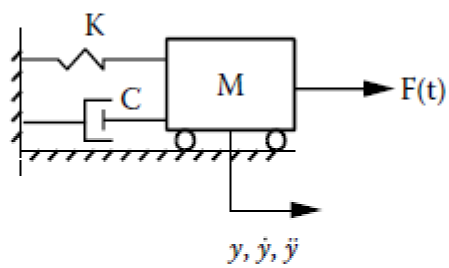

Figure 2.8 Single degree of freedom system

$$M\ddot{y} + C\dot{y} + Ky = F(t) \qquad \text{Equation 2.4}$$

Where *M* is the mass, *C* is the damping constant, *K* is the spring constant, *F(t)* is a time-varying forcing function, and $\ddot{y}$, $\dot{y}$, and y are the acceleration, velocity, and displacement of the system, respectively. Due to the short duration of the blast load, damping effects can typically be neglected (Svecova and Eden 2004; Dumais 2008; Syron 2010). The equation related to the motion for an undamped system with a damping coefficient equal to zero is shown in Equation 2.5.

$$M\ddot{y} + Ky = F(t) \qquad \text{Equation 2.5}$$

As shown in Equation 2.6, the solution of the equation of motion (Equation 2.5) can be solved for a forcing function idealized as triangular. Following the end of the forcing function, the solution is given by   Equation 2.7. This solution is only relevant to an SDOF system in which forces act in the same direction and the mass, stiffness, and forcing function are applied at a single point.

$$y(t) = \frac{F_1}{K}\left(\frac{\sin(w_n t)}{w_n t_d} - \cos(w_n t) - \frac{t}{t_d} + 1\right) \qquad \text{Equation 2.6}$$

$$y(t) = \frac{F_1}{K}\left(\frac{\sin(w_n t) - \sin(wn(t - t_d)}{t_d} - \cos(w_n t)\right) \qquad \text{Equation 2.7}$$

Where k is the stiffness, t_d is the idealized positive phase duration of the triangular forcing function, w_n is the natural frequency as shown in Equation 2.8, and F_1 is the maximum force at the arrival of the shock wave front.

$$w_n = \sqrt{\frac{k}{m}} \qquad \text{Equation 2.8}$$

2.4.4.2 Equivalent SDOF Analysis

For continuous structural systems such as beams and slabs, a transformation to an equivalent SDOF system is needed. In order to define an equivalent SDOF system it is necessary to evaluate transformation factors based on mass K_M, load K_L, and stiffness K_R factors. These transformation factors must be based on the assumed shape of actual structures (Biggs 1964). The equivalent equation of motion is provided in Equation 2.9.

$$K_M(m\ddot{y}) + K_R R(y) = K_L F(t) \qquad \text{Equation 2.9}$$

Equation 2.10 and Equation 2.11 define the mass and load transformation factors, respectively. The factors K_R and K_L represent similar force distributions and therefore have the same value, whereas K_M corresponds to the inertia force, which is dynamic in nature and thus takes a different value (Biggs 1964).

$$K_M = \frac{\int_0^L [\bar{m}\,(x)\varphi^2(x)]dx}{\int_0^L [\bar{m}\,(x)]dx} \qquad \text{Equation 2.10}$$

$$K_L = \frac{\int_0^L [f(x,t)\varphi(x)]dx}{\int_0^L [f\,(x,t)]dx} \qquad \text{Equation 2.11}$$

Where $f(x,t)$ is the distributed forcing function, $\varphi(x)$ is the assumed shape function, $\bar{m}(x)$ is the distributed mass, L is the length of the element with distributed force, stiffness, and mass. By presenting a single transformation factor, K_{LM}, as defined in Equation 2.12 (Biggs 1964), the equation of motion can be defined as outlined in Equation 2.13.

$$K_{LM} = \frac{k_M}{K_L} \qquad \text{Equation 2.12}$$

$$K_{LM}(m\ddot{y}) + R(y) = F(t) \qquad \text{Equation 2.13}$$

2.5 High strain-rate effects on wood properties

2.5.1 Wood Under Impact Loading

The influence of loading rate on the compressive and flexural strength of two hardwood and two softwood species was investigated by (Markwardt and Liska 1956). Their results demonstrated that increasing the loading rate by a factor of ten led to an approximate 8% rise in ultimate strength, with a 2.5% increase observed when the rate was merely doubled. Despite these strength variations, the modulus of elasticity in both flexure and compression-parallel-to-grain tests remained substantially constant across all loading rates.

The effect of loading rate on the tensile strength of Douglas fir was examined by testing specimens with and without intentional notches under strain rates ranging from 3×10^{-7} to 6×10^{2} s^{-1} (Nadeau et al. 1982). The notches were introduced to encourage crack initiation and simulate flaws commonly found in timber elements. The results revealed that only the unnotched specimens exhibited increased strength with higher loading rates. In contrast, the notched specimens showed no significant rate dependence, suggesting that pre-existing flaws dominate failure behaviour regardless of loading speed.

Jansson (1992) conducted an extensive investigation into the behavior of timber beams under both static and impact loading conditions, using a total of 651 specimens. This study found that impact loading generally led to increased failure strength compared to static loading. Additionally, the mode of failure shifted, with a notable decrease in compression-initiated failures as the loading rate increased. The study emphasized the need to use strength ratios, dynamic to static stress, as a more accurate measure of rate effects and highlighted that loading rate significantly influences both failure stress and mode in timber beams.

Sukontasukkul (2000) studied the behavior of Parallel Strand Lumber (PSL) under both static and impact loading conditions through flexural testing. Their results showed that PSL primarily failed through a combination of shear and bending in both types of loading. The material demonstrated strain rate sensitivity, with strength increasing by approximately 30% as the stress rate rose by a factor of 4.7×10^{4}. However, at higher impact rates, localized damage at the point of contact led to a decrease in apparent strength and more brittle failure behaviour.

Syron (2010) investigated the strain rate-dependent behaviour of two grades of laminated strand lumber (LSL) under compression and tension. Results showed significant increases in compressive strength and transverse modulus of elasticity under higher strain rates.

2.5.2 Light-Frame Wood Stud Walls Under Blast Loading

Lacroix and Doudak (2015) carried out an experimental study on 20 full-scale wall specimens with different sheathing types (OSB and plywood). Some walls were tested under static loading, while others were subjected to simulated blast loading using a shock tube. This allowed for a direct comparison between static and dynamic behaviour. The results showed that flexural behaviour controlled failure in both cases. However, the nature of failure was different. As shown in Figure 2.9 under static loading, the walls exhibited a more gradual, splintering type of tension failure. In contrast, under dynamic loading, failure occurred more suddenly through a brittle rupture of wood fibres due to the rapid loading rate.

(a) Static test: W3 (b) Dynamic test W20-3

Figure 2.9 Comparison between static and dynamic failure (Lacroix and Doudak 2015)

The study also highlighted additional behaviours under blast loading, such as nail withdrawal and out-of-phase movement of studs after peak displacement, which were not observed in static tests (Figure 2.10). These effects were mainly attributed to the limited stiffness of the sheathing and the weakness of connections. To quantify the influence of strain rate, the authors used an equivalent SDOF model to DIFs. The results showed that dynamic loading increased the wall capacity and stiffness, with average DIF values of approximately 1.40 for resistance and 1.18 for stiffness. Overall, the study demonstrated that timber walls can exhibit significantly higher strength under blast loading compared to static conditions, and that strain rate effects should be considered in design.

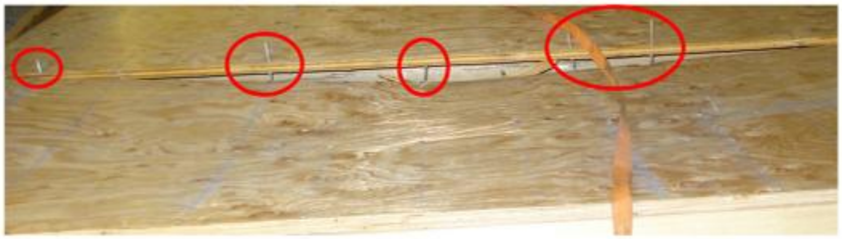

W20-3

Figure 2.10 Nail withdrawal observed in dynamic tests (Lacroix and Doudak 2015)

2.5.3 Glulam Beams and Columns Under Blast Loading

The influence of high strain-rate loading on the flexural behaviour of glulam beams has been investigated experimentally by Lacroix and Doudak (2018a). In their study, thirty-eight glulam beams with three different cross-sections were tested under both static and dynamic loading conditions using four-point bending. Dynamic loading was generated using a shock tube apparatus capable of simulating blast-type pressure waves, allowing strain-rates representative of blast events to be achieved. The results showed that glulam beams subjected to dynamic loading experienced different failure characteristics compared with static loading. Under static conditions, the beams generally exhibited a typical splintering tension failure initiating at defects such as knots or finger joints and propagating along the laminations. However, under dynamic loading, a more brittle brash tension failure was observed, where the fibers fractured more abruptly due to the shorter load duration. Failure mode that was observed during static testing is illustrated in Figure 2.11, where tension failure initiated in the outer lamination and propagated along the beam depth.

B2- [137] (tension side up)

Figure 2.11 Static failure mode of glulam beam (Lacroix and Doudak 2018a)

Figure 2.12 shows the failure mode observed in the dynamic test. In several specimens, failure initiated near the finger joint located in the high moment region, indicating that the presence and location of finger joints can influence the failure mechanism under high strain-rate loading.

(a) B19-[80]

Figure 2.12 Dynamic failure mode glulam beam (Lacroix and Doudak 2018a)

The experimental results indicated that glulam beams without continuous finger joints in the outer tension lamination exhibited an average strength increase of approximately 1.14 for strain-rates between 0.14 and 0.51 s^{-1}. However, when finger joints were present in the high moment region, the dynamic strength increase was not observed, suggesting that the presence of finger joints can significantly influence the dynamic resistance of glulam members.

Lacroix and Doudak (2018b) investigated the behavior of glulam beams and columns under dynamic loading using a shock tube facility to simulate blast-type pressure waves. The experimental program included glulam beams subjected to lateral loading without axial force and glulam columns subjected to combined lateral and axial loads. The results demonstrated that the structural response and failure mechanisms of glulam members are significantly influenced by strain-rate effects and axial load interaction. Representative failure modes observed during the dynamic tests, beam specimens without axial load primarily experienced tensile rupture in the outer tension lamination. In contrast, column specimens subjected to combined axial and lateral loading exhibited more complex failure mechanisms involving both tensile cracking and compression damage near the midspan region.

2.5.4 CLT Panels Under Blast Loading

Poulin et al. (2018) experimentally investigated the out-of-plane behaviour of CLT panels subjected to static and simulated blast loading in order to evaluate strain-rate effects on structural response. The experimental program included eighteen CLT panels consisting of 3-ply (105 mm) and 5-ply (175 mm) panels manufactured from spruce-pine-fir lumber. Static tests were conducted using four-point bending, while dynamic tests were performed using a shock tube facility capable of generating blast-type pressure waves. The results showed that CLT panels generally exhibited linear elastic behaviour up to peak load, followed by failure initiated in the outer tension lamination. Under dynamic loading conditions, two primary failure modes were observed: flexural failure and rolling shear failure within the transverse layers. Representative examples of these failure mechanisms are shown in Figure 2.13 and Figure 2.14, where flexural damage and rolling shear cracking can be observed. The study also reported an average dynamic increase factor (DIF) of approximately 1.28, indicating an increase in resistance under high strain-rate loading while stiffness remained relatively unchanged.

(a) failure of a 3-ply panel (CLT3-5.1)

(b) failure of a 5-ply panel (CLT5-4.1)

Figure 2.13 Representative flexural failure observed in CLT panels subjected to simulated blast (dynamic) load (Poulin et al. 2018)

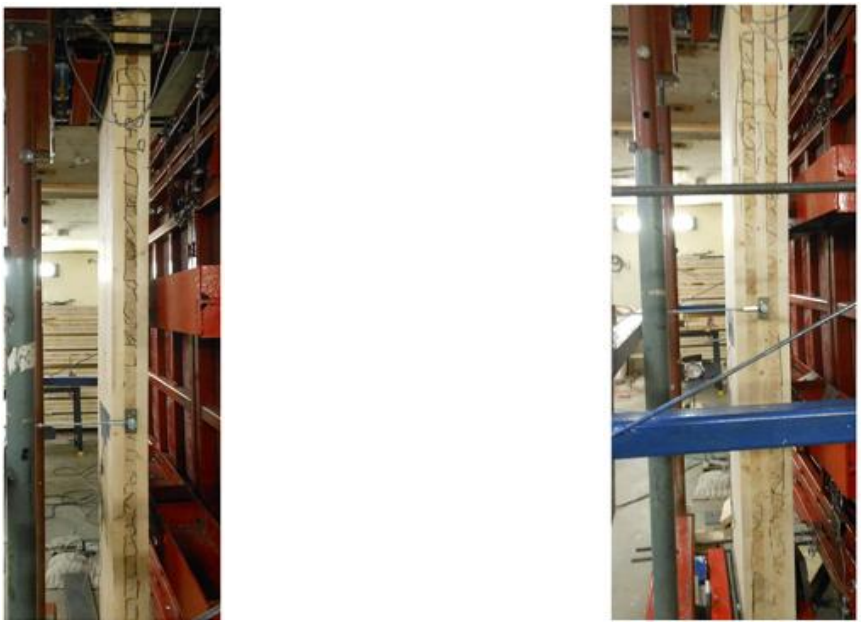

(a) 3-ply panel specimen CLT3-4.2 (b) 5-ply panel specimen CLT5-5.1

Figure 2.14 Representative rolling shear failure observed in CLT panels subjected to simulated blast (dynamic) loading(Poulin et al. 2018)

Oliveira et al.(2023) developed a finite element (FE) model to investigate the behaviour of mass timber members subjected to blast loading. The study focused on glulam beams and CLT panels exposed to shock-tube generated blast pressures. The numerical model was implemented in ABAQUS/Explicit using a user-defined material subroutine based on continuum damage mechanics (CDM) to capture the anisotropic behaviour of wood. Eight failure criteria were incorporated to represent different damage mechanisms in timber. The modelling approach was validated using results from full-scale experimental tests on glulam beams and CLT panels subjected to simulated blast loads under dynamic four-point bending conditions. Overall, the numerical predictions showed good agreement with the experimental results in terms of displacement histories, resistance curves, and observed failure modes. For CLT panels, the structural response was more complex due to the presence of transverse layers. Damage typically initiated as rolling shear failure within the transverse laminations before flexural failure developed in the outer longitudinal layer. Overall, the study showed that finite element models based on continuum damage mechanics can effectively capture the blast response of mass timber members and simulate complex failure mechanisms that are difficult to represent using simplified analytical approaches.

Saloo and Viau (2025) investigated the structural response of CLT panels subjected to contact charge detonations and near-field blast loading using a finite element (FE) approach. The study highlighted an important gap in the literature, particularly related to the behaviour of mass timber under close-in explosions. A numerical model was developed in LS-DYNA using the MAT_143 wood material model, along with the Load Blast Enhanced (LBE) method to simulate blast pressures. The model was validated against experimental results and showed good agreement, indicating that it can reasonably capture both displacement response and failure behavior. The results showed that failure in CLT panels was mainly governed by flexural behaviour, typically initiating in the tension-side lamination.

2.5.6 GLT Under Blast Loading

Krouma and Doudak (2026) studied the behavior of glue-laminated timber panels (GLT) under static and dynamic blast load. A total of sixteen spruce pine GLT subjected to four-point loading with simply supported boundary conditions were tested. The main objective of this study was to establish the strength increase factor (SIF) and DIF, while also investigating the failure mode and capability of the SDOF model to predict the dynamic response of the GLT panels. The results show that the SIF values for GLT panels ranged between 1.6 and 1.9, with values of 1.6 and 1.9 corresponding to the panel depths of 130 mm and 215 mm, respectively. These findings were consistent with the values recommended in the Canadian blast design standard for solid sawn lumber and MSR lumber, indicating that the recommended design values can also be applied to GLT panels.

Under a high strain rate of approximately $0.2s^{-1}$, representing far field blast loading, the GLT panels exhibited increased resistance, and a DIF of 1.1 was found to be suitable for design purposes. However, no significant increase in panel stiffness was observed when comparing static and dynamic responses. The dominant failure modes remained consistent under both static and dynamic loading and were characterized by simple tension flextural failure initiated in tension laminate at mid span. As shown in Figure 2.15 both loading conditions exhibited linear and brittle behaviour up to maximum resistance. Furthermore, SDOF model showed good agreement with experimental results when appropriate input parameters were used, confirming its suitability for predicting the dynamic response of GLT panels and its applicability in blast resistance design.

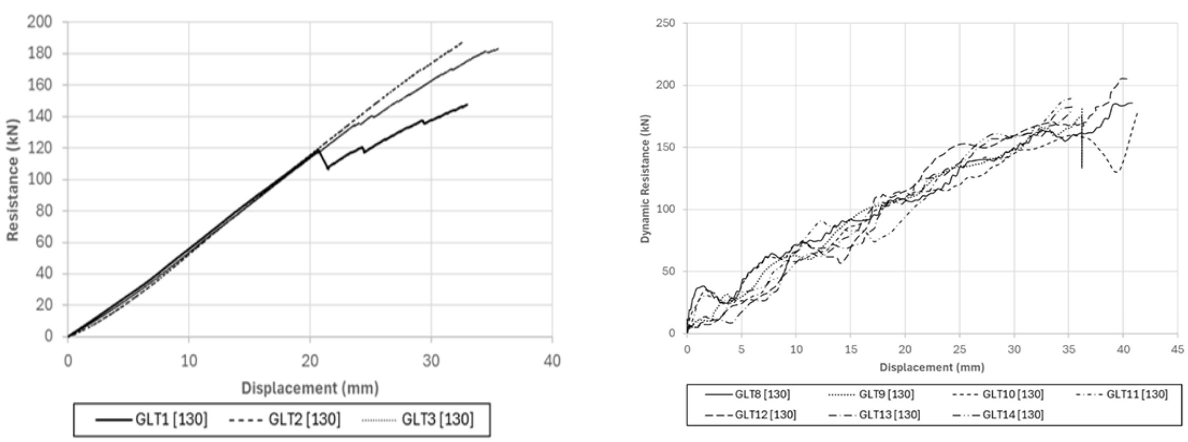

(a) Static (b) Dynamic

Figure 2.15 Static and dynamic resistance of GLT panels with 130 mm depth

2.6 Previous research on retrofitting timber structures

2.6.1 FRP as a retrofit option for flexural strengthening

For enhancing the structural capabilities of wood components through reinforcement, there are two main reinforcing techniques, including near-surface mounted (NSM) and externally bonded reinforcement (EBR). Hernandez et al.(1997) investigated the possibility of employing FRP-reinforced glulam beams to decrease the total depth of the members. The impact of a full-length, unidirectional U-shaped CFRP wrap on 38 mm by 89 mm wood members was examined by Johns and Lacroix (2000). Borri (2001) conducted experiments on beams reinforced with carbon sheets (CFRP) applied on the tension side. The results demonstrated that the application of carbon reinforcement mainly enhanced the bending capacity of beams. Radford et al. (2002) and Hay et al. (2006) conducted similar tests on small beams by using fiberglass sheets. Alam et al. (2009) suggested the use of composite rods and bars placed within the grooves on the tension side of the beams to repair and reinforce timber beams.

Carbon fiber, glass fiber (GF), and high-strength glass fiber (SGF) were selected as strengthening materials by Yang et al. (2013) to improve the strengthening efficiency of wood beams. A flexural experimental study, including 12 strengthened beams and 3 control beams, was conducted to assess their performance. The study analyzed the failure modes, mechanisms, load-displacement behaviour, ultimate moment capacity, and ductility of each strengthened beam type. Results indicated that, compared to using CF or SGF alone, hybrid fiber-reinforced polymer (HFRP) strengthening significantly enhances ductility and increases moment capacity at a lower cost.

Yang et al. (2016) investigated the flexural strengthening of glulam beams using FRP and steel reinforcements through experimental four-point bending tests and theoretical analysis. The results demonstrated that reinforcing glulam beams significantly improved flexural strength, stiffness, and tensile strain capacity compared to unreinforced beams. Increasing the tensile reinforcement ratio enhanced ductility by shifting the failure mode from brittle tensile failure toward compressive failure of timber. In addition, reinforced beams with both tensile and compressive reinforcement showed more improvement in stiffness than in strength due to premature buckling or delamination of the compression reinforcement. Also, a theoretical model based on Buchanan's approach accurately predicted the flexural behaviour of reinforced beams, with most predictions within 10% of the experimental results.

Shekarchi et al. (2020) reinforced timber beams with flat, U-shaped, and L-shaped GFRP on the tensile or both tensile and compressive surfaces of beams. In this research, 24 specimens, including 20 strengthened beams and 4 unstrengthened (control) beams, were tested under a three-point bending test. In comparison to the control specimens, the mean values of modulus of rupture, flexural rigidity, ductility, and energy absorption of strengthened beams increased by up to 61%, 59%, 79%, and 209%, respectively.

O'Callaghan (2021) investigated the effects of varying GFRP composite configurations (fiber direction, thickness) on the behaviour of square-sawn timber columns under compression parallel to the grain. This experimental program tested six unwrapped control specimens and thirty GFRP-wrapped specimens to analyze changes in stress-strain characteristics and identify failure modes. Each specimen was dissected after testing to observe wood failure patterns. Results showed that adequate FRP wrapping thickness effectively prevented splitting and shearing failures, mitigating the impact of natural wood defects and promoting crushing failure in wood fibers.

Bakalarz et al (2022) studied reinforced laminated veneer lumber (LVL) beams using CFRP sheets under a four-point static bending test. The beams were reinforced with U-type reinforcement in three configurations, differing from each other in the thickness of the reinforcement and the coverage of the side surface. The configurations included beams reinforced with one layer of CFRP sheet bonded to the bottom side B, beams reinforced with two layers of CFRP sheet bonded to the bottom side C, beams reinforced with two layers of CFRP sheet covering entire side surfaces with overlap in the tension zone D. In compression to the unreinforced beam the average increase in bending resistance was 42%, 51%, and 58% and the average value of bending stiffness increased by 15%, 31% and 43% for the respective configurations, B, C, D. The failure mode of reinforced beams transitioned from brittle fracture starting in the tensile zone for unreinforced beams to a more ductile fracture, originating in the compression zone.

Chen et al. (2025) studied alternative GFRP reinforcement schemes for glulam under four-point bending, focusing on hoops and tension anchoring as substitutes for fan-type anchorage and full-length confinement. Experimental results demonstrate that both hoops and tension anchoring were effective in preventing undesirable failure modes. Hoops made with unidirectional fabrics provided better confinement and clamping pressure than those made with bidirectional fabrics, while tension anchoring with bidirectional fabrics showed improved peak load, stiffness, displacement capacity, and post-peak resistance. Full-length confinement produced the greatest enhancement in structural response; however, tension anchoring achieved comparable behaviour with less FRP material. In addition, the reinforced beams exhibited an average increase of approximately 16% in tensile failure strain compared to the unreinforced specimens, indicating a shift from shear-dominated failure mode toward more ductile flexural behaviour.

Gergi and Doudak (2026) investigated the flexural performance of timber elements strengthened with FRP systems through an experimental and analytical study. The research focused on glulam beams and CLT panels in order to evaluate how different CFRP reinforcement and confinement configurations influence the structural response of timber members subjected to bending. The experimental program included seven unretrofitted specimens consisting of glulam beams with two different cross-sections and one CLT panel. Several strengthening configurations were examined using externally bonded CFRP fabrics with different orientations such as 0/90° and ±45°. The results indicated that applying CFRP only on the tension face provided limited improvement in peak strength, primarily due to premature debonding of the CFRP from the timber surface. In contrast, configurations that combined tension reinforcement with confinement layers showed better structural performance, resulting in increased load-carrying capacity, stiffness, and deformation capacity. Retrofit layouts relying only on localized confinement were found to be less effective because they were not able to sufficiently restrain the tension reinforcement or prevent debonding failures. In addition to the experimental investigation, the authors developed an analytical model based on cross-sectional equilibrium and the assumption of a perfect bond between the CFRP and timber. The analytical predictions showed good agreement with the experimental results, demonstrating that the model can reasonably capture the flexural behaviour of CFRP-retrofitted timber elements.

2.6.2 Retrofitting structures under Blast load

Lacroix and Doudak (2018c) investigated the use of FRP composites as a strengthening technique for glulam beams subjected to simulated blast loading. The study examined four different retrofit configurations, as well as a repair approach for beams that had been previously damaged. The main objective was to evaluate how various FRP reinforcement schemes influence the strength, ductility, and failure behavior of glulam beams under both static and dynamic loading conditions. he beams were tested under both static loading and simulated blast loading using a four-point bending setup. The results showed that the addition of FRP reinforcement significantly improved the structural performance of the glulam beams. In particular, the use of two layers of GFRP tension reinforcement increased the resistance of the beams by approximately 1.35 times, while the displacement at maximum resistance increased by about 1.30 times compared with unretrofitted specimens. When confinement was included, the failure mode changed and premature debonding was reduced. The configurations using U-shaped reinforcement demonstrated notable post-peak behaviour. Overall, the study showed that combining longitudinal reinforcement with confinement can significantly enhance both the strength and ductility of glulam members subjected to extreme loading conditions.

Lacroix and Doudak (2020) investigated the use of multi-directional FRP fabrics to improve the behaviour of glulam beams subjected to blast loading. The study focused on enhancing the post-peak response and deformation capacity of glulam beams through FRP strengthening. The experimental program included ten FRP-retrofitted glulam beams, which were tested using a shock-tube apparatus. Several retrofit configurations were examined using combinations of unidirectional and bidirectional GFRP fabrics. These configurations were designed to provide both tension reinforcement and confinement of the timber section.

The results showed that the use of multi-directional FRP significantly improved the structural performance of the beams. Compared with unretrofitted specimens, the retrofitted beams exhibited noticeable increases in both strength and stiffness, with peak resistance improvements ranging from approximately 1.2 to 1.7 times that of the unreinforced beams. In addition, the FRP reinforcement led to a considerable increase in ductility, with ductility ratios between 2.3 and 3.6 being reported. The bidirectional FRP fabrics were found to play an important role in confining the timber fibres, which helped limit damage to a localized region of the beam. Another important observation was that the presence of FRP increased the ultimate tensile strain of the wood fibres. The study reported an average increase of approximately 20% in wood tensile failure strain, which was attributed to the ability of the FRP layers to bridge cracks and restrain crack growth. In addition to the experimental investigation, the authors proposed an analytical modelling approach to predict the flexural response of the retrofitted beams. The model was based on moment–curvature analysis combined with stress–strain relationships for wood and FRP materials. While the analytical model was able to predict the peak resistance and corresponding displacement with reasonable accuracy, a simplified two-step resistance model was proposed to represent the post-peak behaviour of the retrofitted members under blast loading.

Lopez and Doudak (2019) investigated retrofit techniques to improve the blast resistance of CLT panels. Seventeen full-scale CLT panels, including 3-ply and 5-ply specimens, were tested under simulated blast loading. Two retrofit strategies were examined steel straps and GFRP reinforcement. The results showed that steel straps had limited influence on peak resistance but significantly improved post-peak behaviour and ductility by confining damage and reducing rolling shear failure. In contrast, GFRP reinforcement provided greater improvements in structural performance, including increases in peak resistance, stiffness, and ductility. Overall, retrofitting increased the stiffness of CLT panels by approximately 10–28% compared with unretrofitted panels. The study concluded that while GFRP provides greater structural enhancement, steel straps offer a simpler and more economical retrofit solution

Gharaibeh (2025) examined the structural behaviour of glulam beams reinforced using the near-surface-mounted (NSM) technique with steel rebars and plates under both static and blast loading conditions. The study was motivated by the brittle tensile failure that often governs glulam beams in flexure, which limits their ability to dissipate energy when subjected to extreme loads such as explosions. The experimental program included sixteen reinforced glulam beams, which were tested under static four-point bending as well as dynamic blast loading generated using a shock tube device. Several reinforcement configurations were investigated using steel rebars (10M, 15M, and 20M) and steel plates embedded in the tension side of the beam. The reinforcement ratios varied between approximately 0.8% and 2.5%, allowing the study to evaluate the influence of reinforcement level on the structural performance of the beams. The results showed that NSM reinforcement significantly improved the structural response of the glulam beams. The load-carrying capacity increased by approximately 23% to 83%, while stiffness improvements ranged from 7.8% to 38.1% compared with unreinforced beams. The improved behaviour of the reinforced specimens can be observed in Figure 2.16, where the reinforced beams show higher resistance and larger deformation capacity relative to the control specimens.

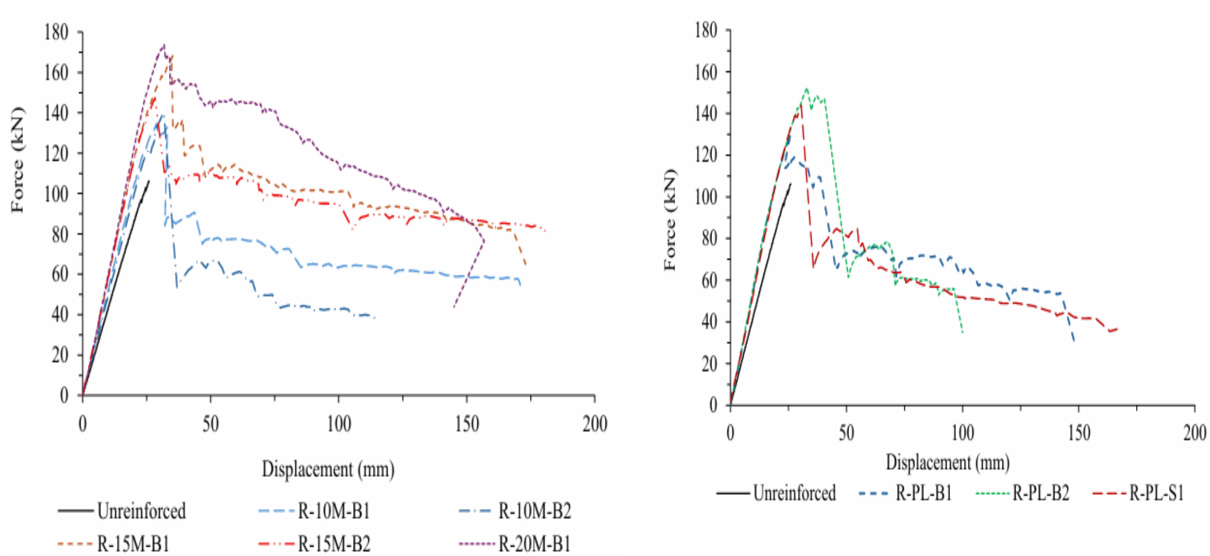

a) Rebars   b) Plates

Figure 2.16 Force-displacement curves of reinforced and unreinforced glulam beams obtained from static tests illustrating the increase in strength and deformation capacity due to NSM reinforcement (Gharaibeh 2025)

In addition to increased strength and stiffness, the reinforcement also enhanced the ductility of the beams, with ductility ratios reported between 1.1 and 7.2. The reinforcement changed the governing failure mechanism from brittle tensile rupture to compression crushing in the compression zone, resulting in a more ductile structural response. Dynamic tests performed using a shock tube further demonstrated that the reinforced beams exhibited higher resistance and improved behaviour under blast loading conditions. The dynamic load–displacement response of the specimens is presented in Figure 2.17, which shows the increased load capacity and deformation response of the reinforced beams under high strain-rate loading.

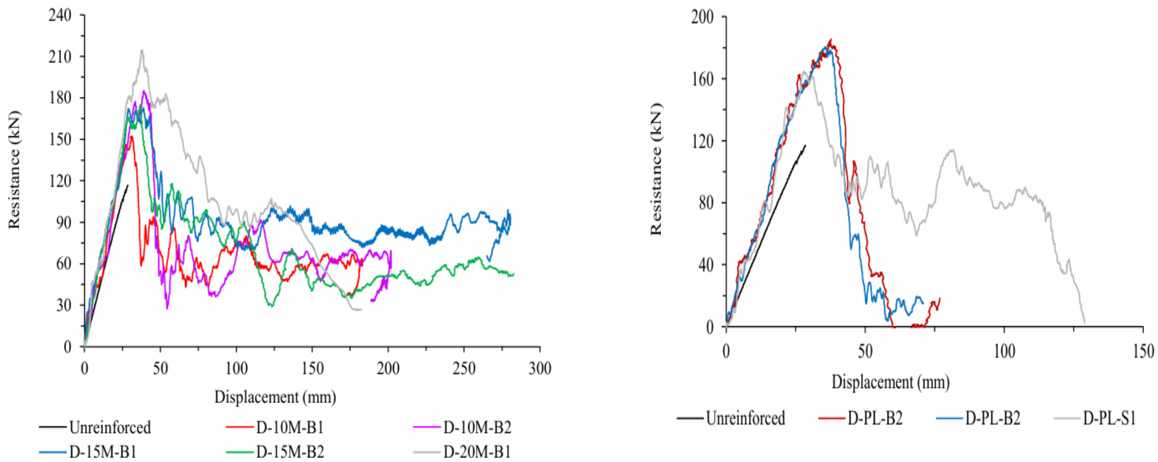

a) Rebars

b) Plates

Figure 2.17 Force-displacement curves of reinforced glulam beams under dynamic blast loading obtained from shock tube tests, illustrating the improved resistance and deformation capacity of NSM reinforced specimens (Gharaibeh 2025)

In addition to the experimental work, an analytical model was developed to simulate the behaviour of the reinforced beams. The model considered elastic, inelastic, and plastic hinge stages and represented the steel reinforcement as concentrated elements within the cross-section. The analytical predictions showed good agreement with the experimental results in terms of displacement response, strain development, and overall force–displacement behaviour. Overall, the study demonstrated that NSM reinforcement using steel rebars and plates is an effective strengthening technique for glulam beams, leading to significant improvements in strength, stiffness, ductility, and resistance to blast loading.

Chapter 3 Experimental Program

3.1 General

This chapter presents the experimental program conducted on unretrofitted and retrofitted CLT panels and glulam beams subjected to static and simulated blast loading. The primary objective of this experimental program is to evaluate the effectiveness of different retrofit strategies in improving the structural response and failure behaviour of timber elements under these loading conditions. The following sections describe the material properties, specimen preparation, retrofit configurations, and testing procedures.

3.2 Description of unretrofitted specimens

The unretrofitted specimens investigated in this study consisted of 3-ply CLT panels and glulam beams. The CLT panels were manufactured using grade E1. The layers in the major axis direction consist of 35 mm by 80 mm lumber with machine stress grade 1950Fb and Spruce-Pine-Fir (SPF) lumber species group. The transverse layers (minor direction) consist of No.3 / Stud grade SPF lumber. The panels have a width of 445 mm, a length of 2500 mm, and a thickness of 105 mm. The grade of glulam specimens was Nordic 24F-ES/NPG (NORDIC LAM+, Architectural Appearance), with beam dimensions of 137 mm x 222 mm and a length of 2500 mm. One glulam specimen with cross-sectional dimensions of 137 mm × 191 mm was also used as an unretrofitted control specimen for the dynamic testing program. The CLT and glulam specimens were conditioned before testing to an average moisture content of 13% and 14% at the time of testing.

3.3 Description of retrofitted specimens

A total of eight CFRP retrofit configurations were investigated for CLT panels, and five configurations were examined for glulam beams to improve their flexural behaviour and failure characteristics. The following sections describe the specimen nomenclature, test matrix, retrofit layouts, and instrumentation of the specimens.

3.4 Specimens Nomenclature

A general labeling system was adopted to distinguish between CLT panels and glulam beams, unretrofitted and retrofitted specimens, and the type of strengthening system applied. Specimen identifiers begin with an abbreviation representing the timber product type, where CLT denotes cross-laminated timber panels, and G denotes glulam beams. Unretrofitted control specimens are identified solely by the timber product abbreviation. Retrofitted specimens are identified by additional notation describing the retrofit material and configuration. For CFRP-retrofitted specimens, the notation further specifies the function and configuration of the CFRP layers, including tension reinforcement (T), confinement (C), U-shaped confinement (U), and application in regions of maximum moment (M) or maximum shear (SH). For some configurations, two specimens were tested. These repeated specimens are identified using numerical suffixes such as “1” and “2”, which indicate duplicate tests conducted for the same retrofit configuration. The fibre orientation of each CFRP layer is indicated in parentheses, and subscripts are used to denote multiple layers when applicable.

3.5 Summary of test matrix

Table 3.1 summarises the specimen identification, retrofit condition, strengthening configuration, and loading types for all CLT panel specimens tested in this study.

Table 3.1 Summary of test matrix for CLT specimens

Retrofit No	Specimen ID	Retrofit Configuration	Confinement Type	Loading type
-	Unretrofitted CLT	Unretrofitted control	-	Static/Dynamic
1	CLT-1	CLT-C(±45)	Full-Length	Static
2	CLT-2	CLT-T(0)C(0)	Full-Length	Dynamic
		CLT-T(0)C(0)-1		Static
		CLT-T(0)C(0)-2		Static
3	CLT-3	CLT-T(0)C(±45)	Full-Length	Dynamic
		CLT-T(0)C(±45)-1		Static
		CLT-T(0)C(±45)-2		Static
4	CLT-4	CLT-T(0)SH(±45)-1	Partial (shear)	Static
		CLT-T(0)SH(±45)-2		Static
5	CLT-5	CLT-T-M(0)C(±45)	Partial (Moment region)	Static
6	CLT-6	CLT-T-M-SH(0)C(±45)	Partial (Moment + shear)	Static
7	CLT-7	CLT-T$(0)_2$C(±45)	Full-length	Static/Dynamic
8	CLT-8	CLT-T(0)U(±45)	U-shaped	Static/Dynamic

Table 3.2 presents the corresponding test matrix for the glulam beam specimens, including specimen identification, CFRP retrofit configuration, and loading type.

Table 3.2 Summary of text matrix for glulam specimens

Retrofit No	Specimen ID	Retrofit Configuration	Confinement type	Loading type
-	G	Unretrofitted control	-	Static/Dynamic
9	G-9	G-T(0)C(±45)	Full-Length	Static/Dynamic
10	G-10	G-T(0)M(±45)	Partial (Moment region)	Static
11	G-11	G-T(0)C(0)	Full-Length	Dynamic
12	G-12	G-T$(0)_2$C(±45)	Full-Length	Dynamic
13	G-13	G-T(0)U(±45)	U-shaped	Dynamic

3.6 Application procedure (CFRP)

The CFRP strengthening system was installed following standard surface preparation and wet lay-up procedures recommended by the manufacturer. Before CFRP installation, the corners of each CLT panel were routed to a radius of 19.05 mm (3/4″) to reduce localized stress concentrations, and the timber surfaces were mechanically roughened to enhance epoxy penetration and bond performance. Following surface treatment, the prepared surfaces were cleaned to remove dust and debris prior to CFRP application. Figure 3.1 Surface preparation of timber specimens before CFRP installation. Figure 3.1 shows the surface preparation of the samples before applying CFRP fabrics.

a) Routing sample

b) Roughening sample

Figure 3.1 Surface preparation of timber specimens before CFRP installation

Figure 3.2 illustrates the prepared specimens, showing the roughened and routed surfaces as well as the attached strain gauges.

a) Prepared CLT

b) Prepared glulam

Figure 3.2 Prepared specimens showing roughened and routed surface with strain gauges attached

The Tyfo® S Epoxy, a two-component epoxy matrix, was used for bonding the Tyfo® CFRP fabrics. A primer epoxy layer was first applied to the timber surface, followed by a layer of saturating resin. The CFRP fabric was then placed onto the resin-coated surface and manually consolidated using rollers and hand pressure to ensure full fibre impregnation and eliminate air voids. Additional resin was applied as required to achieve complete saturation of the fabric. For retrofit configurations involving multiple CFRP layers or different fibre orientations, the fabrics were applied sequentially according to the specified stacking sequence. In cases requiring localized strengthening or confinement, the CFRP fabric was applied only in designated regions, such as near beam ends or within high-moment zones between loading points. After installation, the specimens were cured under laboratory ambient conditions for a minimum of 7 days, as recommended by the manufacturer, before testing. Figure 3.3 illustrates the CFRP installation process on CLT panels and glulam beams.

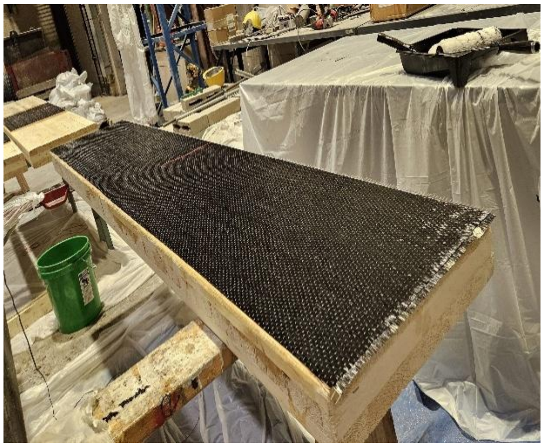

a) CFRP application along the tension side (CLT panel)

b) Localized CFRP strengthening in selected regions (CLT panels)

c) CFRP application along the tension side (Glulam beams)

d) Full-length and partial-length confinement of CFRP before curing (Glulam beams)

Figure 3.3 CFRP strengthening installation on CLT panels and Glulam beams

3.7 Retrofit configurations – (CLT panel and CFRP fabric)

Two types of CFRP fabrics were included in this phase: unidirectional CFRP (Tyfo® SCH-11 UP) and ± 45-degree bidirectional CFRP (Tyfo® BCC). Figure 3.4 shows Retrofits 1 through 4. Retrofit 1 (Figure 3.4a) consisted of a single layer of bidirectional CFRP fabric (±45°) as full-length confinement as a baseline reference, against which the effects of additional tension reinforcement and confinement, such as U-shaped, were evaluated. Retrofit 2 (Figure 3.4b) included one layer of unidirectional CFRP applied as tension reinforcement, and an additional layer of unidirectional CFRP applied perpendicular to the wood grain to investigate the effect of confinement. Retrofit 3 (Figure 3.4c) was identical to Retrofit 2 but used bidirectional CFRP fabric (±45°) for confinement instead of unidirectional fabric. Retrofit 4 (Figure 3.4d) investigated the effect of unidirectional CFRP tension reinforcement combined with partial confinement using a single layer of bidirectional CFRP fabric (±45°).

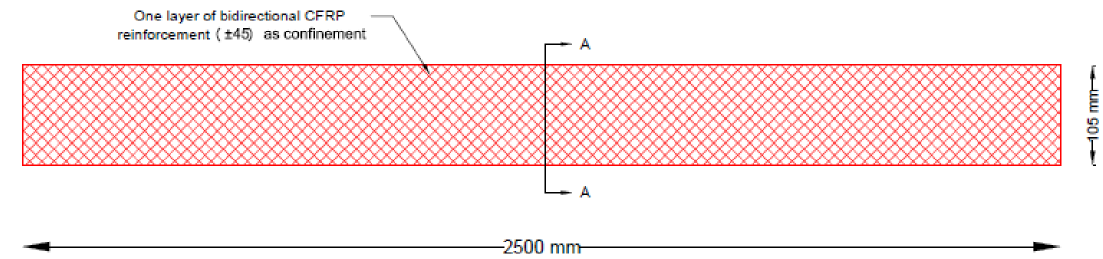

Retrofit 1: CLT-C(±45)

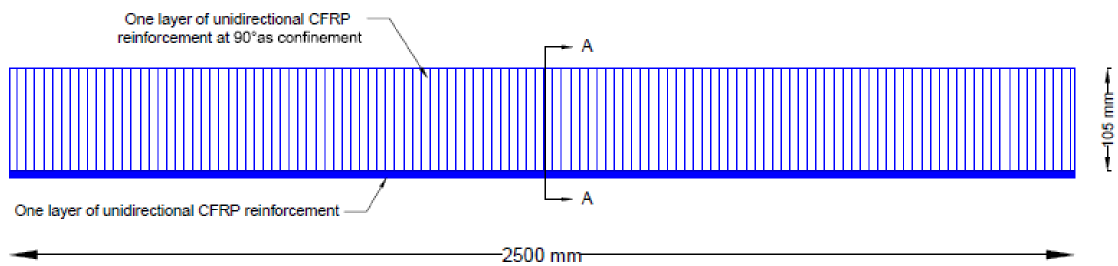

Retrofit 2: CLT-T(0)C(0)

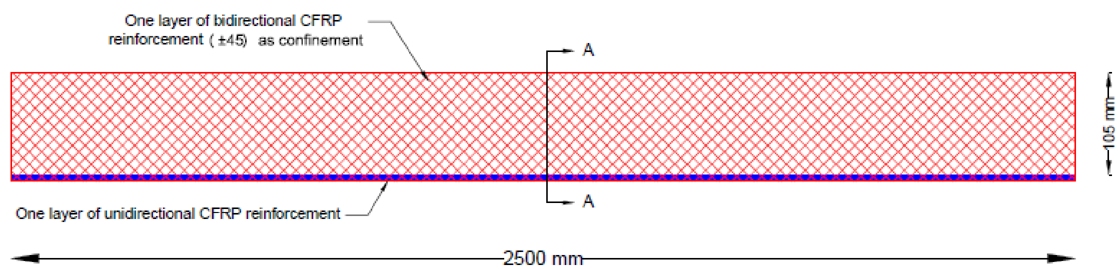

Retrofit 3: CLT-T(0)C(±45)

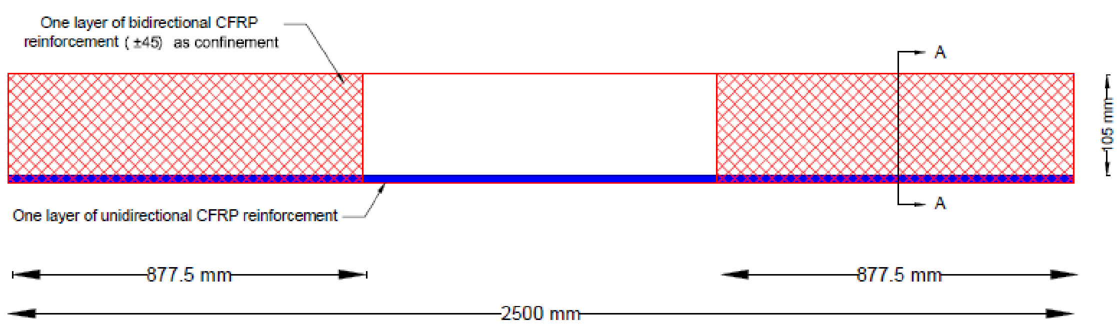

Retrofit 4:CLT-T(0)SH(±45)

Figure 3.4 Description of Retrofit 1 through 4 (CLT and CFRP)

Retrofit 5 (Figure 3.5a) consisted of a single layer of unidirectional CFRP applied as tension reinforcement and restricted to the central one-third of the beam, where the maximum bending moment occurs. This configuration was selected to target the critical flexural region, providing effective strengthening. Retrofit 6 (Figure 3.5b) is identical to Retrofit 5, with the exception that the unidirectional CFRP fabric was extended beyond the central one-third of the beam. This configuration was selected to evaluate whether increasing the bonded length of the tension reinforcement enhances flexural capacity and influences the failure mode. In Retrofit 7 (Figure 3.5c), two layers of unidirectional CFRP fabric were applied to the tension side of the panel to examine the effect of increased reinforcement ratio on flexural capacity, stiffness, and failure behaviour. Finally, in Retrofit 8 (Figure 3.5d), unidirectional CFRP fabric was applied along the full tension side, and a U-shaped wrap of bidirectional CFRP fabric (±45°) was used to provide confinement at the bottom and sides of the panel. This configuration simulates a condition where access to the top of the panel is restricted.

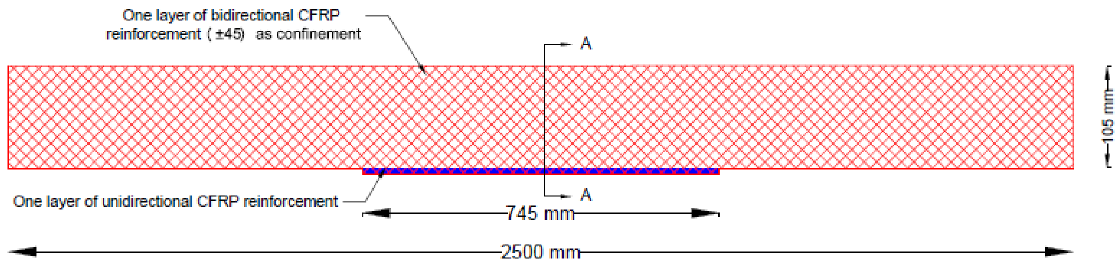

Retrofit 5: CLT-T-M(0)C(±45)

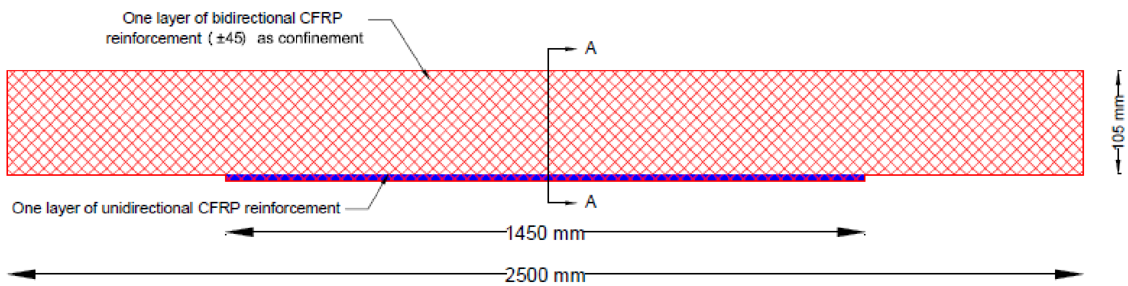

Retrofit 6: CLT-T-M-SH(0)C(±45)

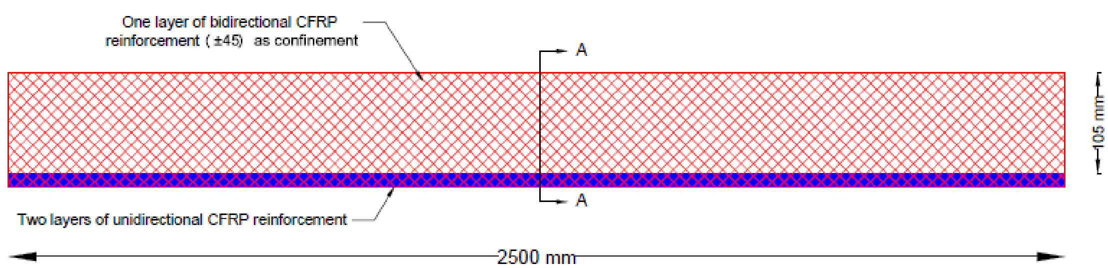

Retrofit 7: CLT-T$(0)_2$C(±45)

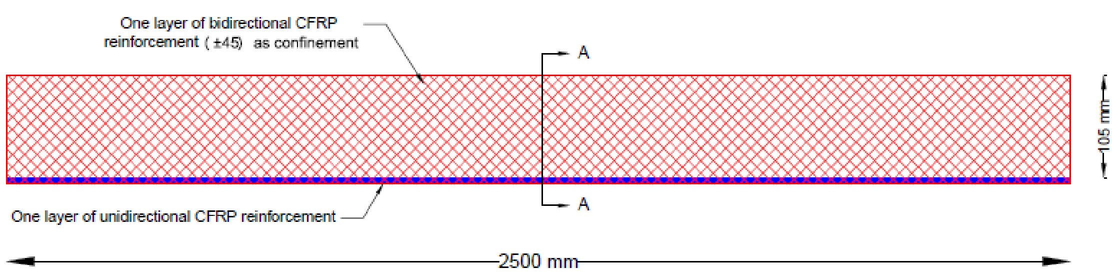

Retrofit 8: CLT-T(0)U(±45)

Figure 3.5 Description of Retrofit 5 through 8 (CLT and CFRP)

The reinforcement summary for all cross sections of the retrofitted CLT panel with CFRP is shown in Table 3.3.

Table 3.3 Cross-section summary of Retrofit 1-8

Cross-section and CFRP retrofit configuration of CLT

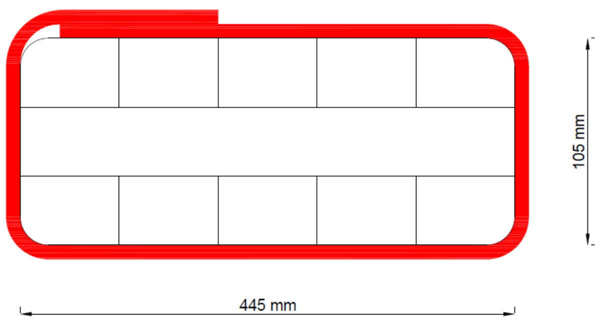

a) Retrofit 1: CLT-C(±45)

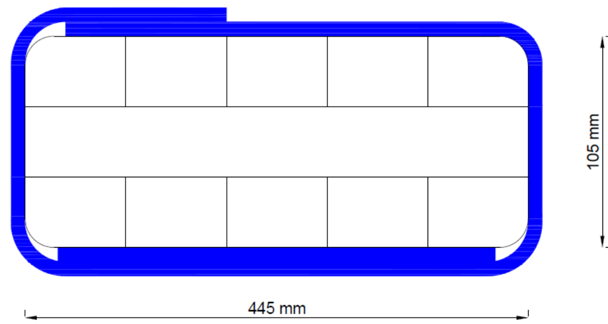

b) Retrofit 2: CLT-T(0)C(0)

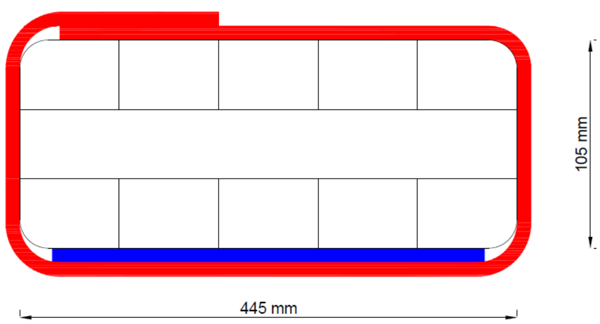

c) Retrofit 3-6: CLT-T(0)C(±45)
CLT-T(0)SH(±45)
CLT-T-M(0)C(±45)
CLT-T-M-SH (0)C (±45)

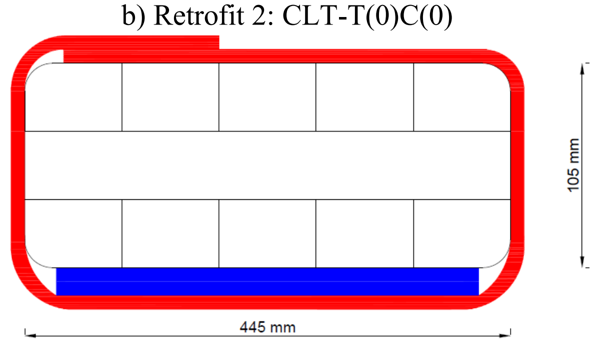

d) Retrofit 7: CLT-T$(0)_2$C(±45)

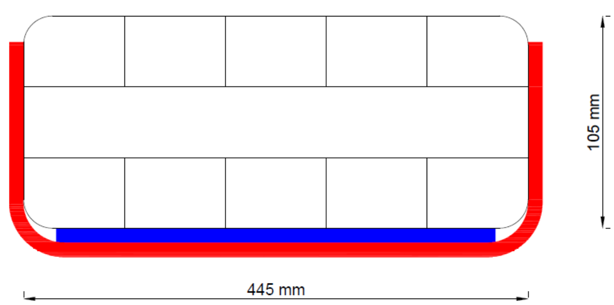

Retrofit 8: CLT-T(0)U(±45)

3.8 Retrofit configurations (Glulam beam and CFRP fabric)

For Retrofit 9 (Figure 3.6a), unidirectional CFRP was applied along the tension side of the glulam beam, while bidirectional CFRP fabric (±45°) was wrapped continuously along the full length of the beam to investigate its influence on post-peak behaviour and overall ductility through distributed confinement. In the case of Retrofit 10 (Figure 3.6b), unidirectional CFRP fabric was applied continuously along the entire length of the tension side, while bidirectional CFRP fabric (±45°) was applied between the concentrated load points to examine the effect of concentrating confinement within the region of maximum bending moment. In Retrofit 11, one layer of CFRP was applied for tension reinforcement, while a second unidirectional CFRP layer was oriented perpendicular to the wood grain to examine confinement effects

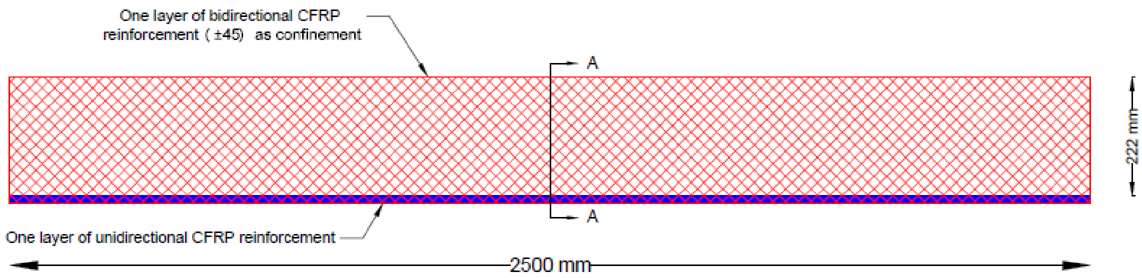

Retrofit 9: G-T(0)C(±45)

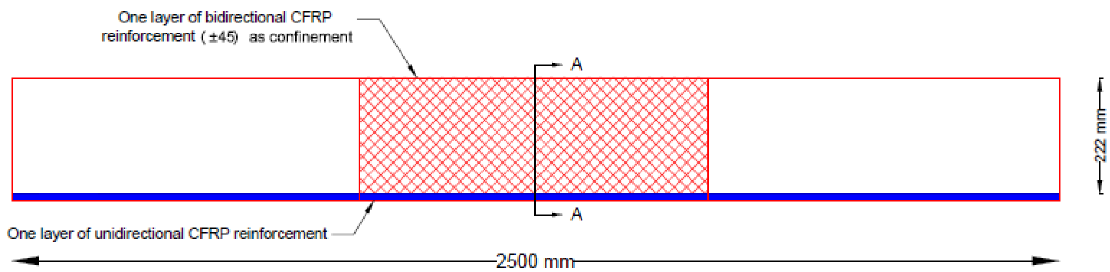

Retrofit 10: G-T(0)M(±45)

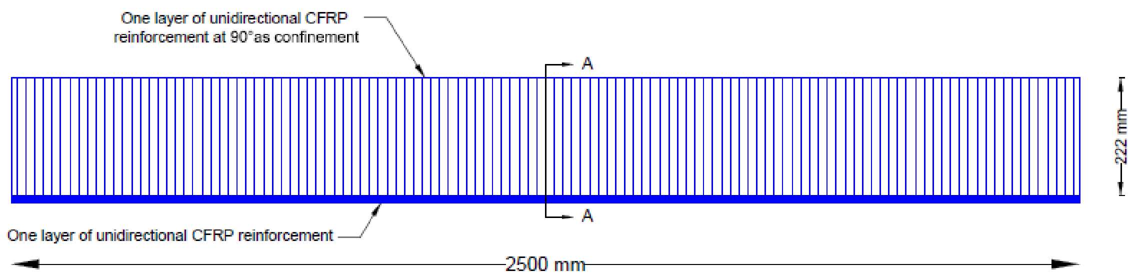

Retrofit 11: G-T(0)C(0)

Figure 3.6 Description of Retrofit 9 through 11 (Glulam and CFRP)

In Retrofit 12, bidirectional fabric was applied as confinement, and the tension side of the panel was strengthened with two layers of unidirectional CFRP fabric to further enhance flexural capacity and stiffness. In Retrofit 13, a unidirectional CFRP fabric was installed along the entire tension face, while a U-shaped bidirectional CFRP (±45) was applied to the bottom and side surfaces to provide localized confinement (Figure 3.7).

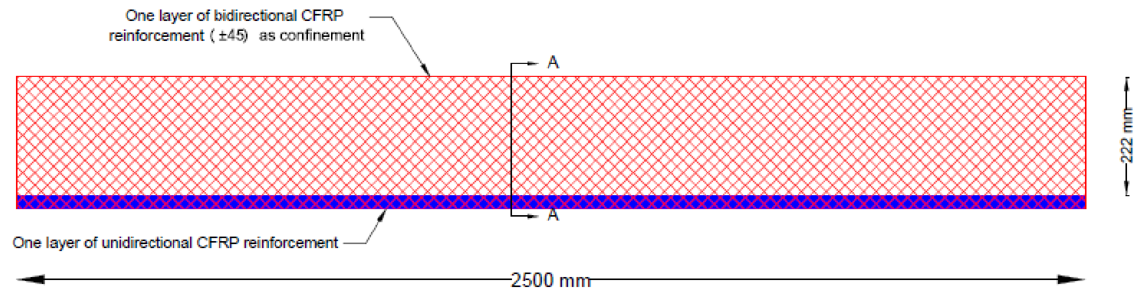

a) Retrofit 12: G-T(0)$_2$C(±45)

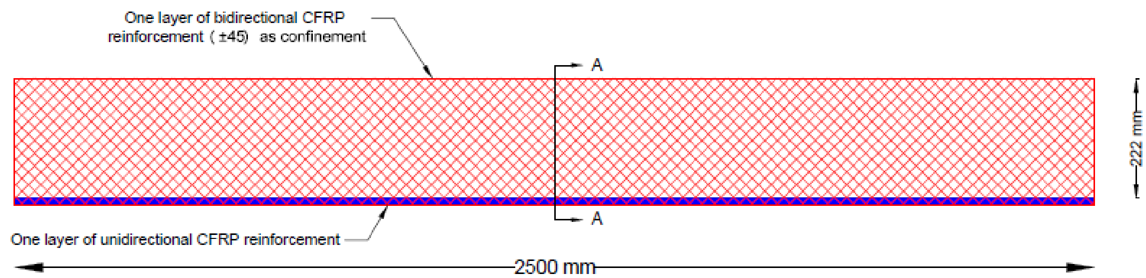

b) Retrofit 13: G-T(0)U(±45)

Figure 3.7 Description of Retrofits 12 and 13 (Glulam and CFRP)

The reinforcement summary for all cross sections of the retrofitted glulam beams with CFRP is shown in Table 3.4.

Table 3.4 Cross-section summary of Retrofit 9-13

Cross-section and CFRP retrofit configuration of glulam

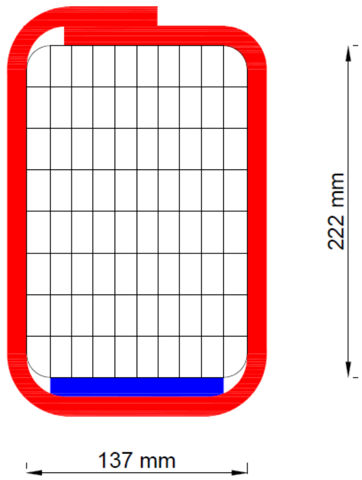

a) Retrofit 9and 10: G-T(0)C(±45), G-T(0)M(±45)

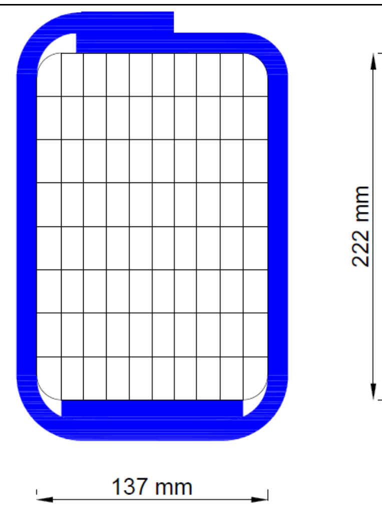

b) Retrofit 11: G-T(0)C(0)

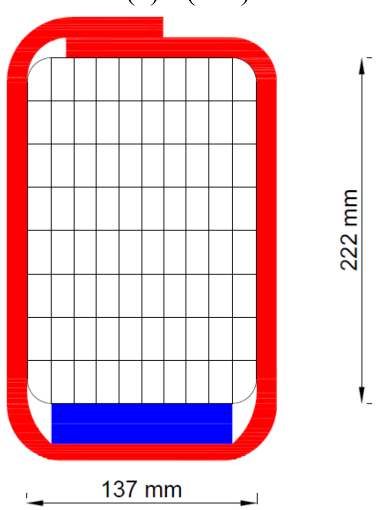

b) Retrofit 12: G-T_2(0)C(±45)

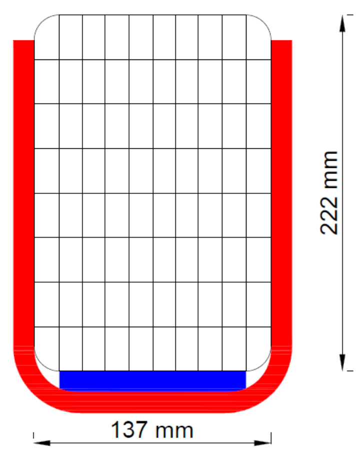

c) Retrofit 13: G-T(0)U(±45)

3.9 Static test setup

Specimens under four-point bending with simply supported boundary conditions were tested statically, as shown in Figure 3.8 and Figure 3.9, for the CLT panel and the glulam beam, respectively.

The static tests were conducted at the University of Ottawa's Structural Laboratory. A reaction frame with a steel I-beam was used for the static testing to transfer the imposed load at the third point of the span.

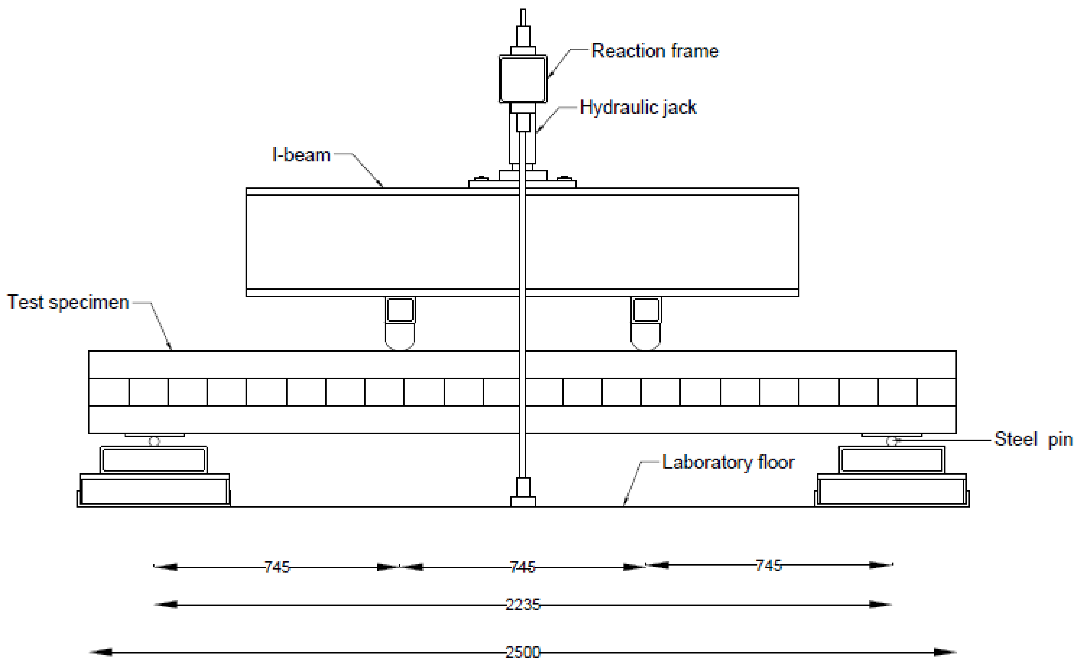

a) Side view

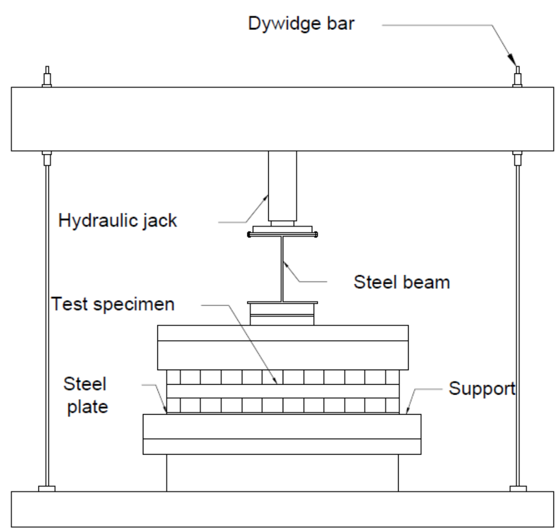

b) Front View

Figure 3.8 Static test setup of CLT panel

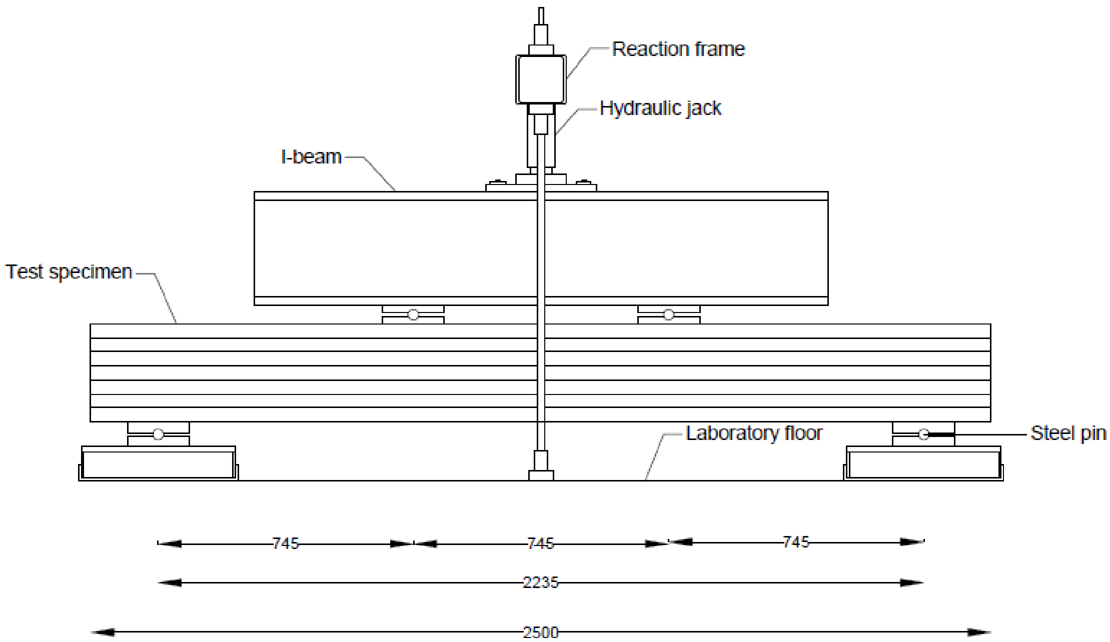

a) Side view

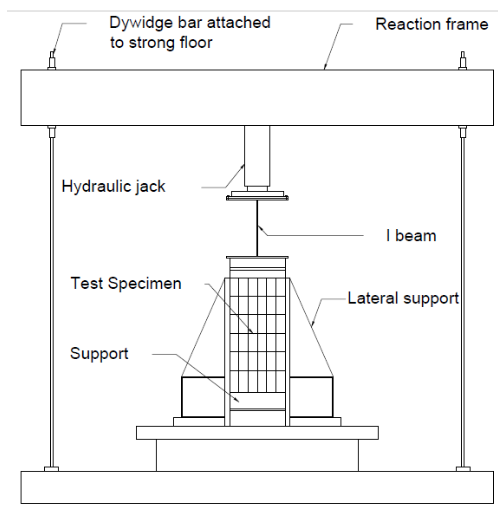

b) Front View

Figure 3.9 Static test setup of glulam beam

The span for all samples was 2235 mm, which is due to the height restrictions imposed by the shock tube opening. The load was measured using a load cell, while two steel plates and a roller provided idealized pin end conditions. The hydraulic jack and pump were used to provide the force, which raised the imposed load steadily until failure was reached. To measure the mid-span deflection a wire gauge was employed. Strain gauges were installed to record strain on the tension and compression faces. Data was gathered during the static testing using a data acquisition system (DAS) at a sampling rate of 10 samples per second.

3.10 Dynamic test setup

The University of Ottawa Shock Tube, a test apparatus capable of creating high strain rates like those found during far-field blast explosions, was used for dynamic testing. The Shock Tube includes three main components: the driver section, the diaphragm section, and the expansion section as shown in Figure 3.10. The three portions are separated by sheets of aluminum foil, with thicknesses and amounts that are predetermined depending on the pressure-impulse combination to which the specimen was subjected. The Shock Tube can produce maximum reflected pressure and impulses of 100 kPa and 2,200 kPa-ms, respectively, and positive phase times ranging from 5 to 70 ms. Driver pressure determines the peak reflected pressure, while driver length determines the peak reflected impulse. A shock front is produced from the release of the compressed air in the driver section, and the driver length can be varied from 305 mm (1 ft) to 5185 mm (17 ft) in 305 mm increments. The opening of the expansion section is 2032 mm x 2032 mm in size which allows for testing of large-scale specimens.

a) Driver section

b) Expansion section

c)End frame

Figure 3.10 University of Ottawa's Shock Tube

The loading pattern, clear span, and boundary conditions reproduced by the dynamic test arrangement (Figure 3.11 and Figure 3.12) were the same as those of the static test setup. A load transfer device (LTD) was installed onto the end frame of the Shock Tube. LTD is comprised of two evenly spaced load transfer steel I-beam sections, top and bottom hinges that allow for lateral movement of up to 200 mm, and steel load-transferring panels. Implementing the LTD led to the transfer of the two-point loads created in the shock tube to the specimens.

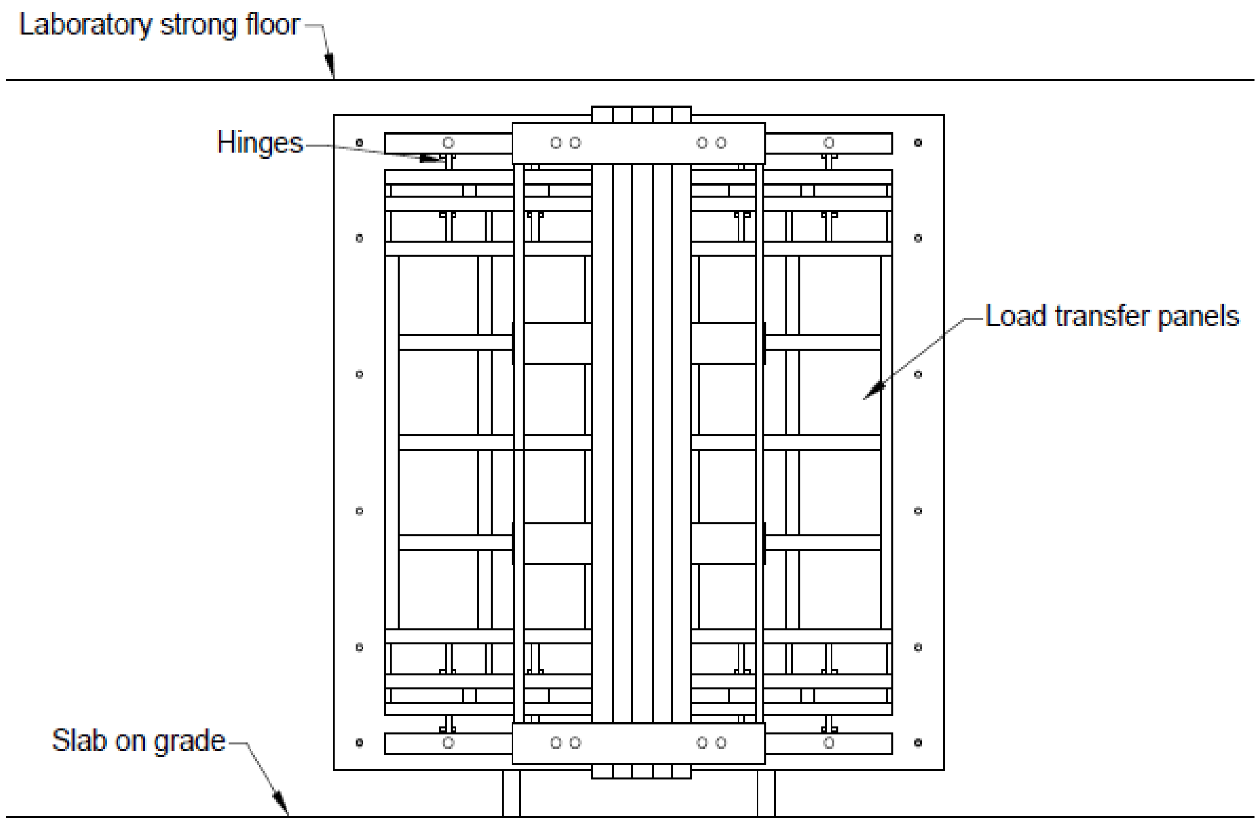

Figure 3.11 Dynamic test setup front view

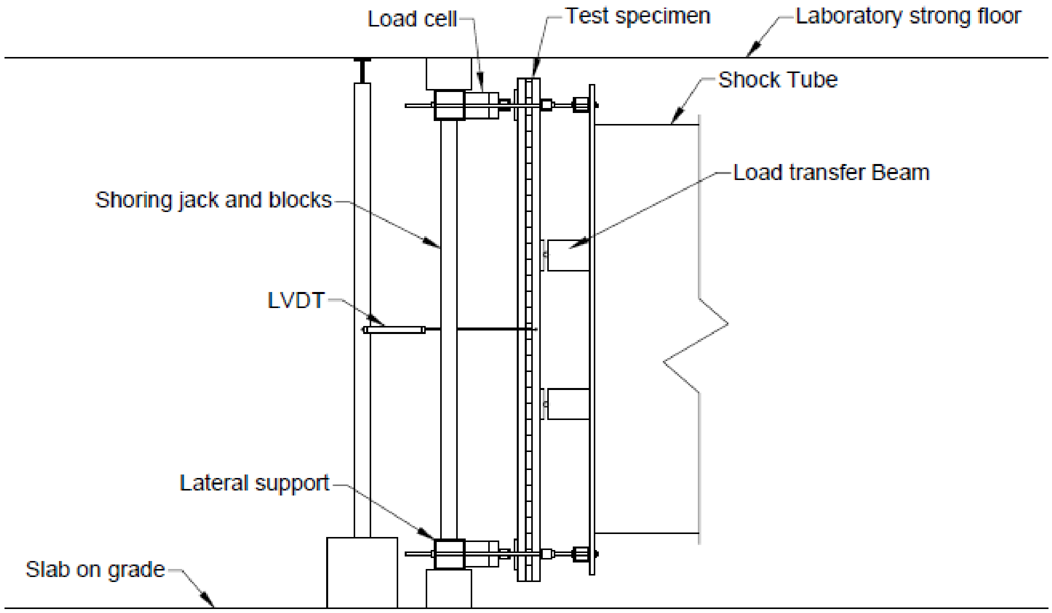

a) Dynamic test setup-side view for CLT panel

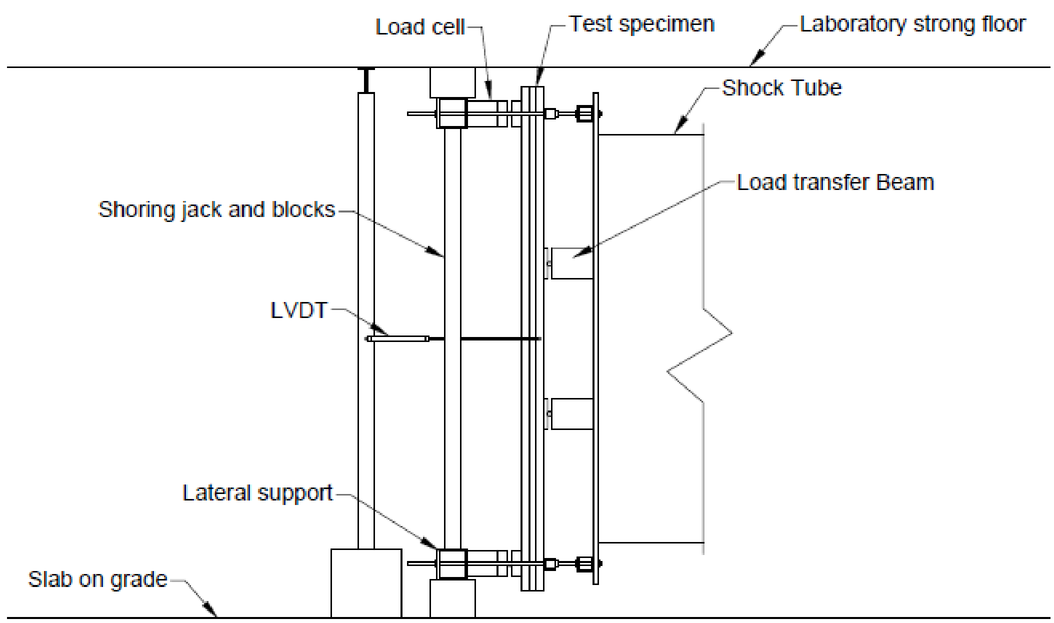

b) Dynamic test setup-side view for glulam beam

Figure 3.12 Dynamic test setup-side view for CLT and glulam beam

Chapter 4 Experimental Results

4.1 General

The experimental results from the static and dynamic tests are presented in this chapter. This includes the full-scale tests conducted on unretrofitted and retrofitted specimens.

4.2 Static Test Results

4.2.1 Static Destructive Testing of unretrfitted and retrofitted CLT panel

A total of 12 specimens, including eight configurations (one unretrofitted and seven retrofitted) were tested destructively under static loading. Table 4.1 summarizes the static test results for the unretrofitted CLT panel, as well as the results for the panels retrofitted with CFRP.

Table 4.1 Summary of static destructive test results for CLT panels

Configuration	R^{a}_{max} (KN)	Δ^{b}_{Rmax} (mm)	K^{c} (KN/mm)	Ductility	$\varepsilon^{d}_{t,w-f}$ x10^{-4} (mm/mm)	$\varepsilon^{e}_{c,w-f}$ x10^{-4} (mm/mm)
Unretrofitted CLT	54.9	40.2	1.50	-	30.63	-28.23
CLT-C(±45)	62	34.7	1.99	1.3	43.33	-
CLT-T(0)C(0)-1	93.7	79.1	1.72	-	42.71	-87.2
CLT-T(0)C(0)-2	80.6	73	1.87	1.2	33.75	-44.4
CLT-T(0)C(±45)-1	115.5	75.8	2.06	1.7	62.14	-123.57
CLT-T(0)C(±45)-2	106.7	74	2.19	1.5	51.54	-152.05
CLT-T(0)SH(±45)-1	108.9	81.9	2.02	-	56.04	-149.73
CLT-T(0)SH(±45)-2	85.4	54	1.88	-	58.85	-60
CLT-T-M(0)C(±45)	92.2	57.2	1.72	1.5	37.12	-65.19
CLT-T-SH-M(0)C(±45)	106.3	67.8	1.77	1.5	79.11	-100.13
CLT-T(0)$_2$C(±45)	127.8	92.1	2.24	2	-	-
CLT-T(0)U(±45)	81.1	60.6	1.56	1.5	49.2	-53.66

[a]Maximum resistance [b]Displacement at maximum resistance [c]Stiffness
[d]Strain at wood tensile rupture [e]Maximum wood compressive strain

The resistance-displacement curves obtained from the static tests for both unreinforced and CFRP-reinforced CLT panels are presented in Figure 4.1.

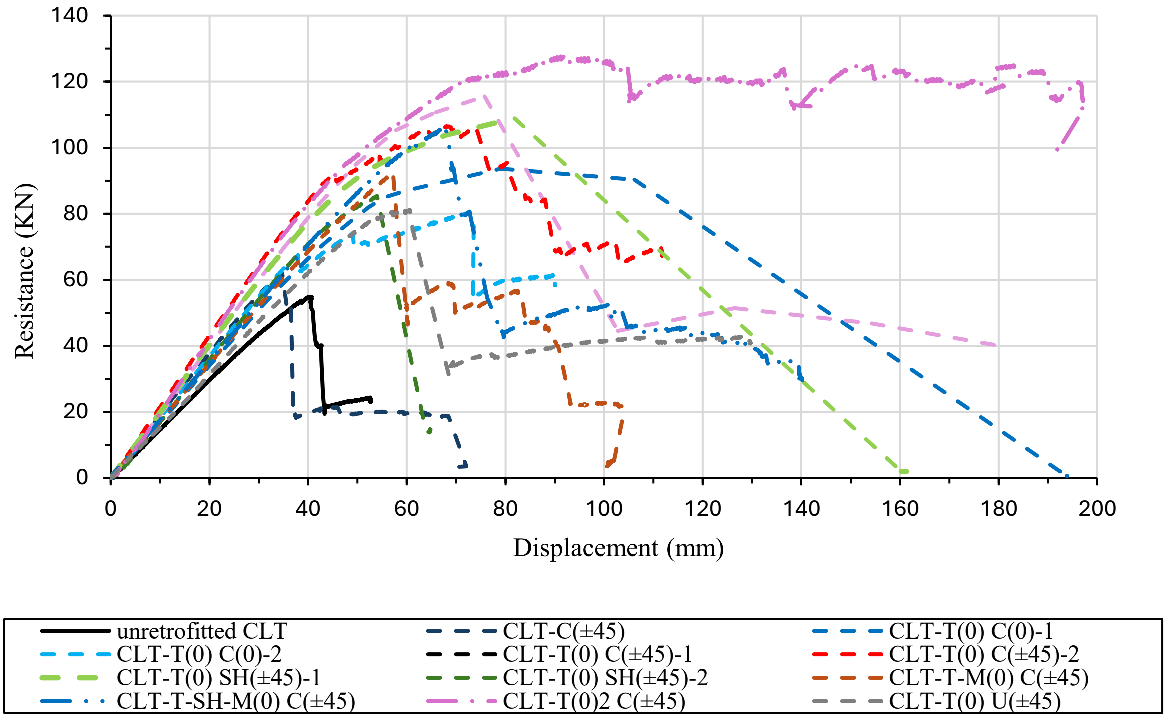

Figure 4.1 Experimental static resistance-displacement curves, unretrofitted CLT panel, and retrofitteed CLT specimens

It is not worthy to mention that the steep descending curve observed for the specimens CLT-T(0)C(0)-1, CLT-T(0)C(±45)-1, and CLT-T(0)SH(±45) is attributed to a limited number of data points recorded for these samples, which was part of the reason why the tests were repeated.

4.2.1.1 Unretrofitted CLT panel

As shown in Figure 4.2, the unretrofitted CLT specimen reached a peak load capacity of 54.9 KN with a corresponding stiffness of 1.5 KN/mm. The unretrofitted panel exhibited a nearly linear behaviour up to the peak load, followed by a sudden drop in resistance, indicating a brittle failure mode with no post-peak deformation capacity. This abrupt load loss reflects the limited energy dissipation capacity of the unretrofitted CLT panel. The small plateau at around 20 kN reflects the residual resistance in the remaining laminate, which has also been observed by Gergi and Doudak (2026).

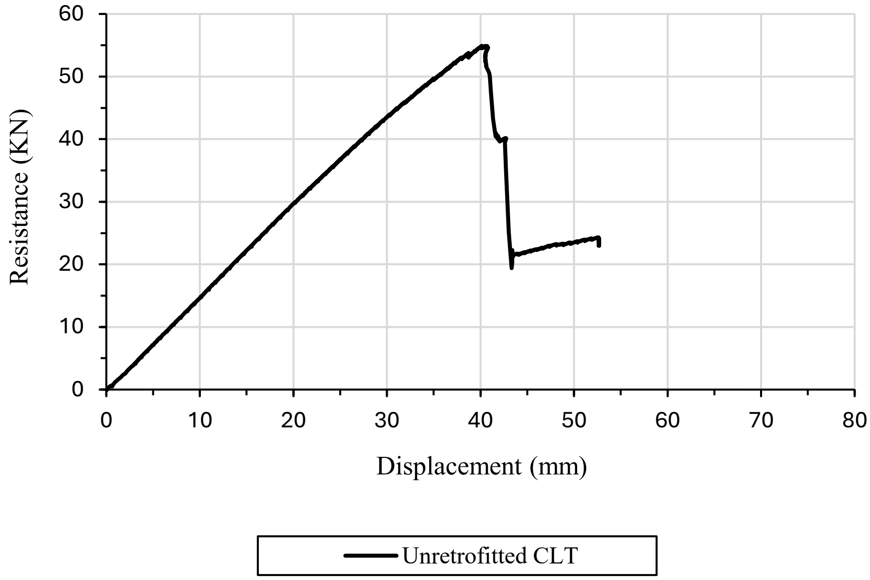

Figure 4.2 Experimental static resistance-displacement unretrofitted CLT panel

The typical failure mode for the unretrofitted CLT panel was characterized primarily by rolling shear failure (Figure 4.3), which started at one end of the panel and propagated towards the centre.

Figure 4.3 Representative static failure mode for unretrofitted CLT panel

4.2.1.2 CLT-C(±45)

For the CLT-C(±45) specimen, the peak load capacity reached 62 kN, representing a 13% increase compared to the unretrofitted reference panel. The stiffness obtained from 10% to 40% of the experimental resistance-displacement relationship increased by 33%, while the post-peak ultimate displacement reached about 68 mm. This post-peak behaviour is considered negligible because it occurs at a level that is below 50% of the peak load. The corresponding resistance–displacement curve for the CLT-C(±45) specimen is shown in Figure 4.4. As noted earlier, the CLT-C(±45) specimen achieved a slightly higher peak load and stiffness, which could indicate the CFRP retrofit provided some confinement that may have delayed the onset of failure. Despite this increase, the curve exhibited a pronounced drop immediately after the peak, in a similar manner to that observed in the unretrofitted panel. Although a similar, yet longer, plateau was observed in the retrofitted specimen, it occurred at a resistance level that is approximately 30% of the peak load, which is too low to be considered significant.

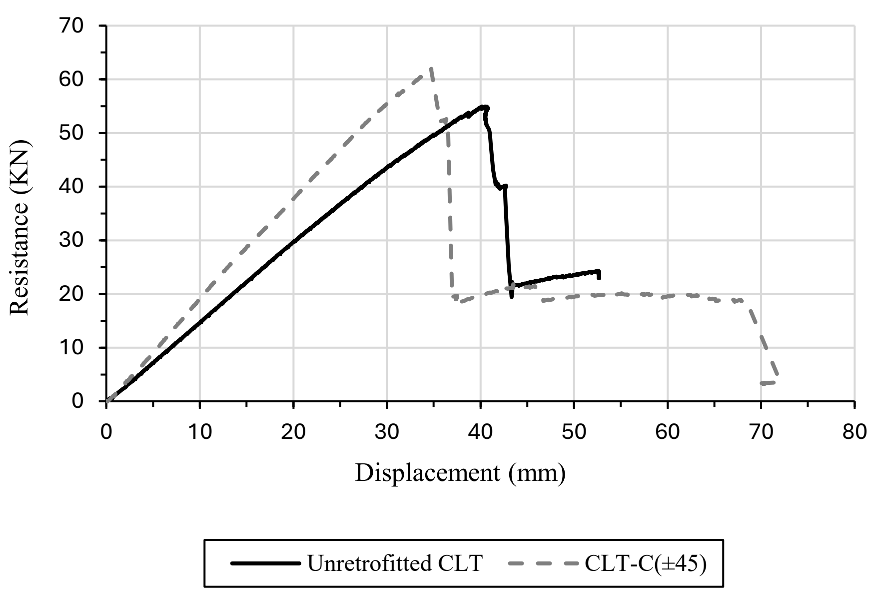

Figure 4.4 Experimental static resistance-displacement curves, unretrofitted CLT panel, and CLT-C(±45)

The failure mode of specimen CLT-C(±45) was predominantly flexure (Figure 4.5a and Figure 4.5b). The specimen exhibited brittle fracture of the CFRP fabric, with fiber rupturing and tearing along the ±45° diagonal directions. This tearing pattern is consistent with stress developing within the laminate during flexural failure, leading to localized separation from and exposure of the underlying CLT layers. As seen in Figure 4.5c, the damaged surface reveals the ruptured and separated fibers, indicating that the CFRP was only partially engaged in resisting the load.

Although the failure mode shifted from that of predominantly rolling shear failure to flexural failure indicate that the CFRP partially contributed to enhancing the shear resistance, likely by preventing the rolling of the transverse boards. The reason the resistance did not increase more sustainably is that for this panel dimension, the rolling shear and bending capacities are close, as was also noted by Gergi and Doudak (2026).

a) Static test CLT-C(±45)

b) Side view CLT-C(±45) c) Tearing of CFRP reinforcement CLT-C(±45)

Figure 4.5 Representative static failure mode for CLT-C(±45)

4.2.1.3 CLT-T(0)C(0)-1 and CLT-T(0)C(0)-2

The resistance–displacement curves for CLT-T(0)C(0)-1 and CLT-T(0)C(0)-2 specimens are shown in Figure 4.6, along with the unretrofitted specimen. For the CLT-T(0)C(0)-1 specimen, the peak load capacity reached 93.7 kN, representing a 71% increase over the unretrofitted CLT panel. The stiffness also increased by 14%, which is similar to that obtained in the CLT-C(±45) configuration. Similarly, CLT-T(0)C(0)-2 specimen reached a peak resistance of 80.6 kN, which is 47% higher than that of the unretrofitted CLT panel. The stiffness increase for this specimen was more substantial, representing a 24% enhancement. Unlike specimen CLT-T(0)C(0)-1, this specimen maintained a gradual load decline over a greater displacement range, reflecting improved post-peak capacity due to the CFRP retrofit. A ratio of 1.2 was obtained for CLT-T(0)C(0)-2.

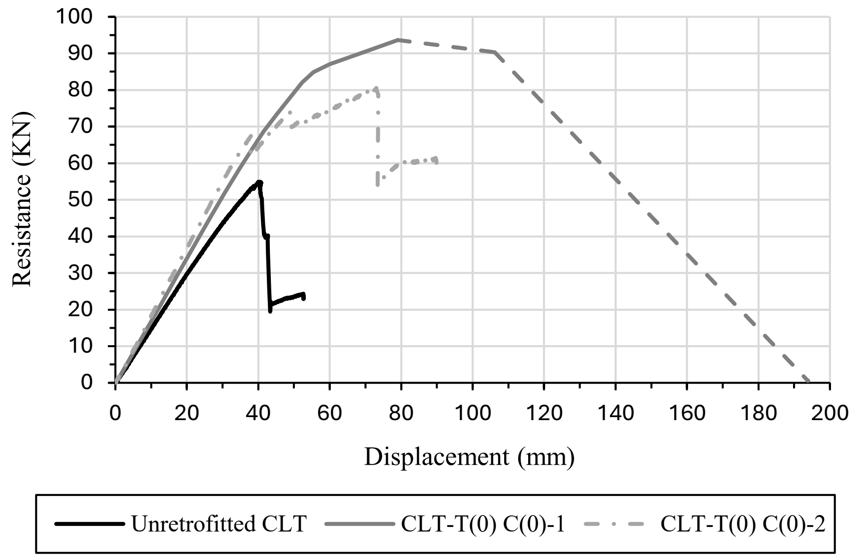

Figure 4.6 Experimental static resistance-displacement curves, unretrofitted CLT panel, CLT-T(0)C(0)-1 and CLT-T(0)C(0)-2

As shown in Figure 4.7, the typical failure mode for sample CLT-T(0)C(0)-1 was a flexural failure. As anticipated, tearing was observed in the CFRP confinement, where the unidirectional fabric was applied at ninety degrees to the wood fibers. The ultimate failure was characterized by rupture in wood fibres on the tension face.

a) Static test CLT-T(0)C(0)-1

b) Tearing of CFRP reinforcement CLT-T(0)C(0)-1

Figure 4.7 Representative static failure mode for CLT-T(0)C(0)-1

Figure 4.8 illustrates the failure mode of the CLT-T(0)C(0)-2 specimen. As Figure 4.8b illustrates, specimen CLT-T(0)C(0)-2 exhibited longitudinal shear at the end of the panel. Also, tearing of the CFRP confinement was observed, particularly the unidirectional fabric used at ninety degrees to the wood fibers. The longitudinal shear failure mechanism was not expected and is likely the cause of the sudden drop in the resistance-displacement curve shown in Figure 4.8.

a) Static test CLT-T(0)C(0)-2

b) Cross section of CLT-T(0)C(0)-2

c) Tearing of unidirectional fabric of CLT-T(0)C(0)-2

Figure 4.8 Representative static failure mode for CLT-T(0)C(0)-2

4.2.1.4 CLT-T(0)C(±45) -1 and CLT-T(0)C(±45)-2

Figure 4.9 represents the resistance–displacement curves for specimen CLT-T(0)C(±45)-1 and CLT-T(0)C(±45)-2, designed to investigate the effect of combining bidirectional CFRP fabric. Specimen CLT-T(0)C(±45)-1 achieved a peak load capacity of 115.5 kN and stiffness of 2.1 kN/mm, corresponding to a 110% increase in strength and a 37% increase in stiffness. By dividing the post-peak displacement at 50% of maximum force by the displacement at the beam's peak load, the post-peak displacement capacity of the reinforced beams was determined. A ratio of 1.7 was also attained. Specimen CLT-T(0)C(±45)-2 reached a peak load of 106.7 kN with a corresponding stiffness of 2.2 kN/mm, indicating strength and stiffness increases of 94% and 46%, respectively, compared to the unretrofitted panel, which are consistent with the values observed for the CLT-

T(0)C(±45)-1 specimen. This specimen also demonstrated a post-peak displacement capacity ratio of 1.5.

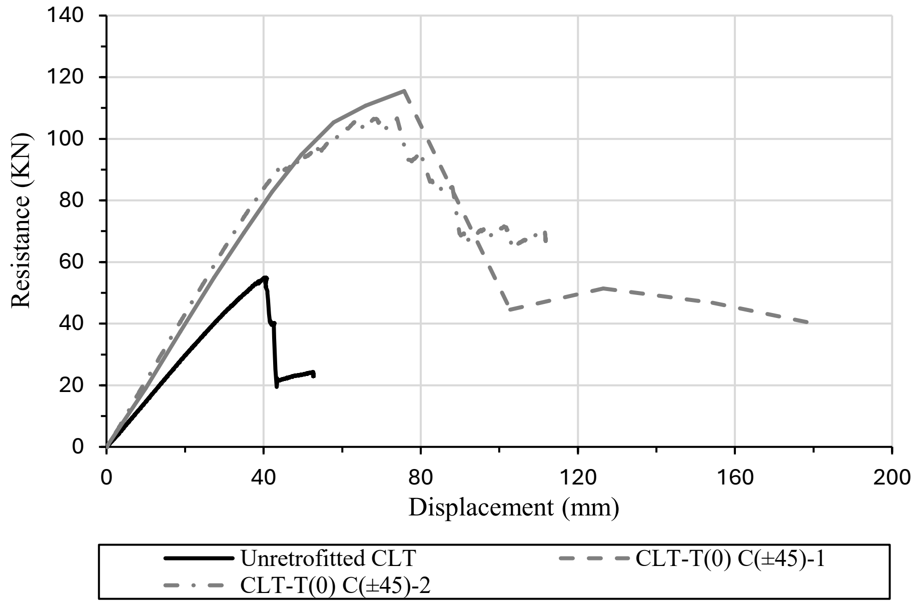

Figure 4.9 Experimental static resistance-displacement curves, unretrofitted CLT panel, CLT-T(0)C(±45)-1 and CLT-T(0)C(±45)-2

Figure 4.10 illustrates the observed failure mode for specimen CLT-T(0)C(±45)-1. The specimen exhibited a predominantly flexural failure, which occurred near mid-span. The diagonal tearing pattern in the CFRP fabric suggests the interaction of both longitudinal (0°) and off-axis (±45°) fibers, with failure propagating preferentially along fiber alignment. This combined failure mode points to the susceptibility of bidirectional CFRP to localized stress concentrations during flexural loading.

a) Static CLT-T(0)C(±45)-1

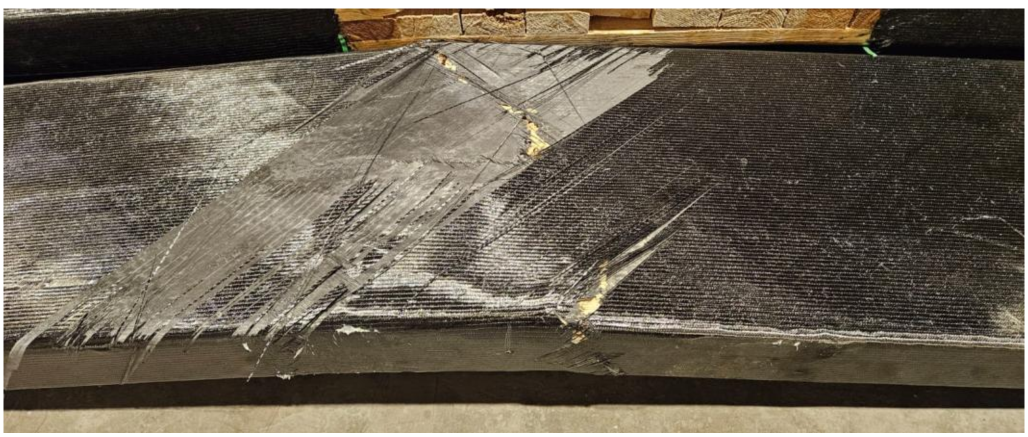

b) Tension side of CLT-T(0)C(±45)-1

Figure 4.10 Representative static failure mode for CLT-T(0)C(±45)-1

The CLT-T(0)C(±45)-2 specimen exhibited a predominantly flexural failure mode, similar to that observed for CLT-T(0)C(±45)-1 (Figure 4.11). Damage was primarily concentrated on the tension face, where tearing and rupture of the bidirectional CFRP fabric were observed along the fiber orientations. The CFRP reinforcement remained partially intact across several areas where wood fibres ruptured beneath it, indicating continued crack-bridging action after the onset of damage.

(a) Static CLT-T(0)C(±45)-2

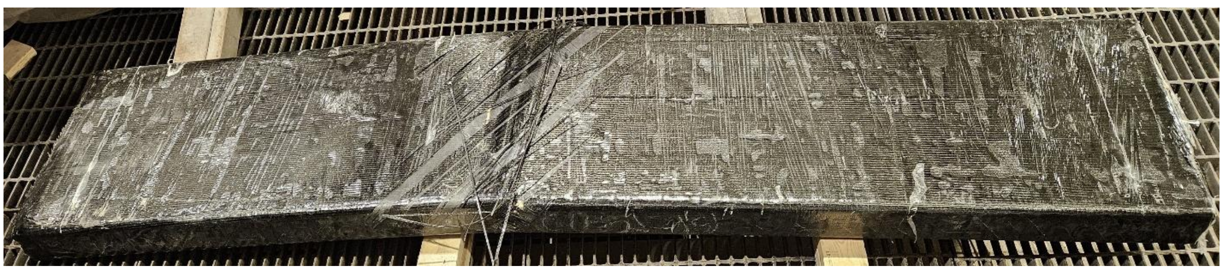

(b) Tension side of CLT-T(0)C(±45)-2

Figure 4.11 Representative static failure mode for CLT-T(0)C(±45)-2

4.2.1.5 CLT-T(0)SH(±45)-1 and CLT-T(0)SH(±45)-2

Figure 4.12 shows that specimen CLT-T(0)SH(±45)-1 reached a peak load capacity of 108.9 kN and stiffness of 2 kN/mm, representing a 98% increase in strength and a 33% increase in stiffness relative to the unretrofitted CLT panel. The CLT-T(0)SH(±45)-2 specimen achieved a peak load capacity of 85.4 kN with a stiffness of 1.9 kN/mm, representing strength and stiffness improvements of 56% and 27%, respectively, compared to the unretrofitted CLT panel.

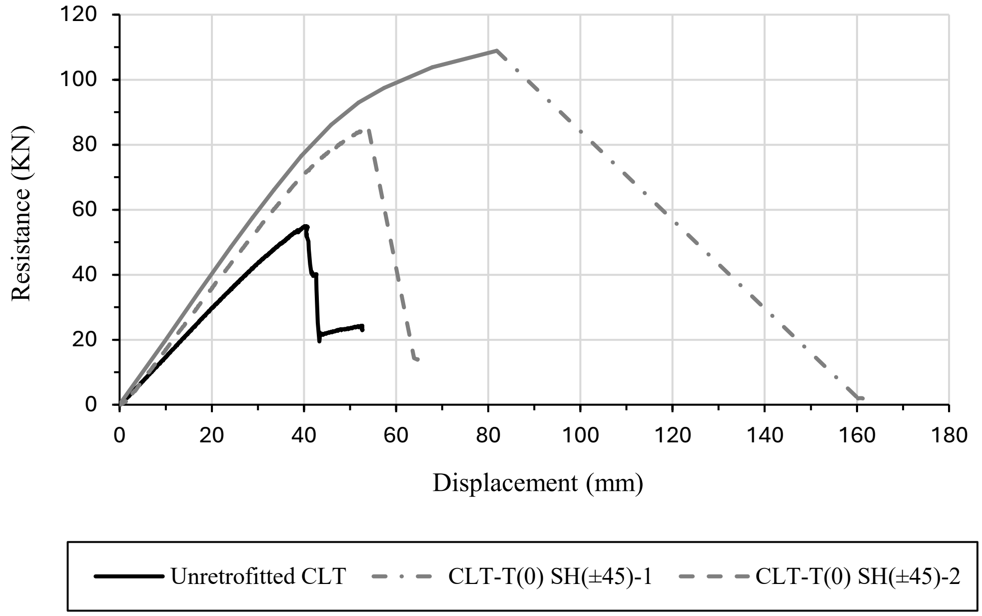

Figure 4.12 Experimental static resistance-displacement curves, unretrofitted CLT panel, CLT-T(0)SH(±45)-1 and CLT-T(0)SH(±45)-2

The typical failure mode for specimen CLT-T(0)SH(±45)-1 was a flexural failure (Figure 4.13a) and was characterized by failure in the outer wood tension laminates, with damage propagating through the entire depth of the cross-section (Figure 4.13b). Following the wood failure, the outer tension laminates pushed outwards on the CFRP, causing separation between the wood and reinforcement (Figure 4.13c).

a) Static test CLT-T(0)SH(±45)-1

b) Static test CLT-T(0)SH(±45)-1 (outer wood tension laminates with damage)

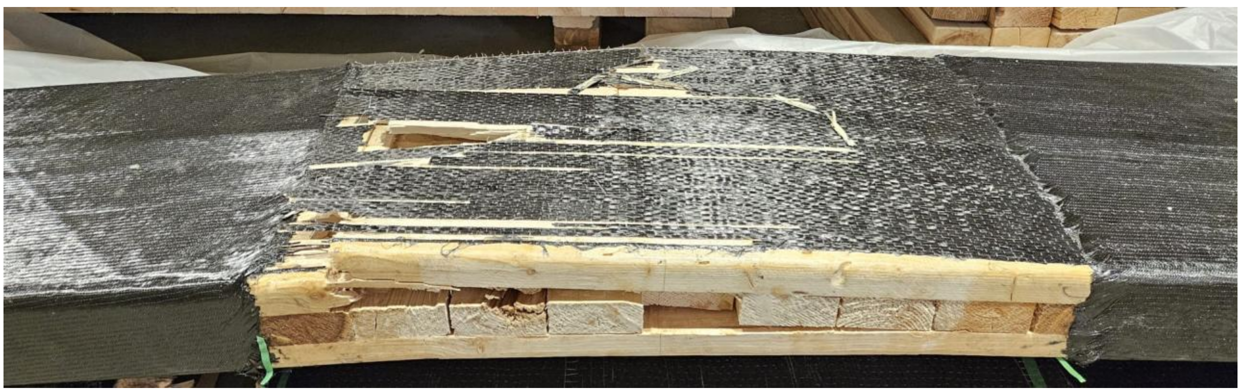

c) Tension side of CLT-T(0)SH(±45)-1

Figure 4.13 Representative static failure mode for CLT-T(0)SH(±45)-1

The typical failure mode for specimen CLT-T(0)SH(±45)-2 was governed by longitudinal shear, as shown in Figure 4.14a. Shear initiated at the member end along the interfaces of the laminate and resulted in slip and separation between the longitudinal laminates (Figure 4.14b), which led to an abrupt drop in the resistance-displacement curve after peak resistance. In addition, localized separation between the unidirectional CFRP fabric and the wood substrate was observed on the tension side (Figure 4.14c).

a) Static test CLT-T(0)SH(±45)-2

b) Tension side of CLT-T(0)SH(±45)-2

c) Longitudinal Shear in CLT-T(0)SH (±45)-2

Figure 4.14 Represenative static failure mode for CLT-T(0)SH(±45)-2

4.2.1.6 CLT-T-M(0)C(±45)

Specimen CLT-T-M(0)C(±45) reached a peak load capacity of approximately 92.2 kN and a stiffness of about 1.7 kN/mm, corresponding to a 68% increase in strength and a 13% increase in stiffness compared to the unretrofitted CLT panel. A ratio of 1.5 was also recorded for this configuration. The response, shown in Figure 4.15, was characterized by a somewhat maintained post-peak capacity, although the drop in capacity was sudden immediately after peak.

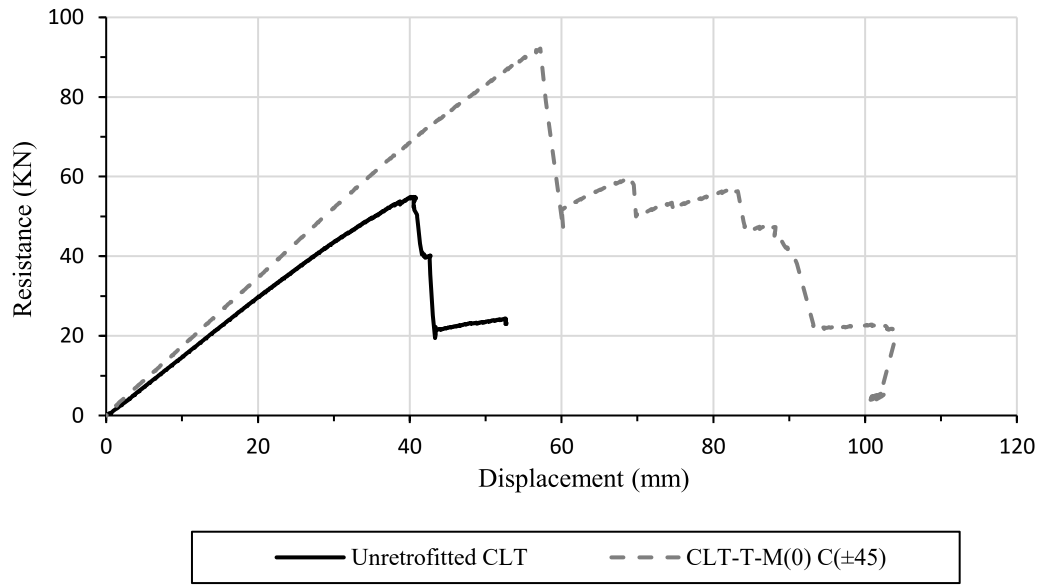

Figure 4.15 Experimental static resistance-displacement curves, unretrofitted CLT panel, and CLT-T-M(0)C(±45)

The typical failure mode for specimen CLT-T-M(0)C(±45) was flexural failure (Figure 4.16a). The failure occurred in the mid-span region, approximately at one-third of the panel span. On the tension side, the CFRP fabric tore along the fiber direction (Figure 4.16b). On the compression side, the CFRP fabric remained intact, with no signs of cracking or separation (Figure 4.16c). No shear-related failures, such as rolling shear or longitudinal shear, were present (Figure 4.16d). Instead, damage propagated through the entire depth of the cross-section. Following the wood failure, the outer tension laminates displaced outward against the CFRP, leading to separation between the wood and the reinforcement.

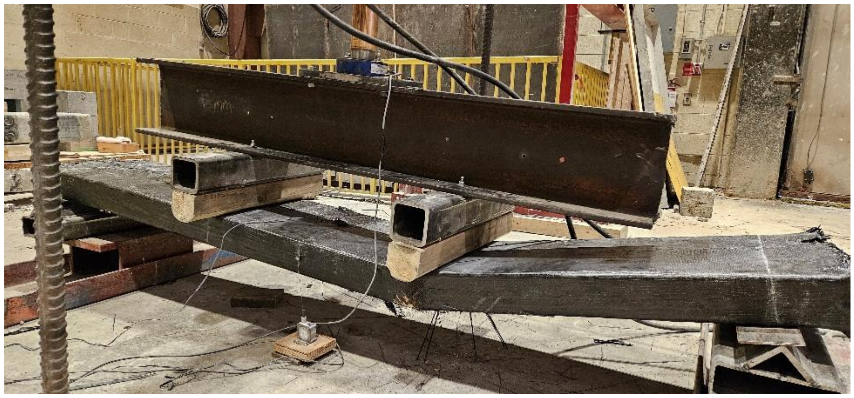

a) Static test CLT-T-M(0)C(±45)

b) Tension side of CLT-T-M(0)C(±45)

c) Compression side of CLT-T-M(0)C(±45)

d) Section view of CLT-T-M(0)C(±45)

Figure 4.16 Representative static failure mode for CLT-T-M(0)C(±45)

4.2.1.7 CLT-T-SH-M(0)C(±45)

The CLT-T-SH-M(0)C(±45) specimen achieved a peak load capacity of about 106.3 kN and a stiffness of 1.8 kN/mm, reflecting a 94% improvement in strength and an 20% gain in stiffness compared to the unretrofitted CLT panel. The ratio of 1.5 was obtained for this configuration. Figure 4.17 highlights a performance distinguished by both higher peak strength and the ability to sustain significant load at large displacements, despite the initial drop, which resembled in principle that of the unretrofitted specimen.

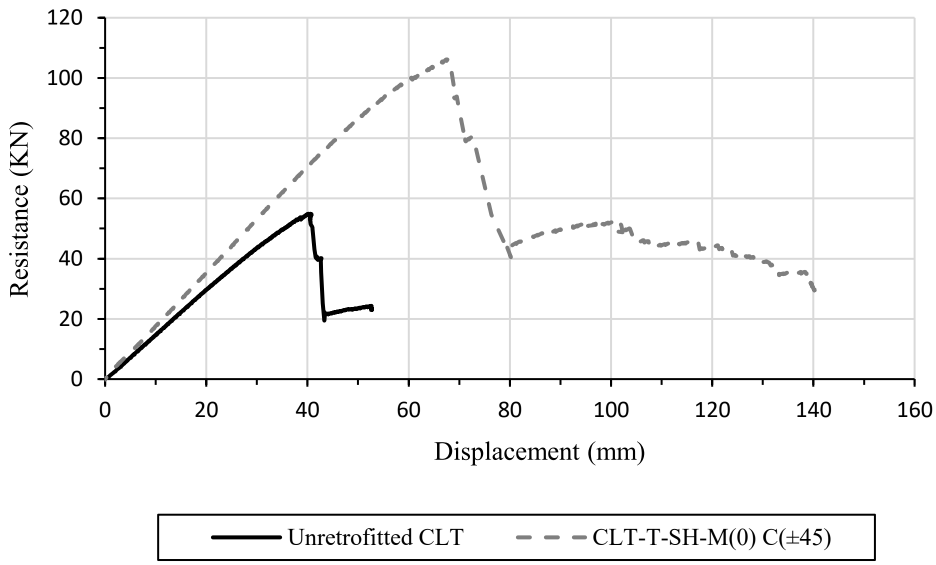

Figure 4.17 Experimental static resistance-displacement curves, unretrofitted CLT panel, and CLT-T-SH-M(0)C(±45)

The dominant failure mode of specimen CLT-T-SH-M(0)C(±45) was flexural failure (Figure 4.18a). On the tension face, the CFRP fabric ruptured along the fiber orientation (Figure 4.18b). No shear-related mechanisms, such as rolling shear or longitudinal shear, were observed (Figure 4.18c). The failure progressed through the full depth of the cross-section, and after the wood fractured, the outer tension laminates moved outward against the CFRP, resulting in partial detachment between the timber and the reinforcement.

a) Static test CLT-T-SH-M(0)C(±45)

b) Section view of CLT-T-SH-M(0)C(±45)

c) Tension side of CLT-T-SH-M(0)C(±45)
Figure 4.18 Representative static failure mode for CLT-T-SH-M(0)C(±45)

4.2.1.8 CLT-T_2(0)C(±45)

The CLT-T_2(0)C(±45) specimen achieved a peak load capacity of about 127.8 kN and a stiffness of 2.3 kN/mm, reflecting a 133% improvement in strength and a 53% gain in stiffness compared to the unretrofitted CLT panel (Figure 4.19). The specimen also maintained a post-peak displacement capacity up to twice the peak load displacement, and five times the failure displacement of the unretrofitted specimen.

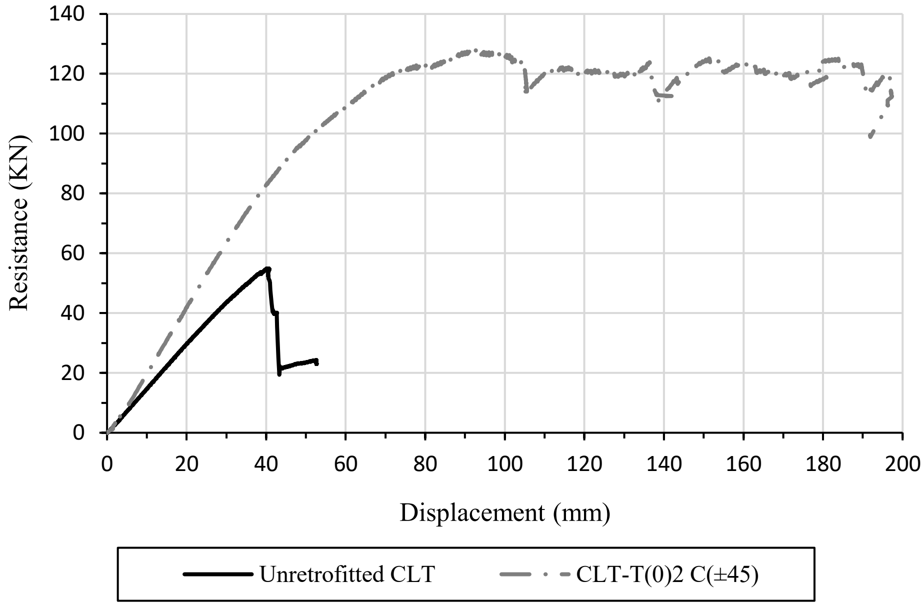

Figure 4.19 Experimental static resistance-displacement curve, unretrofitted CLT panel, and CLT-T_2(0)C(±45)

The observed failure mode, illustrated in Figure 4.20, was predominantly flexural. On the tension side, the CFRP exhibited tearing along both the longitudinal and ±45° fiber orientations, with progressive debonding near mid-span. On the compression face, localized crushing of the timber was evident. The failure observed in the CFRP indicates full engagement of both layers of bidirectional fabric throughout the loading history, providing enhanced reinforcement efficiency compared to a single-layer confinement configuration.

a) Static test CLT-T_2(0)C(±45)

b) Tension side of CLT-T_2(0)C(±45)

c) Side and compression view of CLT-T_2(0)C(±45)

Figure 4.20 Representative static failure mode for CLT-T_2(0)C(±45)

4.2.1.9 CLT-U(0)C(±45)

The CLT-T(0)U(±45) specimen reached a maximum load capacity of approximately 81.1 kN with a stiffness of 1.6 kN/mm, representing a 48% enhancement in strength and a 7% increase in stiffness relative to the unretrofitted CLT panel. For this configuration, a ratio of 1.5 was found. The resistance–displacement curve in Figure 4.21 indicates that this configuration delivered only moderate improvements. While peak load was noticeably higher than the unretrofitted reference, the stiffness gain was marginal, and the post-peak behaviour was more abrupt, with limited residual strength.

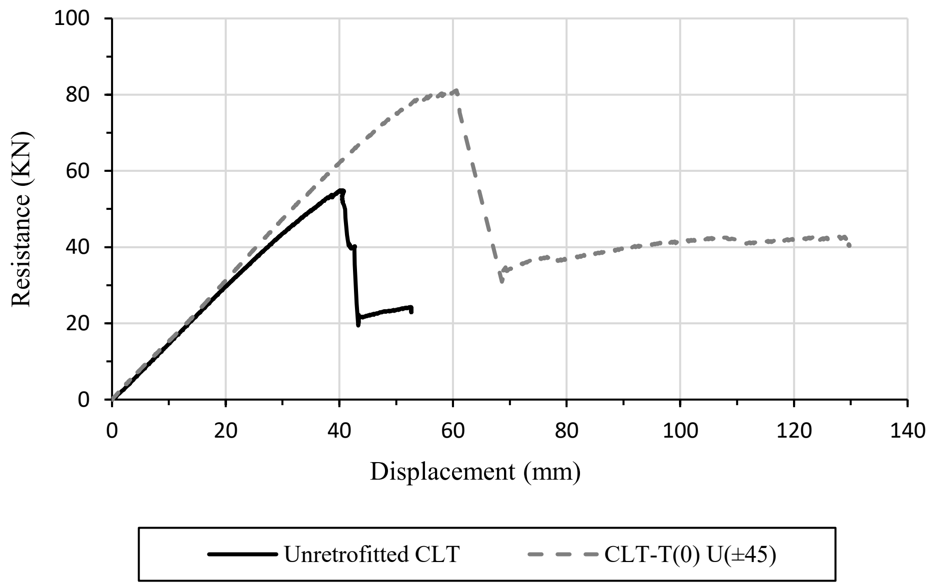

Figure 4.21 Experimental static resistance-displacement curves, unretrofitted CLT panel, and CLT-T(0)U(±45)

As shown in Figure 4.22, the failure mode was primarily governed by longitudinal shear. Cracking initiated along the glue lines between the longitudinal layers of the CLT panel. The U-shaped CFRP retrofit with ±45° fiber orientation remained largely intact during loading and effectively restrained premature flexural cracking; however, shear slip between laminates ultimately controlled the failure.

a) Static test CLT-T (0) U (±45)

b) Section view of CLT-T(0)U(±45)

Figure 4.22 Representative static failure mode for retrofitted CLT panel CLT-T(0)U(±45)

4.2.2 Static Destructive Testing of unretrofitted and retrofitted Glulam beam

A total of three glulam beams were tested destructively under static loading. Table 4.2 summarizes the static test results for an unretrofitted glulam beam, as well as the results for the beams retrofitted with CFRP.

Table 4.2 Summary of static destructive test results of glulam beams

Configuration	R^a_{max} (KN)	Δ^b_{Rmax} (mm)	K^c (KN/mm)	Ductility	$\varepsilon^d_{t,w-f}$ x10^{-4} (mm/mm)	$\varepsilon^e_{c,w-f}$ x10^{-4} (mm/mm)
Unretrofitted glulam	146.6	24.1	6.07	-	65.13	-
G-T (0) C (±45)	214.1	37.8	6.88	1.5	56.84	-77.09
G-T (0) M (±45)	201	34.5	6.70	1.2	50.17	-47.8

[a]Maximum resistance [b]Displacement at maximum resistance [c]Stiffness
[d]Strain at wood tensile rupture [e]Maximum wood compressive strain

The resistance-displacement curves obtained from the static tests for both unreinforced and CFRP-reinforced glulam beams are presented in Figure 4.23.

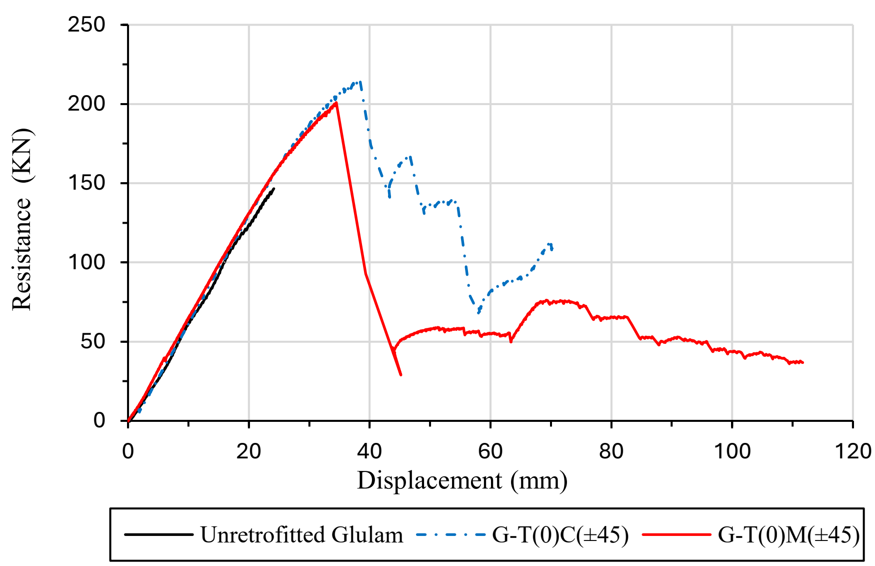

Figure 4.23 Experimental static resistance-displacement curves, unretrofitted glulam beam, and retrofitted glulam specimens

4.3.1 Unretrofitted Glulam

The unretrofitted glulam specimen reached a maximum load capacity of approximately 146.6 kN with a stiffness of 6.1 kN/mm (Figure 4.24).

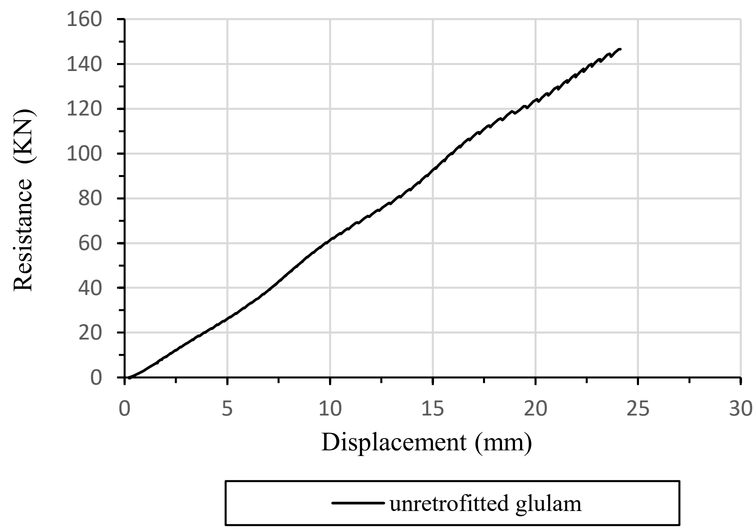

Figure 4.24 Experimental static resistance-displacement curves, unretrofitted glulam beam

The failure of the outer tension laminate and the propagation of cracks along the glulam layers are shown in Figure 4.25a. Failure either occurred at a knot or at an FJ, as seen in Figure 4.25b.

a) Cracks along the glulam layers

b) Tension side

Figure 4.25 Representative static failure mode for unretrofitted glulam beam

4.3.2 G-T(0)C(±45)

For the G-T(0)C(±45) specimen, the peak load capacity reached 214.1 kN, representing a 46% increase over the unretrofitted glulam beam (146.6 kN**).** Stiffness improved from 6.1 kN/mm to 6.9 kN/mm, representing a 13% increase**.** The corresponding resistance–displacement curves are shown in Figure 4.26. After reaching peak resistance, a gradual softening response was observed, accompanied by several load drops, suggesting a progressive damage mechanism rather than sudden brittle failure. Despite this post-peak degradation, the retrofitted beam retained a substantial residual load capacity. This improved performance highlights the effectiveness of this configuration in delaying crack propagation and maintaining structural integrity under large displacements.

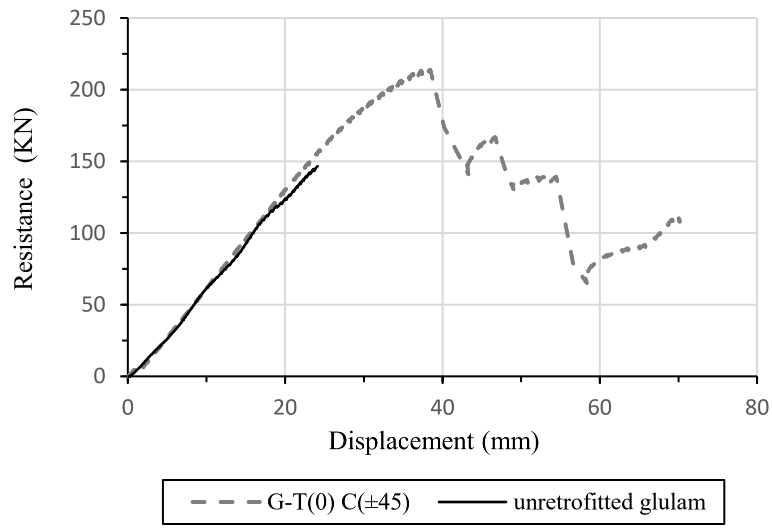

Figure 4.26 Experimental static resistance-displacement curves, unretrofitted glulam beam, and retrofitted glulam beam G-T(0)C(±45)

The observed failure mode, illustrated in Figure 4.27, was predominantly flexural. On the tension side of the glulam beam, tearing of the CFRP reinforcement occurred along the ±45° fiber orientations. This damage was accompanied by cracking of the outer timber laminations, confirming a flexure-controlled response of the retrofitted specimen.

a) Static test G-T (0) C (±45)

b) Side view of G-T (0) C (±45)

Figure 4.27 Representative static failure mode for retrofitted glulam beam G-T(0)C(±45)

4.3.3 G-T(0)M(±45)

The load–displacement curve shows that the G-T(0)M(±45) specimen exhibited higher load resistance compared to the unretrofitted glulam beam. The peak load capacity reached 201 kN, which is about a 37% increase. This demonstrates the effectiveness of the retrofitting method in enhancing the load-bearing capacity. Additionally, the initial slope of the curve indicates an improvement in stiffness. The stiffness increased from 6.1 kN/mm to 6.7 kN/mm, corresponding to a 9.8% enhancement. After peak load, the retrofitted specimen shows a sharp drop, followed by a minimal residual load-carrying capacity, corresponding to approximately 25% of the peak load (Figure 4.28).

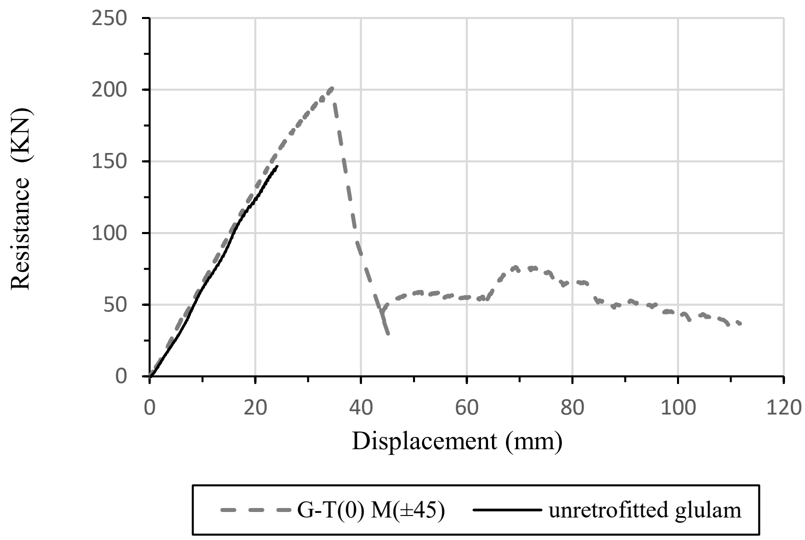

Figure 4.28 Experimental static resistance-displacement curves, unretrofitted glulam beam, and retrofitted glulam beam G-T(0)M(±45)

The observed failure mode of G-T(0)M(±45) was predominantly flexure (Figure 4.29). On the tension side of the timber beam, the CFRP reinforcement exhibited tearing along the longitudinal fiber orientation, accompanied by progressive debonding that initiated around one-third of the span.

a) Static test G-T(0)M(±45)

b) Side view of G-T(0)M(±45)

Figure 4.29 Representative static failure mode for retrofitted glulam beam G-T(0)M(±45)

4.3 Dynamic Test Results

This chapter presents the experimental results from the dynamic testing of both glulam and CLT specimens. As described in Chapter 3, the tests were performed on full-scale members configured with idealized simply-supported boundary conditions and subjected to four-point bending. All specimens were tested using a driver length of 2,745 mm (9 ft). For each specimen, the reported parameters include the driver pressure, peak reflected pressure, positive reflected impulse, and maximum displacement. The overall structural response during testing was documented using images captured during and after each shot. In addition, displacement, resistance, and load-time histories are presented and discussed. A summary of the dynamic experimental results is provided at the end of this chapter in Table 4.3 and Table 4.4, with additional details included in Appendix B.

4.3.1 Dynamic test results of unretrofitted and retrofitted CLT panels

4.3.1.1 Unretrofitted CLT

The unretrofitted specimen was tested using a driver pressure of 413.7 kPa, resulting in a peak reflected pressure of 66.4 kPa and a positive reflected impulse of 585 kPa. ms over a positive phase duration of 21.3 ms. The maximum resistance was 63.1 kN, while the time at maximum resistance was 16.26 ms. The displacements at maximum resistance reached 45.8 mm. The specimen setup and failure mode are presented in Figure 4.30. During dynamic loading, rolling shear cracks initiated in the transverse laminations and progressively developed along the panel length, as illustrated in Figure 4.30b. Figure 4.30c presents the tension face of the specimen after testing, where extensive rupture of wood is observed, confirming that flexural failure governed the ultimate mode of failure of the unretrofitted CLT panel under dynamic loading.

a) Undamaged specimen before testing

b) Development of rolling shear cracks during test

c) Tension view of specimen

Figure 4.30 Representative dynamic failure mode for unretrofitted CLT panel

Dynamic reaction forces were recorded at both supports, and the representative reaction force was taken as the average of the two measured support reactions. A consistent sign convention was adopted such that the positive phase of the blast produced positive displacement and reaction force values. Figure 4.31 presents a representative reflected pressure–time history recorded during a dynamic test, together with the corresponding integrated impulse, for the unretrofitted CLT panel.

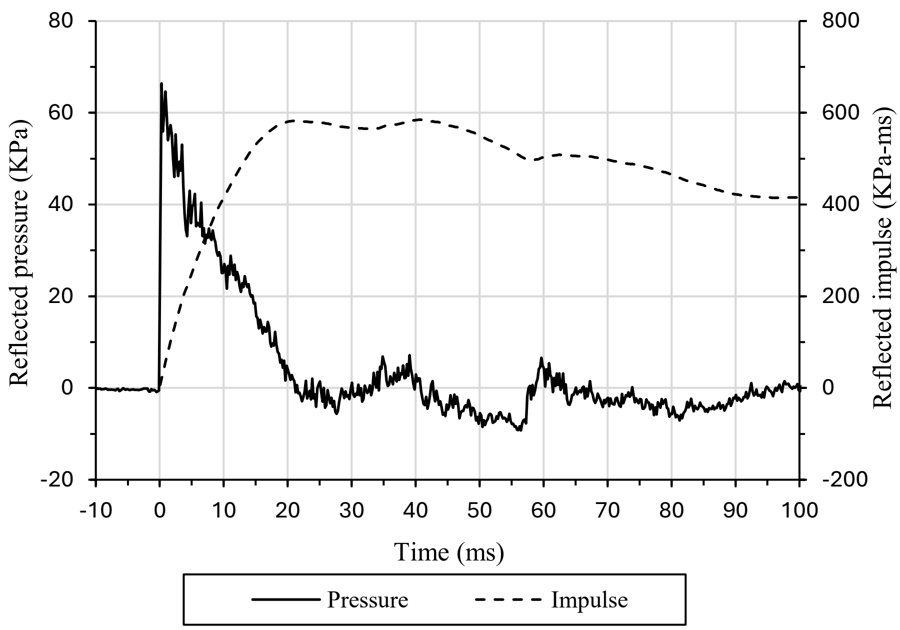

Figure 4.31 Reflected pressure and impulse time history for unretrofitted CLT

Figure 4.32 and Figure 4.33 present the time histories of mid-span displacement, dynamic reaction force, and mid-span tensile strain for the unretrofitted CLT panel subjected to blast loading.

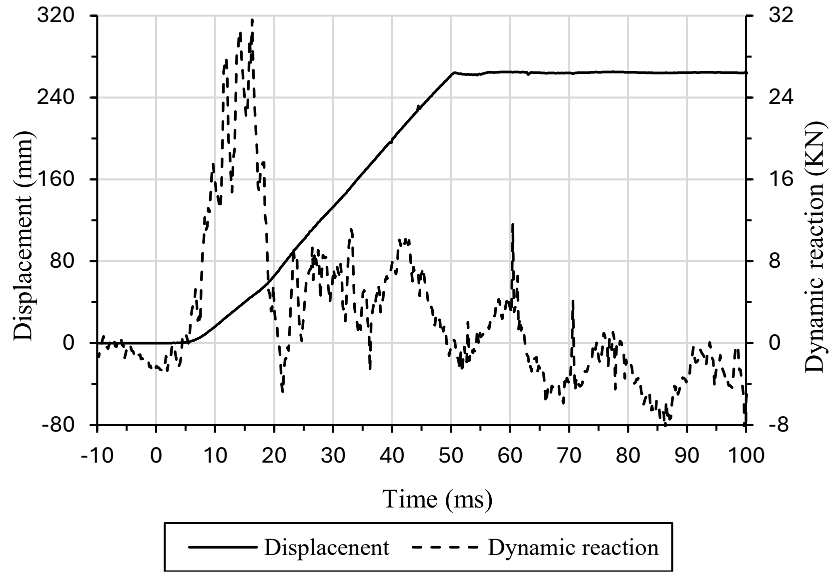

Figure 4.32 Displacement and dynamic reaction time history for unretrofitted CLT

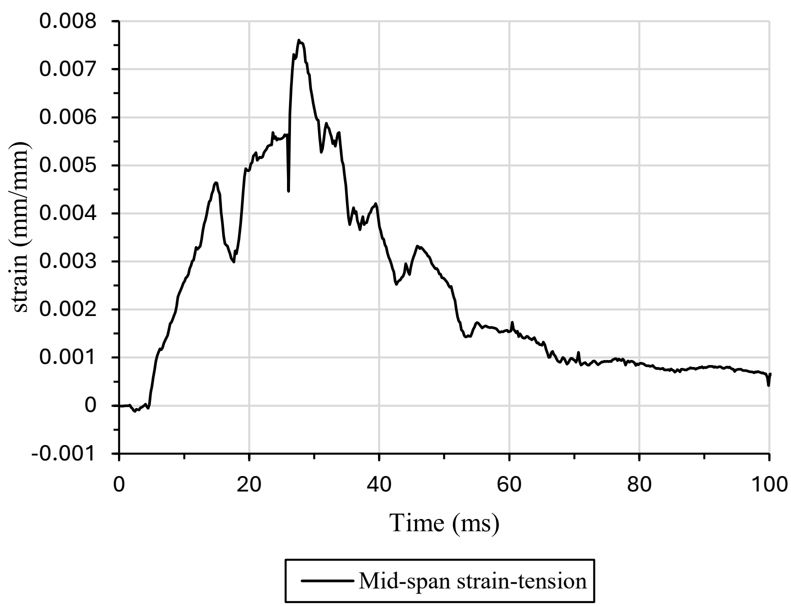

Figure 4.33 Mid span tension strain time history for unretrofitted CLT

4.3.1.2 CLT-T(0)C(0)

Specimen CLT-T(0)C(0) was tested using a driver pressure of 551.6 kPa, resulting in a peak reflected pressure of 83.1 kPa and a positive reflected impulse of 864.1 kPa·ms over a positive phase duration of 23.66 ms. The maximum resistance recorded during the test was 111.9 kN, occurring at 19.66 ms, with the corresponding displacement reaching 93.9 mm. Figure 4.34 represents the dynamic failure mode of the retrofitted panel. As shown in Figure 4.34b, tearing of unidirectional CFRP confinement was observed in a region located approximately at one-third of the panel length from the support, indicating that damage did not develop uniformly along the span. Relatively minor longitudinal shear was also observed at the end of the panel (Figure 4.34c).

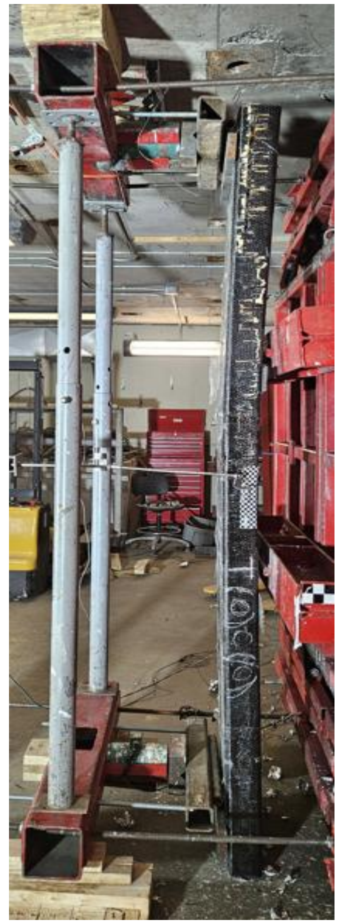

a) Undamaged specimen before testing b) Damaged specimen after testing

c) Compression side view after testing

Figure 4.34 Representative dynamic failure mode for retrofitted CLT panel CLT-T(0)C(0)

Figure 4.35 shows a reflected pressure–time history recorded during a dynamic test, together with the corresponding integrated impulse, for the CLT-T(0)C(0) specimen.

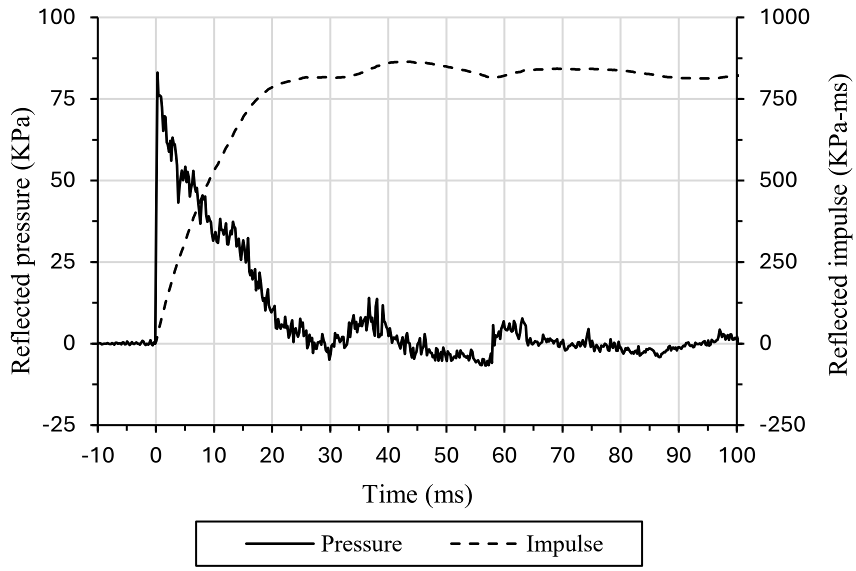

Figure 4.35 Reflected pressure and impulse time history for CLT-T(0)C(0)

The time histories of mid-span displacement, dynamic reaction force, and mid-span tensile strain for the CLT-T(0)C(0) specimen subjected to blast loading are shown in Figure 4.36 and Figure 4.37.

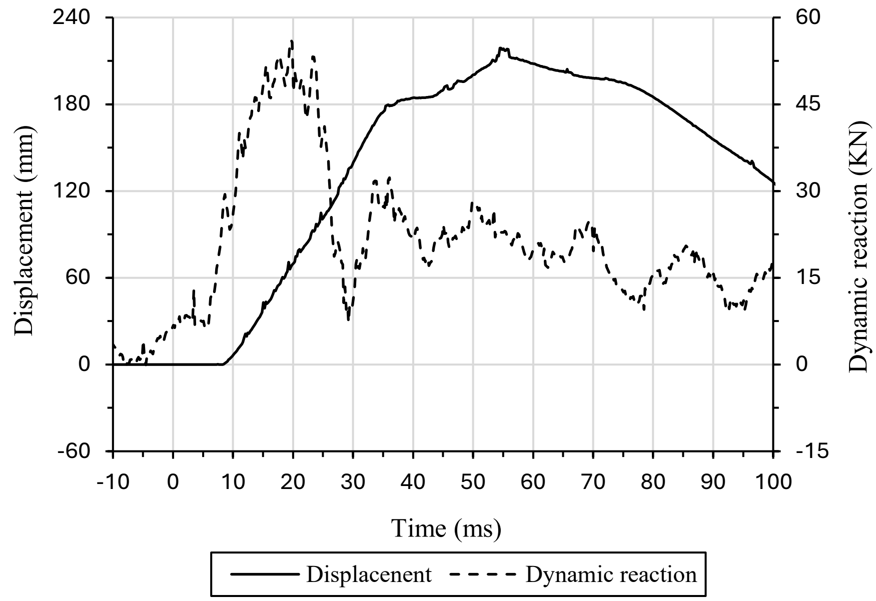

Figure 4.36 Displacement, and dynamic reaction time history for CLT-T(0)C(0)

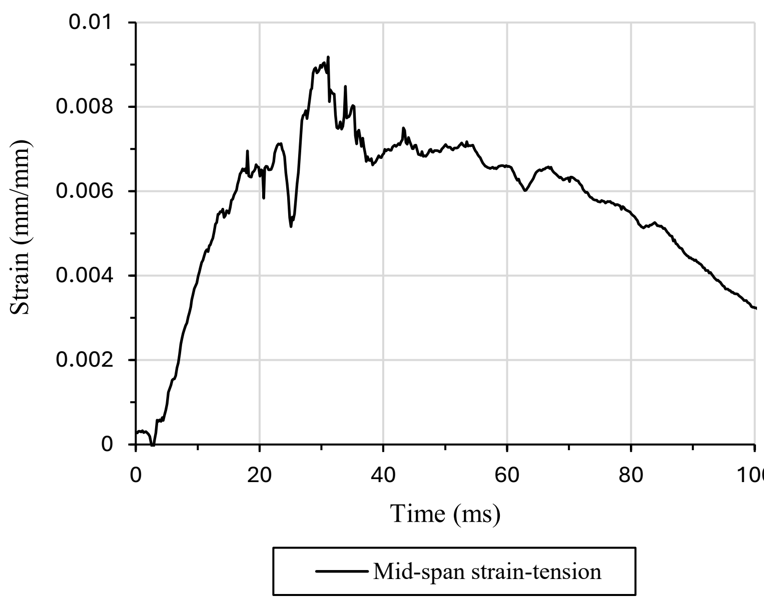

Figure 4.37 Mid span tension strain time history for CLT-T(0)C(0)

4.3.1.3 CLT-T(0)C(±45)

Specimen CLT-T(0)C(±45) was tested under a driver pressure of 517.1 kPa, resulting in a peak reflected pressure of 71 kPa and a positive reflected impulse of 784.2 kPa·ms over a positive phase duration of 21.4 ms. The maximum resistance recorded during the test was 162.4 kN, occurring at 25.4 ms, with the corresponding displacement reaching 101.6 mm. The specimen setup and failure mode are presented in Figure 4.38. The undamaged condition before testing is shown in Figure 4.38a, while the post-test damaged configuration is presented in Figure 4.38b. Under dynamic loading, the panel exhibited flexural failure, followed by tensile rupture of the CFRP reinforcement on the tension side. As shown in Figure 4.38c and Figure 4.38d, tearing of the CFRP fabric initiated near approximately one-third of the panel along the ±45° fiber orientations and propagated along the length of the panel.

a) Undamaged specimen before testing

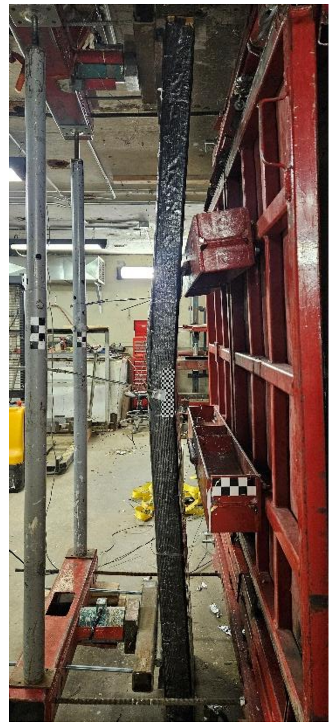

b) Damaged specimen after testing

c) Tearing of fabric on tension side

d) Side view of tearing of fabric

Figure 4.38 Representative dynamic failure mode for retrofitted CLT panel and CLT-T(0)C(±45)

For the CLT-T(0)C(±45) specimen, Figure 4.39 shows a representative reflected pressure-time history obtained during a dynamic test together with the corresponding impulse.

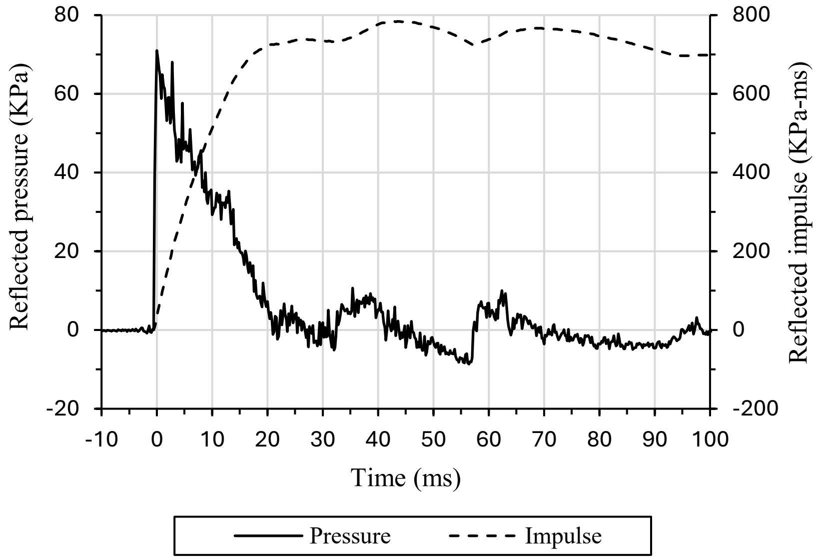

Figure 4.39 Reflected pressure and impulse time history for CLT-T(0)C(±45)

Figure 4.40 and present the time histories mid-span displacement, dynamic reaction

force, and mid-span tensile strain for the CLT-T(0)C(±45) specimen subjected to blast loading.

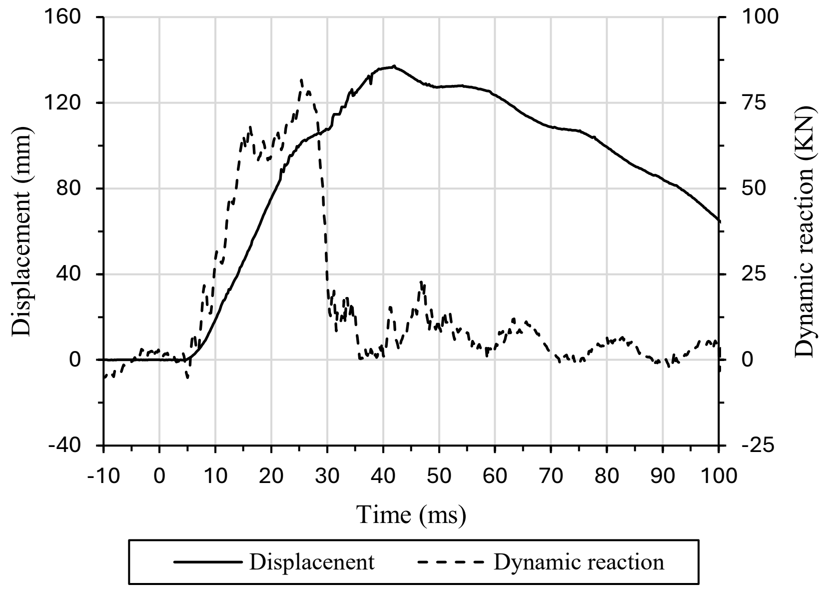

Figure 4.40 Displacement and dynamic reaction time for CLT-T(0)C(±45)

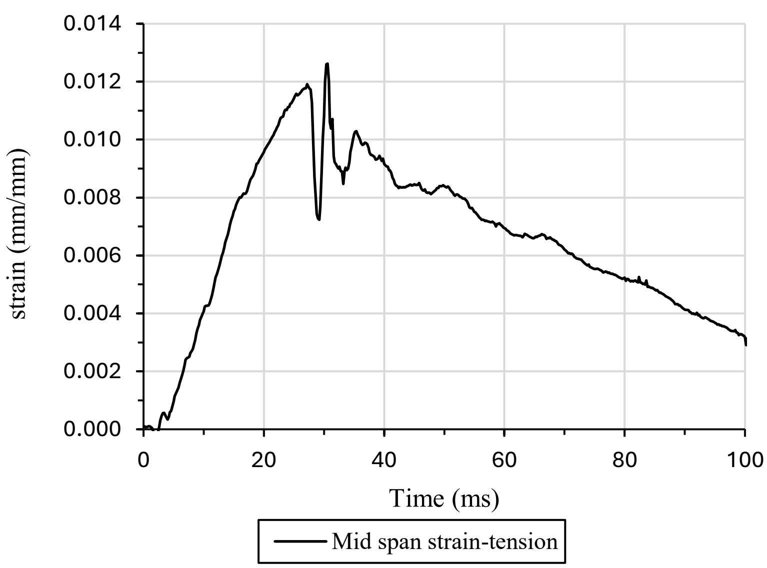

Figure 4.41Mid span tension strain time history for CLT-T(0)C(±45)

4.3.1.4CLT-T(0)$_2$C(±45)

Specimen CLT-T(0)$_2$C(±45) was tested using a driver pressure of 620.5 kPa, resulting in a peak reflected pressure of 85.8 kPa and a positive reflected impulse of 999.4kPa·ms over a positive phase duration of 26.66 ms. The maximum resistance recorded during the test was 167.8 kN, occurring at 19.66 ms, with the corresponding displacement reaching 72.3 mm. For specimen CLT-T$(0)_2$C(±45), the effect of adding extra layers of simple tension to reinforcement was investigated. Figure 4.42 represents the observed failure mode for specimen CLT-T$(0)_2$C(±45). Figure 4.42c shows tearing of the bidirectional CFRP fabric. Limited longitudinal shear failure was also observed at the end of the panel (Figure 4.42d).

a) Undamaged specimen before testing

b) Damaged specimen after testing

c) Compression side view after testing

d) Side view

Figure 4.42 Representative dynamic failure mode for retrofitted CLT panel and CLT-T$(0)_2$C(±45)

For the CLT-T(0)$_2$C(±45) specimen, Figure 4.43 shows a representative reflected pressure-time history obtained during a dynamic test together with the corresponding integrated impulse.

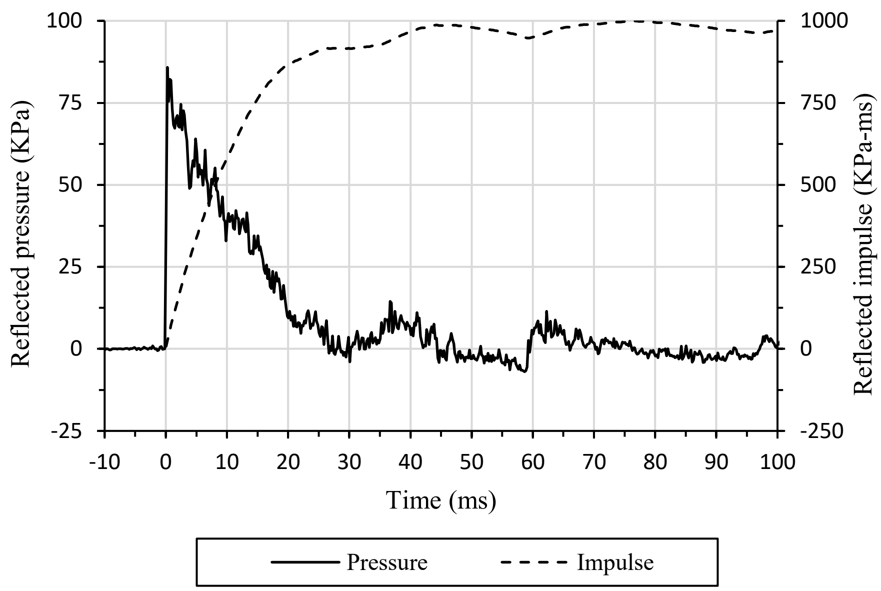

Figure 4.43 Reflected pressure and impulse time history for CLT-T(0)$_2$C(±45)

Figure 4.44 and Figure 4.45 present the time histories of mid-span displacement, dynamic reaction force, and mid-span tensile strain for the CLT-T(0)$_2$C(±45) specimen subjected to blast loading.

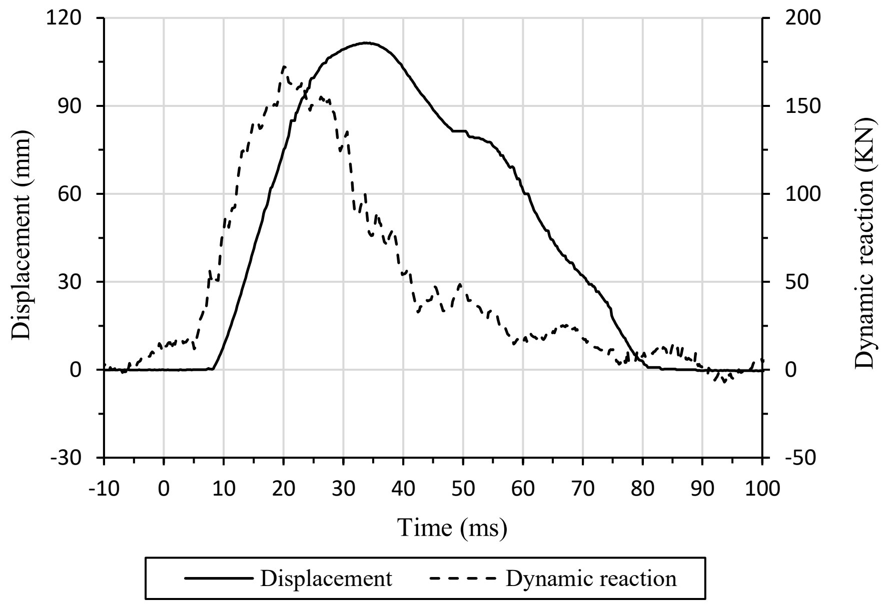

Figure 4.44 Displacement and dynamic reaction time history for CLT-T(0)$_2$C(±45)

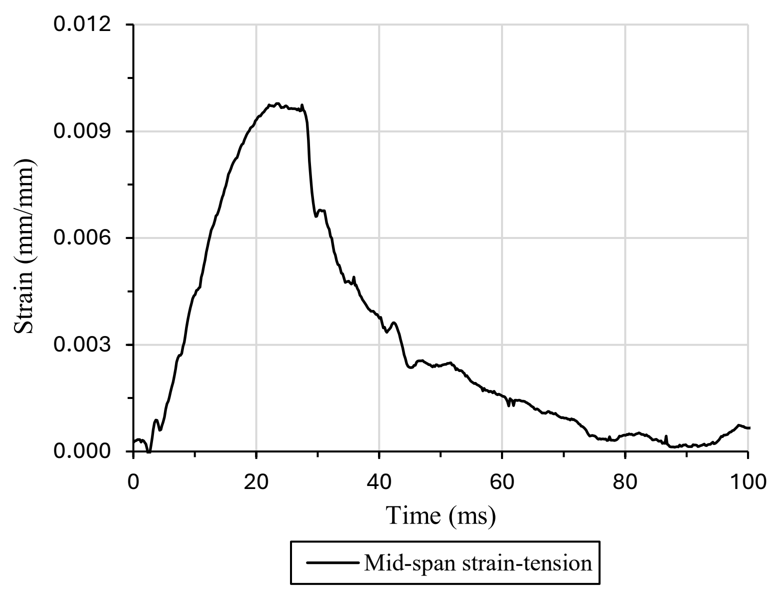

Figure 4.45 Mid span tension strain time history for CLT-T(0)$_2$C(±45)

4.3.1.5 CLT-T(0)U(±45)

Specimen CLT-T(0)U(±45) was tested using a driver pressure of 310.3 kPa, resulting in a peak reflected pressure of 52.6 kPa and a positive reflected impulse of 463.1 kPa·ms over a positive phase duration of 21.85 ms. The maximum resistance recorded during the test was 94.9 kN, occurring at 24.45 ms, with the corresponding displacement reaching 64.6 mm. Following the dynamic loading, significant damage developed in the panel. The failure was characterized by the initiation of shear cracking along the interfaces between adjacent laminates. This cracking led to partial separation of the longitudinal laminates (Figure 4.46b). Figure 4.46c presents the compression side of the specimen after testing, where cracking and laminate separation are clearly observed. The overall failure mode indicates that longitudinal shear failure, combined with damage on the compression face, governed the response of the retrofitted CLT panel under dynamic loading.

a) Undamaged specimen before testing

b) Section view after testing

c) Compression side view after testing

Figure 4.46 Representative dynamic failure mode for retrofitted CLT panel CLT-T(0)U(±45)

For the CLT-T(0)U(±45) specimen, Figure 4.47 shows a representative reflected pressure-time history obtained during a dynamic test together with the corresponding integrated impulse.

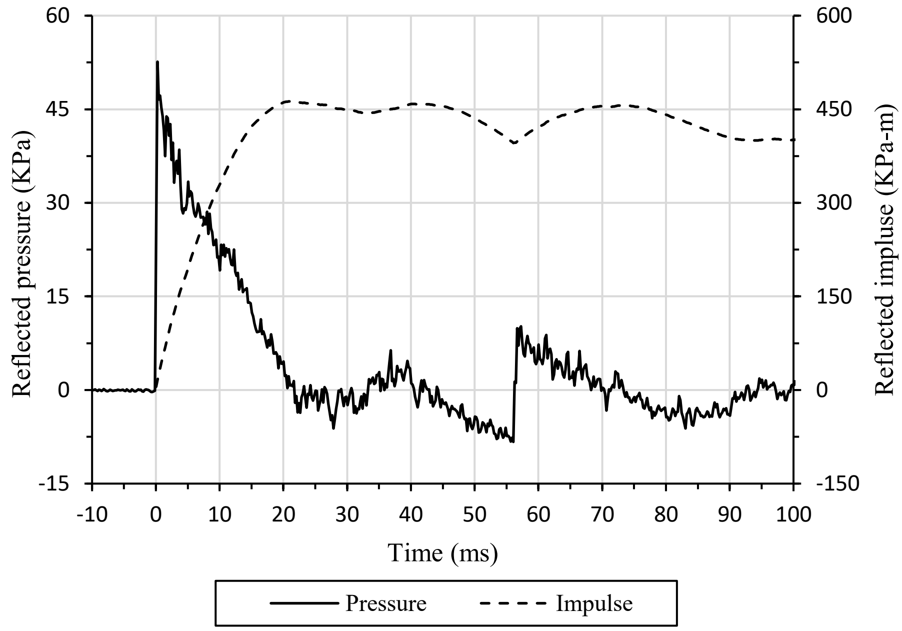

Figure 4.47 Reflected pressure and impulse time history for CLT-T(0)U(±45)

Figure 4.48Figure 4.49 present the time histories of mid-span displacement, dynamic reaction force, and mid-span tensile strain for the CLT-T(0)U(±45) specimen subjected to blast loading.

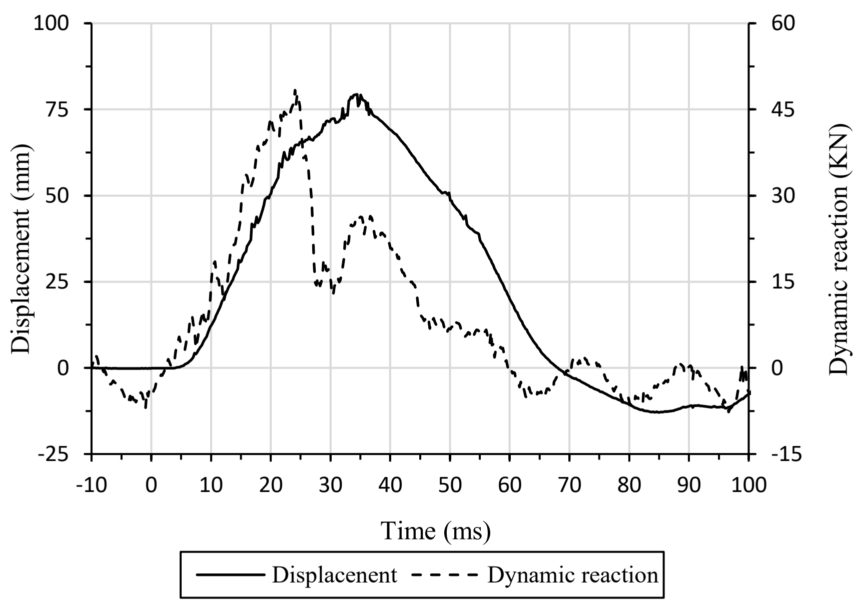

Figure 4.48 Displacement and dynamic reaction time history for CLT-T(0)U(±45)

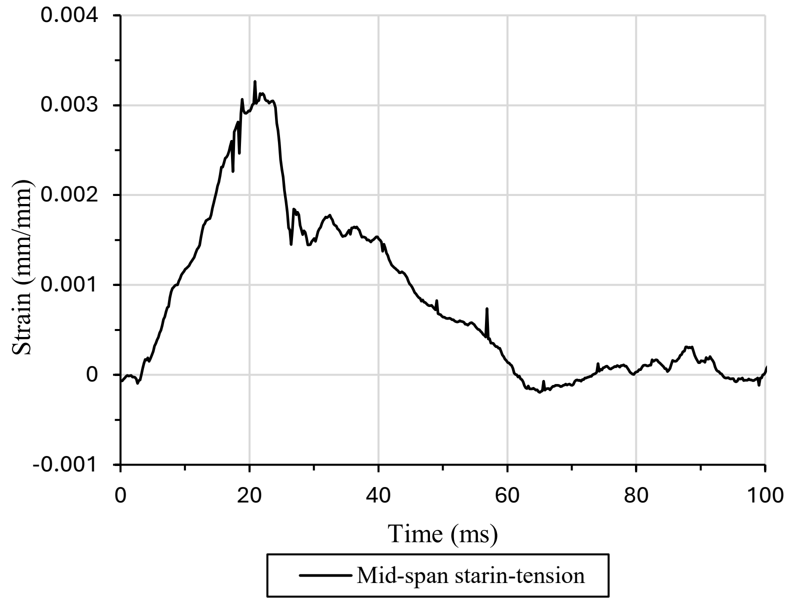

Figure 4.49 Mid span tension strain time history for CLT-T(0)U(±45)

4.3.2 Dynamic test results of unretrofitted and retrofitted glulam beams

4.3.2.1Unretrofitted Glulam

The unretrofitted glulam element was subjected to a driver pressure of 379.2 kPa, resulting in a peak reflected pressure of 63.3 kPa and a positive reflected impulse of 671.1 kPa. ms over a positive phase duration of 24.17 ms. The maximum resistance was 109.2 kN, while the time at maximum resistance was 12.37 ms, and the displacements at the maximum resistance reached 45.6 mm. Figure 4.50 shows that the failure of the wood was dominated by splintering tension failure that was influenced by the presence of a knot (Figure 4.50c).

a) Undamaged specimen before testing

b) Damaged specimen after testing

c) Tension side view of specimen

Figure 4.50 Representative dynamic failure mode for unretrofitted glulam beam

For the unretrofitted glulam beam, Figure 4.51 shows a representative reflected pressure-time history obtained during a dynamic test together with the corresponding integrated impulse.

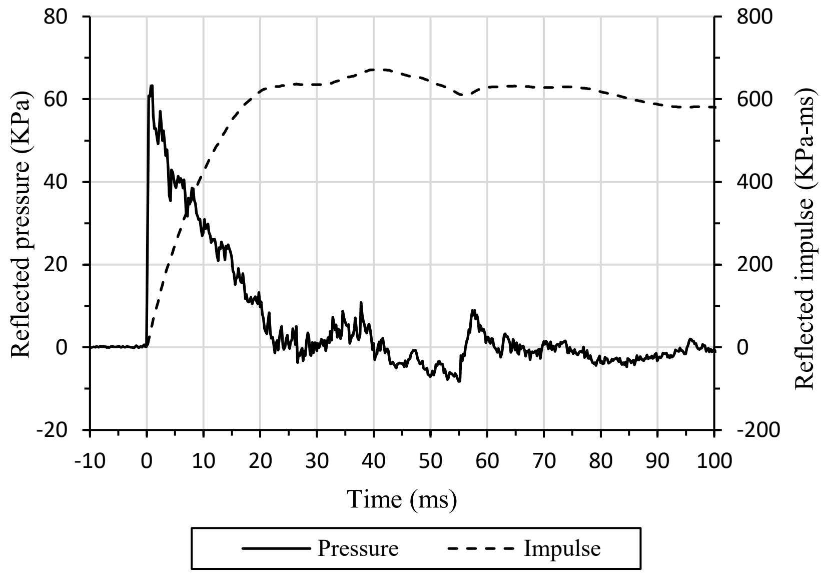

Figure 4.51Reflected pressure and impulse time history for unretrofitted glulam

Figure 4.52 Figure 4.53 present the time histories of mid-span displacement, dynamic reaction force, and mid-span tensile strain for the unretrofitted glulam subjected to blast loading.

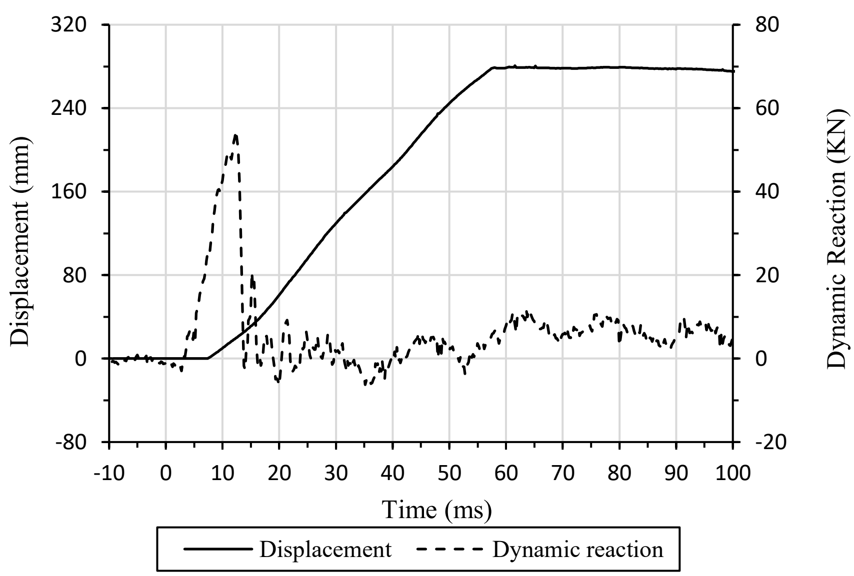

Figure 4.52 Displacement and dynamic reaction time history for unretrofitted glulam

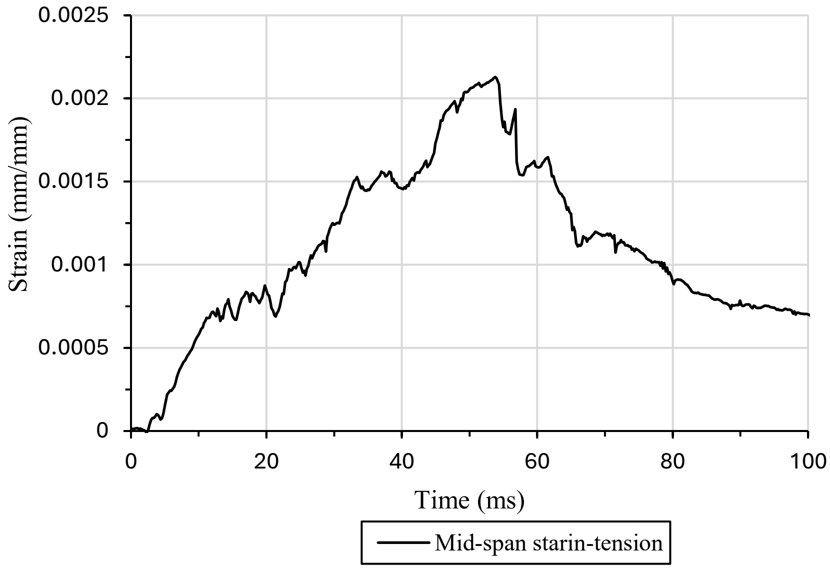

Figure 4.53 Mid span tension strain time history for unretrofitted glulam

4.3.2.2G-T(0)C(0)

Representative failure mode for specimen G-T(0)C(0) is shown in Figure 4.54. The specimen was subjected to a driver pressure of 482.6 kPa, resulting in a peak reflected pressure of 77.3 kPa and a positive reflected impulse of 683.6 kPa·ms over a positive phase duration of 25.16 ms. The maximum resistance recorded during the test was 181.1 kN, occurring at 14.16 ms, with the corresponding displacement reaching 28.2 mm. Following the application of dynamic loading (Figure 4.54) the G-T(0)C(0) specimen exhibited flexural response, leading to a straight cut through the beam width. As illustrated in Figure 4.54b and Figure 4.54c the specimen G-T(0)C(0) was subjected to a pressure and impulse combination exceeding its ability to resist the load, and the damage was primarily concentrated near the mid-height of the specimen.

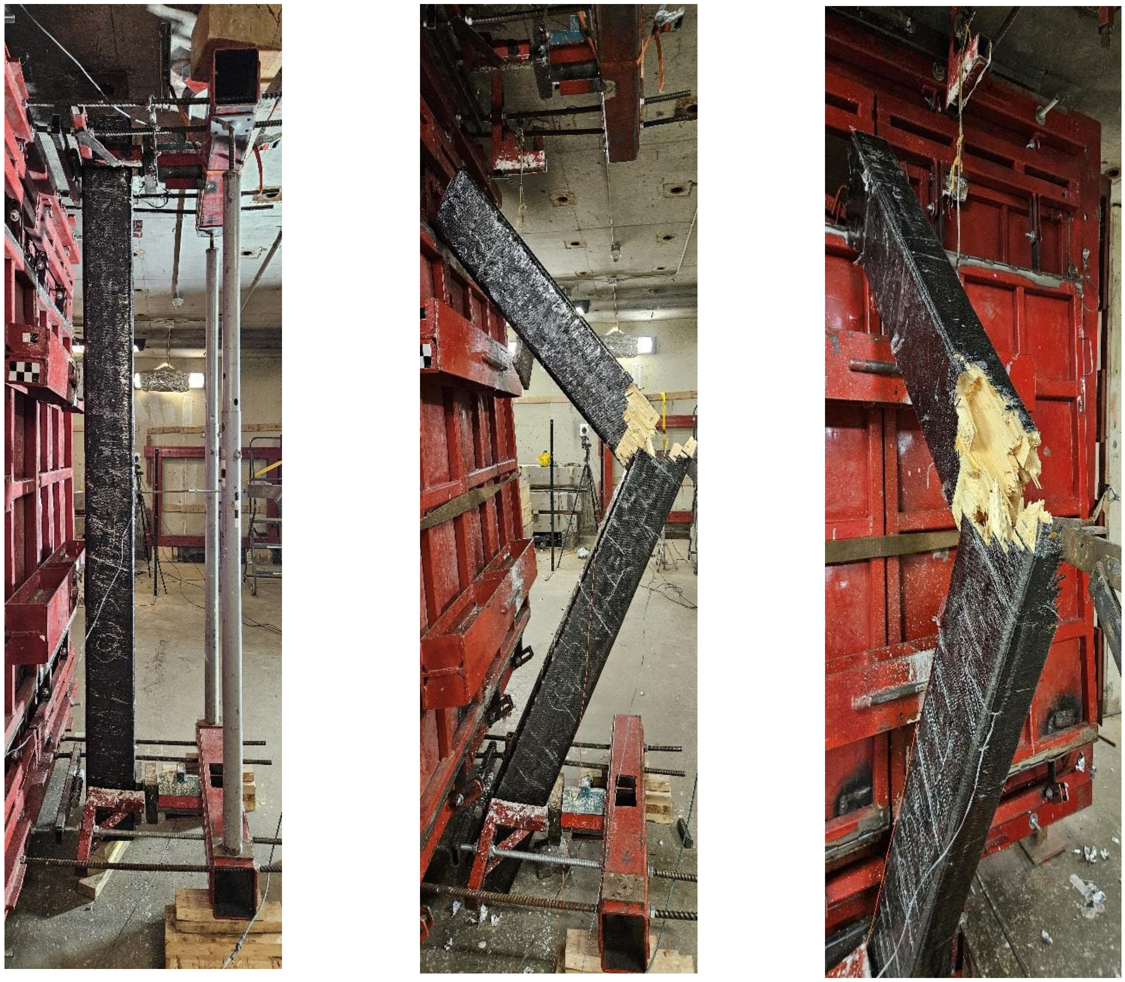

a) Undamaged specimen before testing

b) Damaged specimen after testing

c) Tension side view of specimen

Figure 4.54 Representative dynamic failure mode for reinforced G-T(0)C(0

Figure 4.55 shows a representative reflected pressure-time history with the corresponding integrated impulse for the G-T(0)C(0) specimen obtained during a dynamic test.

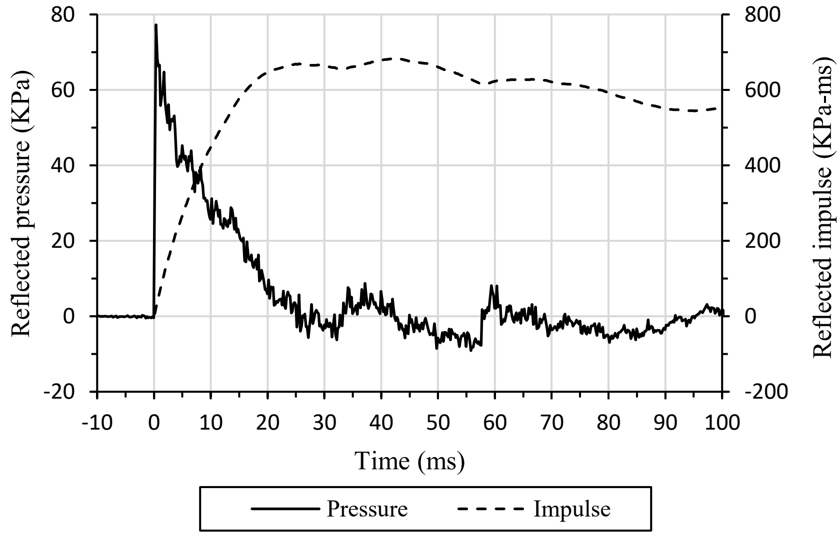

Figure 4.55 Reflected pressure and impulse time history for G-T(0)C(0)

For the G-T(0)C(0) specimen, the time history of mid-span displacement, dynamic reaction, and mid-span tensile strain is shown in Figure 4.56Figure 4.57.

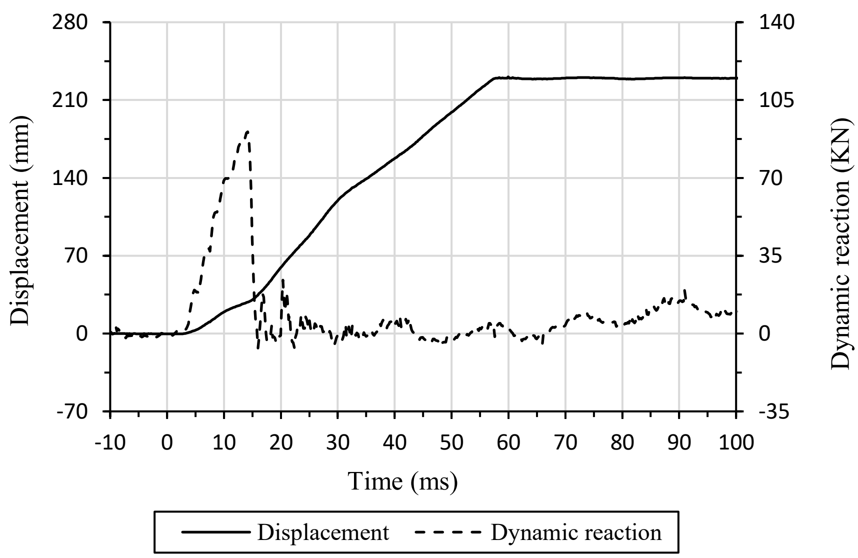

Figure 4.56 Displacement and dynamic reaction time history for G-T(0)C(0)

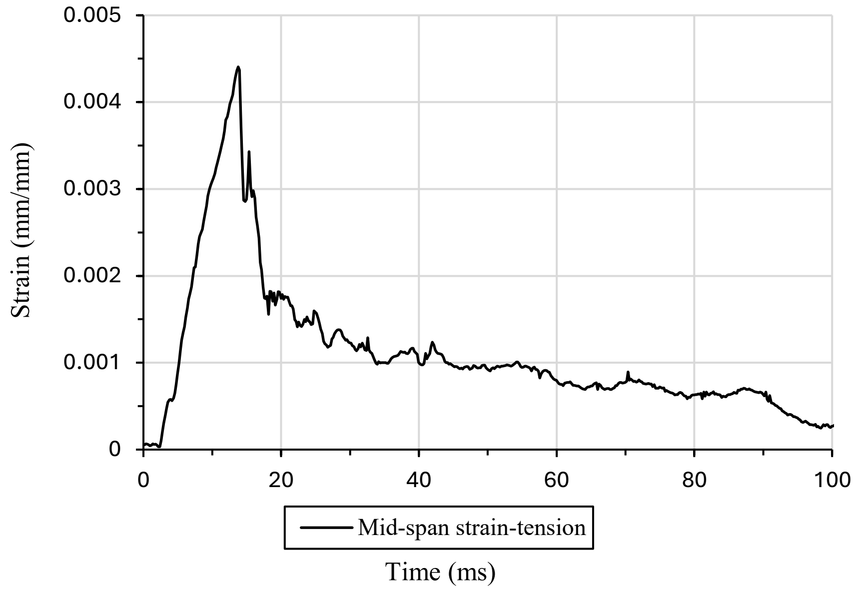

Figure 4.57 Miad span tension strain time history for G-T(0)C(0)

4.3.2.3G-T(0)C(±45)

Specimen G-T(0)C(±45) was tested using a driver pressure of 530.9 kPa, resulting in a peak reflected pressure of 78.6 kPa and a positive reflected impulse of 786 kPa·ms over a positive phase duration of 23.16 ms. The maximum resistance recorded during the test was 191.1 kN, occurring at 13.36 ms, with the corresponding displacement reaching 42.0 mm. Figure 4.58 shows the representative dynamic failure pattern of the retrofitted glulam beam G-T(0)C(±45). As presented in Figure 4.58c, it can be seen that splintering of CFRP confinement occurred along the direction of the fabric.

a) Undamaged specimen before testing

b) Damaged specimen after testing

c) Close-up view of specimen

Figure 4.58 Representative dynamic failure mode for retrofitted glulam G-T(0)C(±45)

Figure 4.59 shows a representative reflected pressure-time history with the corresponding integrated impulse for the G-T(0)C(±45) specimen obtained during a dynamic test.

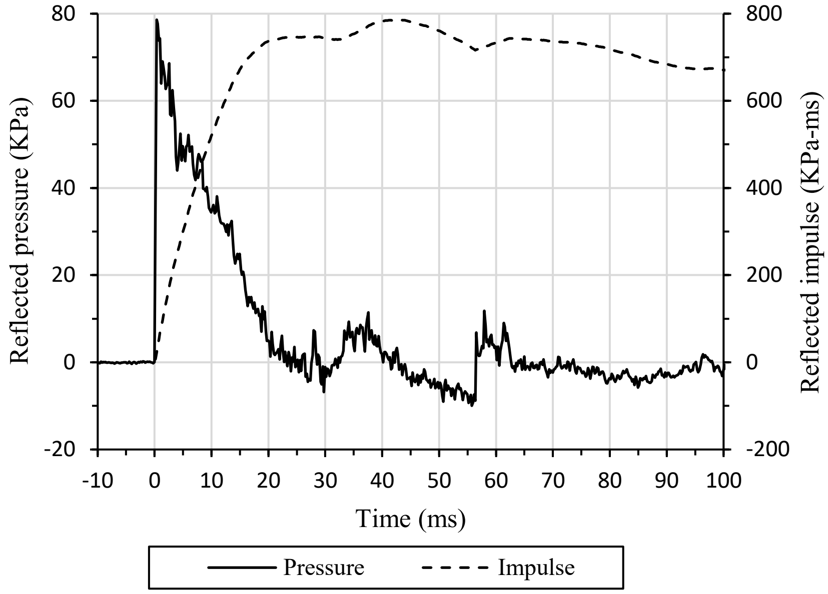

Figure 4.59 Reflected pressure and impulse time history for G-T(0)C(±45)

The time history of mid-span displacement, dynamic reaction, and mid-span tensile strain for the G-T(0)C(±45) specimen subjected to blast loading is shown in Figure 4.60Figure 4.61.

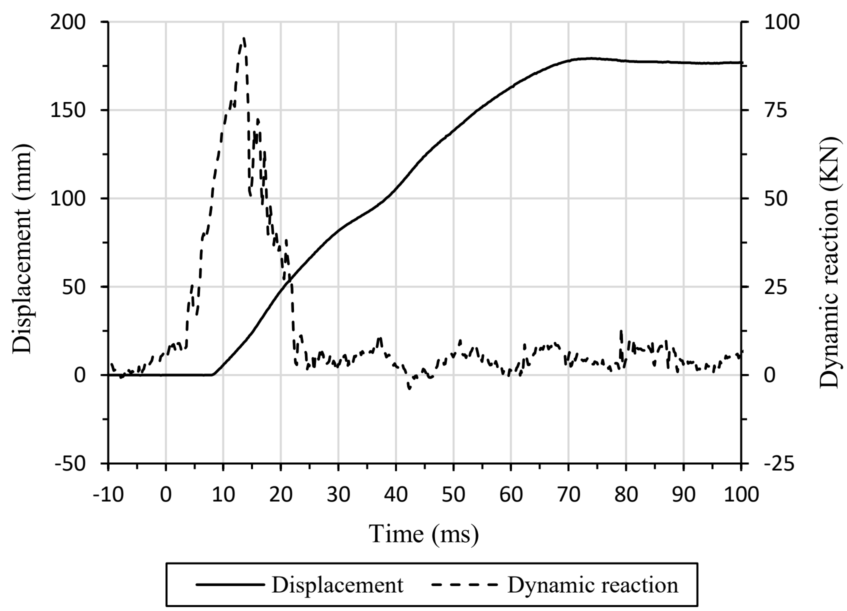

Figure 4.60 Displacement and dynamic reaction time history for G-T(0)C(±45)

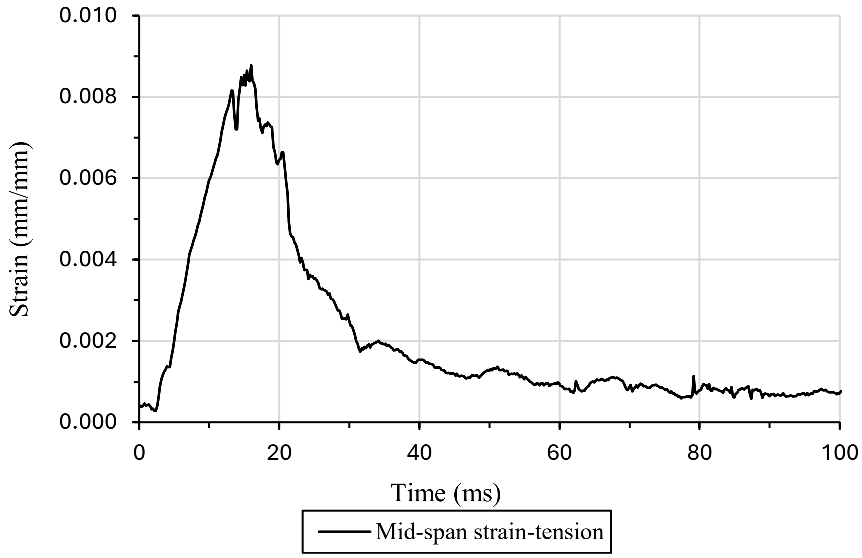

Figure 4.61 Mid span tension strain time history for G-T(0)C(±45)

4.3.2.4G-T(0)$_2$C(±45)

Specimen G-T(0)$_2$C(±45) was tested using a driver pressure of 668.8 kPa, resulting in a peak reflected pressure of 102.5 kPa and a positive reflected impulse of 942.1 kPa·ms over a positive phase duration of 25.03 ms. The maximum resistance recorded during the test was 243.9 kN, occurring at 13.63 ms, with the corresponding displacement reaching 53 mm. Figure 4.62 presents the representative dynamic failure mode of the retrofitted glulam beam G-T(0)$_2$C(±45). Figure 4.62c shows that specimen G-T(0)$_2$C(±45) was subjected to a pressure and impulse combination higher than its ability to resist the load, and the damage was in a region located approximately at one-third of the panel.

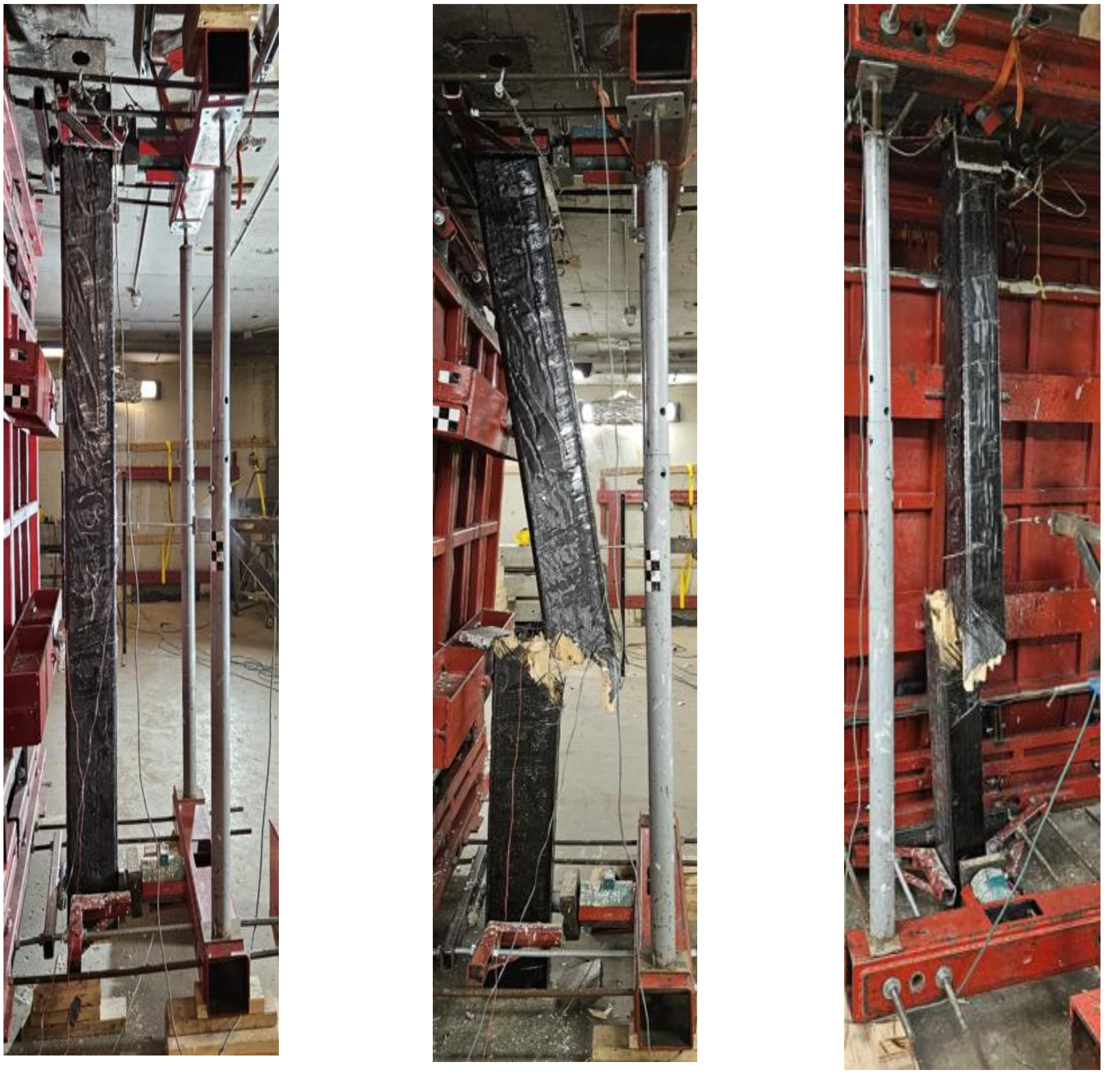

a) Undamaged specimen before testing

b) Damaged specimen after testing

c)Tension side view of specimen

Figure 4.62 Representative dynamic failure mode for retrofitted glulam beam G-T(0)$_2$C(±45)

Figure 4.63 shows a representative reflected pressure-time history with the corresponding integrated impulse for the G-T(0)$_2$C(±45) specimen obtained during a dynamic test.

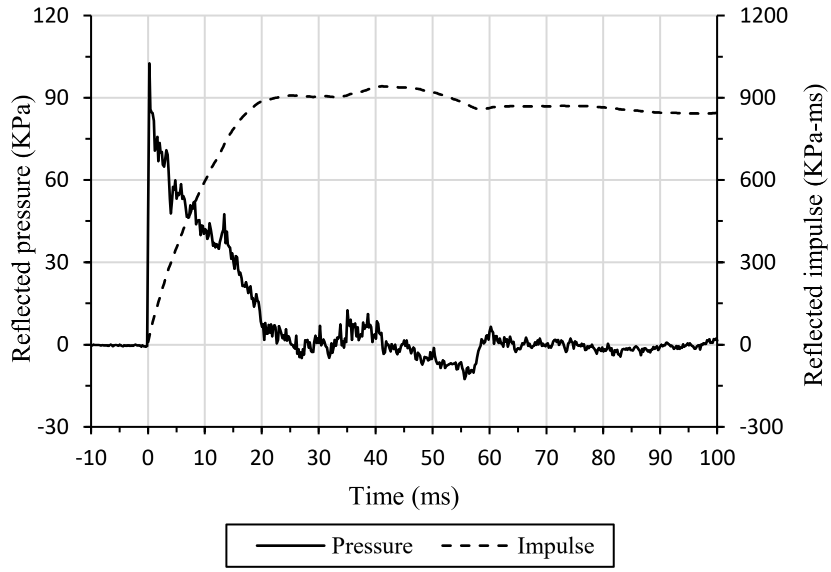

Figure 4.63 Reflected pressure and impulse time history for G-T(0)$_2$C(±45)

The time history of mid span displacement, dynamic reaction, and mid span tensile strain for G-T(0)$_2$C(±45) specimen subjected to blast loading is shown in Figure 4.64Figure 4.65.

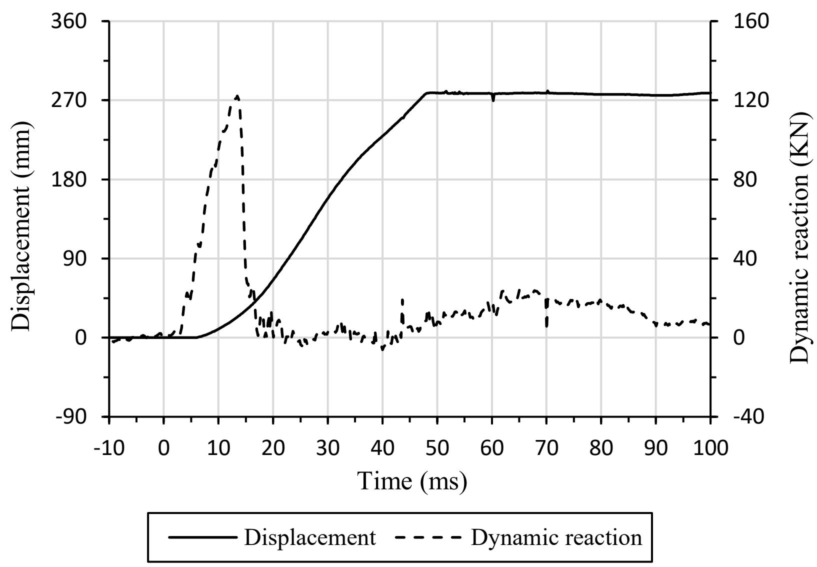

Figure 4.64 Displacement and dynamic reaction time history for G-T(0)$_2$C(±45)

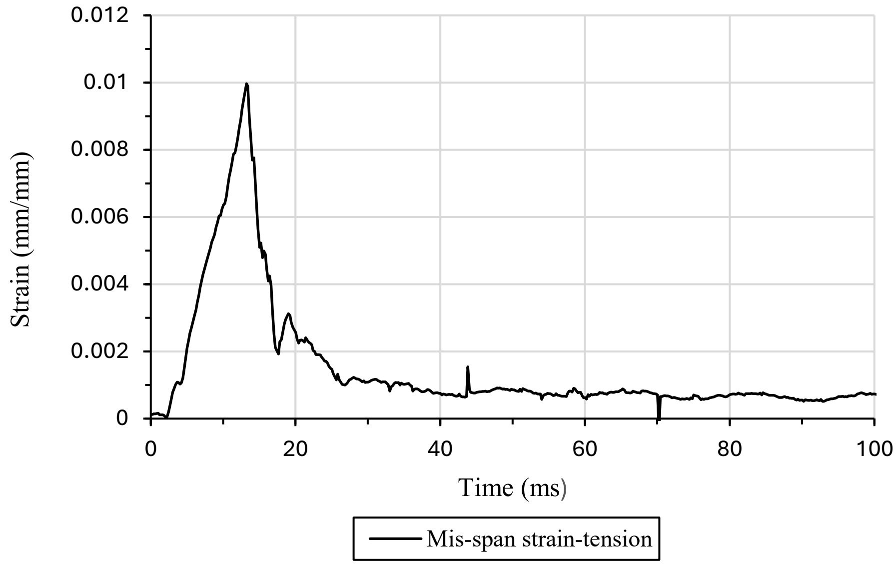

Figure 4.65 Mid span tension strain stress time history for G-T(0)$_2$C(±45)

4.3.2.5 G-T(0)U(±45)

Specimen G-T(0)U(±45) was tested using a driver pressure of 517.1 kPa, resulting in a peak reflected pressure of 81 kPa and a positive reflected impulse of 742.6 kPa·ms over a positive phase duration of 21.16 ms. The maximum resistance recorded during the test was 196.7 kN, occurring at 13.76 ms, with the corresponding displacement reaching 31.3 mm. Figure 4.66 illustrates the representative dynamic failure mode of the retrofitted glulam beam G-T(0)U(±45). The specimen failed in flexure, and slight separation between the CFRP fabric as partial confinement and wood surface was also observed (Figure 4.66b).

a) Undamaged specimen before testing   b) Damaged specimen after testing

Figure 4.66 Representative dynamic failure mode for retrofitted glulam G-T(0)U(±45)

Figure 4.67 shows a representative reflected pressure-time history with the corresponding integrated impulse for the G-T(0)U(±45) specimen obtained during a dynamic test.

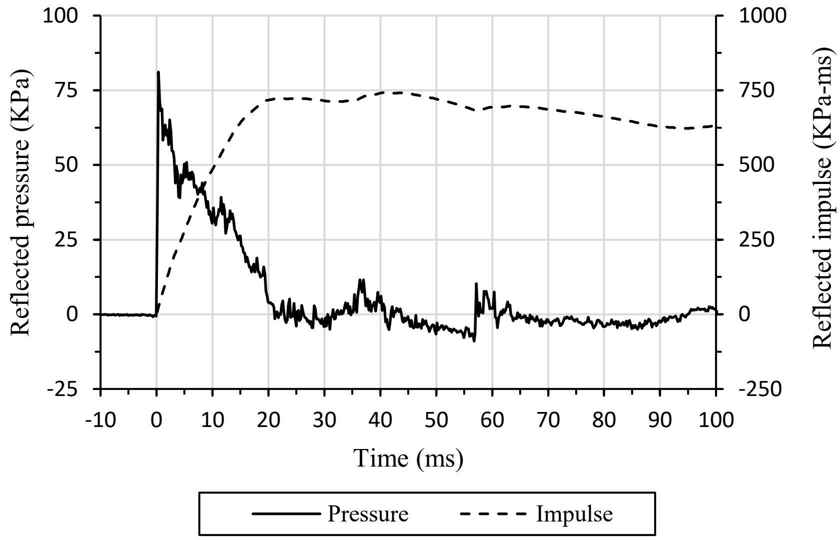

Figure 4.67 Reflected pressure and impulse time history for G-T(0)U(±45)

The time history of mid-span displacement, dynamic reaction, and mid span tensile strain for G-T (0)U(±45) specimen subjected to blast loading is shown in Figure 4.68Figure 4.69.

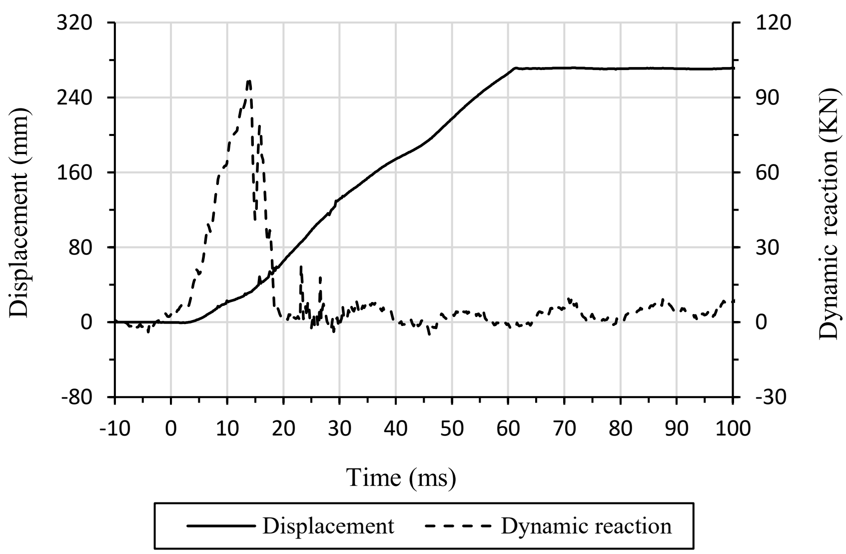

Figure 4.68 Displacement and dynamic reaction time history for G-T(0)U(±45)

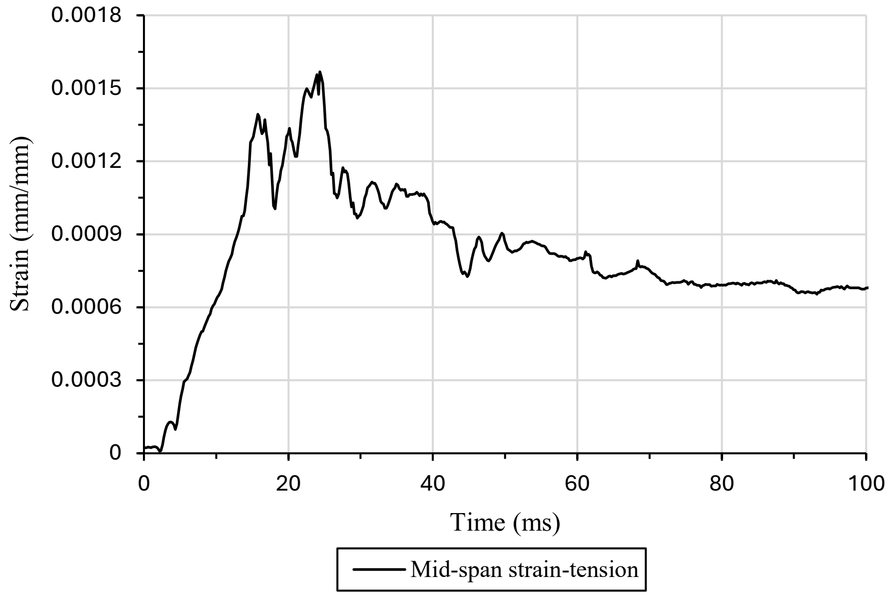

Figure 4.69 Mid span tension strain time history for G-T(0)U(±45)

4.4 Resistance Curves

The resistance curve of each specimen was determined using the measured pressure, reaction, and displacement time histories. To evaluate the specimen resistance, Equation 4.1 was used, which establishes a relationship between the time-dependent support reactions, $V(t)$, the applied load, $F(t)$, and the element resistance, $R(t)$. This relationship was obtained by enforcing moment equilibrium over half of the specimen span about the equivalent inertial force vector, located at a distance $x_{eq}$from the support. Figure 4.70 illustrates the idealized system represented by the governing equation, highlighting the relationship between the moment capacity M_R and the ultimate member resistance $R,$ as expressed in Equation 4.2.

$$\mathrm{R(t)}=\left(\frac{6}{\mathrm{L}}\right)\left(\mathrm{V(t)x_{eq}}+0.5\left(\frac{\mathrm{L}}{3}-\mathrm{x_{eq}}\right)\ \mathrm{F(t)}\right) \qquad \text{Equation 4.1}$$

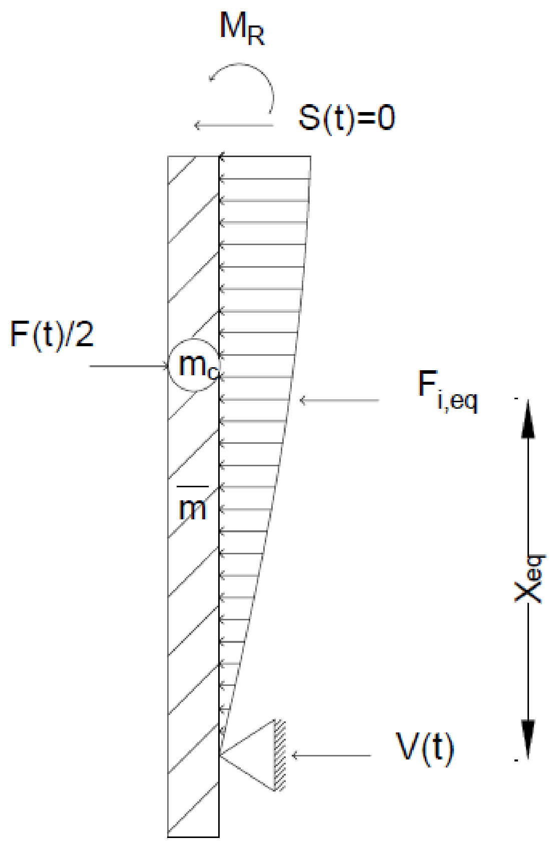

Figure 4.70 Idealized system for the derivation of resistance equation

$$M_R = \frac{R.L}{6}$$ Equation 4.2

The position of the resultant inertial force, x_{eq}, was calculated using Equation (4-3), in which $m_c$denotes the discrete mass acting at the loading points under the four-point bending configuration, and $\overline{m}$ represents the distributed mass of the specimen. A tributary area of 3.55 m^2 was assumed as the effective load transfer area, and the LTD mass was reduced appropriately to 284 kg. As a result, the concentrated mass m_c used in Equation 4.3 was defined as half of the effective LTD mass, corresponding to 142 kg.

$$X_{eq} = \frac{0.102\overline{m}\, L^2 + 0.29 m_c L}{0.319\, \overline{m}\, L + 0.870 m_c}$$ Equation 4.3

The experimentally obtained dynamic resistance curves for unretrofitted and retrofitted CLT specimens are presented in Figure 4.71-Figure 4.75.

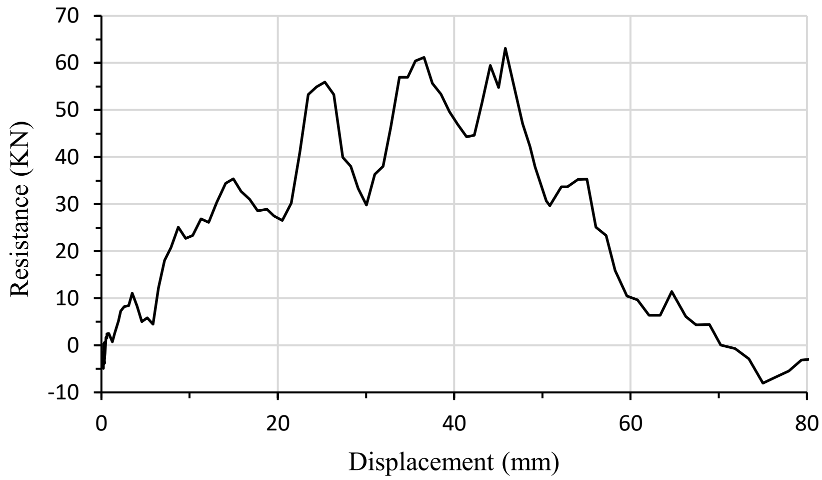

Figure 4.71 Dynamic resistance curve for unretrofitted CLT

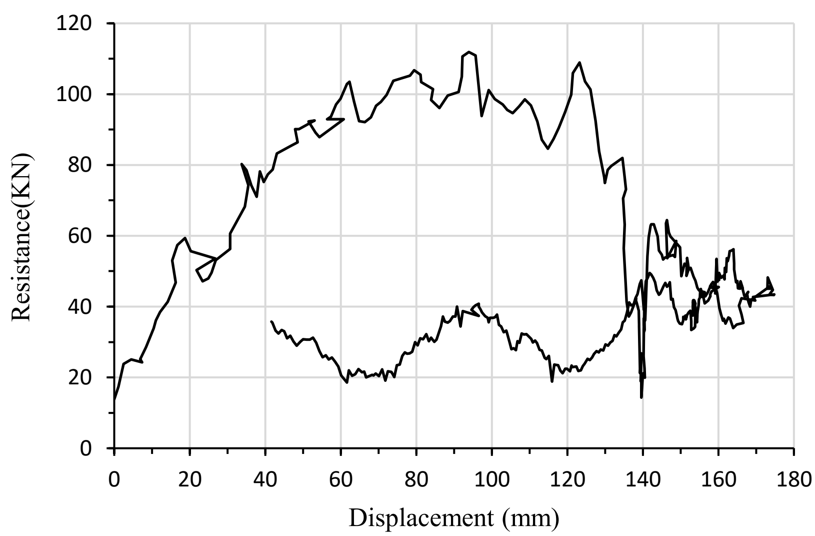

Figure 4.72 Dynamic resistance curve for CLT-T(0)C(0)

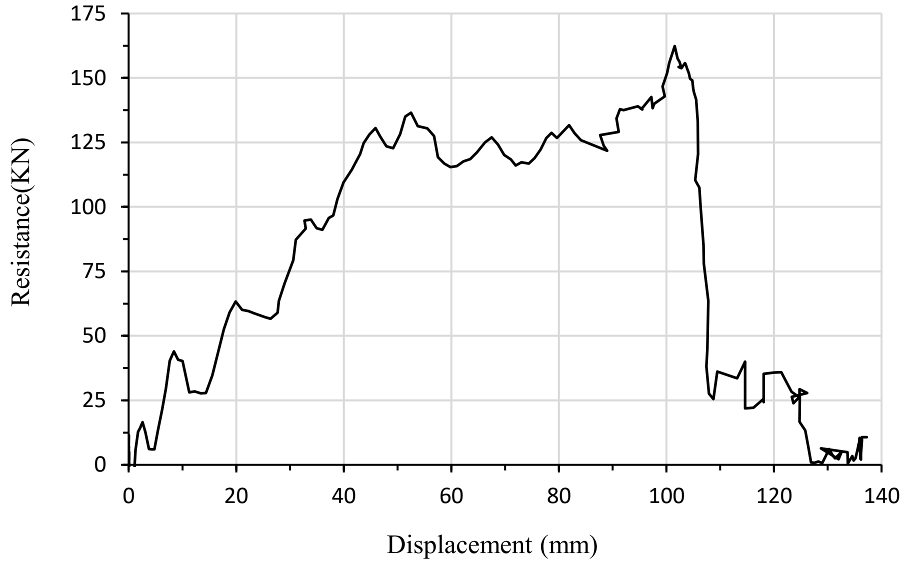

Figure 4.73 Dynamic resistance curve for CLT-T(0)C(±45)

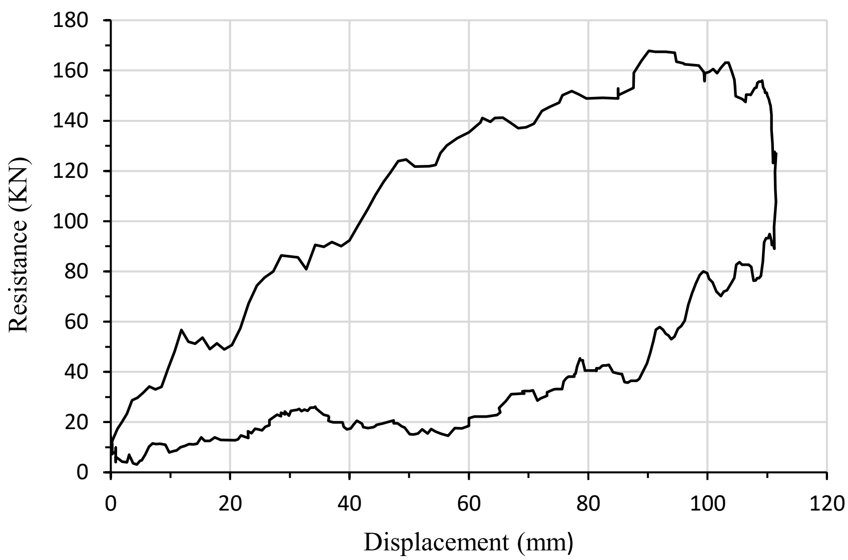

Figure 4.74 Dynamic resistance curve for CLT-T$(0)_2$C(±45)

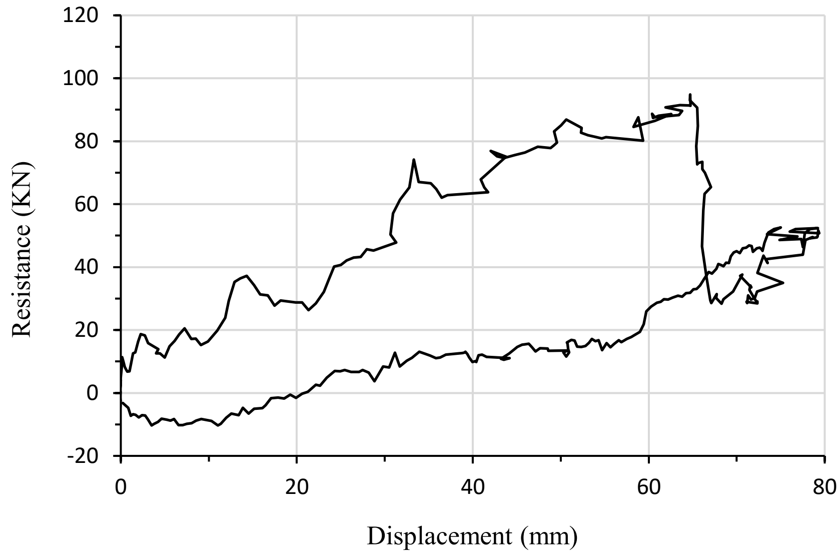

Figure 4.75 Dynamic resistance curve for CLT-T(0)U(±45)

The key experimental parameters for all CLT specimens are summarized in Table 4.3, including reflected pressure, impulse, maximum resistance, and deflection at maximum resistance, as well as specimen stiffness, maximum tensile strain, and compressive strains in wood. The stiffness of specimens was determined from the slope of the resistance-displacement curve using the linear trendline function in Microsoft Excel.

Table 4.3 Summary of dynamic destructive test results (CLT panel)

Configuration	$\mathbf{P_R^a}$ **(KPa)**	$\mathbf{I_R^b}$ **(mm)**	$\mathbf{R^c_{max-d}}$ **(KN)**	$\mathbf{\Delta^d_{Rmax}}$ **(mm)**	$\mathbf{K^e}$ **(KN/mm)**	$\boldsymbol{\varepsilon^f_{t,w-f}}$ **x10^{-4} (mm/mm)**	$\boldsymbol{\varepsilon^g_{c,w-f}}$ **x10^{-4} (mm/mm)**
Unretrofitted CLT	66.4	585	63.1	45.8	1.98	76.1	-
CLT-T(0)C(0)	83.1	864.1	111.9	93.9	2.21	91.85	74.12
CLT-T(0)C(±45)	71	784.2	162.4	101.5	3	126.23	-
CLT-T(0)$_2$C(±45)	85.8	999.4	167.8	90.2	2.05	97.79	52.28
CLT-T(0)U(±45)	52.6	463.1	94.9	64.6	1.56	32.65	37.24

[a]Reflected pressure [b]Reflected impulse [c]Maximum dynamic resistance [d]Deflection at maximum resistance [e]Stiffness [f]Strain at wood tensile [g]Maximum wood compressive strain

The experimentally obtained dynamic resistance curves for unretrofitted and retrofitted glulam beams are presented in Figure 4.76-Figure 4.80.

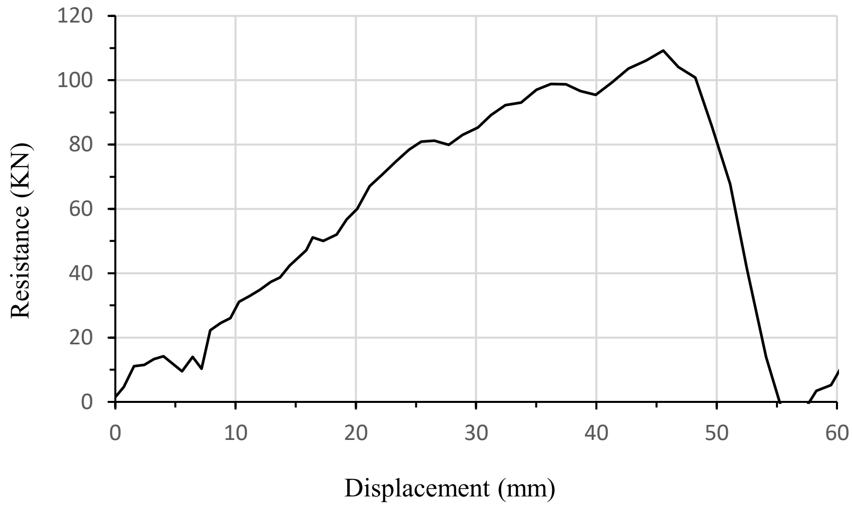

Figure 4.76 Dynamic resistance curve for unretrofitted glulam

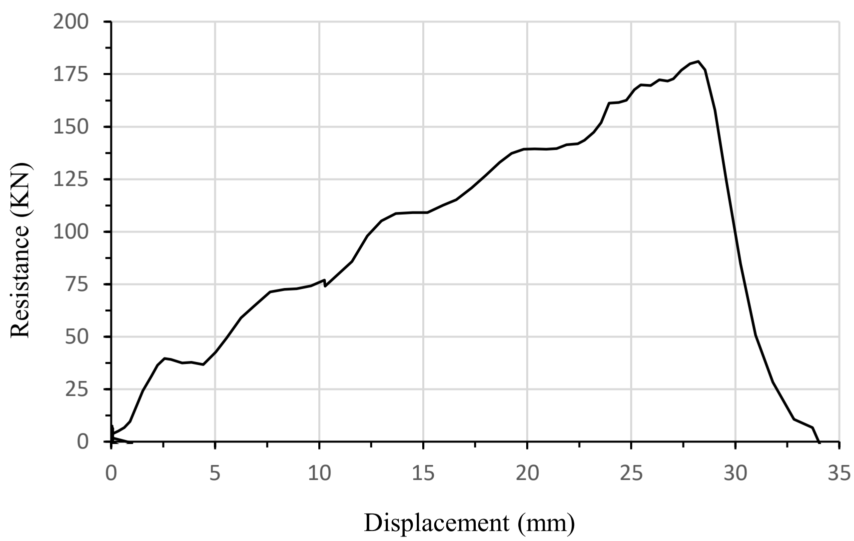

Figure 4.77 Dynamic resistance curve for G-T(0)C(0)

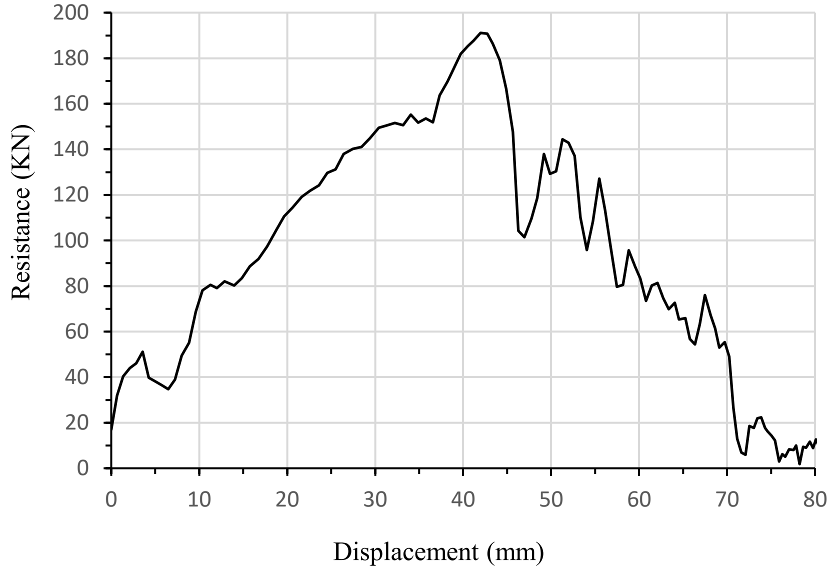

Figure 4.78 Dynamic resistance curve for G-T(0)C(±45)

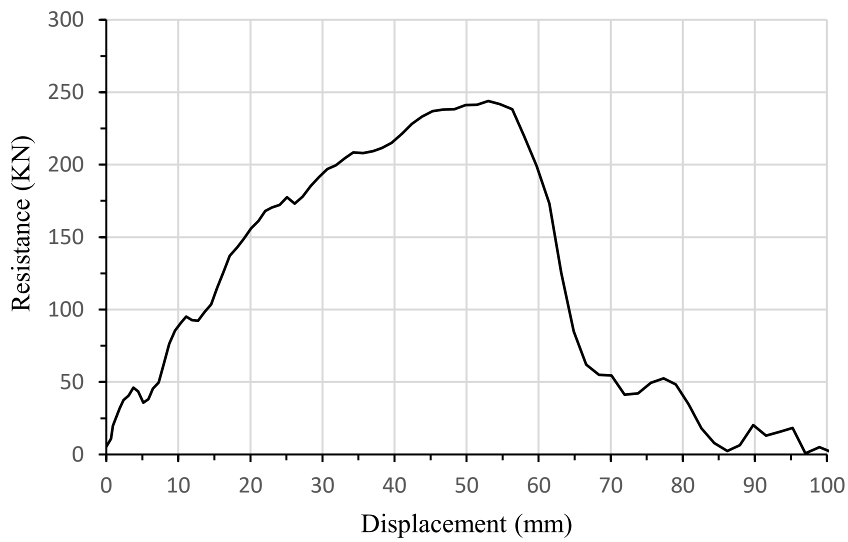

Figure 4.79 Dynamic resistance curve for G-T(0)$_2$C(±45)

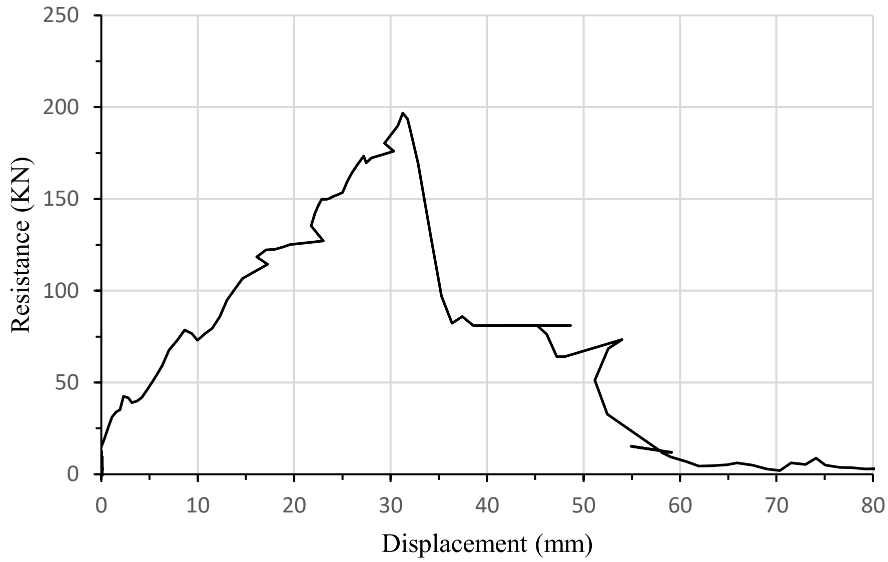

Figure 4.80 Dynamic resistance curve for G-T(0)U(±45)

The key experimental parameters for all glulam specimens are summarized in Table 4.4.

Table 4.4 Summary of dynamic destructive test results (Glulam beam)

Configuration	$\mathbf{P_R^a}$ **(KPa)**	$\mathbf{I_R^b}$ **(mm)**	$\mathbf{R^c_{max-d}}$ **(KN)**	$\mathbf{\Delta^d_{Rmax}}$ **(mm)**	$\mathbf{K^e}$ **(KN/mm)**	$\mathbf{\varepsilon^f_{t,w-f}}$ **x10**$^{-4}$ **(mm/mm)**	$\mathbf{\varepsilon^g_{c,w-f}}$ **x10**$^{-4}$ **(mm/mm)**
Unretrofitted Glulam	63.3	671.1	109.2	45.6	2.71	21.29	61.17
G-T (0)C(0)	77.3	683.6	181.1	28.2	6.78	44.07	42.29
G-T (0)C(±45)	78.6	786	191.1	42	4.74	87.80	78.70
G-T $(0)_2$C(±45)	102.5	942.1	243.9	53	6.06	99.67	94.65
G-T (0)U (±45)	81	742.6	196.7	31.3	3.15	15.68	52.19

[a]Reflected pressure [b]Reflected impulse [c]Maximum dynamic resistance [d]Deflection at maximum resistance [e]Stiffness [f]Strain at wood tensile [g]Maximum wood compressive strain

Chapter 5 Analytical Modelling and Results

5.1 General

This chapter presents the methodology used to predict the response of full-scale timber members under static and simulated blast loading. This includes fiber-section analysis and single-degree-of-freedom (SDOF) modeling, and the outcomes obtained from each approach are presented and discussed. For consistency, all analytical results are reported using the same specimen identification nomenclature established in the experimental program. The inputs and simplifications for both methods, as well as the underlying theories, are also outlined.

5.2Constitutive Material Relationship (Fiber section analysis)

In this research, the stress-strain relationship for wood under tension and compression, as proposed by Buchanan (1990), was utilized. The wood material model adopted in this study to simulate wood behaviour is depicted in Figure 5.1, where ε_{uc} and ε_{ut} represent the ultimate strain in compression and tension, respectively. ε_y and σ_{yc} represents the yield (crushing) strain and stress, respectively, while σ_{uc} and σ_{ut} refer to the ultimate stress in compression and tension, respectively.

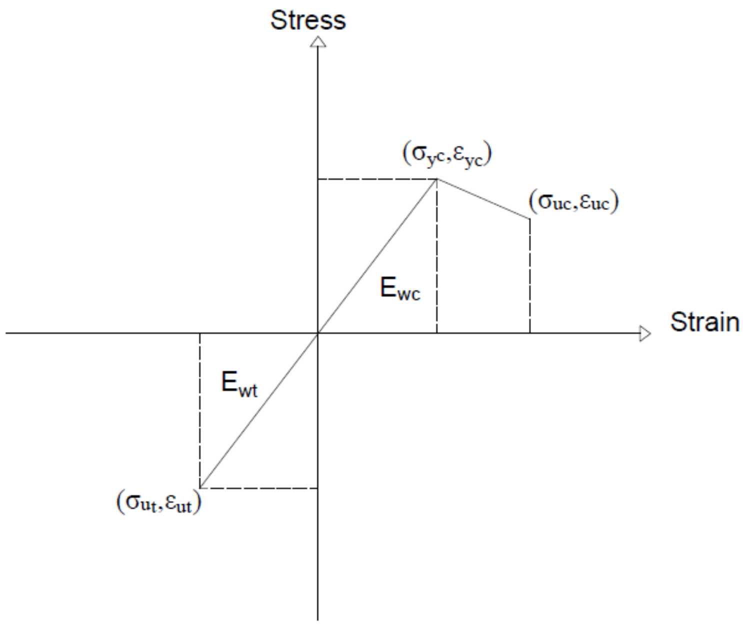

Figure 5.1 Compression and tension stress strain of wood

For the descending branch in compression (m) a value of 0.1 was adopted based on the literature (Lacroix and Doudak 2018c; Gergi and Doudak 2026). The stress–strain relationship and modulus of elasticity (MOE) presented in Table 5.1 were obtained from coupon test results reported by Lacroix and Doudak (2018c) for glulam and Oliveira (2021) for CLT, from similar samples obtained from the same manufacturer.

Table 5.1 Material properties for unretrofitted CLT panels (Oliveira 2021) and glulam beams (Lacroix and Doudak 2018c) used in the static analytical modeling

Cross section	**σ_y[a] (MPa)**	**ε_y[b] x10^{-4} (mm/mm)**	**MOE[c] (MPa)**
Unretrofitted CLT	30.4	43.43	7342
Unretrofitted glulam	41.9	43.30	9676

[a]Yield stress [b]Yield strain [c]Modulus of elasticity

Figure 5.2 and Figure 5.3 present the static stress–strain curves for the unretrofitted CLT panels and glulam beams, respectively.

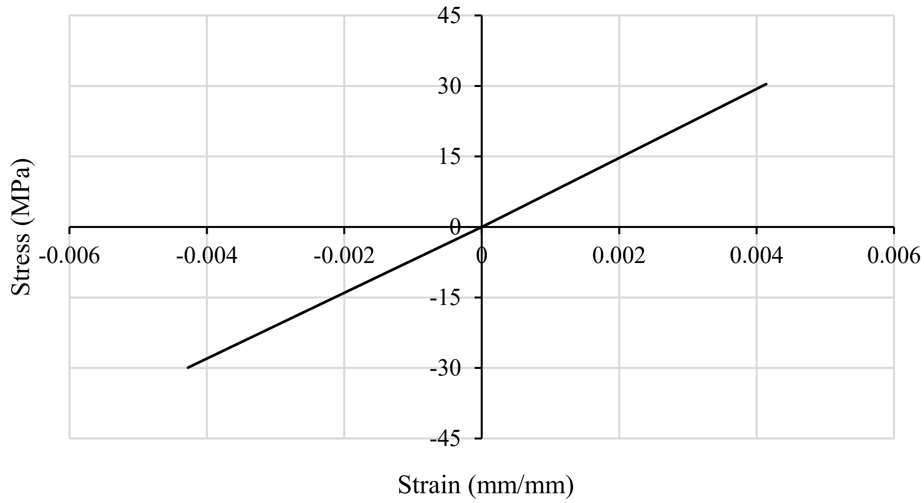

Figure 5.2 Static stress-strain curve for unretrofitted CLT (static)

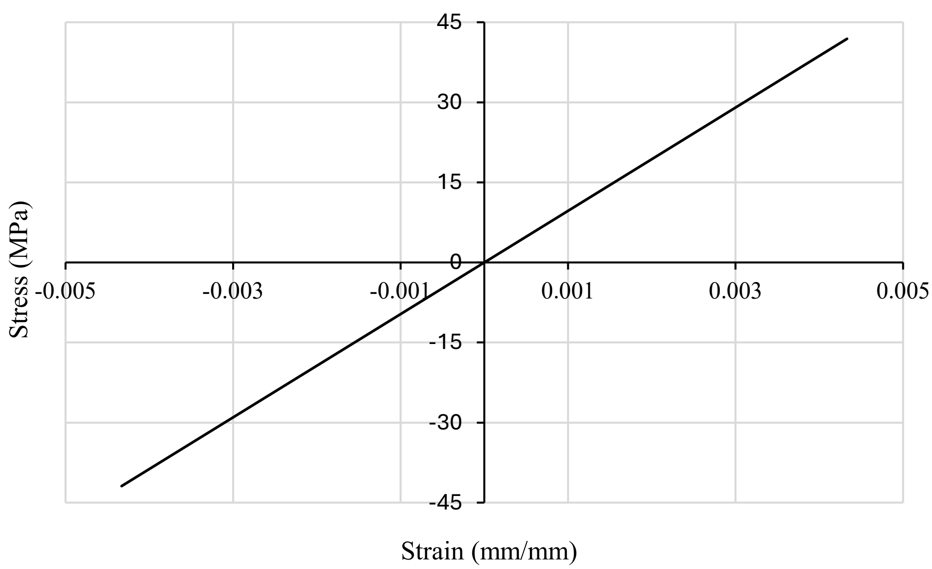

Figure 5.3 Static stress-strain curve for unretrofitted glulam (static)

The tensile stress that develops in the outermost wood fibers under bending are significantly higher than those observed under direct tension. This behaviour is commonly referred to as the stress distribution effect, as described by Buchanan (1990). The extreme wood tension fibre stress, $f_{m,r}$, at which failure of the wood is reached, can be obtained using Equation 5.1, adapted from Buchanan (1990).

$$f_{mr} = \alpha_m \left(\frac{h-c}{h(1+k_3)}\right)^{-1/k_3} f_t \qquad \text{Equation 5.1}$$

The parameter α_m represents the modification factor proposed by Gentile et al. (2002). In this expression, c denotes the depth of the neutral axis measured from the compression face, k_3 reflects the variability of strength properties through the member depth, h is the cross-sectional height, and f_t is the tensile strength of the material.

In Table 5.2, the average static and dynamic wood tensile failure strains for each retrofit are compared with those of the unretrofitted CLT panel. An average value of α_m = 1.59 was adopted for CLT to represent the enhancement in bending capacity provided by the CFRP reinforcement (Lacroix and Doudak 2020).

Table 5.2 Wood tensile failure strain for CLT panel

Wood tensile failure strain $\varepsilon_{f\text{-}T}$ x 10^{-4}				
Configuration	Static	Dynamic	Average	Retrofit/unretrofit
Unretrofitted	30.63	76.1	53.37	-
CLT-T(0)C(0)	38.23	91.85	65.04	1.22
CLT-T(0)C(±45)	56.84	126.23	91.54	1.72
CLT-T$(0)_2$C(±45)	-	97.79	97.79	1.83

In Table 5.3, the average static and dynamic wood tensile failure strains for each retrofit are compared with those of the unretrofitted glulam beam. In this study, an average value of α_m = 1.42 was considered for the glulam beam. Since the experimental resistance-displacement curves were very close to the model, α_m was not considered in moment-curvature diagrams.

Table 5.3 Wood tensile failure strain of glulam beam

Wood tensile failure strain $\varepsilon_{f\text{-}T}$ x 10^{-4}				
Configuration	Static	Dynamic	Average	Retrofit/unretrofit
Unretrofitted	65.13	36	50.57	-
G-T(0)C(0)	-	44.07	44.07	0.87
G-T(0)C(±45)	56.84	87.8	72.32	1.43
G-T$(0)_2$C(±45)	-	99.67	99.67	1.97

Table 5.4 shows the tensile strength, rupture strain, and tensile modulus of elasticity of the CFRP fabrics that were used in this study based on the manufacturer's data sheet.

Table 5.4 Material properties of unidirectional and bidirectional (±45) CFRP fabric

CFRP Fabric	**σy[a] (MPa)**	**ε_y x10^{-4} (mm/mm)**	**E[b] (MPa)**
Unidirectional Fabric	834.3	101.7	82000
Bidirectional Fabric (±45)	558.5	137.29	40680

[a]Tensile strength [b]Rupture strain [c]Tensile Modulus

The stress-strain curves for the unidirectional and bidirectional fabric (±45°) are illustrated in Figure 5.4 based on the manufacturer's data sheet.

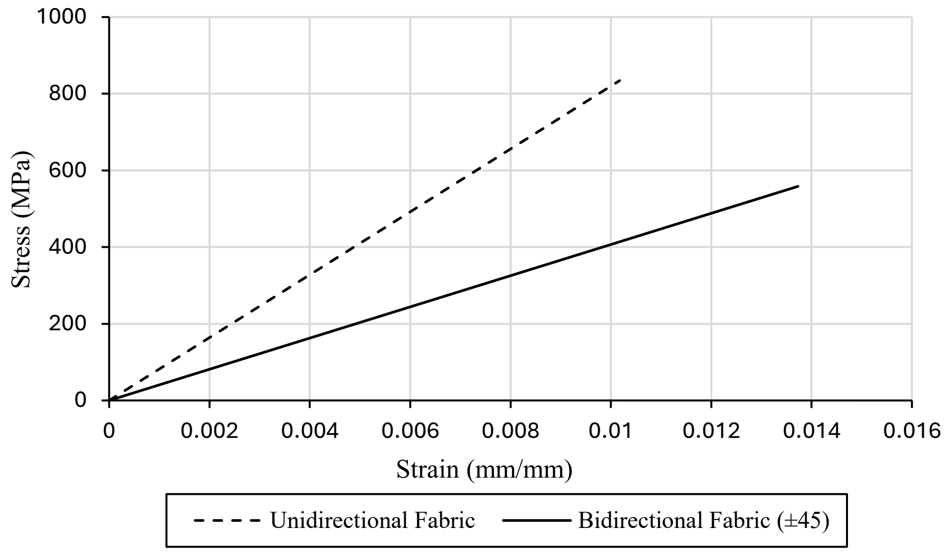

Figure 5.4 Stress-strain curves for unidirectional fabric and bidirectional one (±45)

The fiber section analysis method provides a generalized framework for evaluating the flexural response of multi-layer timber members composed of laminations with different thicknesses and material properties, making it suitable for engineered wood products such as CLT panels, glulam beams, and other layered timber systems. The flexural behaviour of CFRP-retrofitted members is characterized using the moment–curvature relationship, which is derived from the stress–strain response of the wood laminates and the externally bonded reinforcement. In fiber section analysis, the cross-section is discretized into a series of small fibers, each representing a portion of the section and assumed to respond independently to the applied stress. In the analytical model, for the elastic behaviour, the strain distribution along the depth of the section is assumed to be linear according to Euler–Bernoulli beam theory, which states that plane sections remain plane after bending. The strain at a given depth z is calculated using Equation 5.2, where $c$is the neutral axis depth measured from the top of the section and ε_{cy} is the compressive yield strain. The initial neutral axis depth c is assumed to be located at the mid-depth of the section.

$$\varepsilon_i\ (z) = \left(\frac{\varepsilon_{cy}}{c}\right)(c - z) \qquad \text{Equation 5.2}$$

The stress in each fiber, $\sigma_i(z)$, is determined by multiplying the corresponding strain by the modulus of elasticity of that fiber, as expressed in Equation 5.3.

$$\sigma_i\ (z) = \varepsilon_i\ (z)\ E_i \qquad \text{Equation 5.3}$$

Figure 5.5 illustrates the resulting strain, stress, and internal force distributions along the cross-section of the CFRP-retrofitted CLT panel obtained from the fiber section analysis.

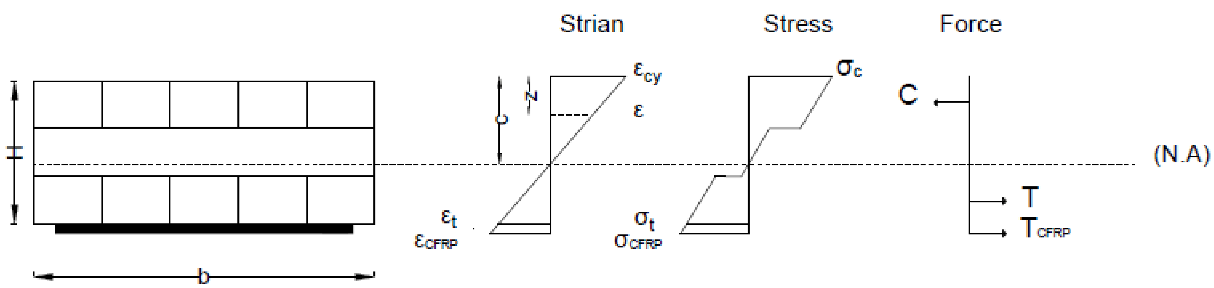

Figure 5.5 Strain, stress, and force diagrams for the cross section of the CFRP retrofitted CLT panel (one layer of unidirectional CFRP fabric)

The internal force in each fiber strip is calculated using the average stress over the strip thickness (t_f). The average stress is obtained by taking the mean of the stresses at the top and bottom of the strip and multiplying it by the strip area to determine the force carried by the fiber, obtained using Equation 5.4.

$$F_i = \frac{1}{2}\left(\sigma_i(z) + \sigma_i(z + t_f)\right)(t_f b) \qquad \text{Equation 5.4}$$

The stress in the CFRP fabric is determined using the material model shown in Figure 5.5. The corresponding force in the CFRP reinforcement is calculated by multiplying this stress by the cross-sectional area of the fabric. For equilibrium of the section (Equation 5.5), the sum of the internal forces from all wood fibers in both tension and compression, together with the tensile force carried by the reinforcement, must be equal to zero (Equation 5.6). An Excel Solver function VBA was utilized to perform the iterations and achieve equilibrium.

$$\sum \mathrm{F} = \sum \mathrm{F_i} + \mathrm{F_{CFRP}} \qquad \text{Equation 5.5}$$

$$\mathrm{F_{CFRP}} = \sigma_{\mathrm{CFRP}}(\mathrm{t_{CFRP}}\, \mathrm{b_{CFRP}}) \qquad \text{Equation 5.6}$$

The bending moment (Equation 5.7) consists of the contribution from the wood cross-section, M_i(Equation 5.8), and the moment generated by the CFRP reinforcement, M_{CFRP}(Equation 5.9). Each component is calculated as the sum of the internal tensile and compressive forces multiplied by their respective lever arms.

$$\sum \mathrm{M} = \sum \mathrm{M_i} + \mathrm{M_{CFRP}} \qquad \text{Equation 5.7}$$

$$\sum \mathrm{M_i} = \mathrm{F_i x_i} \qquad \text{Equation 5.8}$$

$$\mathrm{M_{CFRP}} = \mathrm{F_{CFRP} x_{CFRP}} \qquad \text{Equation 5.9}$$

Moment equilibrium is evaluated about the neutral axis (N.A.). The lever arm x_i associated with each force F_i, as well as the lever arm $x_{CFRP}$for the reinforcement, is defined as the perpendicular distance from the neutral axis to the centroid of the corresponding fiber or reinforcement layer (Figure 5.6).

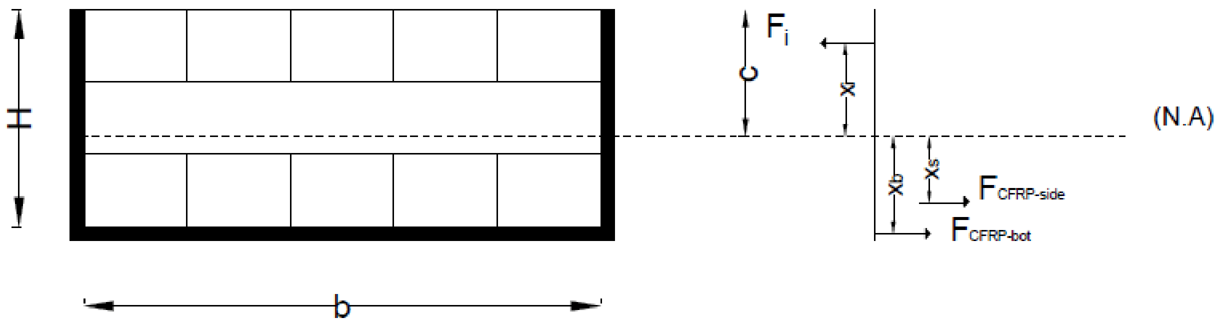

Figure 5.6 Lever arm x_i, x_s, x_b

The equation used to calculate the lever arms of fibers in both tension and compression is presented in Equation 5.10.

$$x_i = C - \left(z + \frac{t_f}{2}\right) \qquad \text{Equation 5.10}$$

The lever arms corresponding to the CFRP on the sides and bottom of the cross-section are given in Equation 5.11 and Equation 5.12, respectively.

$$x_b = (H - C) + \frac{t_{CFRP}}{2} \qquad \text{Equation 5.11}$$

$$x_s = \frac{2}{3}(H - C + t_{CFRP}) \qquad \text{Equation 5.12}$$

The expression provided in Equation 5.13 is developed for a flexural element with simply supported boundary conditions, subjected to four-point bending, where *L* represents the clear span of the panels and beams

$$R = \frac{M\,6}{L} \qquad \text{Equation 5.13}$$

The curvature, ϕ, can be obtained from Equation 5.14. In this equation, E is the modulus of elasticity, I is the moment of inertia of the cross-section, P is the applied load, and a is the distance between each concentrated load and the nearest support.

$$\emptyset = \frac{\mathrm{Pa}}{\mathrm{EI}} = \frac{\varepsilon_c}{C} \qquad \text{Equation 5.14}$$

The maximum mid-span displacement, Δ_{max}, can be obtained from Equation 5.15, which is derived from classical Euler–Bernoulli beam theory. Because the loading is symmetric, the maximum deflection occurs at mid-span. The term $(3L^2 - 4a^2)$reflects the influence of the load position on the deformation response.

$$\Delta_{\mathrm{max}} = \frac{\mathrm{Pa}}{24\mathrm{EI}}(3\mathrm{L}^2 - 4\mathrm{a}^2) \qquad \text{Equation 5.15}$$

The flow chart for the approach employed in the developed program to derive the moment-curvature relationships and resistance curves is illustrated in Figure 5.7.

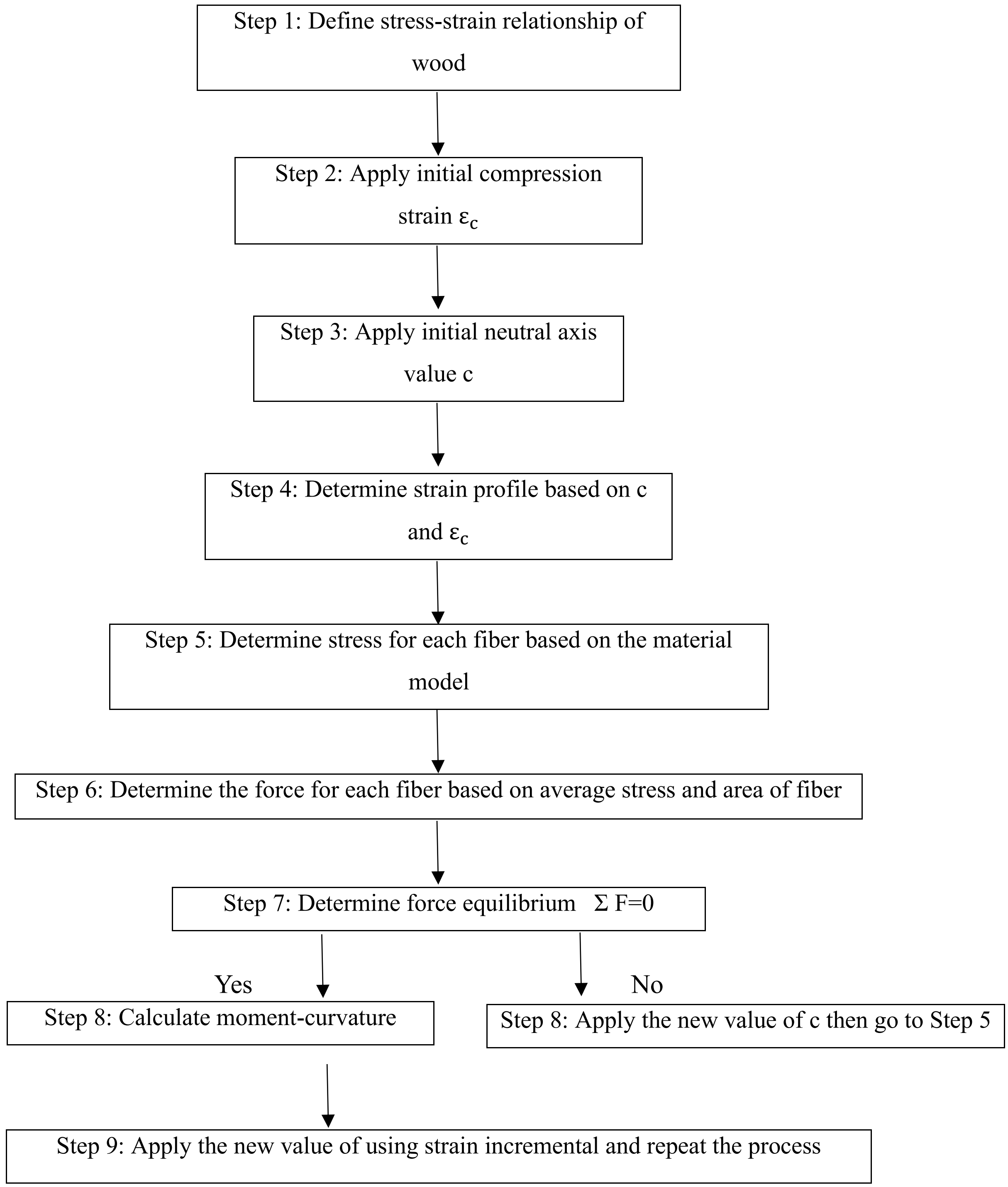

Figure 5.7 Flow chart for section analysis procedure

5.3 Static Analysis results

Configurations used in the analytical static model include configurations CLT-C(±45), CLT-T (0)C(0), CLT-T(0)C(±45), CLT-T(0)$_2$C(±45), CLT-T(0)U(±45), for retrofitted CLT panels and for retrofitted glulam beam configuration G-T(0)C(±45) was analyzed. Since in fiber section analysis it is not possible to consider partial length of panel (shear and moment regions), only configurations with full length confinement and tensile reinforcement with full length were considered in the analysis. Figure 5.8 presents the comparison between the analytical predictions and the experimental responses of the unretrofitted CLT panels and glulam beams under static loading**.** The results show that the analytical model reasonably captures the overall static structural behaviour of the specimens. The predicted resistance shows good agreement with experimental results, with an average analytical-to-experimental ratio of 1.08 and low variability (COV = 0.12). Similarly, the displacement at peak resistance is predicted with excellent precision, yielding an average ratio of approximately 1.05. The stiffness predictions are also in close agreement with the experimental values, with an average ratio of 0.99.

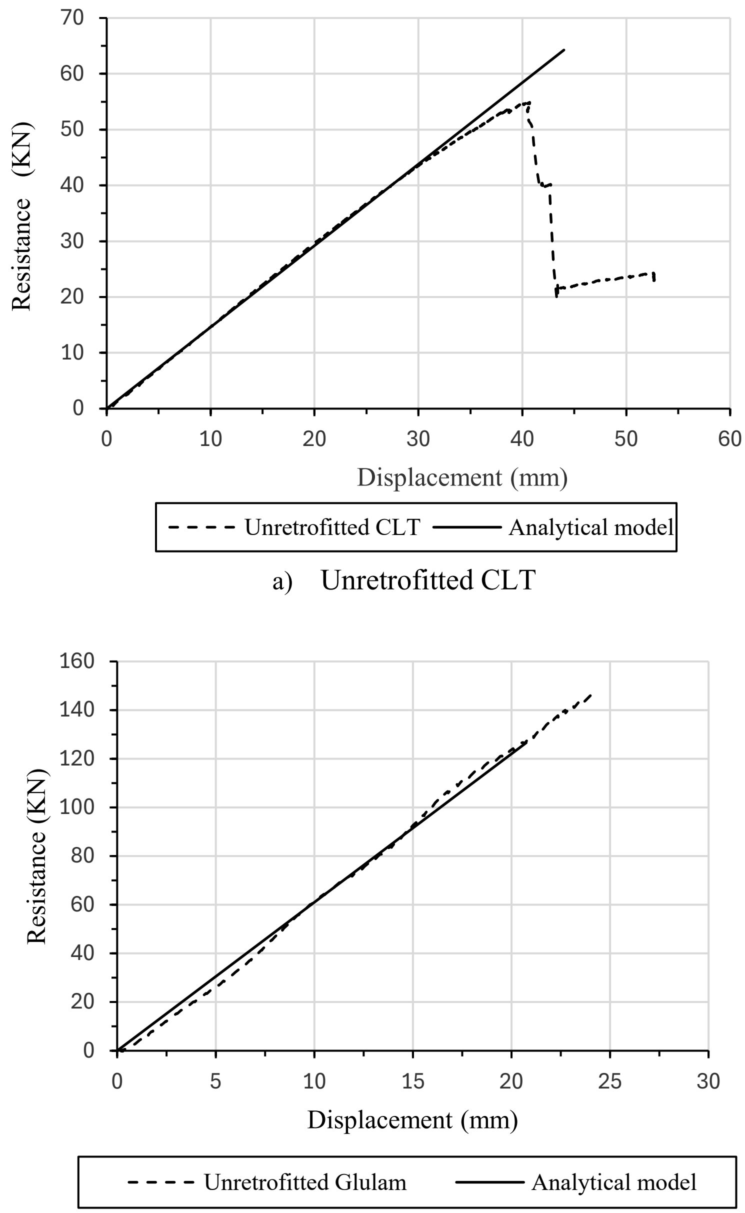

a) Unretrofitted CLT

b) Unretrofitted glulam

Figure 5.8 Comparison of the analytical model and experimental static response of unretrofitted CLT and glulam

Table 5.5 presents a detailed quantitative comparison of the maximum resistance, the corresponding displacement, and the stiffness of the unretrofitted specimens.

Table 5.5 Experimental and analytical static results for unretrofitted CLT panel and glulam beam

	Experimental			Analytical Model			Model to experimental ratio		
	$\mathbf{R^{a}_{max}}$	$\mathbf{\Delta^{b}_{Rmax}}$	$\mathbf{K^{c}}$	$\mathbf{R^{d}_{max}}$	$\mathbf{\Delta^{e}_{Rmax}}$	$\mathbf{K^{f}}$	**R**	**Δ**	**K**
Specimen	**(KN)**	**(mm)**	**(KN/mm)**	**(KN)**	**(mm)**	**(KN/mm)**			
Unretrofitted CLT	54.9	40.2	1.5	63.7	42.6	1.50	1.16	1.06	1
Unretrofitted glulam	146.6	24.1	6.07	126.6	20.8	6.09	0.86	0.86	0.99
Average							1.01	0.96	0.99
St. Dev							0.21	0.14	0.007
COV							0.21	0.15	0.007

Figure 5.9 (Retrofit 1-3) and Figure 5.10 (Retrofit 7, 8) present the load–displacement curves for CLT configurations with different confinement types, including one configuration with full-length bidirectional confinement only and four configurations with unidirectional CFRP tension reinforcement combined with different confinement schemes.

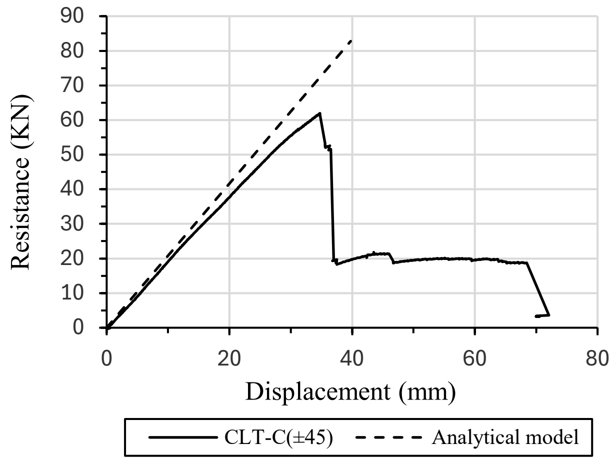

a) Retrofit 1: CLT-C(±45)

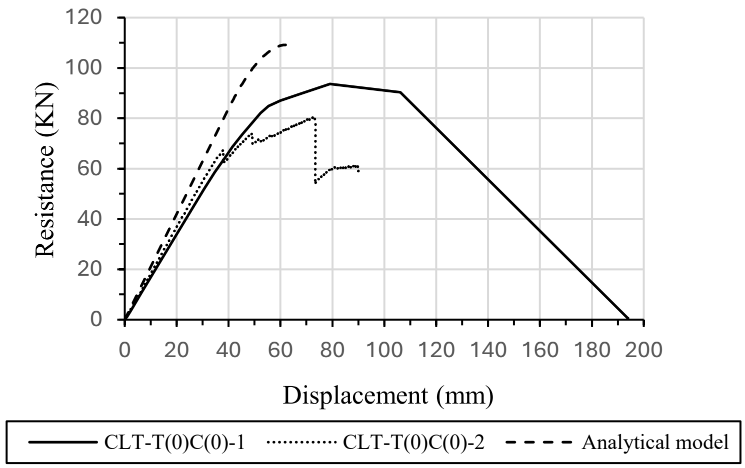

b) Retrofit 2: CLT-T(0)C(0)

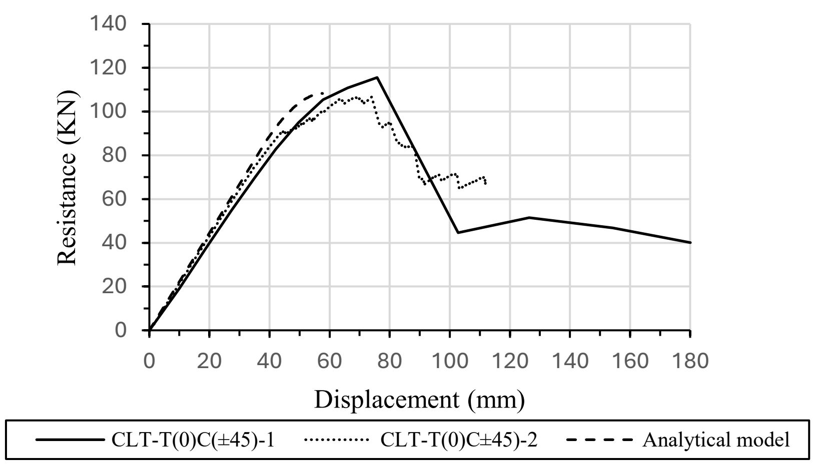

c) Retrofit 3: CLT-T(0)C(±45)

Figure 5.9 Compression of the analytical model and experimental static response of Retrofit 1,2 and 3

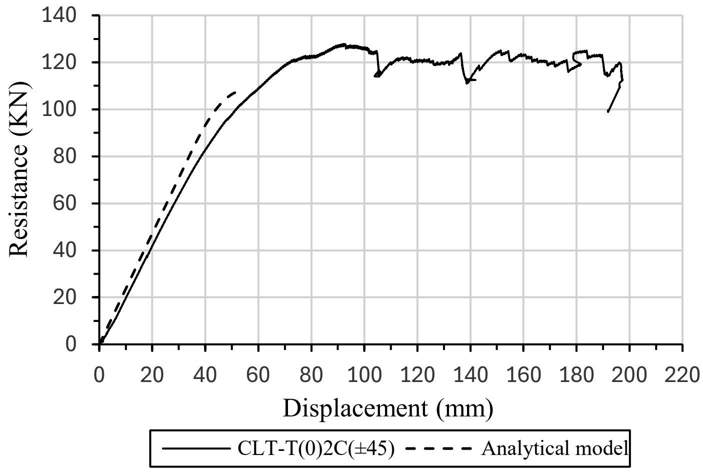

a) Retrofit 7: CLT-T(0)$_2$C(±45)

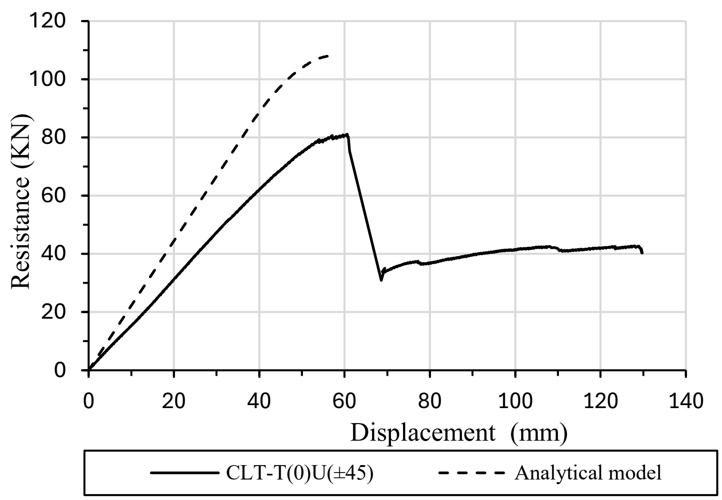

b) Retrofit 8: CLT-T(0)U(±45)

Figure 5.10 Compression of analytical model and experimental static response of Retrofit 7,8

Figure 5.11 shows the load–displacement response of glulam beam strengthened by full-length bidirectional fabric (±45) combined with one layer of unidirectional fabric on the tension side.

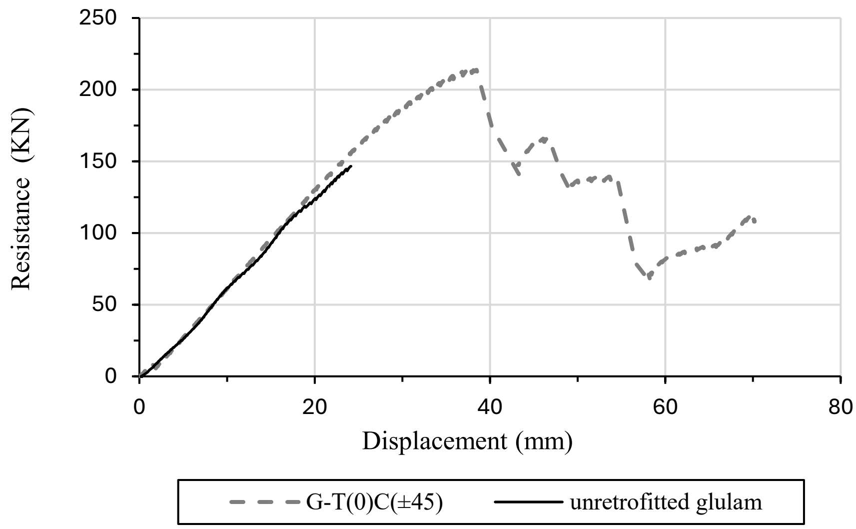

Figure 5.11 Compression of the analytical model and experimental static responses of Retrofit 9, G-T(0)C(±45)

Table 5.6 shows a detailed quantitative comparison of peak resistance, the corresponding displacement, and stiffness for retrofits presented herein.

Table 5.6 Experimental and analytical static results for Retrofit 1-3, 7-9

	Experimental			Analytical Model			Model to experimental ratio		
Configuration	$\mathbf{R^a_{max}}$ **(KN)**	$\mathbf{\Delta^b_{Rmax}}$ **(mm)**	$\mathbf{K^c}$ **(KN/mm)**	$\mathbf{R^d_{max}}$ **(KN)**	$\mathbf{\Delta^e_{Rmax}}$ **(mm)**	$\mathbf{K^f}$ **(KN/mm)**	**R**	**Δ**	**K**
CLT-C(±45)	62	34.7	1.99	83	39.8	2.08	1.34	1.15	1.04
CLT-T (0)C(0)-1	93.7	79.1	1.72	109.2	62	2.09	1.17	0.78	1.22
CLT-T (0)C(0)-2	80.6	73	1.87	109.2	62	2.09	1.36	0.85	1.12
CLT-T (0)C(±45)-1	115.5	75.8	2.06	108.2	57.7	2.22	0.94	0.76	1.08
CLT-T (0)C(±45)-2	106.7	74	2.19	108.2	57.7	2.22	1.01	0.78	1.01
CLT-T $(0)_2$C(±45)	127.8	92.1	2.24	107.9	54.3	2.36	0.84	0.60	1.05
CLT-T (0)U(±45)	81.1	60.6	1.56	108.2	57.7	2.22	1.33	0.95	1.43
G-T (0)C(±45)	214.1	37.8	6.88	208.8	39	6.78	0.98	1.03	0.99

5.4 Dynamic Analysis results

Configurations used in the analytical dynamic model include configurations CLT-T(0)C(±45), CLT-T(0)C(0), CLT-T$(0)_2$C(±45), CLT-T(0)U(±45) for retrofitted CLT panels, and configurations G-T(0)C(±45), G-T(0)C(0), G-T$(0)_2$C(±45), G-T(0)U(±45) for glulam beams. The inputs for the dynamic analytical model were obtained by applying a DIF to the yield stress. The DIF used for CLT and Glulam was 1.28 and 1.1, respectively. Figure 5.12 presents the static and dynamic stress–strain curves for unretrofitted CLT panels and Figure 5.13 shows the dynamic stress-strain curve for the glulam beam.

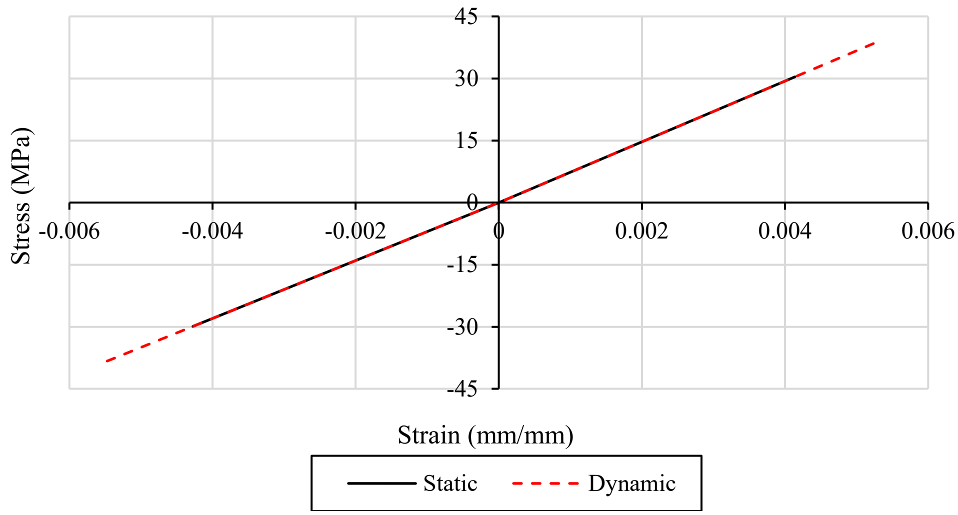

Figure 5.12 Static and Dynamic stress-strain curves for unretrofitted CLT

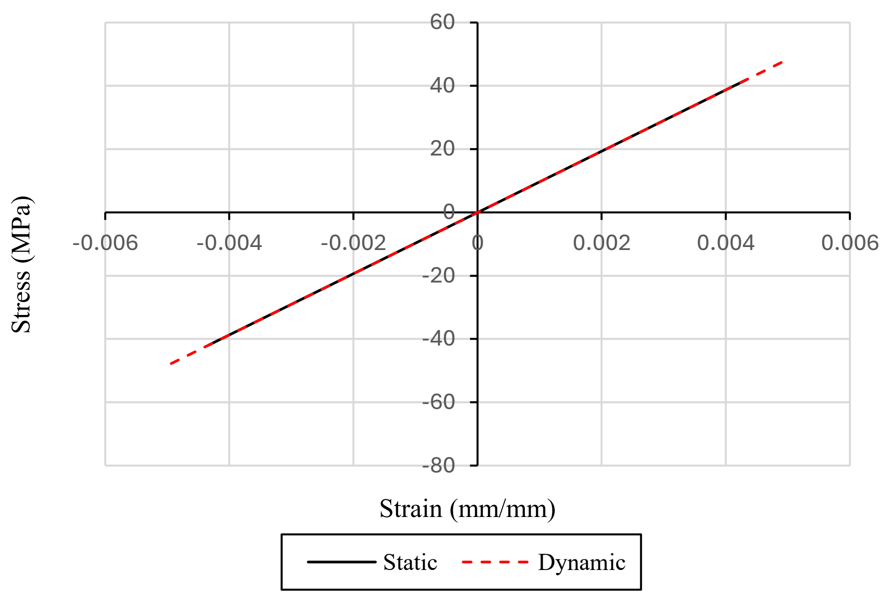

Figure 5.13 Static and Dynamic stress-strain curves for unretrofitted glulam

Figure 5.14 presents the comparison between the analytical predictions and the experimental responses of the unretrofitted CLT panels and glulam beams under dynamic loading**.**

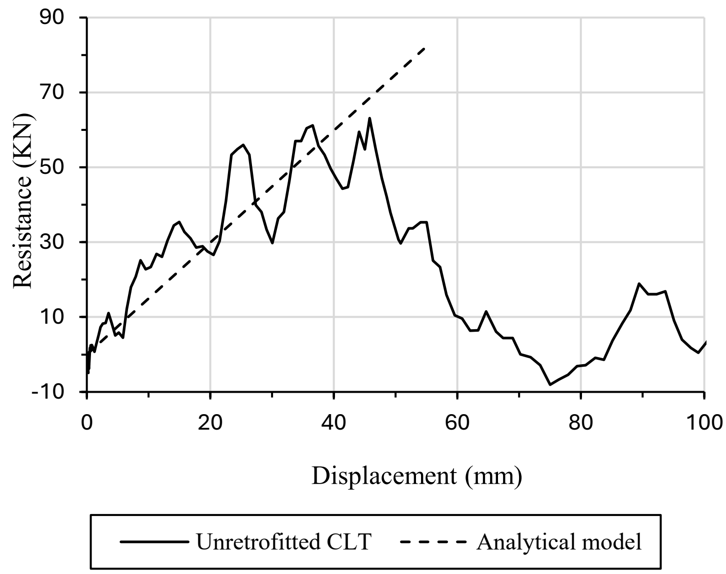

a) Unretrofitted CLT

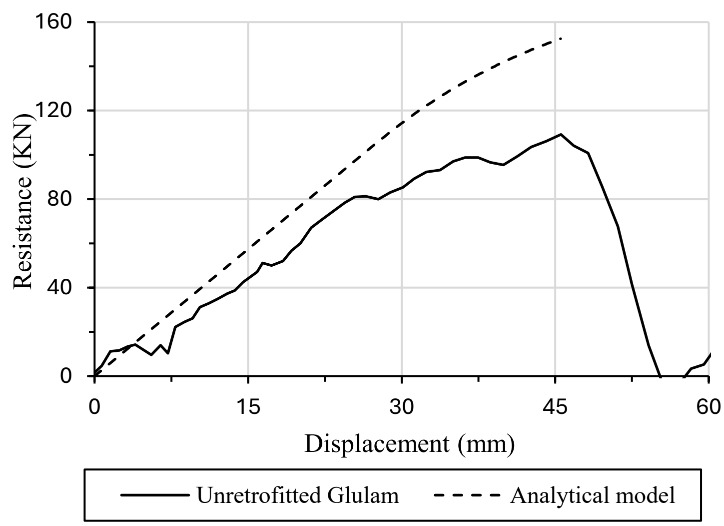

b) Unretrofitted glulam

Figure 5.14 Comparison of analytical model and experimental dynamic responses of unretrofitted CLT and glulam

Table 5.7 presents a detailed quantitative comparison of the maximum resistance, the corresponding displacement, and the stiffness of the unretrofitted specimens. The predicted resistance represents an average analytical-to-experimental ratio of 1.35 (COV=0.05), and the displacement corresponding to the peak resistance and stiffness predictions shows an average ratio of approximately 1.11 and 1.08, respectively.

Table 5.7 Experimental and analytical dynamic results for unretrofitted CLT panel and glulam beam

	Experimental			Analytical Model			Model to experimental ratio		
Specimen	$\mathbf{R^a_{max}}$ **(KN)**	$\mathbf{\Delta^b_{Rmax}}$ **(mm)**	$\mathbf{K^c}$ **(KN/mm)**	$\mathbf{R^d_{max}}$ **(KN)**	$\mathbf{\Delta^e_{Rmax}}$ **(mm)**	$\mathbf{K^f}$ **(KN/mm)**	**R**	**Δ**	**K**
Unretrofitted CLT	63.1	45.8	1.98	81.6	54.6	1.50	1.29	1.19	0.76
Unretrofitted glulam	109.2	45.6	2.7	105.7	27.6	3.82	0.97	0.61	1.41
Average							1.13	0.9	1.07
St. Dev							0.23	0.41	0.48
COV							0.21	0.46	0.45

Figure 5.15 and Figure 5.16 present the load–displacement curves for Retrofit 2, 3, 7, and 8.

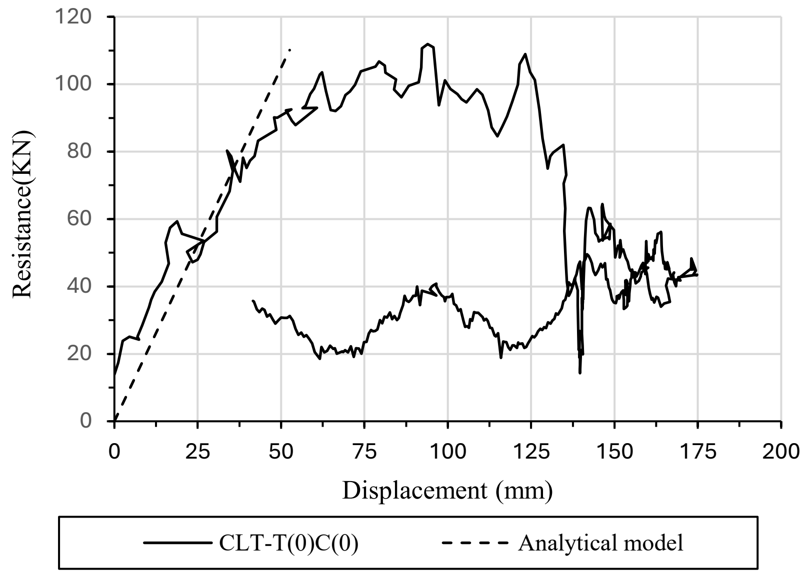

Retrofit 2: CLT-T(0)C(0)

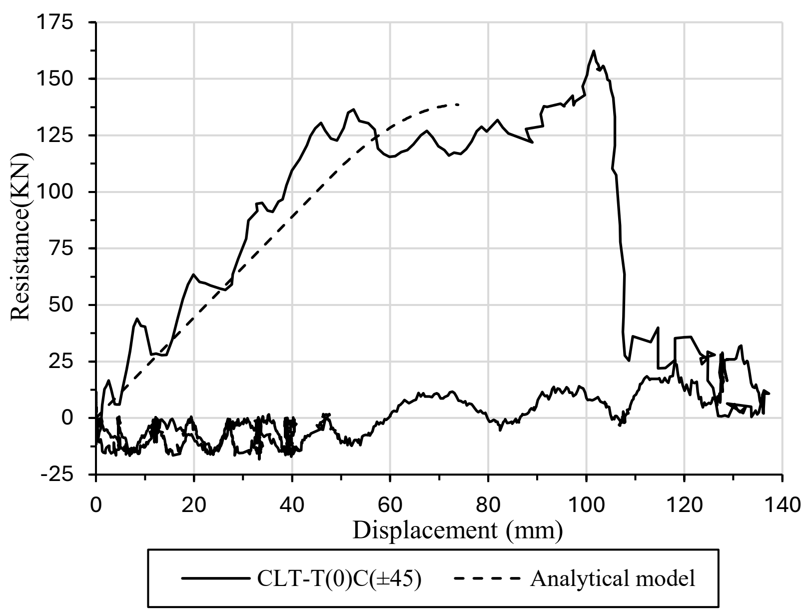

Retrofit 3: CLT-T(0)C(±45)

Figure 5.15 Comparison of analytical model and experimental dynamic responses of Retrofit 2,3

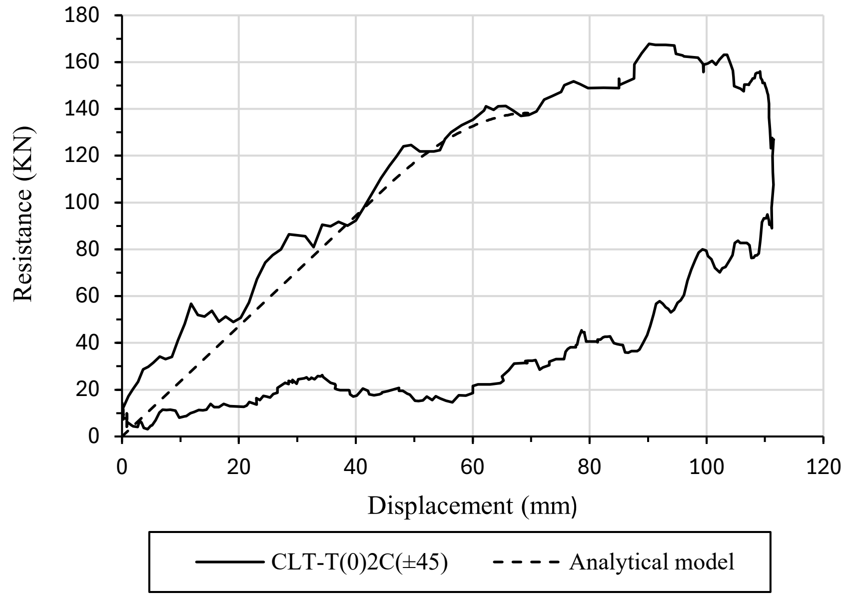

Retrofit 7: CLT-T$(0)_2$C(±45)

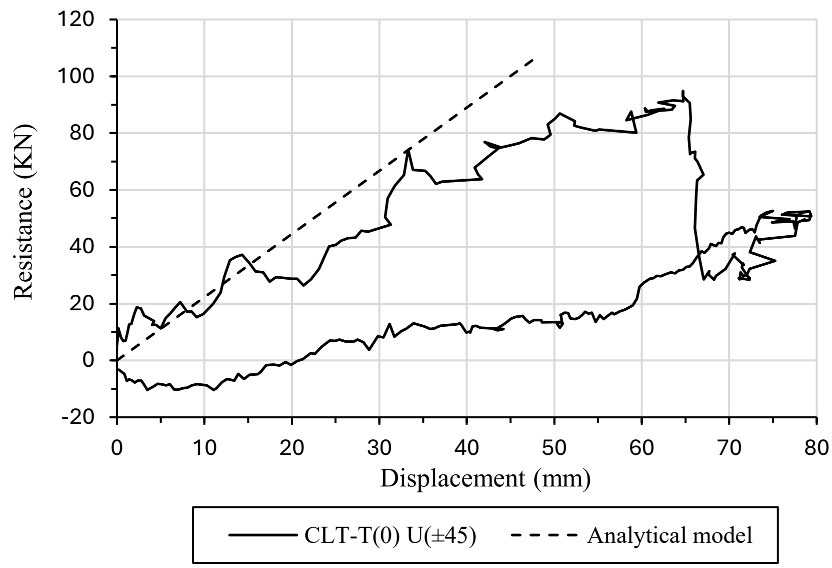

Retrofit 8: CLT-T(0)U(±45)

Figure 5.16 Comparison of the analytical model and experimental dynamic responses of Retrofit 7,8

Table 5.8 shows a detailed quantitative comparison of peak resistance, the corresponding displacement, and stiffness for Retrofits 2,3,7,8.

Table 5.8 Experimental and analytical dynamic results for Retrofit 2,3,7,8

	Experimental			Analytical Model			Model to experimental ratio		
Configuration	$\mathbf{R^{a}_{max}}$ **(KN)**	$\mathbf{\Delta^{b}_{Rmax}}$ **(mm)**	$\mathbf{K^{c}}$ **(KN/mm)**	$\mathbf{R^{d}_{max}}$ **(KN)**	$\mathbf{\Delta^{e}_{Rmax}}$ **(mm)**	$\mathbf{K^{f}}$ **(KN/mm)**	**R**	**Δ**	**K**
CLT-T (0)C(0)	111.9	93.9	2.06	106.3	50.7	2.1	0.95	0.54	1.02
CLT-T(0)C(±45)	162.4	101.5	3	138.5	73.8	2.22	0.85	0.73	0.74
CLT-T(0)$_2$C(±45)	167.8	90.2	2.05	138.2	69.5	2.36	0.82	0.77	1.15
CLT-T(0)U(±45)	94.9	64.6	1.56	106.6	47.9	2.22	1.12	0.74	1.43

Figure 5.17 and Figure 5.18 present the load–displacement curves for Retrofit 9, 11, 12, and 13.

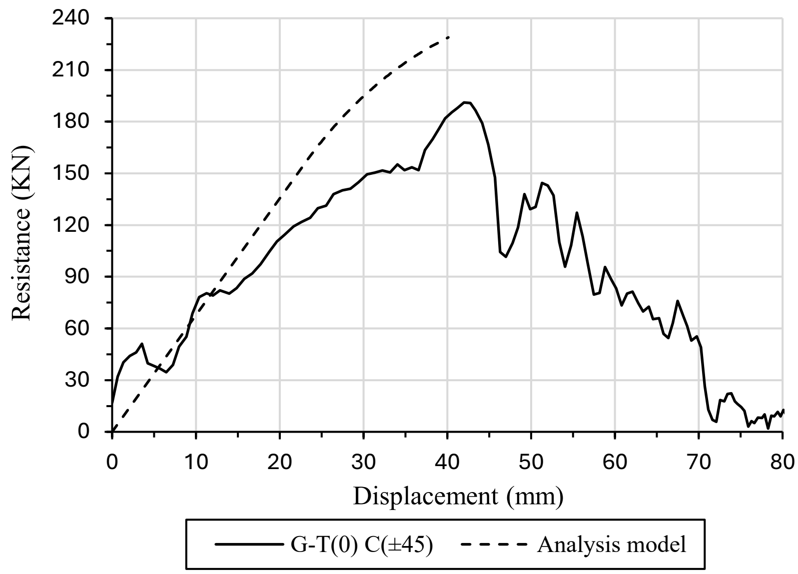

Retrofit 9: G-T(0)C(±45)

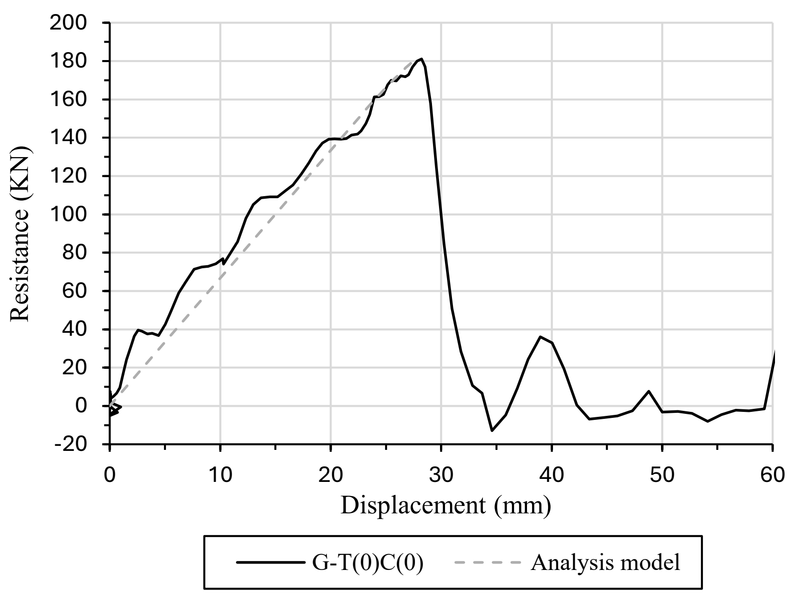

Retrofit 11: G-T(0)C(0)

Figure 5.17 Comparison of analytical model and experimental dynamic responses of Retrofit 9,11

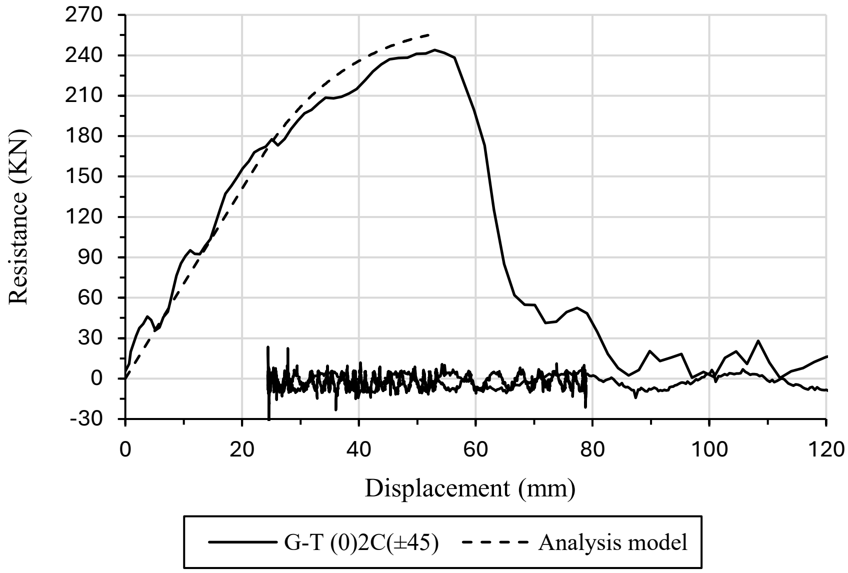

Retrofit 12: G-T_2(0)C(±45)

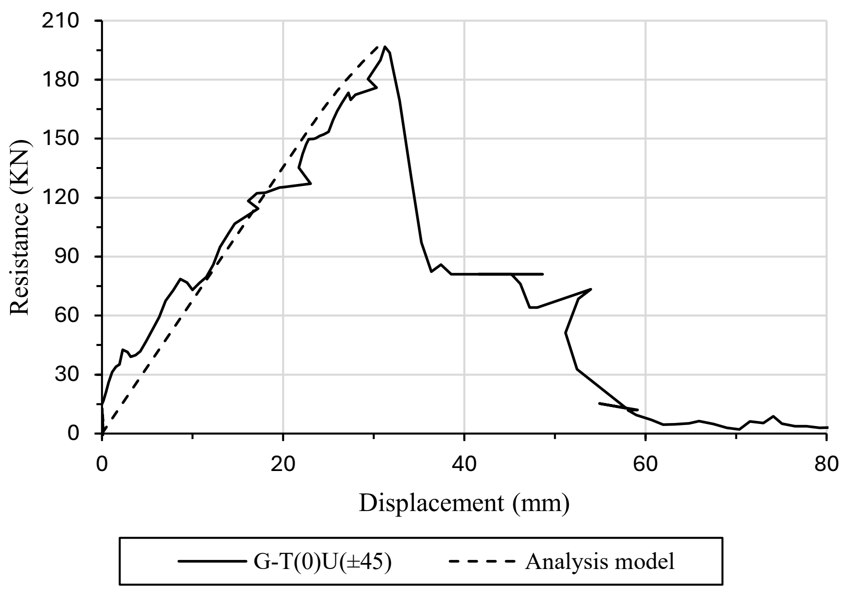

Retrofit 13: G-T(0)U(±45)

Figure 5.18 Comparison of analytical model and experimental dynamic responses of Retrofit 12,13

Table 5.9 shows a detailed quantitative comparison of peak resistance, the corresponding displacement, and stiffness for Retrofits 9,11, 12, and 13.

Table 5.9 Experimental and analytical dynamic results for Retrofits 9, 11, 12, and 13

	Experimental			Analytical Model			Model to experimental ratio		
Configuration	$\mathbf{R^{a}_{max}}$ **(KN)**	$\mathbf{\Delta^{b}_{Rmax}}$ **(mm)**	$\mathbf{K^{c}}$ **(KN/mm)**	$\mathbf{R^{d}_{max}}$ **(KN)**	$\mathbf{\Delta^{e}_{Rmax}}$ **(mm)**	$\mathbf{K^{f}}$ **(KN/mm)**	**R**	**Δ**	**K**
G-T(0)C(±45)	191.1	45.7	4.74	186.6	28.3	6.78	0.98	0.62	1.43
G-T(0)C(0)	181.1	28.2	6.78	180.6	27.6	6.67	1	0.98	0.98
G-T_2(0)C(±45)	243.9	53	6.06	254.9	51.8	7.05	1.05	0.98	1.16
G-T(0)U(±45)	196.7	31.3	3.15	199.8	31.2	6.78	1.02	1	2.15

5.5 Single degree of freedom model

The SDOF analysis was conducted using RCBlast® (Jacques 2014) , a blast-analysis program that performs equivalent lumped-mass calculations through numerical integration of the equation of motion. The software employs the average acceleration method, which ensures numerical stability independent of the selected time step. Single-degree-of-freedom (SDOF) modelling assumes that the structural system can be represented by a single generalized coordinate describing the motion of the entire structure. In this study, the mid-span deflection was selected as that coordinate. The deflected shape was assumed to correspond to that of a simply supported beam subjected to four-point bending. Instead of using a conventional stiffness–displacement relationship, the restoring force was expressed as a nonlinear resistance function, $R(y)$. Under these assumptions, the equation of motion for an undamped SDOF system can be written as:

$$K_{LM} m\ddot{y}(t) + R(y) = AP_R\left(1 - \frac{t}{t_d}\right) \qquad \text{Equation 5.16}$$

Equation 5.16 requires two different load–mass transformation factors to represent the change in the assumed deformation shape as the system response shifts from the elastic range to the plastic range (Biggs 1964; UFC 2008). In this study, load–mass factors of 0.87 and 1.0 were adopted for the elastic and plastic regions, respectively. The mass of the LTD was treated as a concentrated mass, with one-half assumed to act at each load application point. Several approaches have been proposed to determine the effective location of the equivalent mass in systems containing both distributed and concentrated masses. However, because the LTD contributed a substantially larger portion of the total mass, particularly in comparison with the CLT panels and glulam beams, the system was reasonably approximated as having two concentrated load for the purpose of applying these transformation factors. The mass of each specimen was measured before testing and adjusted according to the clear span used in the analysis. Mass located outside the clear span was assumed to have a negligible influence on the system response. The total system mass was determined to be 344 kg for the unretrofitted CLT panel and 319 kg for the unretrofitted glulam. Figure 5.19 shows the RCblast program's output for specimen G-T(0)C(±45) including the applied pressure–time history, theoretical resistance–displacement curves, and the predicted displacement–time response of the reinforced beam.

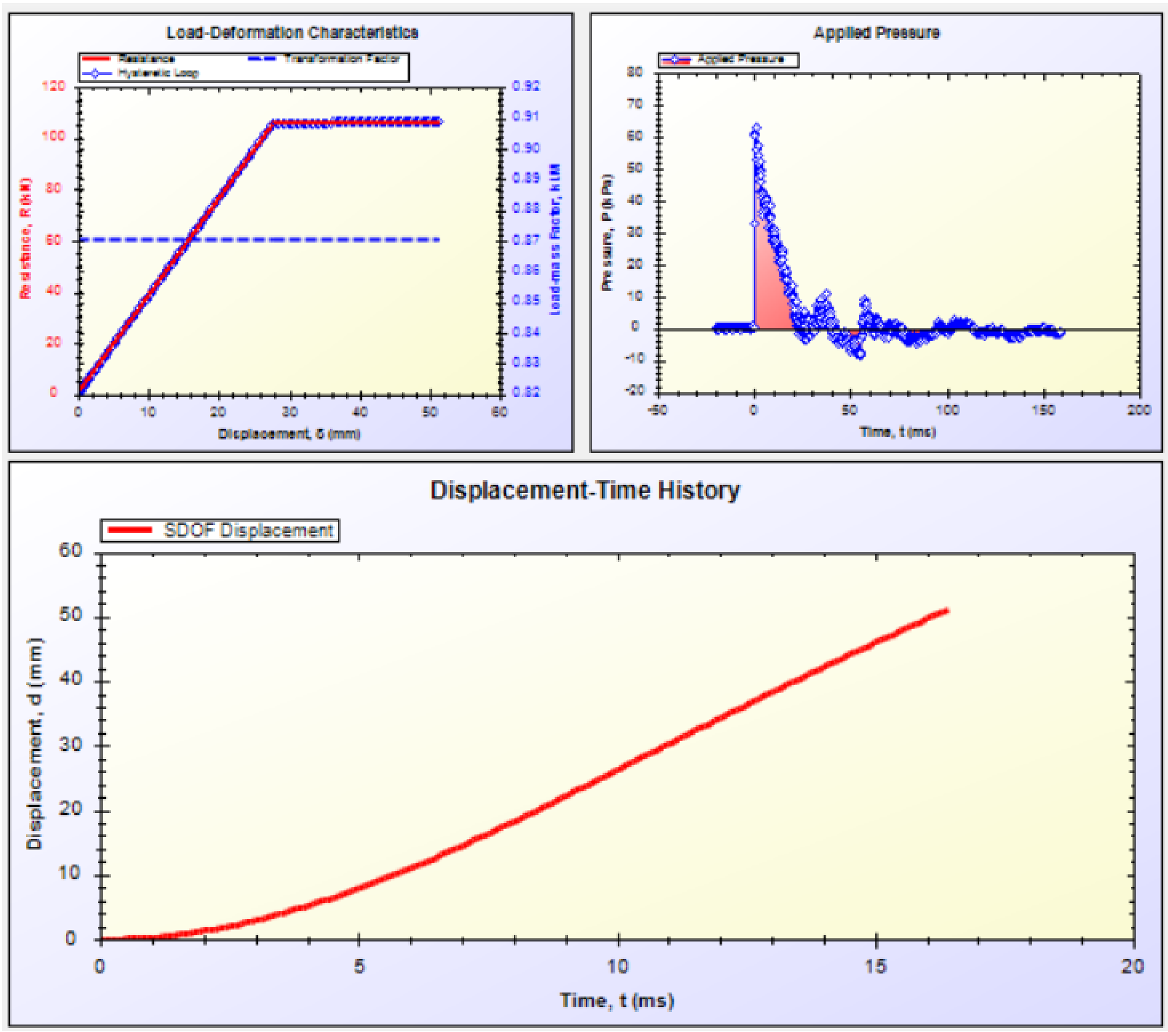

Figure 5.19 RCBlast analysis of G-T(0)C(±45

The comparisons between the SDOF analysis (displacement) of unretrofitted and retrofitted CLT specimens (Retrofit 2 and 3) and experimental results are shown in Figure 5.20.

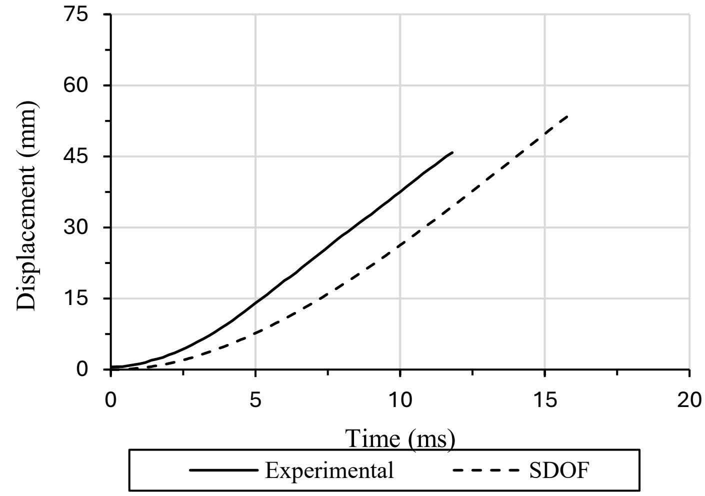

a) Unretrofitted CLT

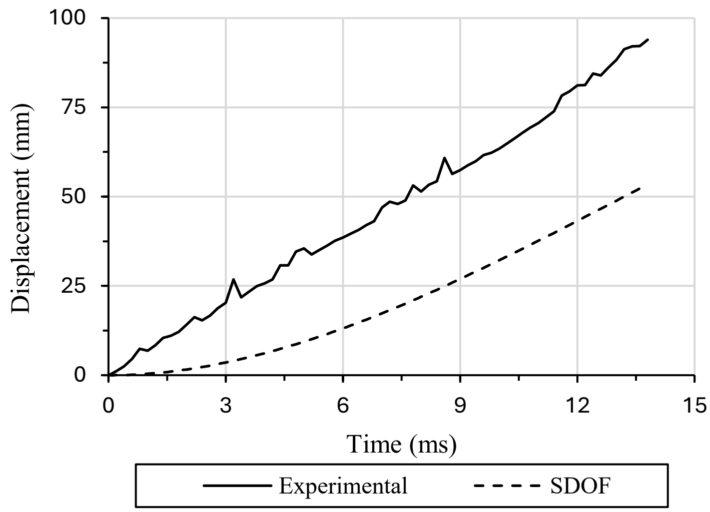

b) CLT-T(0)C(0) (Retrofit 2)

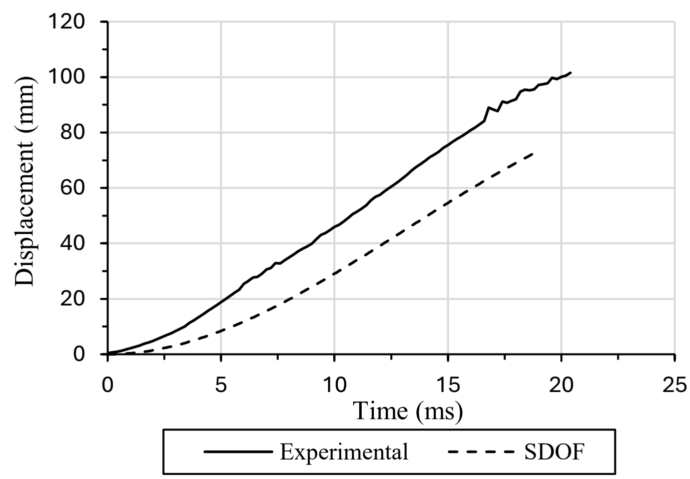

c) CLT-T(0)C(±45) (Retrofit 3)

Figure 5.20 Comparisons between the SDF analysis (displacement) and Experimental (unretrofitted CLT, CLT-T(0)C(0)-, and CLT-T(0)C(±45))

Figure 5.21 compares experimental findings with the SDOF analysis (displacement) of Retrofit 7 and 8.

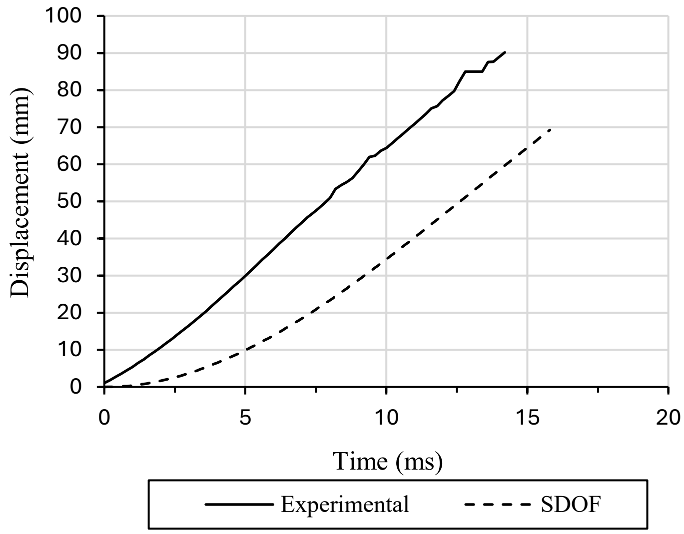

a) CLT-T(0)$_2$C(±45) (Retrofit 7)

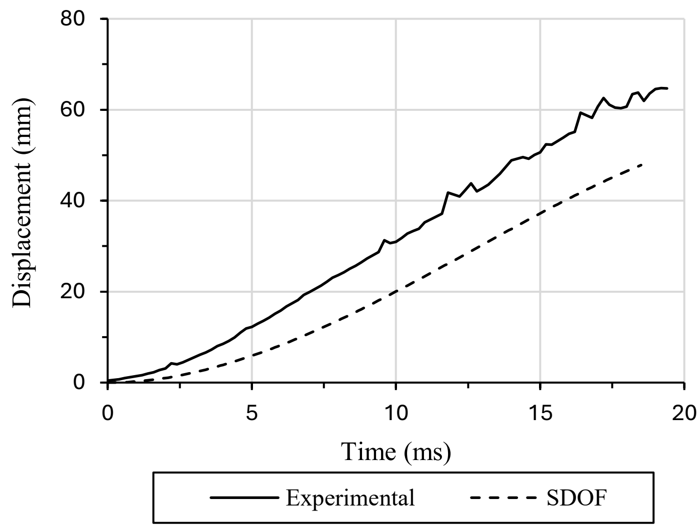

b) CLT-T(0)U(±45) (Retrofit 8)

Figure 5.21 Comparison between SDOF analysis (displacement) and Experimental (CLT-T(0)$_2$C(±45) and CLT-T(0)U(±45))

Figure 5.22 compares experimental findings with SDOF analysis (displacement) of unretrofitted Glulam, Retrofit 9, and 11.

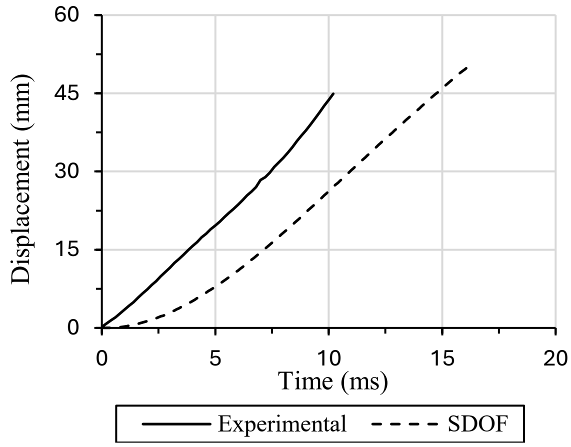

a) Unretrofitted Glulam

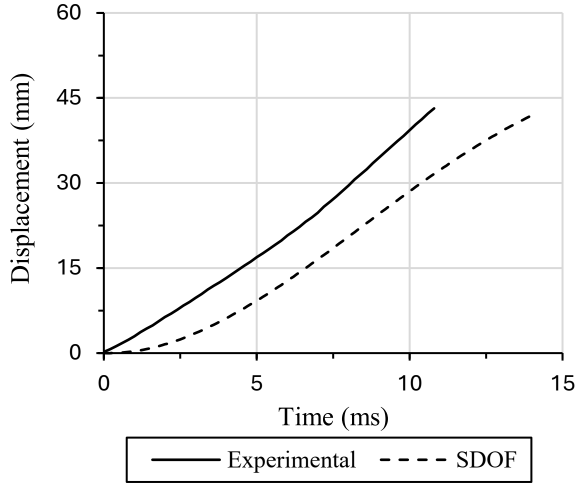

b) G-T(0)C(±45) (Retrofit 9)

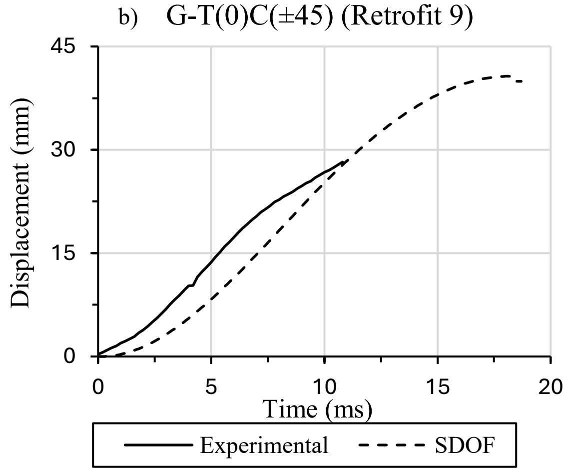

c) G-T(0)C(0) (Retrofit 11)

Figure 5.22 Comparison between SDOF analysis (displacement) and Experimental (unretrofitted Glulam, G-T(0)C(±45) and G-T(0)C(0))

Figure 5.23 shows the comparison between experimental findings and SDOF analysis (displacement) of Retrofit 12 and 13.

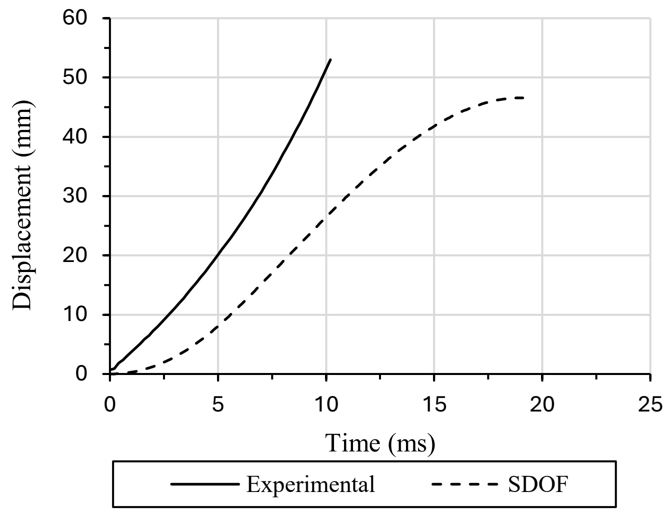

a) G-T(0)$_2$C(±45) (Retrofit 12)

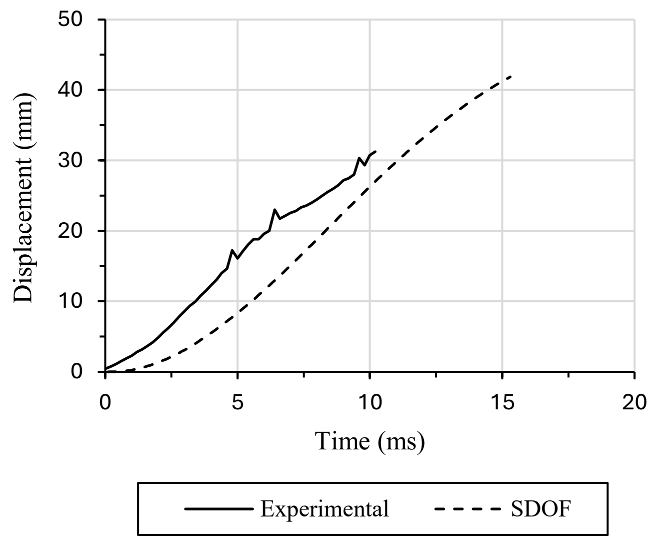

b) G-T(0)U(±45) (Retrofit 13)

Figure 5.23 Comparison between SDOF analysis (displacement) and Experimental (unretrofitted Glulam, G-T(0)$_2$C(±45) and G-T(0)U(±45))

Table 5.10 shows the displacement at maximum resistance and the corresponding time to maximum resistance for all SDOF models.

Table 5.10 Summary of SDOF analysis results

Model ID	Displacement at maximum resistance (mm)	Time to maximum resistance (ms)
Unretrofitted CLT	54.4	16
CLT-T(0)C(0)	52.3	13..6
CLT-T(0)C(±45)	73.6	19.1
CLT-T(0)$_2$C(±45)	69.3	15.8
CLT-T(0)U(±45)	47.8	18.5
Unretrofitted Glulam	51.1	16.4
G-T(0)C(0)	39.9	18.7
G-T(0)C(±45)	42.2	14.1
G-T(0)$_2$C(±45)	46.6	19.1
G-T(0)U(±45)	42.1	15.3

Chapter 6 Discussion

6.1 General

A total of fourteen retrofit configurations of CLT panels and glulam beams were tested to failure under both static and dynamic loading conditions. The study focused on simply supported elements with constant span and width, maintaining a consistent aspect ratio throughout. The following sections discuss the experimental results as well as the corresponding analytical evaluation.

6.2 Characterization of Static and Dynamic Failure Modes

The unretrofitted CLT panel exhibited a brittle failure response, primarily initiated by rolling shear. The CLT-C(±45) configuration, consisting of full bidirectional CFRP confinement, showed a transition from rolling shear to flexural failure. The resistance did not increase substantially compared to the unretrofitted CLT panel since rolling shear and bending capacities were in proximity for this panel dimension. Two specimens with the same configuration, CLT-T(0)C(0), exhibited different failure modes. Although both specimens showed an increase in strength capacity, longitudinal shear, which is the predominant failure mode in CLT panel, was still observed in one of the specimens. Therefore, the results indicate that unidirectional confinement is not sufficient to shift the failure mode from longitudinal shear to flexural behaviour in the CLT panel and consequently does not significantly improve the post-peak behaviour and ductility of the specimen. Similarly, two specimens with configuration CLT-T(0)SH(±45) demonstrated different failure modes. One specimen showed flexural failure with damage propagating through the section depth, while the other was governed by longitudinal shear due to interlaminar slip. This indicates that although the regions subjected to maximum shear under two concentrated loads were confined, partial confinement is not sufficient to shift longitudinal shear to flexural failure; therefore, due to the brittle failure mode, its effectiveness in improving post-peak behaviour remains limited. Configurations

CLT-T(0)C(±45)-1 and CLT-T(0)C(±45)-2 showed further improvement in the behaviour, with flexural failure accompanied by CFRP tearing. The interaction between longitudinal unidirectional fabric and ±45° fiber enhanced crack control and resistance to multidirectional stresses. Configuration CLT-T-M(0)C(±45) and CLT-T-M-SH(0)C(±45) both exhibited flexural failure near the maximum moment region. This confirms that combining confinement with appropriately placed tension reinforcement effectively shifts the governing behaviour toward flexural response, while extending the reinforcement into both shear and moment regions improves strength capacity. Configuration CLT-T$(0)_2$C(±45) exhibited a flexural failure mode. Compared to configuration CLT-T(0)C(±45), the observed CFRP failure indicates full engagement of both unidirectional fabrics throughout the loading duration, providing improved strengthening efficiency. In contrast, Configuration CLT-T(0)U(±45) remained governed by longitudinal shear. Although the U-shaped CFRP limited flexural cracking, shear slip between laminates controlled the failure. This indicates that partial confinement without full surface coverage is insufficient to prevent longitudinal shear failure.

The unretrofitted glulam beam shows splintering tension failure. Compared to retrofitted CLT panels, the response of the retrofitted glulam beams was more uniform, suggesting that CFRP strengthening is more effective in modifying failure behaviour in homogeneous members. Overall, CFRP strengthening shifted the failure of timber elements toward more controlled flexural responses. However, the level of improvement depends strongly on the configuration, distribution, and orientation of the reinforcement.

Under dynamic loading, the unretrofitted CLT panel exhibited a brittle response, initially governed by rolling shear. Cracking initiated within the transverse laminations and propagated rapidly through the panel depth. Extensive rupture of the wood on the tension side of the panel confirmed that flexural failure controlled the ultimate failure mode. For configurations incorporating unidirectional fabric as tension reinforcement and confinement, such as CLT-T(0)C(0), the failure mode was predominantly flexural and was characterized by minor longitudinal shear cracks at the end of the panel. For confinement with bidirectional fabric, such as CLT-T(0)C(±45), the failure mode shifted away from rolling shear to a more flexural-dominated behaviour, indicating that confinement with bidirectional fabric (±45) effectively restrained deformation between laminates and contributed to maintaining structural continuity. Increasing the reinforcement ratio was investigated in configuration CLT-T$(0)_2$C(±45), and it led to a flexural failure mode similar to configuration with one layer of tension reinforcement, providing more consistent post-peak behaviour. In contrast, configurations with partial confinement, such as CLT-T(0)U(±45), remained governed by longitudinal shear, and damage on the compression side was observed. This indicates that incomplete wrapping is insufficient to control longitudinal shear. For glulam beams, the dynamic response was consistently governed by flexural behaviour. The unretrofitted specimen failed due to splintering tension failure, which was influenced by the existence of knots and other defects. Increasing the reinforcement ratio, as in G-T$(0)_2$C(±45), improved peak resistance significantly. The U-shaped configuration in glulam, G-T(0)U(±45), demonstrated limiting fabric separation.

Overall, CFRP strengthening improved the dynamic performance of both CLT and glulam specimens by increasing resistance and modifying damage development. However, its effectiveness depended strongly on the configuration. Full confinement systems were more effective in preventing rolling and longitudinal shear failures and improving peak resistance and stiffness in CLT, while in glulam members, CFRP primarily enhanced the strength and stiffness of the beams.

6.3 Effect of Unidirectional vs. Bidirectional CFRP Confinement

The main purpose of confinement was to improve the post-peak behaviour by maintaining the structural integrity, reducing fragmentation, and limiting the possibility of splitting. The compression between configurations CLT-T(0)C(±45) and CLT-T(0)C(0) (Figure 6.1) shows that the configuration with full-length bidirectional CFRP confinement led to a significant increase in peak resistance compared to the unidirectional one. In addition, the ductility ratio within the range of 1.5-1.7 was obtained for configuration CLT-T(0)C(±45), while for the configuration CLT-T(0)C(0) it was 1.2. These results present that confinement with full-length bidirectional fabric is more effective in enhancing load-carrying capacity and energy dissipation by providing restraint in multiple directions.

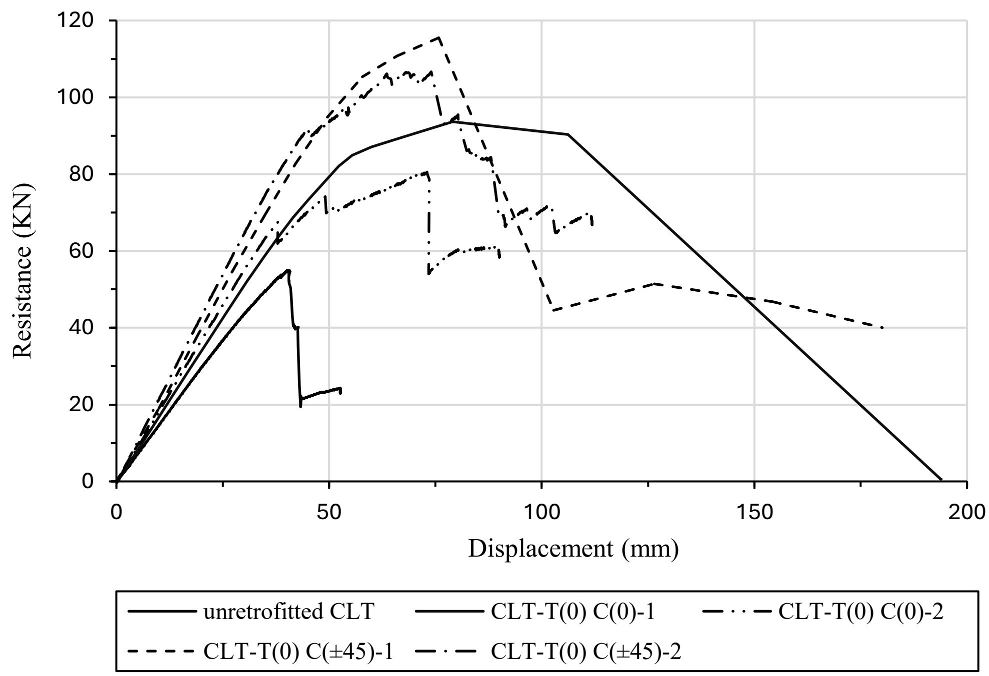

Figure 6.1 Resistance-displacement static curve of unretrofitted CLT, CLT-T(0)C(±45), and CLT-T(0)C(0)

The dynamic results presented in Figure 6.2 show that bidirectional fabric confinement significantly enhances the structural response of CLT panels under high strain rate loading. In particular, bidirectional confinement in CLT-T(0)C(±45) resulted in a substantial increase in peak resistance and stiffness by factors of 2.57 and 1.52, respectively, compared to the unretrofitted CLT panel. While configuration CLT-T(0)C(0) showed ratios of 1.77 and 1.12 for peak resistance and stiffness, respectively. These observations are anticipated and consistent with static findings, indicating that although unidirectional confinement contributes to enhancing structural behaviour, bidirectional fabric is more effective at improving due to its strength in multiple directions.

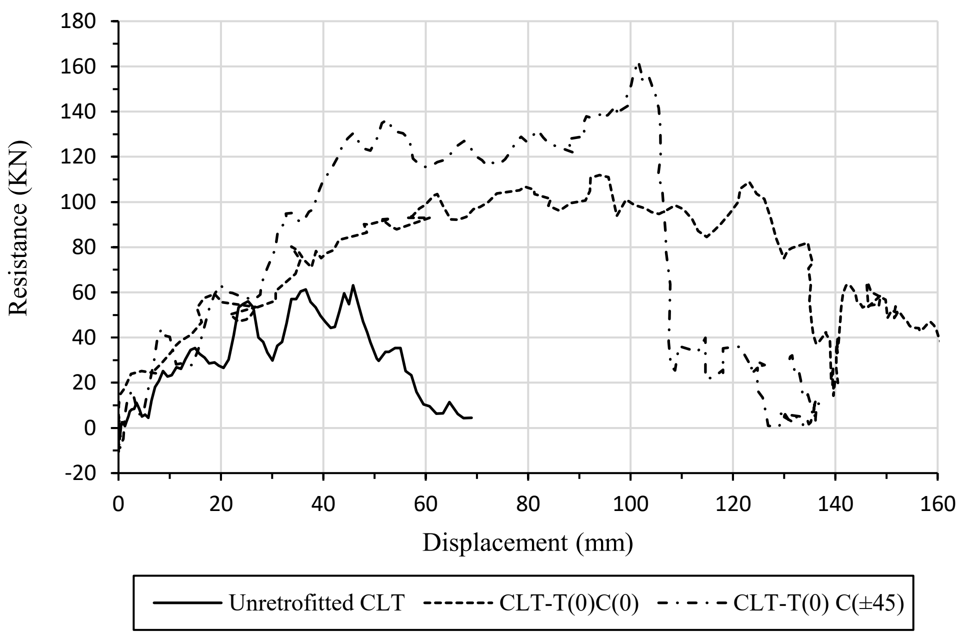

Figure 6.2 Resistance-displacement dynamic curve of unretrofitted CLT, CLT-T(0)C(±45) and CLT-T(0)C(0)

The dynamic results in Figure 6.3 compare the behavior of the full confinement configuration, G-T(0)C(±45), and configuration G-T(0)C(0). Both configurations improved resistance with ratios of 1.30 and 1.23, respectively; however, G-T(0)C(±45) showed less stiffness than configuration

G-T(0)C(0). As seen in Figure 6.3, the resistance-displacement curve of configuration G-T(0)C(0) sharply decreased to zero after reaching the peak resistance. In contrast, in configuration G-T(0)C(±45), after decreasing to about 50% of the peak resistance, it diminished gradually. These results confirm that the significant effect of bidirectional fabric is to improve the post-peak region, where the residual resistance can still significantly contribute to increasing energy dissipation.

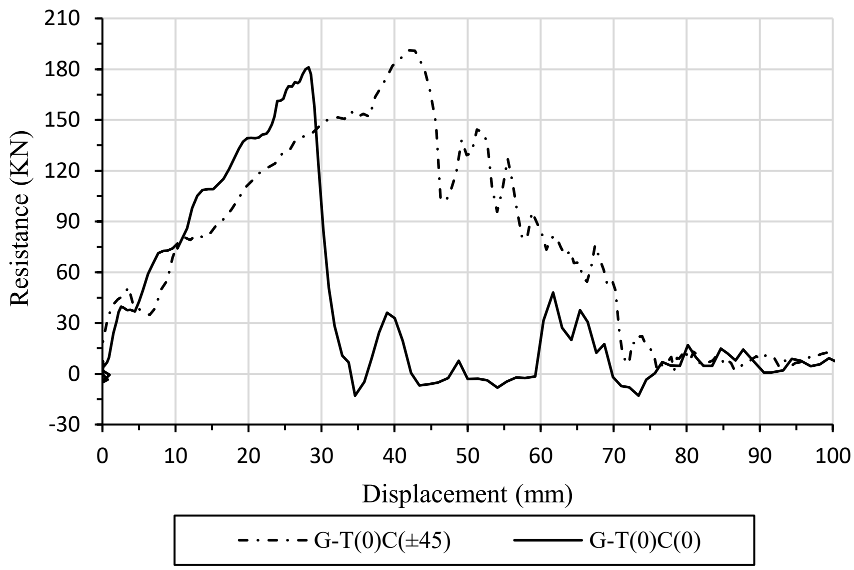

Figure 6.3 Resistance-displacement dynamic curve of unrerofitted glulam, G-T(0)C(±45), and G-T(0)C(0)

6.4 Effect of Full-Length vs. Partial Length CFRP Confinement

As shown Figure 6.4, the peak resistance ratio for CLT-T(0)C(±45) ranged from 1.94 to 2.1, while for CLT-T(0)SH(±45) it ranged from 1.56 to 1.98. The compression results under full-length and partial-length confinement indicate that full-length confinement, by providing residual resistance, improves ductility and energy dissipation. In contrast, the brittle post-peak failure exhibited by partial-length confinement demonstrates that it is less effective at improving strength capacity and ductility due to rolling shear failure, which was the main failure mode for this configuration.

.

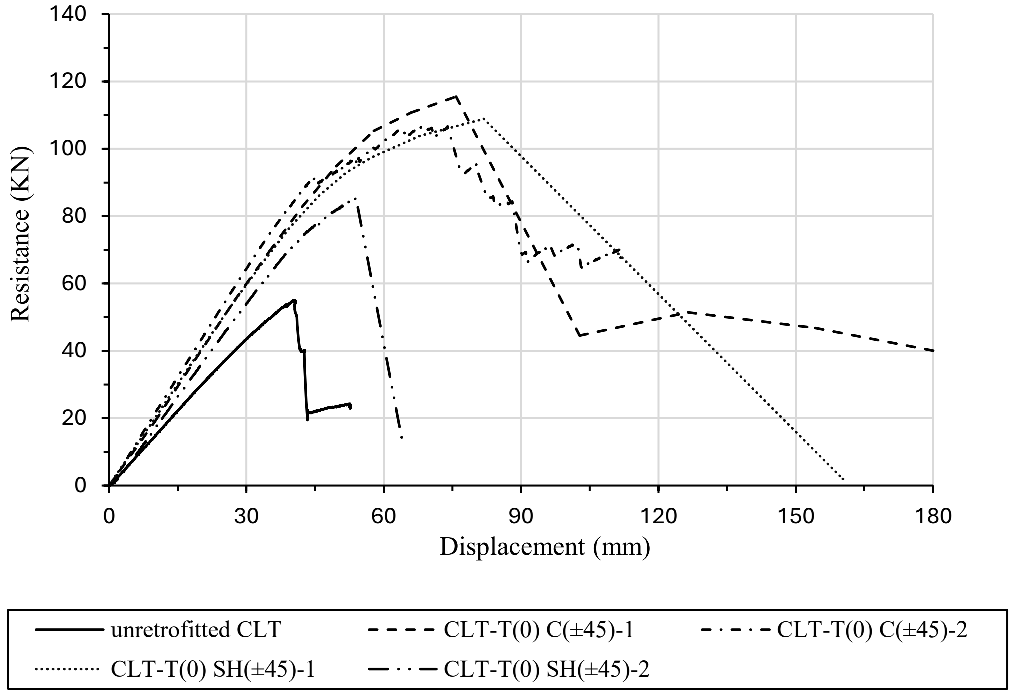

Figure 6.4 Resistance-displacement static curve of unretrofitted CLT, CLT-T(0)C(±45), and CLT-T(0)SH(±45)

For the glulam beams, a similar trend was observed, as shown in Figure 6.5, where full-length CFRP confinement in static tests resulted in the most effective improvement in structural performance, with an increase in peak resistance and stiffness by factors of 1.46 and 1.13, respectively, relative to the unretrofitted beam. Overall, full-length bidirectional confinement has generally been shown to be one of the most effective retrofit configurations for both CLT panel and glulam beam. However, its effectiveness is often more pronounced in the CLT panel due to its susceptibility to rolling shear failure, which can be more effectively restrained through CFRP confinement.

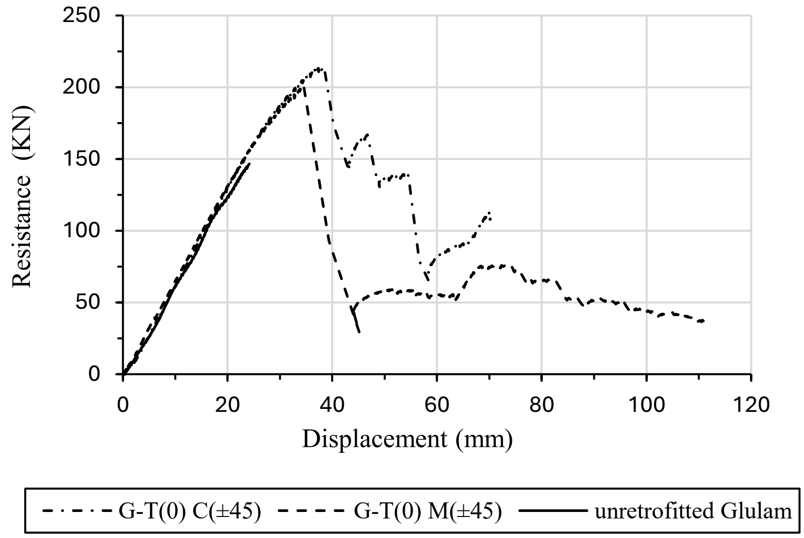

Figure 6.5 Resistance-displacement static curve of unretrofitted glulam, G-T(0)C(±45) and G-T(0)M(±45)

6.5 Effect of U-Shape Confinement

The comparison between fully confined and U-shaped CFRP configurations under static load (Figure 6.6) highlights the importance of confinement continuity. Although the U-shaped reinforcement improved resistance and stiffness relative to the unretrofitted panel, with the ratios of 1.48 and 1.04, respectively, its effectiveness was lower than that of full confinement.

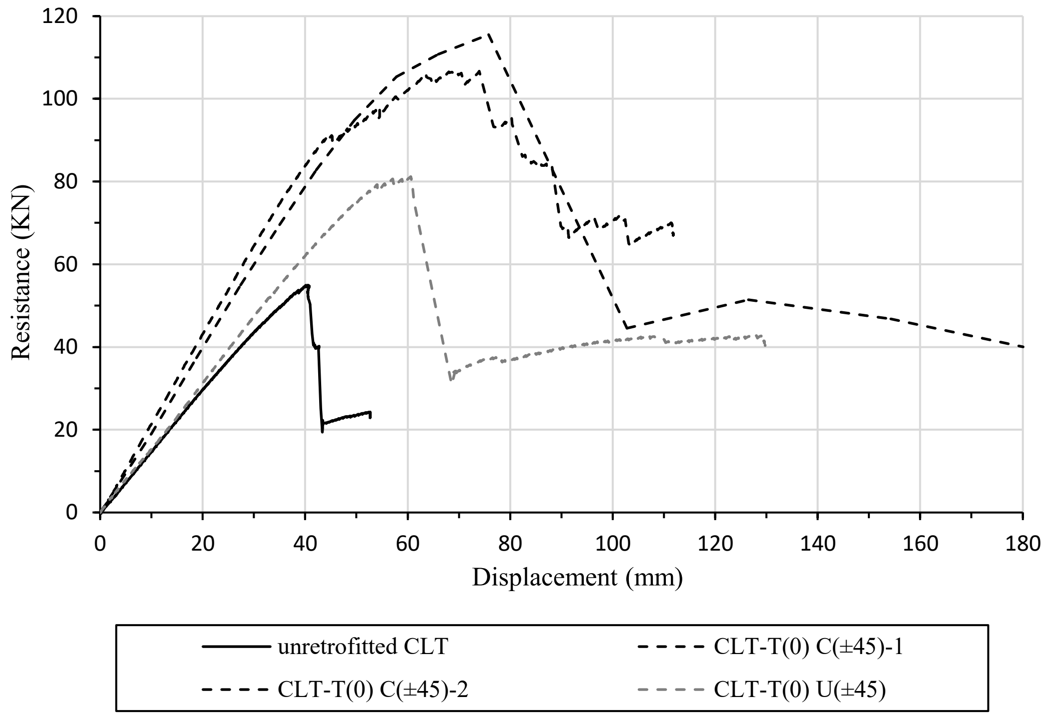

Figure 6.6 Resistance-displacement static curve of unretrofitted CLT, CLT-T(0)C(±45), and CLT-T(0)U(±45)

The dynamic results presented in Figure 6.7 show that the U-shaped confinement exhibited limited improvement, with a peak resistance ratio of 1.5. In contrast, the bidirectional confinement showed a significant increase in both peak resistance and stiffness, with ratios of 2.57 and 1.52, respectively. The static and dynamic results suggest that U-shaped confinement does not significantly increase strength capacity and ductility compared to full confinement, since the lack of confinement on the top surface prevents it from effectively restraining the governing failure mode, which was longitudinal shear failure in this configuration; therefore, its effectiveness remains limited.

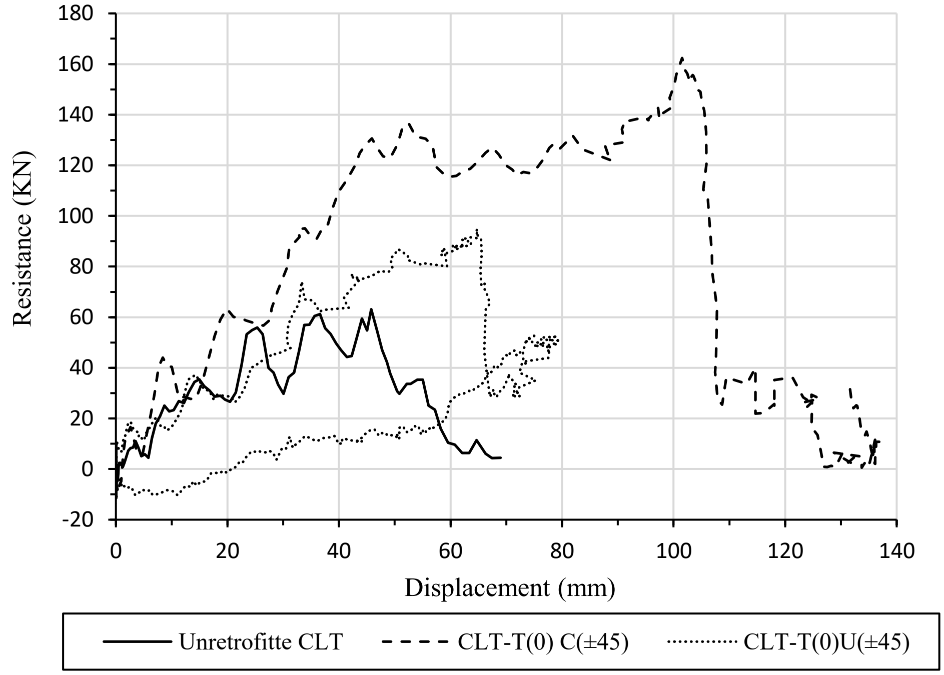

Figure 6.7 Resistance-displacement dynamic curve of unretrofitted CLT, CLT-T(0)C(±45) and CLT-T(0)U(±45)

The dynamic results in Figure 6.8 compare the behaviour of full confinement, G-T(0)C(±45), with the U-shaped confinement configuration, G-T(0)U(±45). Both configurations improved resistance with ratios of 1.30 and 1.33, respectively; however, G-T(0)C(±45) showed slightly lower peak resistance than the U-shaped configuration. In contrast, the fully confined configuration demonstrated greater enhancement in stiffness compared to the U-shaped configuration, which is aligned with other studies by Lacriox and Doudak (2018c) on glulam retrofitted by GFRP under the shock tube test, as the incomplete confinement in the U-shaped configuration allowed separation between the CFRP fabric and the wood surface, resulting in lower stiffness.

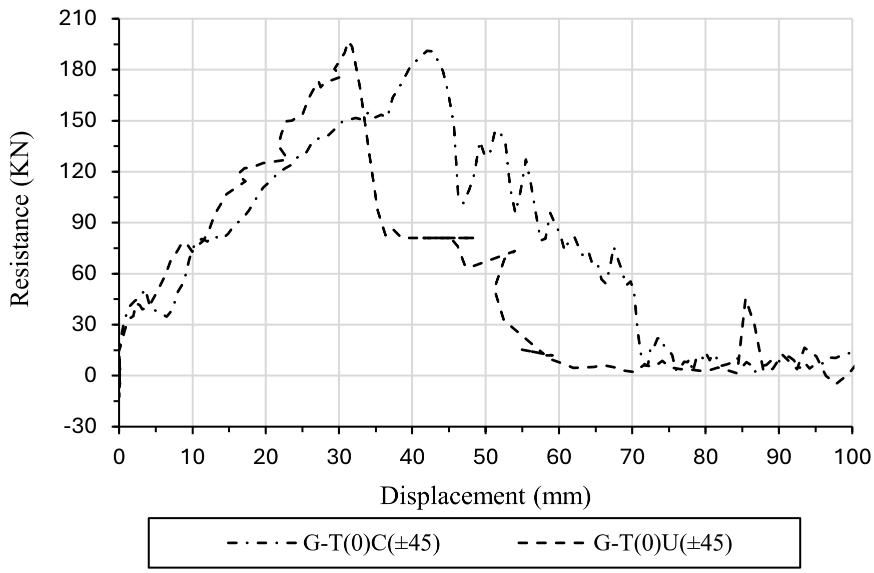

Figure 6.8 Resistance-displacement dynamic curve of unretrofitted glulam, G-T(0)C(±45) and, G-T(0U(±45)

6.6 Effect of Localization of Unidirectional Tensile Reinforcement

The results in Figure 6.9 present that the effectiveness of unidirectional CFRP reinforcement depends strongly on its extent along the tension zone. Full-length reinforcement (CLT-T(0)C(±45)) provided the best overall performance with a higher load capacity ratio of 1.94-2.1, an improvement in stiffness with a ratio of 1.37-1.46, and enhanced post-peak response, with a ductility ratio of 1.5-1.7. When the reinforcement was limited to the moment region (CLT-T-M(0)C(±45)), the improvement was reduced. Although this configuration exhibited an increase in strength, stiffness, and ductility ratio, the unreinforced areas remained vulnerable to early damage. Extending the reinforcement in CLT-T-SH-M(0)C(±45) to both shear and moment regions improved strength by a ratio of 1.94, stiffness to 1.18, and ductility ratio by 1.5, but did not achieve the same level of ductility as the full-length configuration. Although the primary effect of tensile reinforcement is the improvement of structural performance and strength, these findings indicate that increasing the length of tensile reinforcement can also result in larger post-peak displacement.

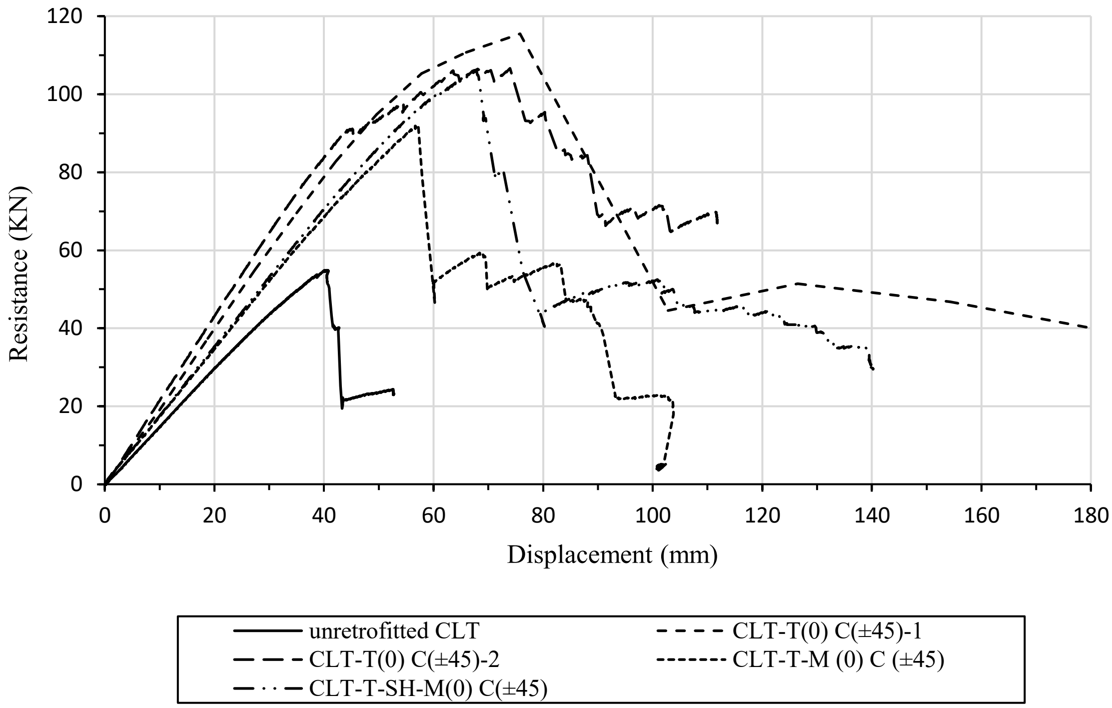

Figure 6.9 Resistance-displacement static curve of unretrofitted CLT, CLT-T(0)C(±45), CLT-T-M(0)C(±45), and CLT-TT-SH-M(0)C(±45)

6.7 Effect of Reinforcement Ratio (Number of Layers)

The static results (Figure 6.10) demonstrate that increasing the CFRP reinforcement ratio, through the addition of unidirectional layers on the tension side, plays a significant role in enhancing the strength capacity of the CLT panel. The addition of a second unidirectional CFRP layer in CLT-T$(0)_2$C(±45) resulted in substantial improvements observed in peak resistance and stiffness, with ratios of 2.33 and 1.49, respectively. This indicates that the tension reinforcement governs the flexural capacity more effectively than confinement alone. In particular, the increase in displacement at peak load and the improved post-peak response suggest that higher reinforcement ratios contribute not only to strength enhancement but also to a more ductile failure behavior.

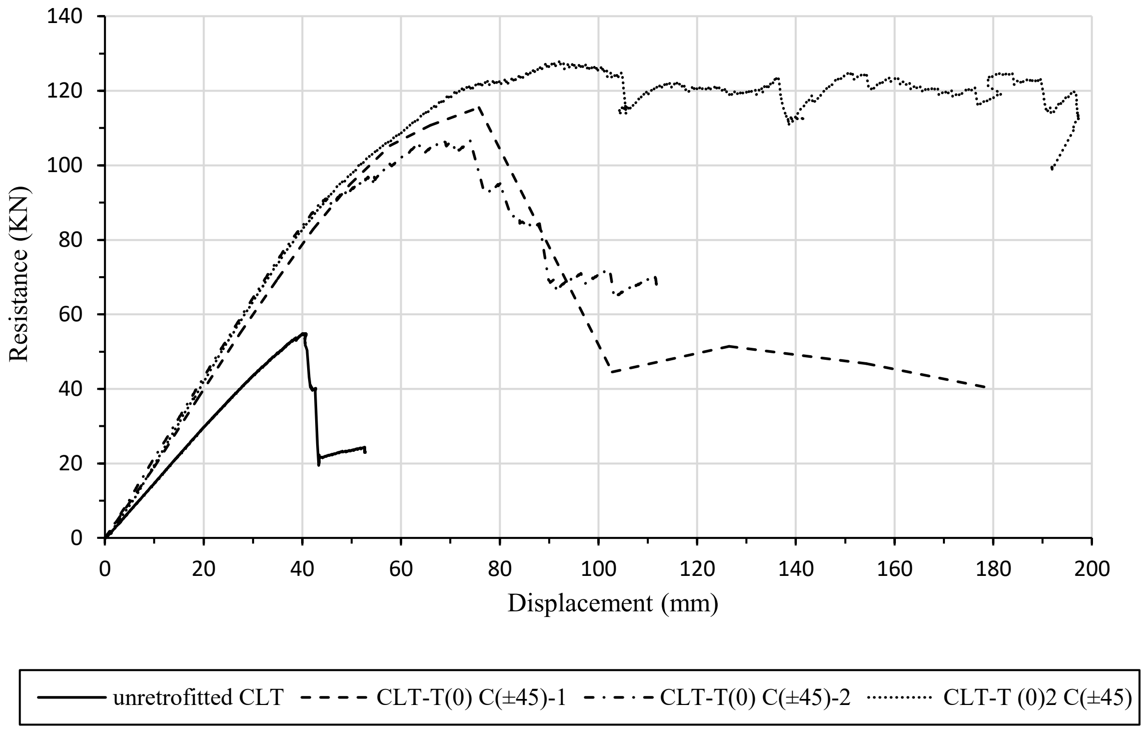

Figure 6.10 Resistance-displacement static curve of unretrofitted CLT, CLT-T(0)C(±45) and CLT-T(0)$_2$C(±45)

The dynamic results of configuration CLT-T(0)C(±45) and CLT-T(0)$_2$C(±45) show that the addition of a unidirectional layer on the tension side increased the strength capacity of the panel and also contributed to improving stiffness compared to the unretrofitted panel. However, the stiffness ratio of the configuration with two layers of tensile reinforcement (1.04) was lower than that of the configuration with one layer of tensile reinforcement (1.52). This suggests that increasing the tensile reinforcement ratio does not necessarily lead to an increase in stiffness due to reasons such as tensile failure.

The dynamic results of configurations G-T(0)C(±45), and G-T(0)$_2$C(±45)(Figure 6.11) indicate that increasing the CFRP ratio, through the addition of unidirectional fabric on the tension side in

G-T(0)$_2$C(±45), led to increase in peak resistance and stiffness, with ratios of 1.65 and 6.07, respectively, both of which are higher than those observed for G-T(0)C(±45).

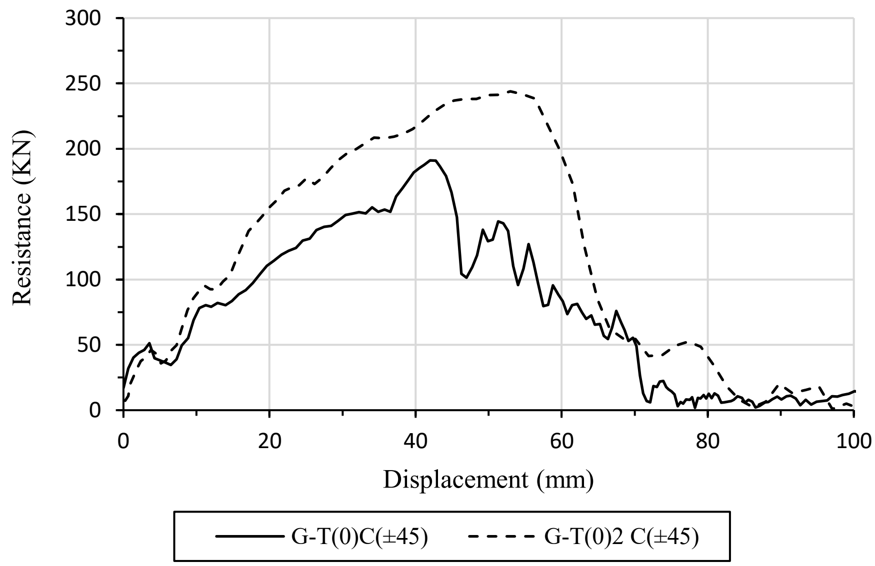

Figure 6.11 Resistance-displacement dynamic curve of unretrofitted glulam, G-T(0)C(±45), and G-T(0)$_2$C(±45)

Overall, static and dynamic results show that increasing the ratio of the tensile reinforcement enhances the ability of the CFRP fabric to delay tensile failure, leading to improved flexural capacity of both the CLT panel and the glulam beam. This observation is consistent with the findings by Gergi and Doudak (2026) on CFRP retrofitted glulam beams under static load.

6.8 Comparison between Static and Dynamic Responses

Figure 6.12 and Table 6.1 compare the static and dynamic response of the unrerofitted CLT panel. Under dynamic loading, the panel exhibited an increase in peak resistance, displacement at maximum resistance, and stiffness with dynamic-to-static ratios of 1.15, 1.14, and 1.32, respectively. This enhancement in structural response is attributed to strain-rate effects, which increase the apparent strength and stiffness of timber under high loading rates.

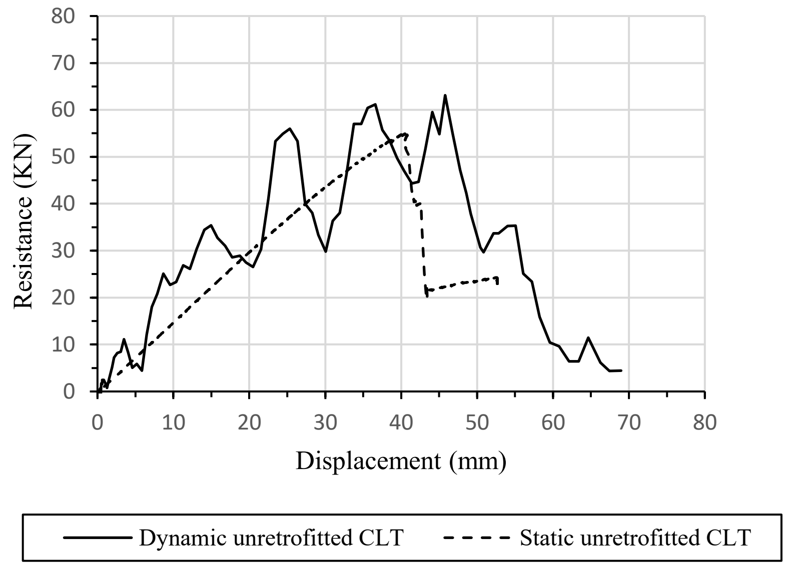

Figure 6.12 Resistance-displacement response of unretrofitted CLT panels under static and dynamic load

Table 6.1 Experimental static and dynamic results of unretrofitted CLT

Configuration	R^a_{max} (KN)	Δ^b_{Rmax} (mm)	K^c (KN/mm)	Dynamic to static ratio R	Δ_{Rmax}	k
UN CLT (Static)[d]	54.9	40.2	1.5	1.15	1.14	1.32
UN CLT (Dynamic)[e]	63.1	45.8	1.98			

[a]Maximum resistance [b]Displacement at maximum resistance [c]Stiffness

[d]Unretrofitted CLT (Static) [e]Unretrofitted CLT (Dynamic)

The results presented in Figure 6.13 and Table 6.2 compare the static and dynamic results of the CLT-T(0)C(0) configuration. Under dynamic loading, the specimen exhibited increased peak resistance, displacement at maximum resistance, and stiffness compared to the static tests. The dynamic to static ratios ranged from 1.19 to 1.39 for peak resistance, 1.19 to 1.29 for displacement, and 1.18 to 1.28 for stiffness. Findings indicate that although a longitudinal shear failure mechanism occurred under dynamic loading for this configuration, an enhancement in the strength capacity and stiffness of the panel was observed due to high strain rate effects.

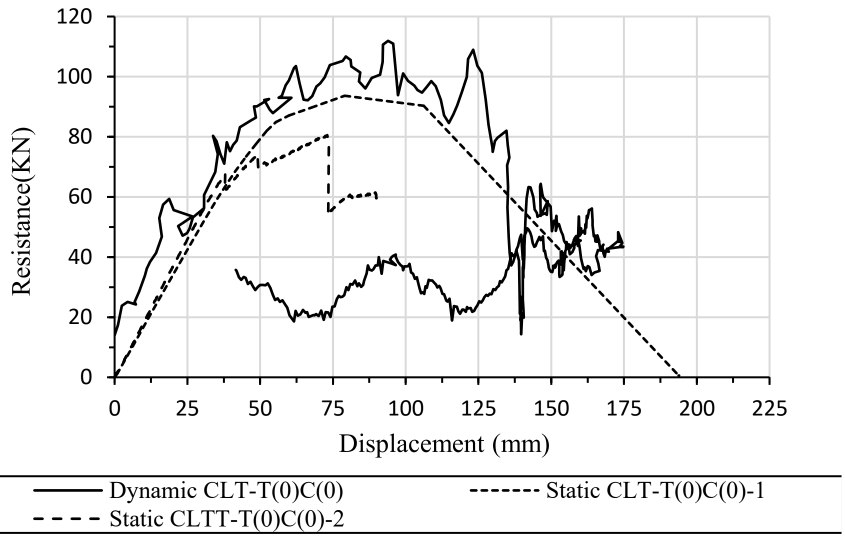

Figure 6.13 Resistance-displacement response of CLT-T(0)C(0) under static and dynamic loa

Table 6.2 Experimental static and dynamic results of CLT-T(0)C(0)

Configuration	R^{a}_{max} (KN)	Δ^{b}_{Rmax} (mm)	K^{c} (KN/mm)	Dynamic to static ratio R	Δ_{Rmax}	k
CLT-T(0)C(0)-1 (Static)[d]	93.7	79.1	1.72	1.19	1.19	1.28
CLT-T(0)C(0)-1 (Static)	80.6	73	1.87	1.39	1.29	1.18
CLT-T(0)C(0) (Dynamic)[e]	111.9	93.9	2.21			

[a]Maximum resistance [b]Displacement at maximum resistance [c]Stiffness [d]Unretrofitted CLT (Static)

[e]Unretrofitted CLT (Dynamic)

The results presented in Figure 6.14 and Table 6.3 compare the static and dynamic response of the CLT-T(0)C(±45) configuration. Under dynamic load, the specimen exhibited significant increases in peak resistance, displacement at peak resistance, and stiffness compared to the static test. The dynamic to static ratios is from 1.41 to 1.52 for peak resistance, 1.37 to 1.46 for stiffness, and 1.34 to 1.37 for displacement. These results show that compared to the CLT-T(0)C(0) configuration, the presence of bidirectional confinement further contributes to improving structural performance in both static and dynamic conditions.

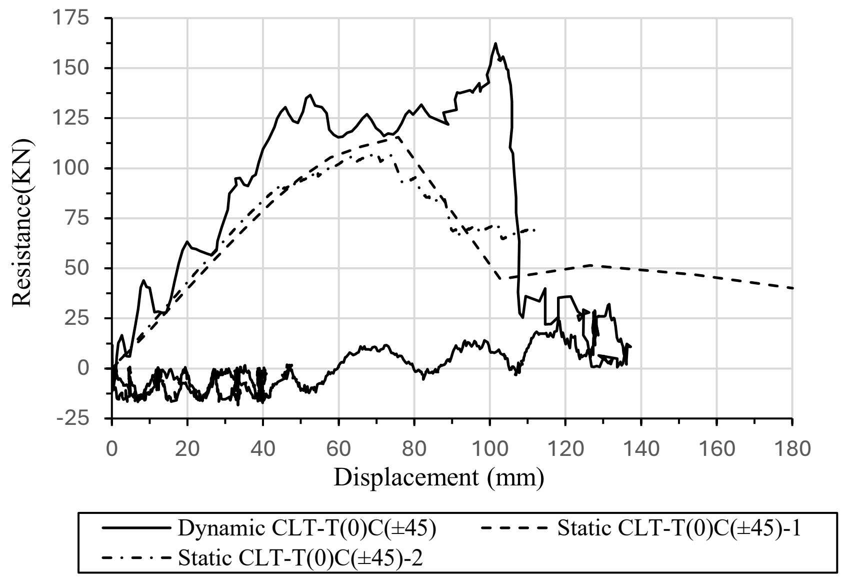

Figure 6.14 Resistance-displacement response of CLT-T(0)C(±45) under static and dynamic load

Table 6.3 Experimental static and dynamic results of CLT-T(0)C(±45)

Configuration	R^a_{max} (KN)	Δ^b_{Rmax} (mm)	K^c (KN/mm)	Dynamic to static ratio R	Δ_{Rmax}	k
CLT-T(0)C(±45)-1 (Static)[d]	115.5	75.8	2.06	1.41	1.34	1.46
CLT-T(0)C(±45)-1 (Static)	106.7	74	2.19	1.52	1.37	1.37
CLT-T(0)C(±45) (Dynamic)[e]	162.4	101.5	3			

[a]Maximum resistance [b]Displacement at maximum resistance [c]Stiffness

[d]Unretrofitted CLT (Static) [e]Unretrofitted CLT (Dynamic)

Comparing the results of static and dynamic responses of the CLT-T(0)$_2$C(±45) is shown in Figure 6.15 and Table 6.4. Although limited longitudinal shear failure was observed in this specimen under dynamic loading, the specimen experienced a higher peak resistance due to strain rate effects, with a peak resistance ratio of 1.31 compared to the static response. This behaviour is associated with the interaction between longitudinal unidirectional fabrics and bidirectional CFRP fabric (±45), which contributes to improving resistance. However, the displacement at peak resistance and stiffness slightly decreased compared to static results, with ratios of 0.98 and 0.92, respectively.

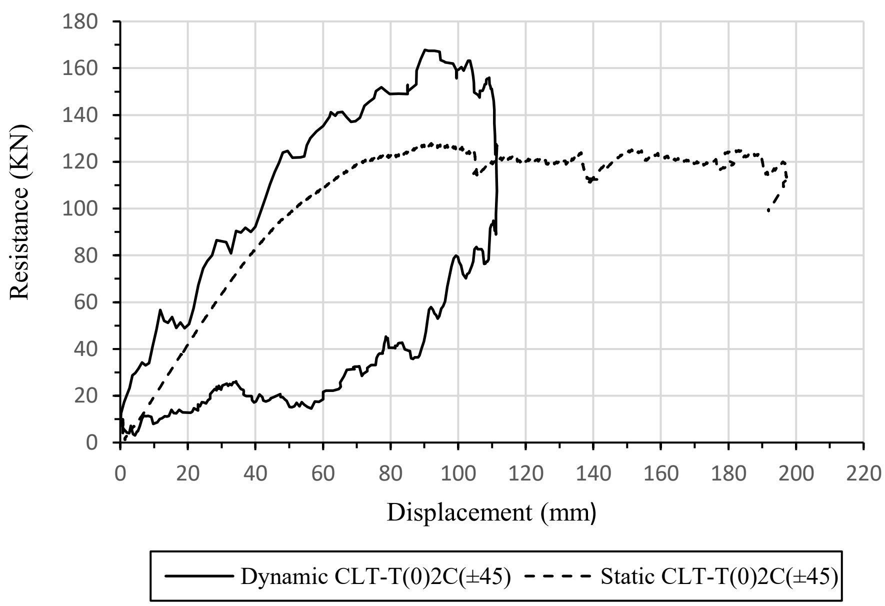

Figure 6.15 Resistance-displacement response of CLT-T(0)2C(±45) under static and dynamic load

Table 6.4 Experimental static and dynamic results of CLT-T(0)$_2$C(±45)

Configuration	R^a_{max} (KN)	Δ^b_{Rmax} (mm)	K^c (KN/mm)	Dynamic to static ratio R	Δ_{Rmax}	k
CLT-T(0)$_2$C(±45)-1 (Static)[d]	127.8	92.1	2.24	1.31	0.98	0.92
CLT-T(0)$_2$C(±45) (Dynamic)[e]	167.8	90.17	2.05			

[a]Maximum resistance [b]Displacement at maximum resistance [c]Stiffness [d]Unretrofitted CLT (Static) [e]Unretrofitted CLT (Dynamic)

Figure 6.16 and Table 6.5 show the static and dynamic results of the CLT-T(0)U(±45) configuration. Under dynamic loading, the specimen exhibited slight increases in peak resistance and peak displacement, with ratios of 1.17 and 1.07, respectively, while the stiffness remained the same, with a ratio of 1.0.

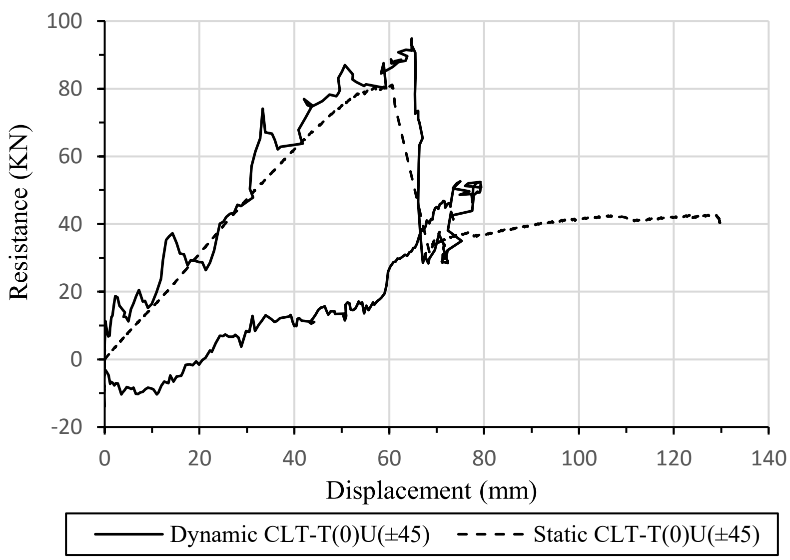

Figure 6.16 Resistance-displacement response of CLT-T(0)U(±45) under static and dynamic load

Table 6.5 Experimental static and dynamic results of CLT-T(0)U(±45)

Configuration	R^{a}_{max} (KN)	Δ^{b}_{Rmax} (mm)	K^{c} (KN/mm)	Dynamic to static ratio R	Δ_{Rmax}	k
CLT-T(0)U(±45)-1 (Static)[d]	81.1	60.6	1.56	1.17	1.07	1
CLT-T(0)U(±45) (Dynamic)[e]	94.9	64.6	1.56			

[a]Maximum resistance [b]Displacement at maximum resistance [c]Stiffness [d]Unretrofitted CLT (Static)
[e]Unretrofitted CLT (Dynamic)

Figure 6.17 and Table 6.6 present the static and dynamic results of the G-T(0)C(±45) configuration. Under dynamic loading, this configuration exhibited lower peak resistance and stiffness compared to the static response due to the possibility of the presence and distributions of defects such as finger joints and knots, with dynamic to static ratios of 0.89 and 0.68, respectively.

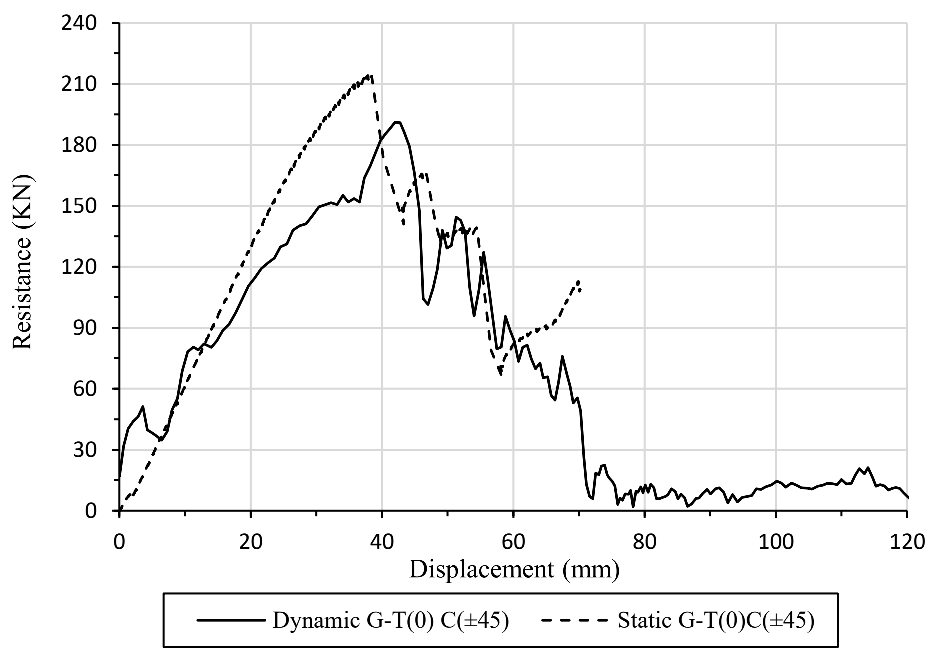

Figure 6.17 Resistance-displacement response of G-T(0)C(±45) under static and dynamic load

Table 6.6 Experimental static and dynamic results of G-T(0)C(±45

Configuration	R^{a}_{max} (KN)	Δ^{b}_{Rmax} (mm)	K^{c} (KN/mm)	Dynamic to static ratio R	Δ_{Rmax}	k
G-T(0)C(±45)-1 (Static)[d]	214.1	37.8	6.88	0.89	1.11	0.68
G-T(0)C(±45) (Dynamic)[e]	191.1	45.7	4.7			

[a]Maximum resistance [b]Displacement at maximum resistance [c]Stiffness

[d]Unretrofitted CLT (Static) [e]Unretrofitted CLT (Dynamic)

Overall, the comparison between statically and dynamically loaded specimens indicated that specimens tested in the Shock Tube under high strain rates exhibited higher strength and stiffness, although there was an exception for some configurations, which may have had defects such as knots or finger joists in glulam beams and shear slip between laminates in CLT panels.

6.9 Fiber section analysis

Figure 6.18 shows the comparison between analytical and experimental static peak resistance, displacement corresponding to the peak resistance, and stiffness values for unretrofitted CLT and glulam. For the peak resistance and displacement prediction, the analytical model overestimated the response of unretrofitted CLT and glulam beam by approximately 15% and 10%. The average prediction for peak resistance and corresponding displacement is 1.01 and 0.96, with COV values of 0.21 and 0.15, respectively. In terms of stiffness prediction, both CLT and glulam beam showed good agreement with the prediction.

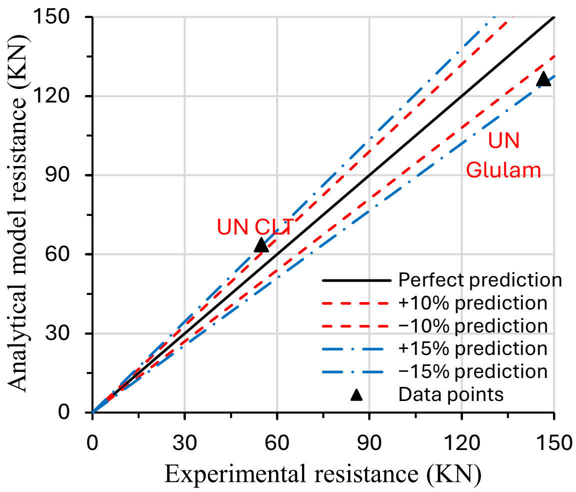

a) Resistance prediction

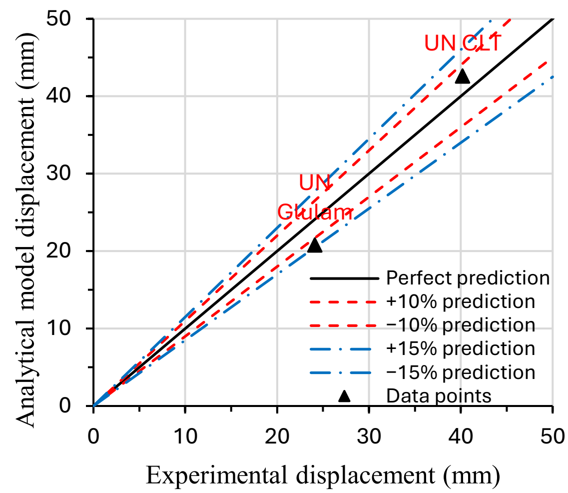

b) Displacement prediction

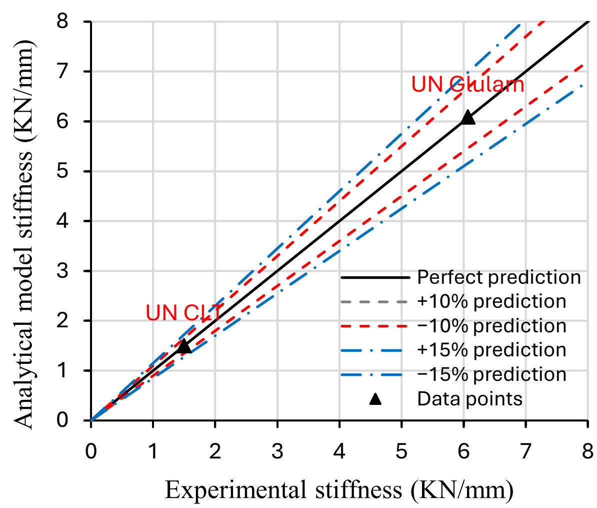

c) Stiffness prediction

Figure 6.18 Comparison between analytical and experimental static resistance, displacement and stiffness for unretrofitted CLT and glulam specimens

Figure 6.19 presents the comparison between analytical and experimental static peak resistance and stiffness values of retrofitted CLT panels. For the resistance, most retrofitted CLT specimens remained within the ±15% prediction bound with an average ratio of 1.14 and COV 0.19, while several specimens were also within the ±10%. The analytical model slightly overestimated the stiffness response of some specimens, with an average ratio of 1.14 and a COV of 0.13; the overall prediction model is consistent.

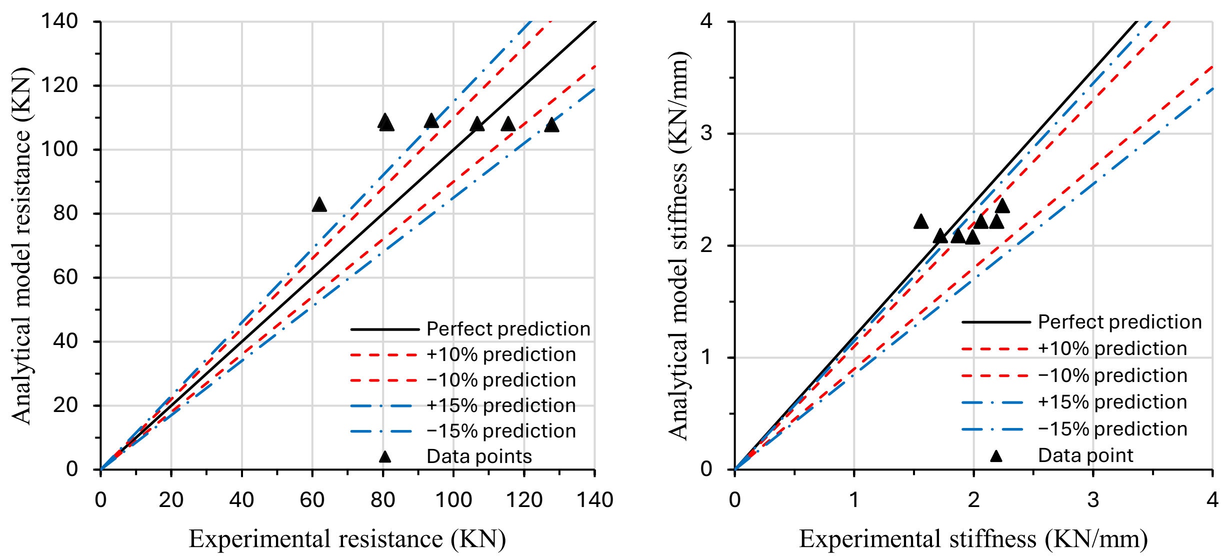

a) Resistance prediction

b) Stiffness prediction

Figure 6.19 Comparison between analytical and experimental static resistance and stiffness for retrofitted CLT panels

Figure 6.20 shows the comparison between analytical and experimental dynamic resistance, displacement, and stiffness of the unretrofitted CLT and glulam. For resistance prediction, the analytical model overestimated the response, placing the results out of ±15% prediction range with an average prediction ratio of 1.13 and a COV of 0.21. For displacement prediction, the CLT panel showed close agreement with ±15% prediction range, while the glulam beam remained out of the +15% prediction range. The average displacement prediction ratio is 0.9 with a COV of 0.46. For stiffness, the analytical model showed an average ratio of 1.07, which was out of +15% prediction range, with a COV of 0.45. The main reason for being outside of this range for CLT is the rolling shear failure mode, not considered in the analytical method, and for glulam, the presence of defects such as knots contributed to the difference between the analytical and experimental results.

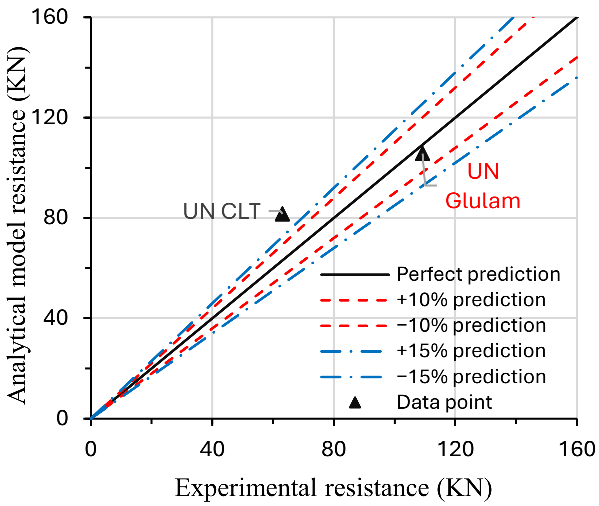

a) Resistance prediction

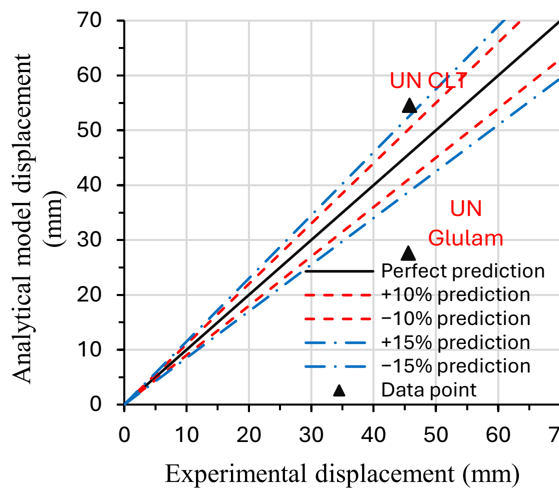

b) Displacement prediction

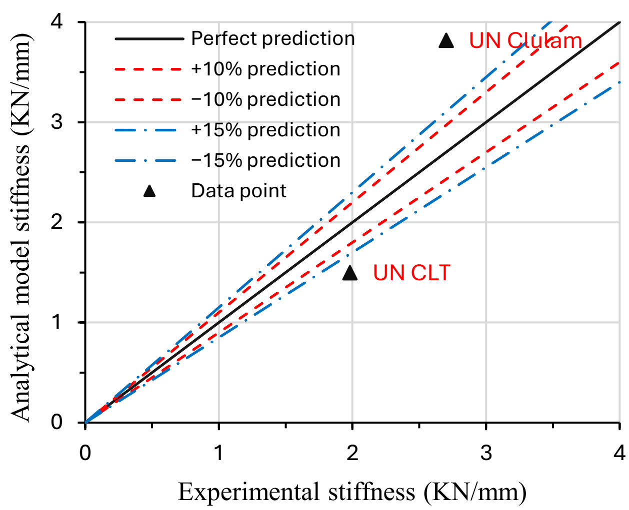

c) Stiffness prediction

Figure 6.20 Comparison between analytical and experimental dynamic resistance, displacement, and stiffness for unretrofitted CLT and glulam specimens

Figure 6.21 shows the comparison between the analytical and experimental dynamic resistance and stiffness for retrofitted CLT panels. For resistance prediction with an average resistance prediction of 0.94 and a COV of 0.15, most of the configurations remained within the ±15% prediction range. For one sample that was outside this range, the main reason is that the highest ratio of CFRP and effects of strain rates caused the prediction to be underestimated. For stiffness prediction, the analytical model exhibited an average prediction ratio of 1.07 with a COV of 0.27. The scatter in the stiffness prediction can be attributed to the failure mode of the specimens, since some of them exhibited a longitudinal failure mode that was not captured by the analytical model.

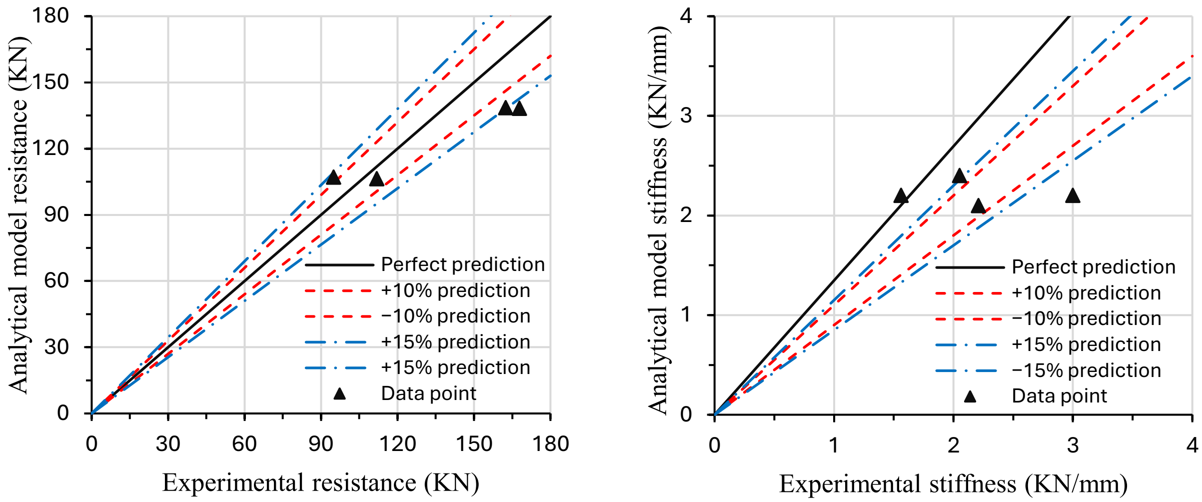

a) Resistance prediction

b) Stiffness prediction

Figure 6.21 Comparison between analytical and experimental dynamic resistance and stiffness for retrofitted CLT panel

Figure 6.22 shows the comparison between the analytical and experimental dynamic resistance and stiffness for the retrofitted glulam beam. For resistance prediction, the analytical model is very close to agreement with experimental results, with an average prediction ratio of 1.00 and a COV of 0.03. Result indicating consistent prediction of the dynamic resistance. For stiffness prediction, the analytical model presents an average prediction ratio of 1.43 with a COV of 0.36, indicating the stiffness response was overestimated and showed greater scatter compared to the resistance prediction. The higher stiffness prediction may be attributed to the presence of defects such as knots and finger joints in the beams that are not considered in the analytical model.

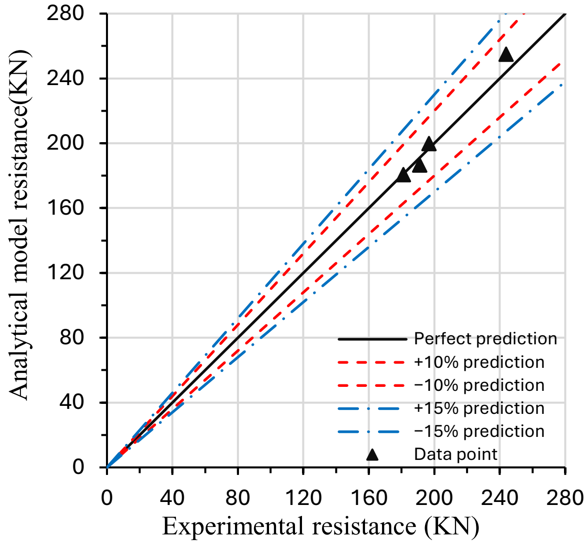

a) Resistance prediction

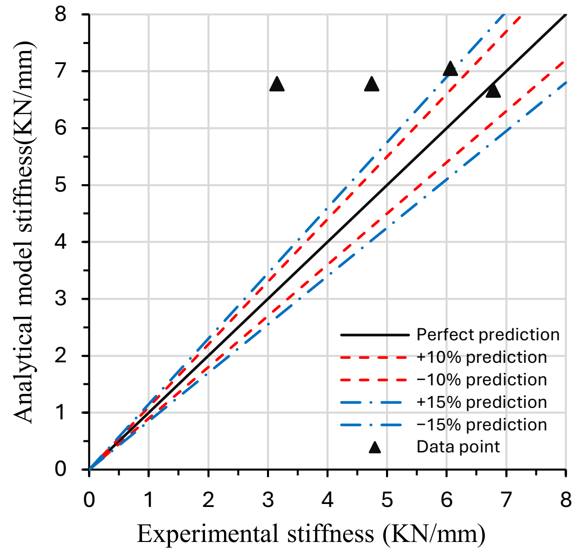

b) Stiffness prediction

Figure 6.22 Comparison between analytical and experimental dynamic resistance and stiffness for retrofitted glulam beams

6.10 SDOF analysis

The dynamic response of the specimens under blast load was simulated using SDOF modeling. Figure 6.23 shows the results for CLT, for which the predicted and experimental results are compared for both the displacement at maximum resistance and time to maximum resistance. An average predicted to experimental displacement at maximum resistance of 0.80 with a COV of 0.3 for CLT was obtained. The predicted displacement at maximum resistance values were underestimated. Similarly, the SDOF model generally underestimated the time to maximum resistance compared with the experimental results.

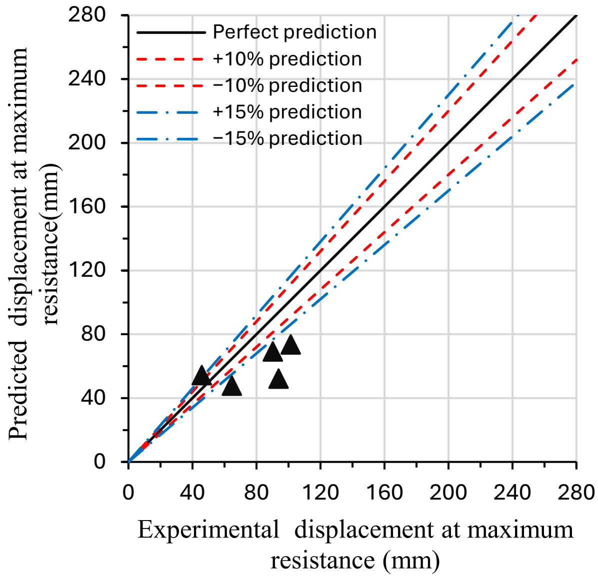

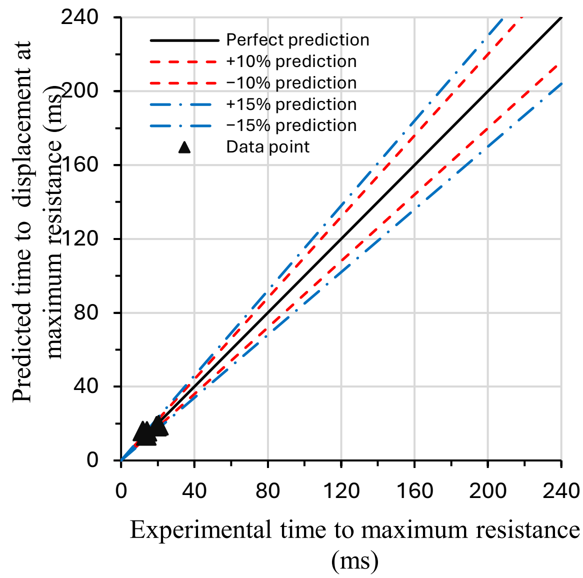

a) Displacement at maximum resistance

b) Time to maximum resistance

Figure 6.23 Comparison between analytical and experimental results of unretrofitted and retrofitted CLT panels (a) displacement at maximum resistance, (b) time to maximum resistance

Figure 6.24 shows the results for glulam specimens. The predicted and experimental responses were compared based on the displacement at maximum resistance and time to maximum resistance. For glulam, the average predicted to experimental displacement at maximum resistance and COV were 1.15 and 0.20, respectively. For displacement at maximum resistance prediction, most data points are within ±10% of the prediction range, indicating that the SDOF model can reasonably capture the flexural behaviour of glulam beams under dynamic loading. For the time to maximum resistance, the results were overestimated. This may be attributed to the fact that defects such as finger joists and knots are not represented in SDOF analysis. The overall findings demonstrate that SDOF analysis can reasonably predict the dynamic behaviour of the specimens.

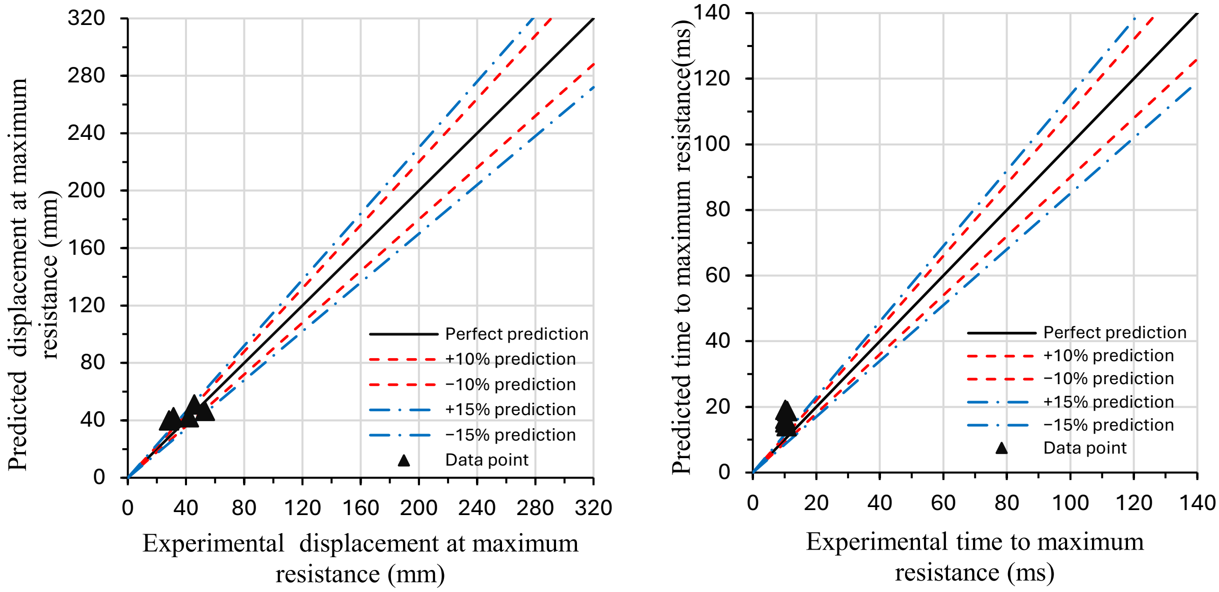

a) Displacement at maximum resistance

b) Time to maximum resistance

Figure 6.24 Comparison between analytical and experimental results of unretrofitted and retrofitted glulam beams (a) displacement at maximum resistance, (b) time to maximum resistance

Chapter 7 Conclusion

7.1 General

This research investigated the structural performance of CFRP retrofitted CLT panels and glulam beams under static and dynamic loading conditions. An experimental program consisting of thirteen retrofit configurations was conducted using both static testing and simulated blast testing. Different retrofit parameters were evaluated, including CFRP orientation, confinement continuity, and placement of tensile reinforcement, U-shaped confinement, and reinforcement ratio. In addition, analytical and SDOF models were developed to predict the resistance and stiffness response of both unretrofitted and retrofitted timber members. Based on the experimental and analytical investigation, the following conclusions are obtained.

7.2 Failure modes

1. The unrerofitted CLT panel exhibited brittle behavior governed by rolling shear and longitudinal shear failure modes under both static and dynamic loading conditions. In contrast, the unretrofitted glulam beam mainly failed in flexural through splintering tension failure.

2. Bidirectional CFRP confinement (±45°) was more effective than unidirectional confinement in controlling transverse laminations slip, maintaining integrity, and improving post-peak behaviour due to its ability to resist multidirectional stresses.

3. Full-length confinement was more effective in restraining rolling shear and longitudinal shear compared to U-shaped confinement. Partial confinement configurations were insufficient to fully prevent shear-related failures.

4. Increasing the CFRP reinforcement ratio through additional unidirectional layers improved tensile resistance, delayed crack propagation, and enhanced ductility and energy dissipation capacity.

5. Compared to CLT panels, glulam beams showed more uniform structural behavior after retrofitting due to the homogenous nature of glulam members and the absence of transverse laminations susceptible to rolling shear.

7.3 Static Behavior of Retrofitted CLT Panels and Glulam Beams

1. Under static loading, CFRP retrofitting significantly improved the peak resistance, stiffness, and ductility of both CLT panels and glulam beams.

2. For CLT panels, the configuration CLT-T$(0)_2$C(±45) showed the most significant improvement, with peak resistance and stiffness ratios of approximately 2.33 and 1.49, respectively, relative to the unretrofitted CLT panel.

3. The use of bidirectional confinement (±45°) together with unidirectional tensile reinforcement resulted in better post-peak behavior and improved energy dissipation compared to unidirectional confinement alone.

4. For glulam beams, full-length CFRP confinement increases peak resistance and stiffness up to approximately 46% and 13%, respectively, while the ductility ratio reached approximately 1.5.

7.4 Dynamic Behavior of Retrofitted CLT Panels and Glulam Beams

1. Under dynamic loading, most of the CFRP retrofit configurations improved the structural response compared to the unretrofitted specimens due to both CFRP strengthening and strain rate effects.

2. Configuration CLT-T(0)C(±45) demonstrated the most improved dynamic behaviour among single-layer retrofit configurations, with peak resistance and stiffness ratios of approximately 2.57 and 1.52 relative to the unrerofitted CLT panel.

3. Increasing the reinforcement ratio in configuration CLT-T$(0)_2$C(±45) further improved peak resistance under dynamic loading, reaching a resistance ratio of approximately 2.66 relative to the unretrofitted panel. However, the stiffness response did not increase proportionally.

4. U-shaped confinement showed limited effectiveness under dynamic loading because incomplete confinement allowed longitudinal shear slip and localized separation between the CFRP and the wood underneath

7.5Analytical and SDOF Modeling

1. The results show that the analytical model accurately predicts the static and dynamic responses of CLT panels and glulam beams, particularly for specimens with flexural behaviour.

2. For retrofitted CLT panels under static loading, the analytical model predicted peak resistance with an average prediction ratio of 1.14 and a COV of 0.19, while stiffness prediction showed an average ratio of 1.14 with a COV of 0.13.

3. For retrofitted CLT panel under dynamic loading, the analytical model predicted resistance with an average ratio of 0.94 and a COV of 0.15, indicating reasonable consistency with the experimental response.

4. For retrofitted glulam beams under dynamic loading, the analytical model predicted resistance accurately with an average ratio of 1.00 and a COV of 0.03.

5. The SDOF analytical model reasonably predicted the dynamic response of both unretrofitted and retrofitted CLT panels and glulam beams under blast loading. For CLT panels, the displacement at maximum resistance showed adequate prediction with experimental results, with an average prediction ratio of 0.80 and a COV of 0.3.

6. For glulam beams, the SDOF model underestimated the displacement at maximum resistanceresponse with an average prediction ratio of 1.15 and a COV of 0.2. However, most predictions remain within the ±10% prediction range.

7. The prediction of the time to maximum displacement exhibited scatter and was generally underestimated for both CLT panels and glulam beams.

7.6 Recommendation for Future Research

1. Future analytical models should include rolling shear and longitudinal shear failure modes to improve prediction accuracy for CLT panels.

2. Numerical finite element modeling should be developed to better capture damage propagation, transverse lamination slip, and strain rate effects under dynamic load conditions.

3. The effect of different CFRP anchorage systems could be investigated to improve confinement and reduce separations.

References

Alam, Parvez, Martin P. Ansell, and Dave Smedley. 2009. “Mechanical Repair of Timber Beams Fractured in Flexure Using Bonded-in Reinforcements.” *Composites Part B: Engineering* 40 (2): 95–106. https://doi.org/10.1016/j.compositesb.2008.11.010.

ASCE. 2011. *Blast Protection of Buildings*. American Society of Civil Engineers.

ASTM (American Society for Testing and Materials). 2011. *ASTM D2555 - Standard Practice for Establishing Clear Wood Strength Values*. American Society for Testing and Materials.

ASTM (American Society for Testing and Materials). 2014. *ASTM D143 - Standard Test Methods for Small Clear Specimens of Timber*. American Society for Testing and Materials.

Bakalarz, Michał Marcin, and Paweł Grzegorz Kossakowski. 2022. “Strengthening of Full-Scale Laminated Veneer Lumber Beams with CFRP Sheets.” *MDPI* 15. https://doi.org/10.3390/ma15196526.

Bazan, I. M. M. 1980. “Ultimate Bending Strength of Timber Beams.” Ph.D., Nova Scotia Technical College.

Biggs, J. M. 1964. *Introduction to Structural Dynamics*. McGraw-Hill.

Borri, A., M. Corradi, and A. Grazini. 2001. “FRP Reinforcement of Wood Elements Under Bending Loads.”

Borri, A., M. Corradi, and E. Speranzini. 2013. “Reinforcement of Wood with Natural Fibers.” *Composites Part B: Engineering* 53 (October): 1–8. https://doi.org/10.1016/j.composites b.2013.04.039.

Brandner, R., G. Flatscher, A. Ringhofer, G. Schickhofer, and A. Thiel. 2016. “Cross Laminated Timber (CLT): Overview and Development.” *European Journal of Wood and Wood Products* 74 (3): 331–51. https://doi.org/10.1007/s00107-015-0999-5.

Buchanan, A. H. 1984. “Strength Model and Design Methods for Bending and Axial Load Interaction in Timber Members.” PhD thesis, University of British Columbia.

Buchanan, A. H. 1986. “Combined Bending and Axial Loading in Lumber.” *Journal of Structural Engineering* 112 (1).

Buchanan, A. H. 1990. “Bending Strength of Lumber.” *Journal of Structural Engineering* 116 (5): 17.

Canadian Standards Association. 2024. *Engineering Design in Wood*. Standard CSA O86-24. CSA Group.

Chen, Herry, Yannick Vetter, Catherine Shrimpton, and Daniel Lacroix. 2025. “Experimental Investigation of the Behaviour of Short-Span FRP-Reinforced Glulam Beams with Hoops and Tension Anchoring.” *Fibers* 13 (6): 80. https://doi.org/10.3390/fib13060080.

Chopra, A. K. 2017. *Dynamics of Structures: Theory and Applications to Earthquake Engineering*. Pearson.

Ciornei, Laura. 2012. “PERFORMANCE OF POLYUREA RETROFITTED UNREINFORCED CONCRETE MASONRY WALLS UNDER BLAST LOADING.” M.A.Sc, University of Ottawa,.

Cormie, D., G. Mays, and P. Smith. 2009. *Blast Effects on Buildings*. Thomas Telford Publishing.

Corradi, Marco, Antonio Borri, Luca Righetti, and Emanuela Speranzini. 2017. “Uncertainty Analysis of FRP Reinforced Timber Beams.” *Composites Part B: Engineering* 113 (March): 174–84. https://doi.org/10.1016/j.compositesb.2017.01.030.

CSA. 2025. *Design and Assessment of Buildings Subjected to Blast Loads*. CSA S850. CSA.

DHS. 2011. *Reference Manual to Mitigate Potential Terrorist Attacks Against Buildings*. Department of Homeland Security.

Dumais, A. J. 2008. “Optimized Wood Components and Subassemblies for Maximum Ductility.” University of Maine.

Dusenberry, D. O. 2010. *Handbook for Blast-Resistant Design of Buildings*. J. Wiley.

Fiorelli, Juliano, and Antonio Alves Dias. 2003. “Analysis of the Strength and Stiffness of Timber Beams Reinforced with Carbon Fiber and Glass Fiber.” *Materials Research* 6 (2): 193–202. https://doi.org/10.1590/S1516-14392003000200014.

Gentile, Chris, Dagmar Svecova, and Sami H. Rizkalla. 2002. “Timber Beams Strengthened with GFRP Bars: Development and Applications.” *Journal of Composites for Construction* 6 (1): 11–20. https://doi.org/10.1061/(ASCE)1090-0268(2002)6:1(11).

Gergi, Milad, and Ghasan Doudak. 2026. "Behaviour of Glulam and CLT Elements Reinforced with CFRP." *Engineering Structures* 351 (March): 121987. https://doi.org/10.1016/j.engstruct.2025.121987.

Gharaibeh, Laith Ismail Ahmad. 2025. "Investigating the Performance of Reinforced Glulam Beams Under Shock Tube Induced Blast Loading." PhD dissertation, University of Ottawa.

Hassanieh, A., H. R. Valipour, and M. A. Bradford. 2017. "Experimental and Numerical Investigation of Short-Term Behaviour of CLT-Steel Composite Beams." *Engineering Structures* 144 (August): 43–57. https://doi.org/10.1016/j.engstruct.2017.04.052.

Hay, Shaun, Kenton Thiessen, Dagmar Svecova, and Baidar Bakht. 2006. "Effectiveness of GFRP Sheets for Shear Strengthening of Timber." *Journal of Composites for Construction* 10 (6): 483–91. https://doi.org/10.1061/(ASCE)1090-0268(2006)10:6(483).

Hernandez, R., J. F. Davalos, S. S. Sonti, Y. Kim, and R. C. Moody. 1997. "Strength and Stiffness of Reinforced Yellow-Poplar Glued Laminated Beams." *U.S. Department of Agriculture, Forest Service, Forest Products Laboratory*, 30.

Jacques, E. 2014. *RCBlast*. Version 0.5.1. Released. http://www.rcblast.ca.

Jansson, B. 1992. *Impact Loading of Timber Beams*. University of British Columbia.

Johns, K. C., and S. Lacroix. 2000. "Composite Reinforcement of Timber in Bending." *Can J Civ Eng* 27: 899–906.

Karacabeyli, Erol, and Sylvain Gagnon. 2020. *Canadian CLT Handbook*. 2019 ed. FPInnovations.

Krouma, Abla, and Ghasan Doudak. 2026. “High Strain Rate Effects on the Performance of Glued-Laminated Timber (GLT) Panels Subjected to Far-Field Blast Loads.” *Structures* 87 (May): 111669. https://doi.org/10.1016/j.istruc.2026.111669.

Lacriox, Daniel. 2017. “Investigating the Behaviour of Glulam Beams and Columns Subjected to Simulated Blast Loading.” PhD Dissertation, University of Ottawa.

Lacroix, Daniel, and Ghasan Doudak. 2015. “Investigation of Dynamic Increase Factors in Light-Frame Wood Stud Walls Subjected to Out-of-Plane Blast Loading.” *Journal of Structural Engineering* 141 (6): 04014159. https://doi.org/10.1061/(ASCE)ST.1943-541X.0001139.

Lacroix, Daniel, and Ghasan Doudak. 2018a. “Determining the Dynamic Increase Factor for Glued-Laminated Timber Beams.” *Journal of Structural Engineering* 144 (9): 04018160. https://doi.org/10.1061/(ASCE)ST.1943-541X.0002146.

Lacroix, Daniel, and Ghasan Doudak. 2018b. “Effects of High Strain Rates on the Response of Glulam Beams and Columns.” *Journal of Structural Engineering* 144 (5): 04018029. https://doi.org/10.1061/(ASCE)ST.1943-541X.0002020.

Lacroix, Daniel, and Ghasan Doudak. 2018c. “Experimental and Analytical Investigation of FRP Retrofitted Glued-Laminated Beams Subjected to Simulated Blast Loading.” *Journal of Structural Engineering* 144 (7): 04018089. https://doi.org/10.1061/(ASCE)ST.1943-541X.0002084.

Lacroix, Daniel, and Ghasan Doudak. 2019. "Design and Analysis of Unretrofitted and Retrofitted Glulam Beams and Columns under Blast Loading." *Structures Congress 2019*, April 22, 137–46. https://doi.org/10.1061/9780784482247.013.

Lacroix, Daniel, and Ghasan Doudak. 2020. "Towards Enhancing the Post-Peak Performance of Glued-Laminated Timber Beams Using Multi-Directional Fibre Reinforced Polymers." *Engineering Structures* 215 (July): 110680. https://doi.org/10.1016/j.engstruct.2020.110680.

Lopez-Molina, A., and G. Doudak. 2019. "Retrofit Techniques for Cross-Laminated Timber (CLT) Elements Subjected to Blast Loads." *Engineering Structures* 197 (October): 109450. https://doi.org/10.1016/j.engstruct.2019.109450.

Mallick, P. K. 2007. *Fiber-Reinforced Composites*.

Markwardt, L. J., and J. A. Liska. 1956. In *The Influence of Rate of Loading on the Strength of Wood and Wood-Base Materials*. ASTM International.

Nadeau, J., R. Bennett, and E. Fuller. 1982. "An Explanation for the Rate-of-Loading and the Duration-of-Load Effects in Wood in Terms of Fracture Mechanics." *Journal of Materials Science* 17 (10): 2831–40.

O'Callaghan, Robert Benjamin. 2021. *Effects of GFRP Reinforcement on the Compressive Behaviour of Square SPF Timber Columns*.

Office of the Deputy Prime Minister. 2004. *The Building Regulations 2000 —Approved Document A: Structure. A3 — Disproportionate Collapse*. Her Majesty's Stationery Office.

Oliveira, Damian. 2021. *Modeling of Mass Timber Components Subjected to Blast Loads*.

Oliveira, Damian, Christian Viau, and Ghasan Doudak. 2023. “Modelling the Behaviour of Heavy and Mass Timber Members Subjected to Blast Loads.” *Engineering Structures* 291 (September): 116397. https://doi.org/10.1016/j.engstruct.2023.116397.

PDC. 2008. *Methodology Manual for the Single-Degree-of-Freedom Blast Effects Design Spreadsheets (SBEDS)*. Technical Report 06-01 Rev 1. U.S. Army Corps of Engineers, Protective Design Center (PDC).

Poulin, Mathieu, Christian Viau, Daniel N. Lacroix, and Ghasan Doudak. 2018. “Experimental and Analytical Investigation of Cross-Laminated Timber Panels Subjected to Out-of-Plane Blast Loads.” *Journal of Structural Engineering* 144 (2): 04017197. https://doi.org/10.1061/(ASCE)ST.1943-541X.0001915.

Radford, D. W., D. Van Goethem, R. M. Gutkowski, and M. L. Peterson. 2002. “Composite Repair of Timber Structures.” *Construction and Building Materials* 16 (7): 417–25. https://doi.org/10.1016/S0950-0618(02)00044-2.

Ross, R. J. 2010. *Wood Handbook - Wood as an Engineering Material*. Forest Products Laboratory, USDA Forest Service.

Saloo, Mehdi, and Christian Viau. 2025. “Modelling of Cross-Laminated Timber Panels Subjected to Contact Charge Detonations and Near-Field Blast Loads.” Paper presented at World Conference on Timber Engineering (WCTE 2025). https://doi.org/10.52202/080513-0060.

Shekarchi, Mohammad, Asghar Vatani Oskouei, and Gary M. Raftery. 2020. “Flexural Behavior of Timber Beams Strengthened with Pultruded Glass Fiber Reinforced Polymer Profiles.” *Composite Structures* 241 (June): 112062. https://doi.org/10.1016/j.compstruct.2020.112062.

Sukontasukkul, P., F. Lam, and S. Mindess. 2000. “Fracture of Parallel Strand Lumber (PSL) under Impact Loading.” *Materials and Structures* 33: 445–49.

Svecova, D., and R. J. Eden. 2004. “Flexural and Shear Strengthening of Timber Beams Using Glass Fibre Reinforced Polymer Bars — an Experimental Investigation.” *Canadian Journal of Civil Engineering* 31 (1): 45–55. https://doi.org/10.1139/l03-069.

Syron, W. D. 2010. “Strain Rate-Dependent Behavior of Laminated Strand Lumber.” University of Maine.

Unified Facilities Criteria Program. 2008. *Structures to Resist the Effects of Accidental Explosions*. UFC 03-340-02. United States of America Department of Defense.

Unified Facilities Criteria (UFC) 03-340-02: Structures to Resist the Effects of Accidental Explosions. 2008. United States Department of Defense.

Viau, Christian, and Ghasan Doudak. 2016. “Investigating the Behavior of Light-Frame Wood Stud Walls Subjected to Severe Blast Loading.” *Journal of Structural Engineering* 142 (12): 04016138. https://doi.org/10.1061/(ASCE)ST.1943-541X.0001622.

Viau, Christian, and Ghasan Doudak. 2019. “Behaviour and Modelling of Cross-Laminated Timber Panels with Boundary Connections Subjected to Blast Loads.” *Engineering Structures* 197: 109404. https://doi.org/10.1016/j.engstruct.2019.109404.

Yang, Huifeng, Weiqing Liu, Weidong Lu, Shijun Zhu, and Qifan Geng. 2016. “Flexural Behavior of FRP and Steel Reinforced Glulam Beams: Experimental and Theoretical Evaluation.” *Construction and Building Materials* 106 (March): 550–63. https://doi.org/10.1016/j.conbuildmat.2015.12.135.

Yang, You-long, Jin-wei Liu, and Guang-jing Xiong. 2013. “Flexural Behavior of Wood Beams Strengthened with HFRP.” *Construction and Building Materials* 43 (June): 118–24. https://doi.org/10.1016/j.conbuildmat.2013.01.029.

Yi, Na Hyun, Jin Won Nam, Sung Bae Kim, In Soon Kim, and Jang-Ho Jay Kim. 2010. “Evaluation of Material and Structural Performances of Developed Aqua-Advanced-FRP for Retrofitting of Underwater Concrete Structural Members.” *Construction and Building Materials* 24 (4): 566–76. https://doi.org/10.1016/j.conbuildmat.2009.09.008.

Appendix A Static test results

Table A.1Static test results for unretrofitted and retrofitted CLT panels

Configuration	$\mathbf{R^{a}_{max}}$ **(KN)**	$\mathbf{\Delta^{b}_{Rmax}}$ **(mm)**	$\mathbf{K^{c}}$ **(KN/mm)**	**Ductility**	$\boldsymbol{\varepsilon^{d}_{t,w-f}}$ **x10^{-4} (mm/mm)**	$\boldsymbol{\varepsilon^{e}_{c,w-f}}$ **x10^{-4} (mm/mm)**
Unretrofitted CLT	54.9	40.2	1.50	-	30.63	-28.23
CLT-C(±45)	62	34.7	1.99	1.3	43.33	-
CLT-T(0)C(0)-1	93.7	79.1	1.72	-	42.71	-87.2
CLT-T(0)C(0)-2	80.6	73	1.87	1.2	33.75	-44.4
CLT-T(0)C(±45)-1	115.5	75.8	2.06	1.7	62.14	-123.57
CLT-T(0)C(±45)-2	106.7	74	2.19	1.5	51.54	-152.05
CLT-T(0)SH(±45)-1	108.9	81.9	2.02	-	56.04	-149.73
CLT-T(0)SH(±45)-2	85.4	54	1.88	-	58.85	-60
CLT-T-M(0)C(±45)	92.2	57.2	1.72	1.5	37.12	-65.19
CLT-T-SH-M(0)C(±45)	106.3	67.8	1.77	1.5	79.11	-100.13
CLT-T(0)$_2$C(±45)	127.8	92.1	2.24	2.1	-	-
CLT-T (0)U(±45)	81.1	60.6	1.56	1.5	49.2	-53.66

[a]Maximum resistance [b]Displacement at maximum resistance [c]Stiffness
[d]Strain at wood tensile rupture [e]Maximum wood compressive strain

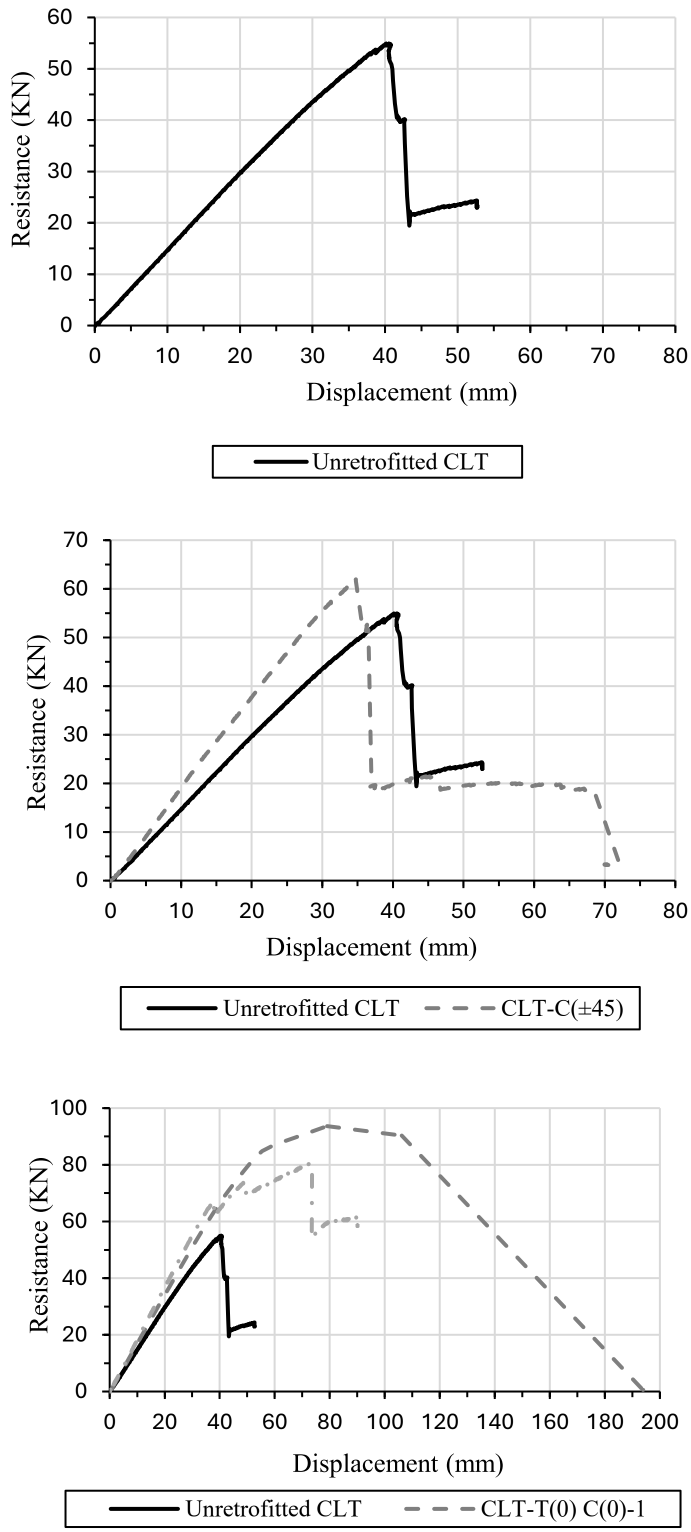

Figure A.1Static test results unretrofitted and retrofitted CLT panels (Retrofit 1 and 2)

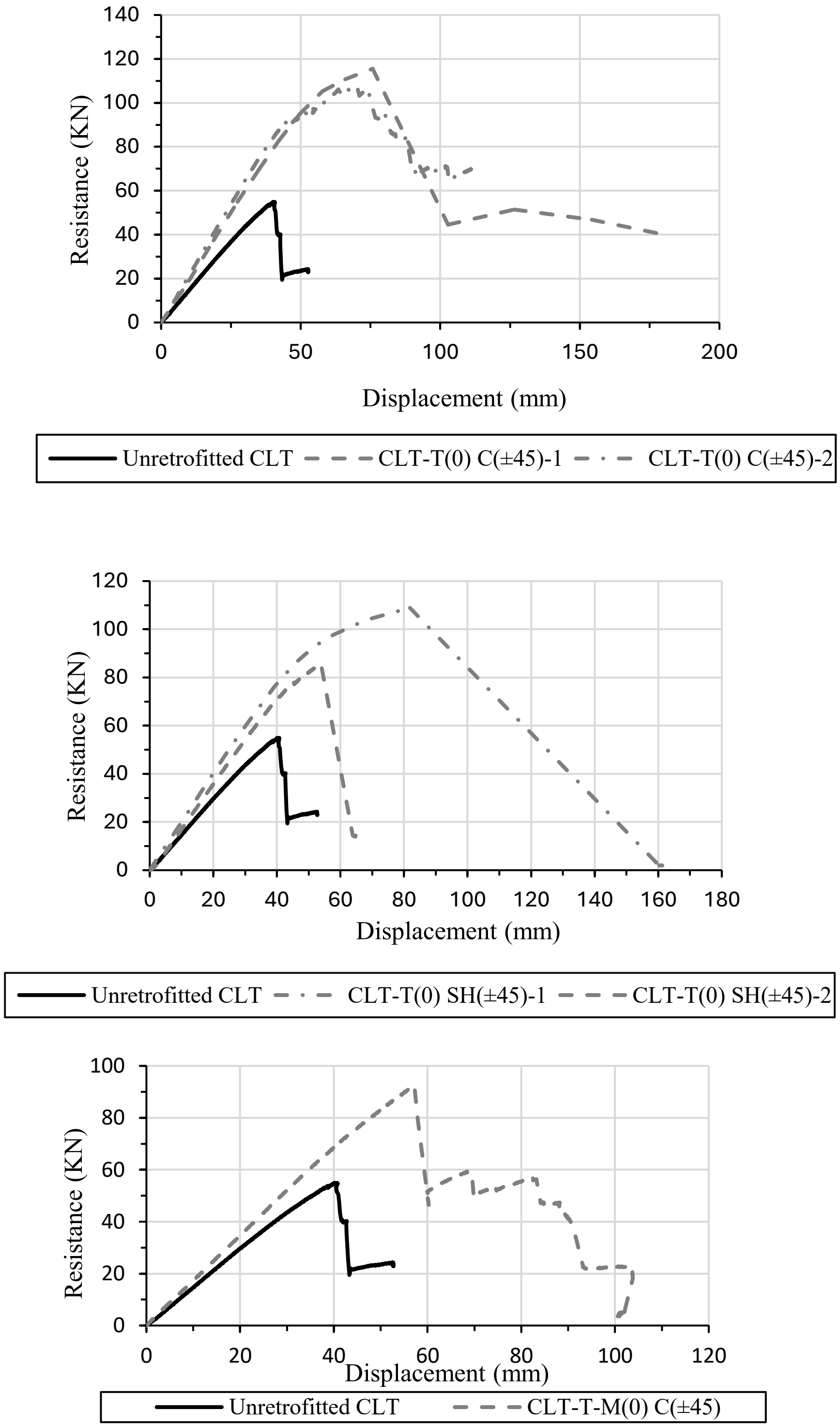

Figure A.2 Static test results retrofitted CLT panels (Retrofit 3-5)

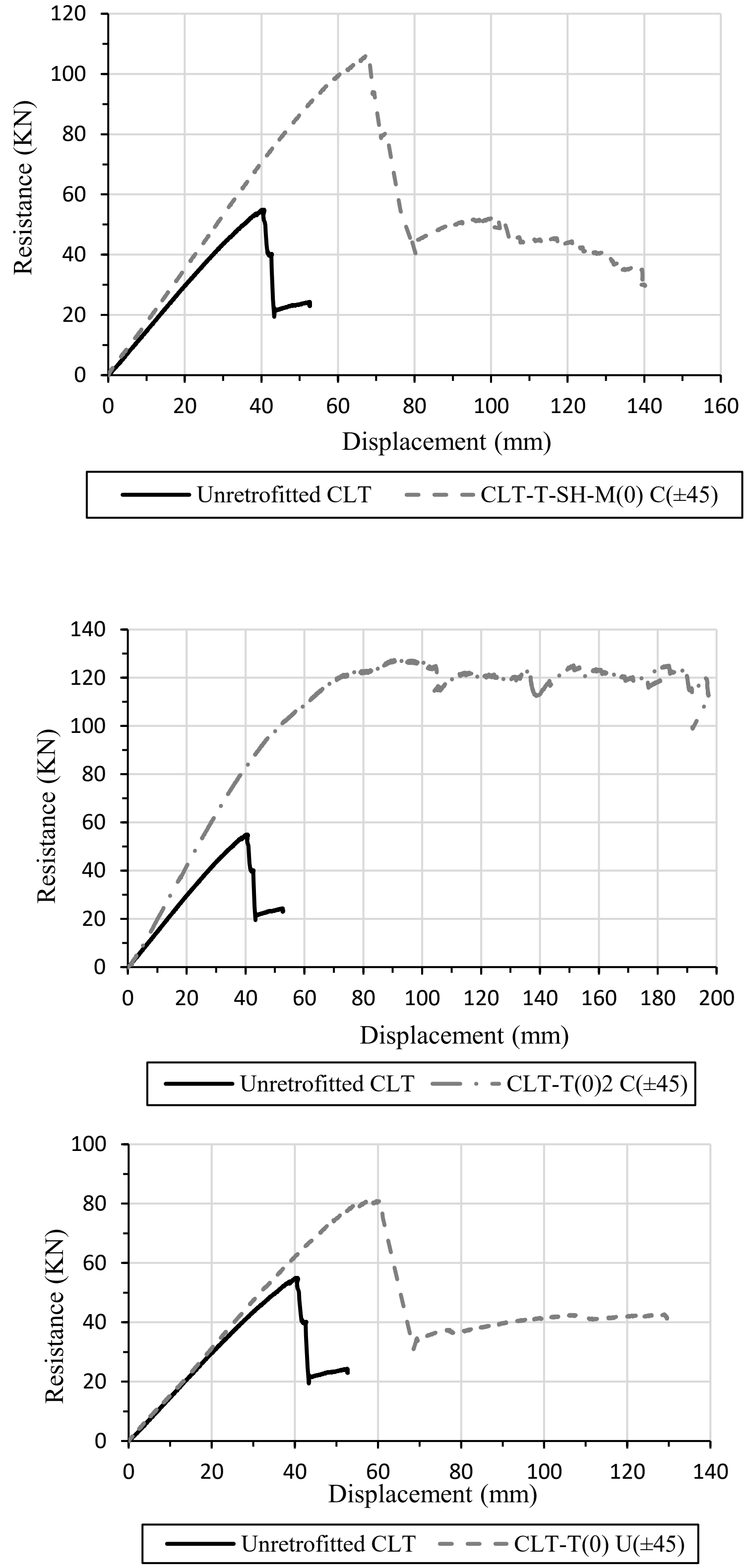

Figure A.3 Static test results retrofitted CLT panels (Retrofit 6-8)

Unretrofitted CLT

(a) Before uploading

(b) After uploading

Figure A.4 Static test unretrofitted CLT panel

CLT-C(±45)

(a) Static failure mode of CLT-C(±45)

(b) Side view of CLT-C(±45)

Figure A.5 Static test of CLT-C(±45)

CLT-T(0)C(0)

(a) After uploading CLT-T(0)C(0)-1

(a) Side view of CLT-T(0)C(0)-2

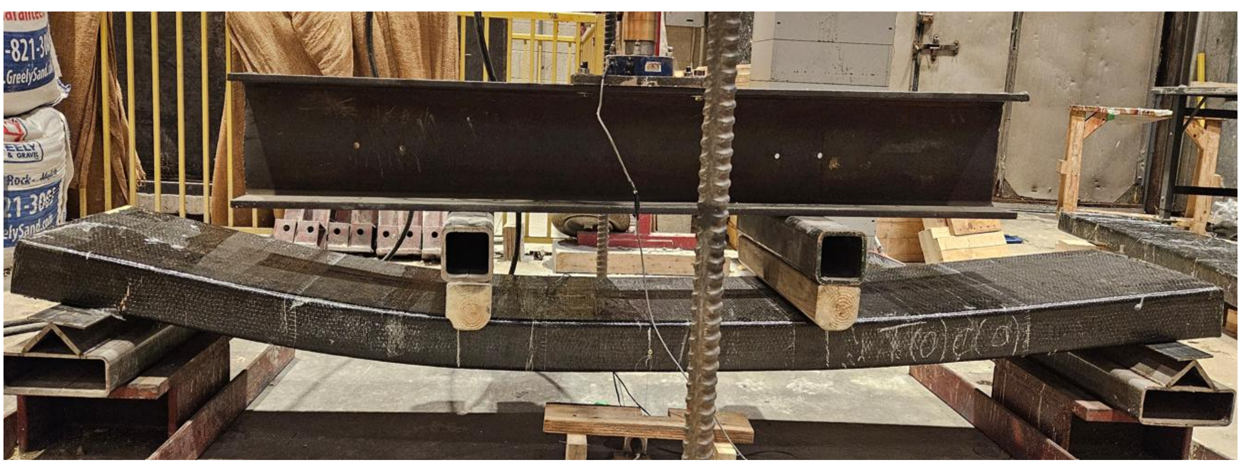

(C) Static failure mode of CLT-T(0)C(0)-2

Figure A.6 Static failure mode of CLT-T(0)C(0)-2

CLT-T(0)C(±45)-1

(b) Before uploading CLT-T(0)C(±45)-1

(b) Close view of CLT-T(0)C(±45)-1

Figure A.7 Static test of CLT-T(0)C(±45)-1

CLT-T(0)C(±45)-2

(a) Static failure mode of CLT-T(0)C(±45)-2

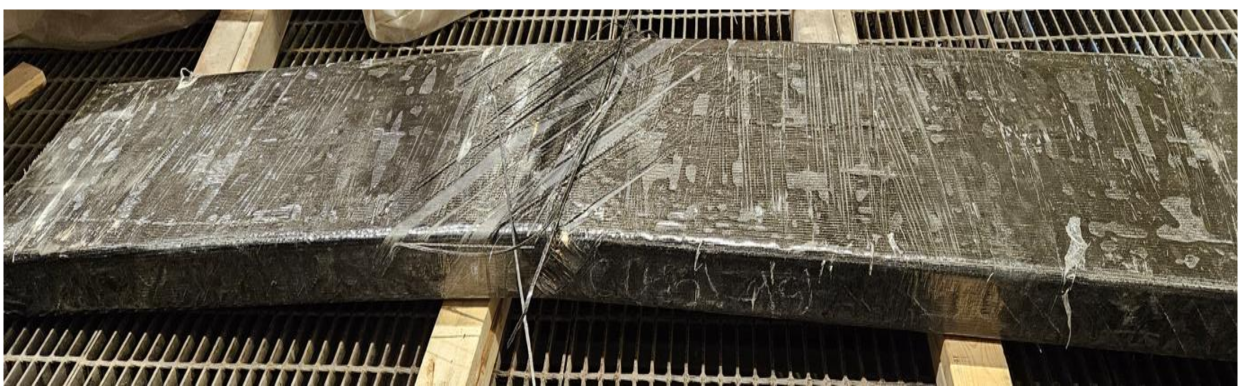

(b) Tension side view of CLT-T(0)C(±45)-2

Figure A.8 Static test of CLT-T(0)C()-2.8 Static test of CLT-T(0)C(±45)-2

CLT-T(0)SH(±45)-1

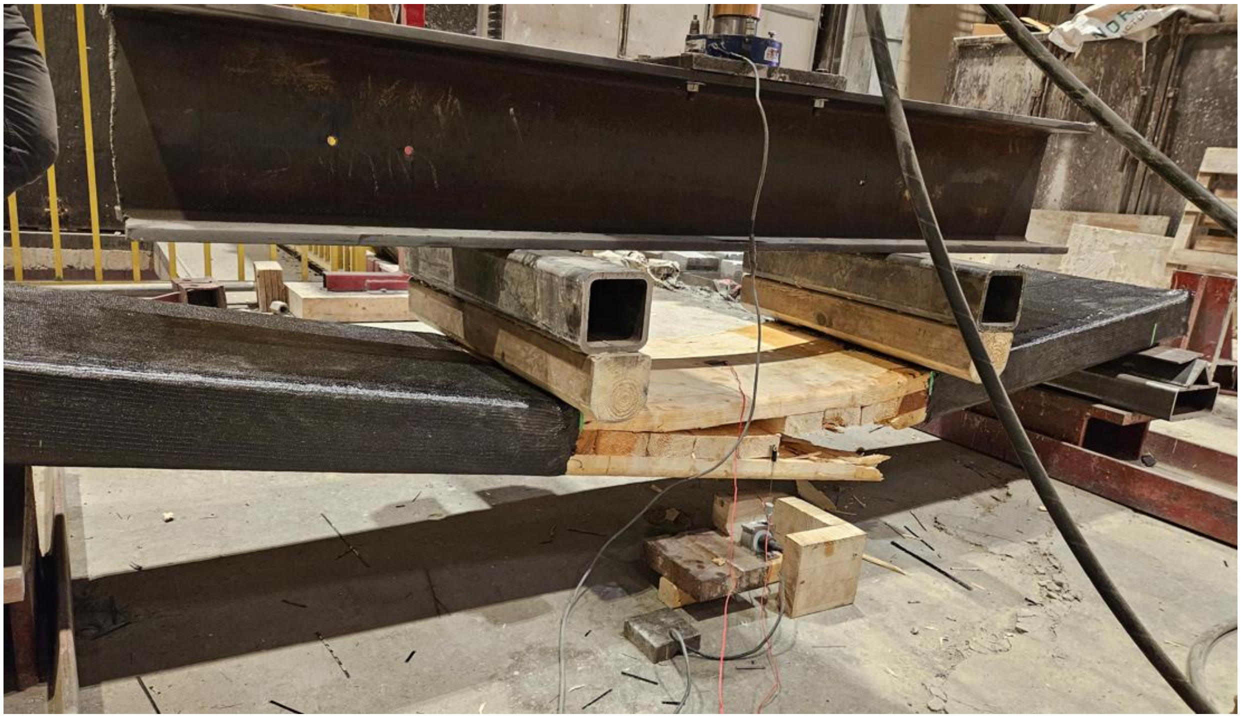

(a) Static failure mode of CLT-T(0)SH(±45)-1

Figure A.9 Static test of CLT-T(0)SH(±45)-1

CLT-T-M(0)C(±45)

(a) Static failure mode of CLT-T-M(0)C(±45)

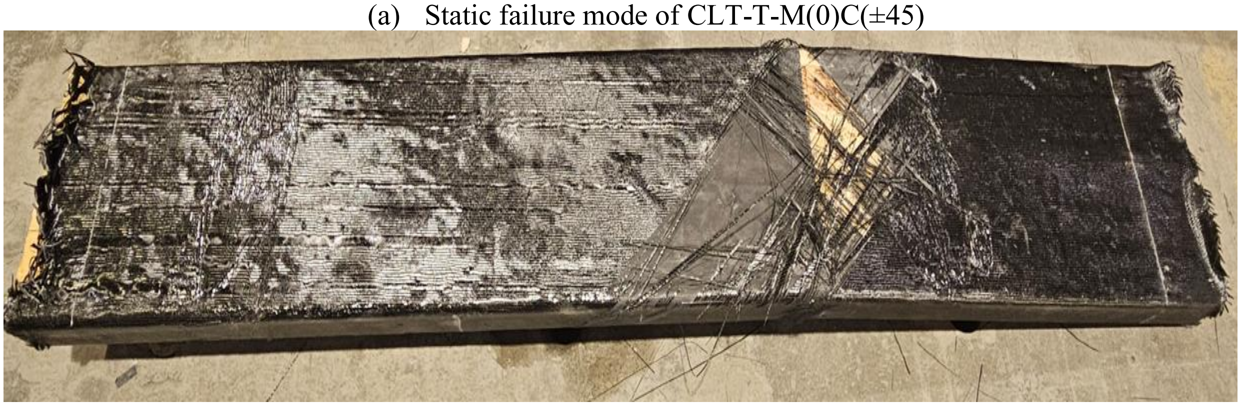

(b) Tension side of CLT-T-M(0)C(±45)

Figure A.10 Static test of CLT-T-M(0)C(±45)

CLT-T-SH-M(0)C(±45)

(a) Static failure mode of CLT-T-SH-M(0)C(±45)

(b) Tension side of CLT-T-SH-M(0)C(±45)

Figure A.11Static test of CLT-T-SH-M(0)C(±45)

CLT-T(0)$_2$C(±45)

(a) Static failure test of CLT-T(0)$_2$C(±45)

(b) side view of CLT-T(0)$_2$C(±45)

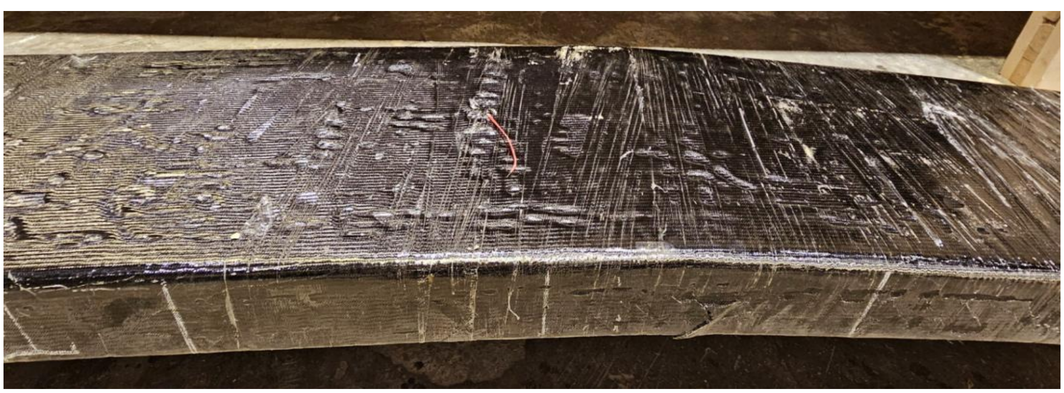

(c) Tension view of CLT-T(0)$_2$C(±45)

7

CLT-T(0)U(±45)

(a) Static failure mode of CLT-T(0)U(±45)

(b) Cross section view of CLT-T(0)U(±45)

Figure A.12 Static test of CLT-T(0)U(±45)

Table A.2 Static test results for unretrofitted and retrofitted Glulam beams

Configuration	$\mathbf{R^{a}_{max}}$ **(KN)**	$\mathbf{\Delta^{b}_{Rmax}}$ **(mm)**	$\mathbf{K^{c}}$ **(KN/mm)**	**Ductil-ity**	$\boldsymbol{\varepsilon^{d}_{t,w-f}}$ **x10^{-4} (mm/mm)**	$\boldsymbol{\varepsilon^{e}_{c,w-f}}$ **x10^{-4} (mm/mm)**
Unretrofitted glulam	146.6	24.1	6.07	-	50	-
G-T (0) C (±45)	214.1	37.8	6.88	1.5	56.84	-77.09
G-T (0) M (±45)	201	34.5	6.70	1.2	50.17	-47.8

[a]Maximum resistance [b]Displacement at maximum resistance [c]Stiffness
[d]Strain at wood tensile rupture [e]Maximum wood compressive strain

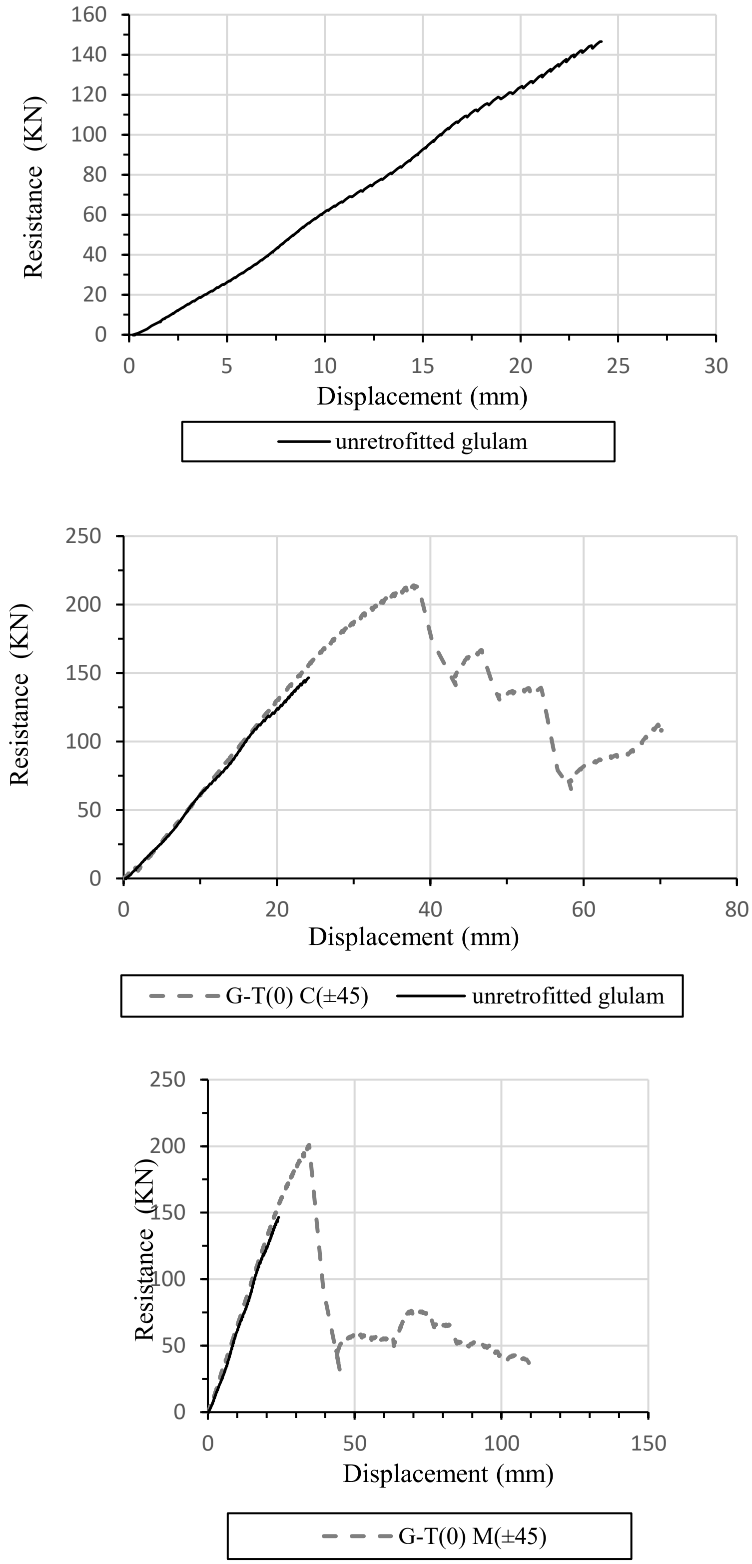

Figure A.13 Static test results unretrofitted and retrofitted Glulam beams (Retrofit 9 and 11)

Unretrofitted Glulam

(a) Static failure mode of unretrofitted glulam

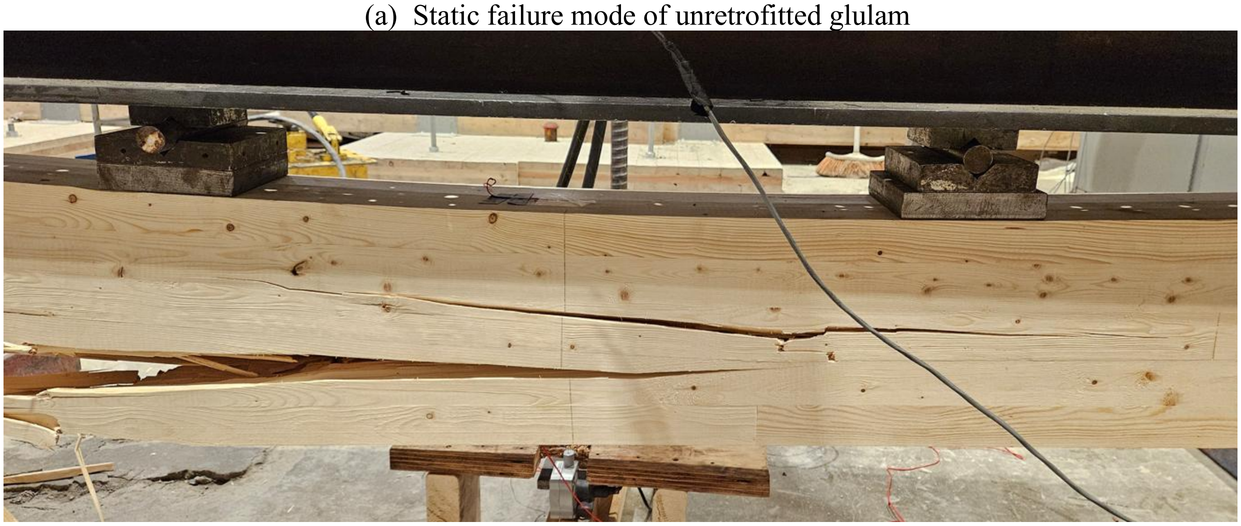

(b) Close view of G-T(0)C(±45) between to concentrated loads

Figure A.14 Static test of unretrofitted glulam

G-T(0)C(±45)

(c) Static failure mode of G-T(0)C(±45)

(d) After uploading G-T(0)C(±45)

Figure A.15 Static test of G-T(0)C(±45)

G-T(0)M(±45)

(a) Static failure mode of G-T(0)M(±45)

(b) Tension view of G-T(0)M(±45)

(c) Tearing of tensile unidirectional fabric of G-T(0)M(±45)

Figure A.16 Static test of G-T(0)M(±45)

Appendix B Dynamic test results

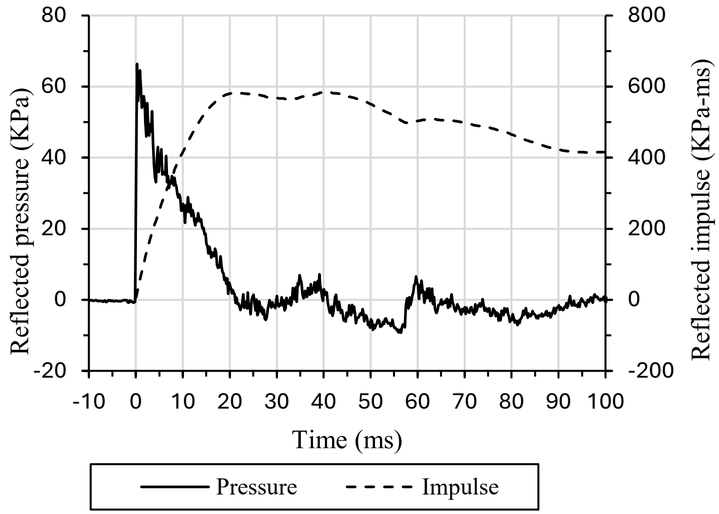

a) Pressure and impulse

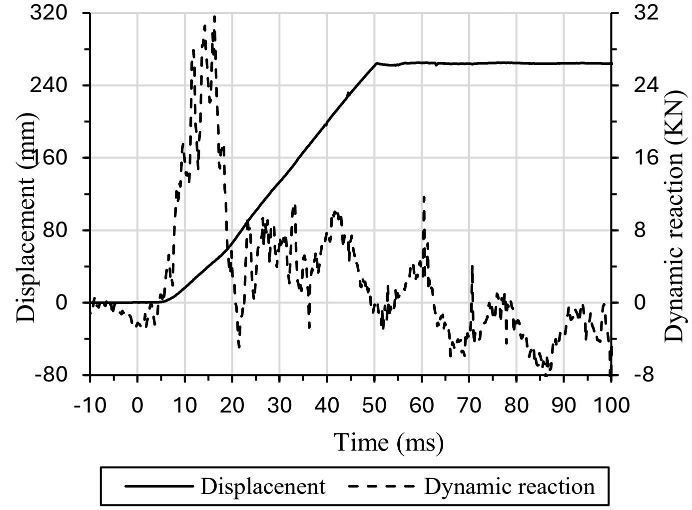

b) Displacement and reaction

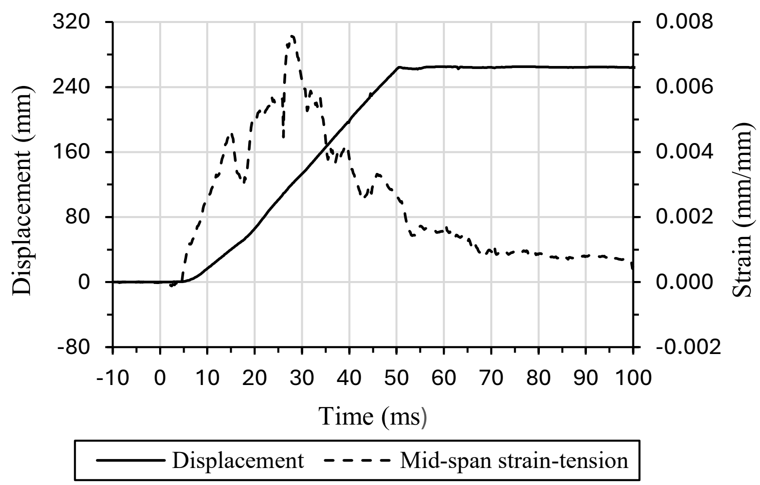

c) Displacement and strain

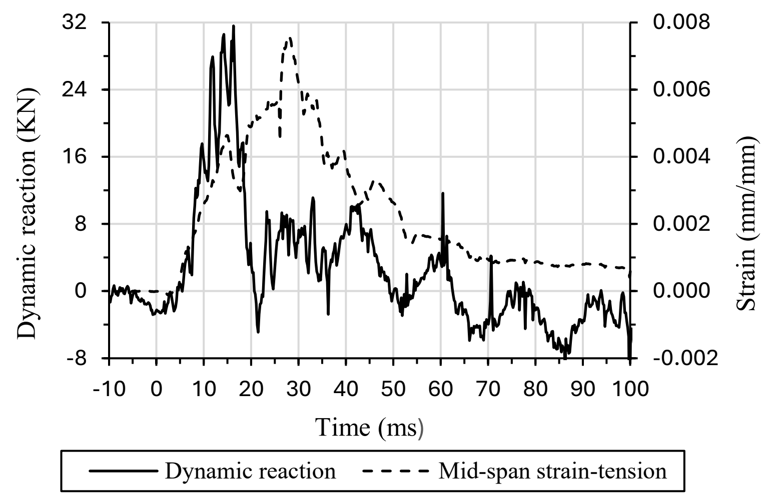

d)Dynamic reaction and strain

Figure B.1 Dynamic test results for unretrofitted CLT

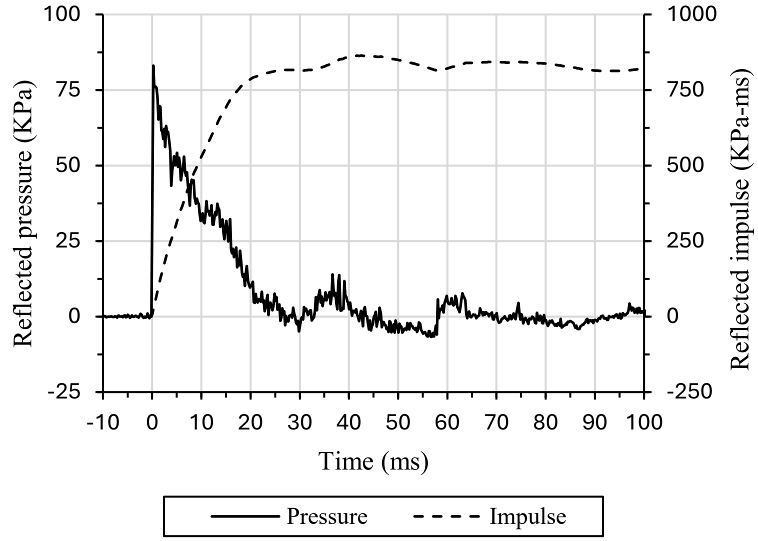

a) Pressure and impulse

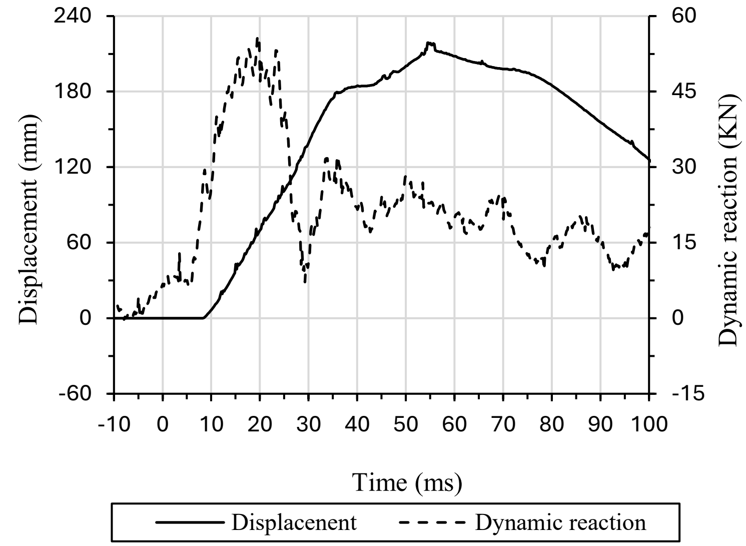

b) Displacement and reaction

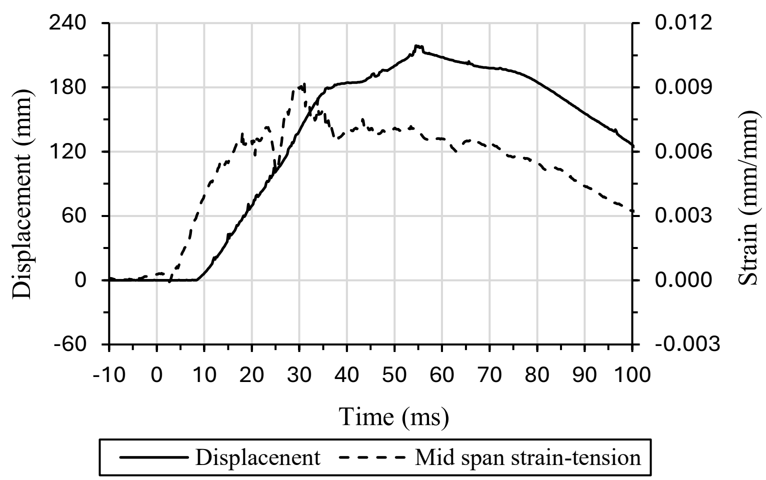

c) Displacement and strain

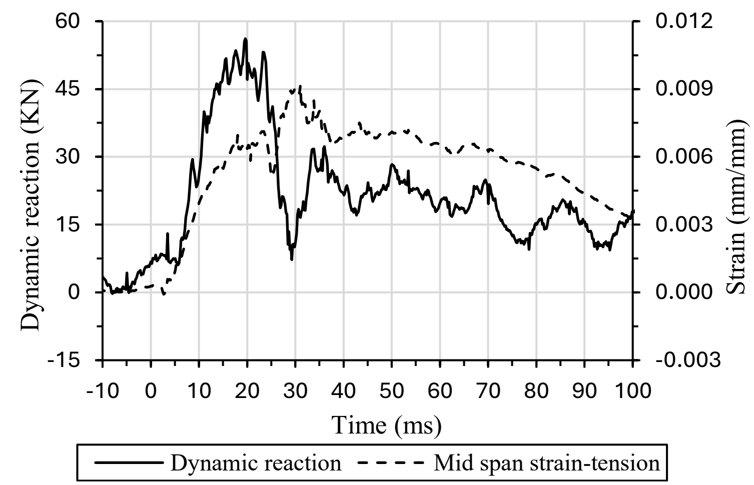

d)Dynamic reaction and strain

Figure B.2 Dynamic test results for CLT-T(0)C(0)

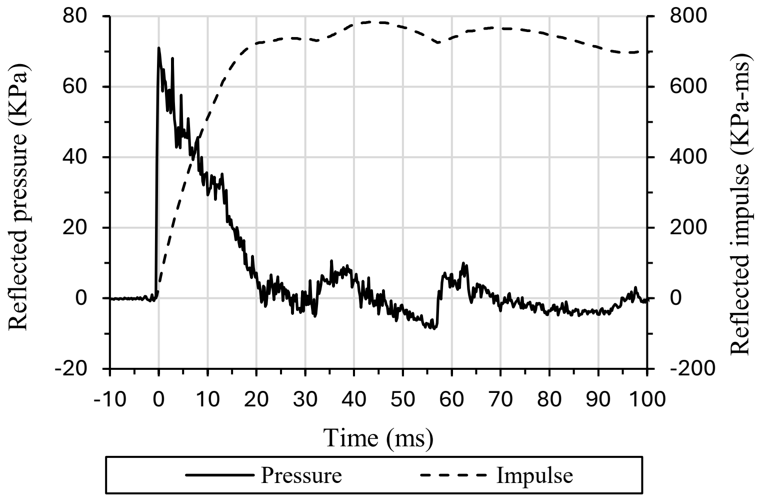

a) Pressure and impulse

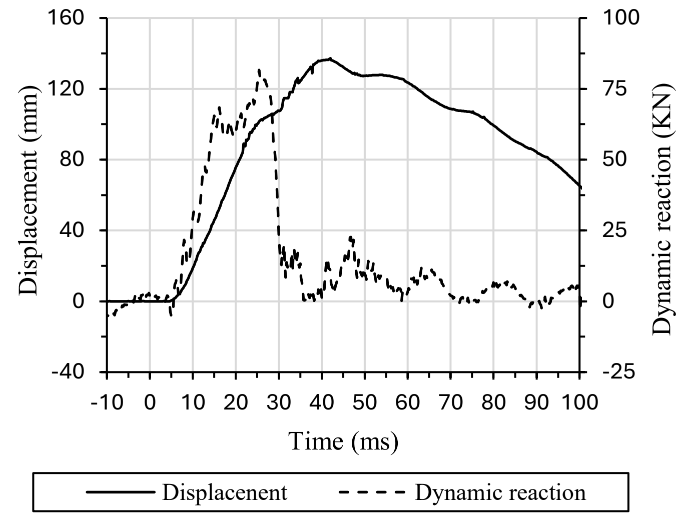

b) Displacement and reaction

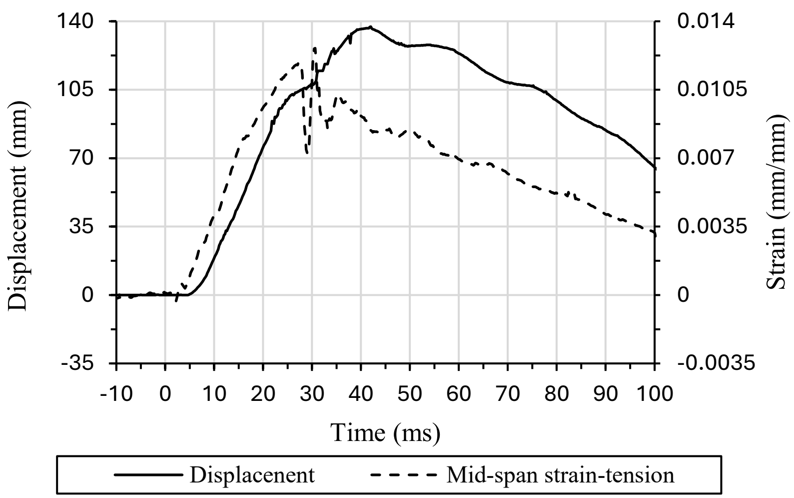

c) Displacement and strain

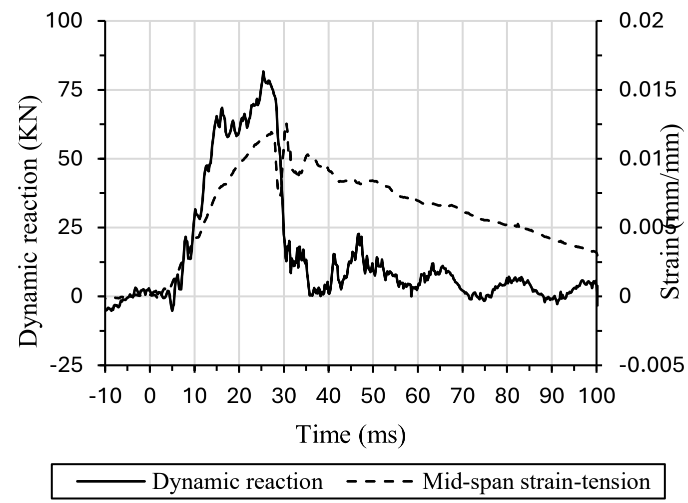

d)Dynamic reaction and strain

Figure B.3 Dynamic test results for CLT-T(0)C(±45)

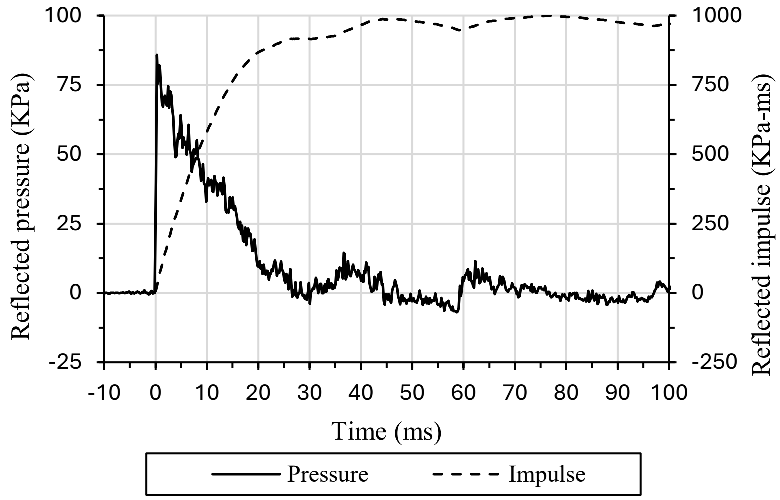

a) Pressure and impulse

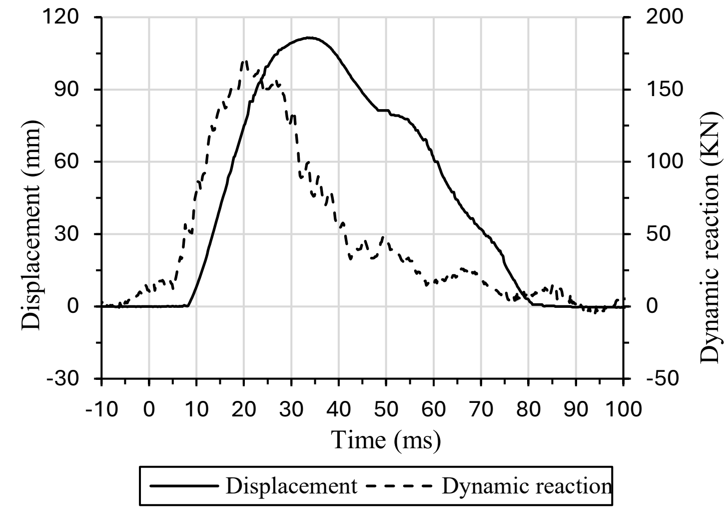

b) Displacement and reaction

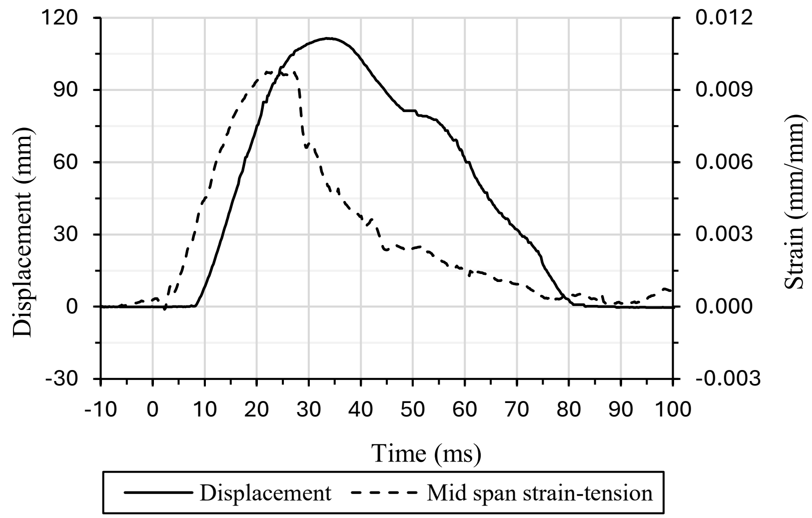

c) Displacement and strain

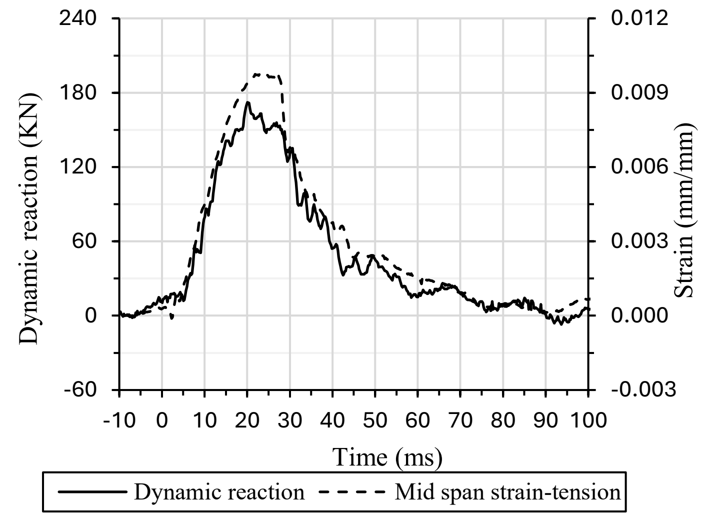

d)Dynamic reaction and strain

Figure B.4 Dynamic test results of CLT-T$(0)_2$C(±45)

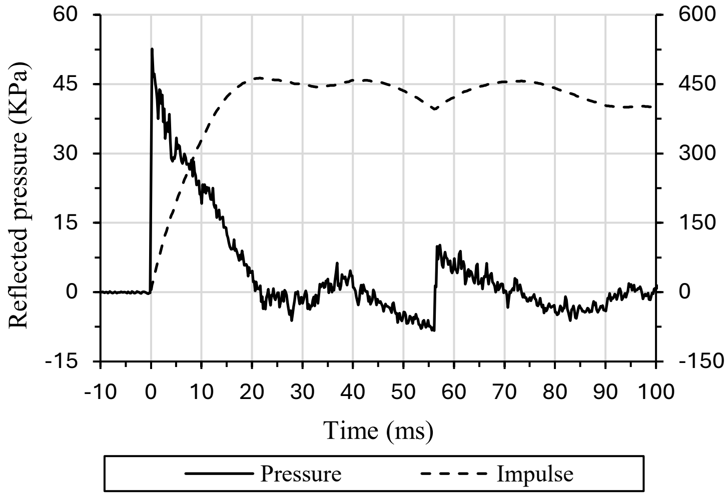

a) Pressure and impulse

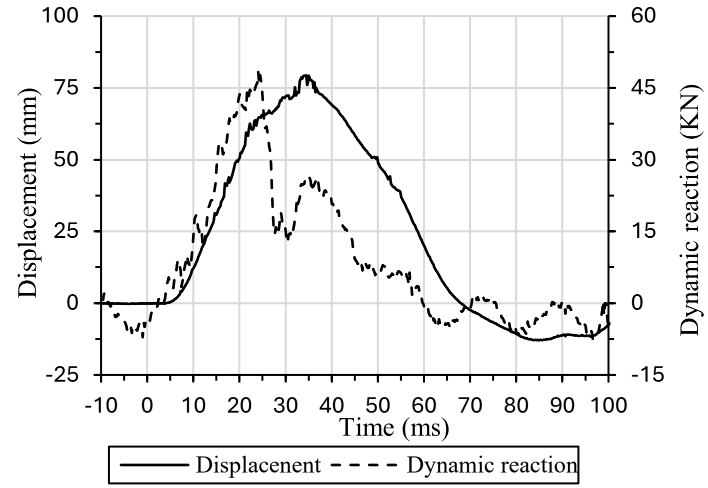

b) Displacement and reaction

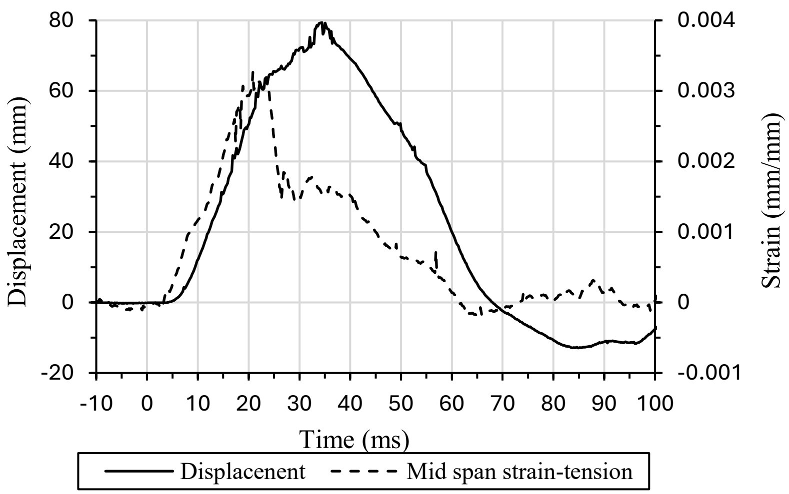

c) Displacement and strain

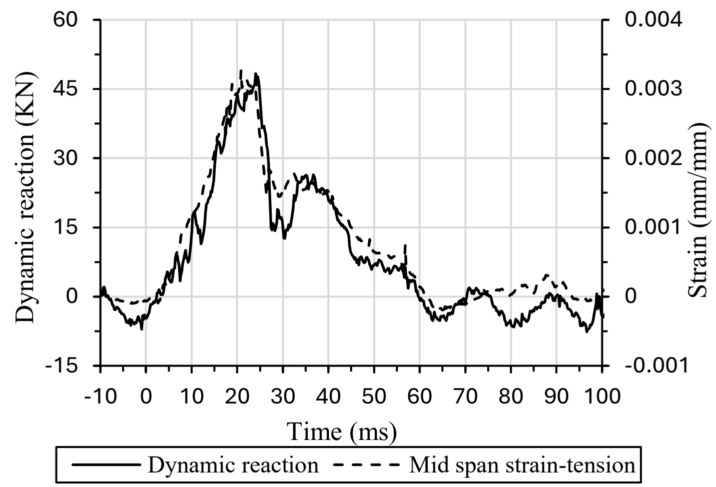

d)Dynamic reaction and strain

Figure B.5 Dynamic test results of CLT-T(0)U(±45)

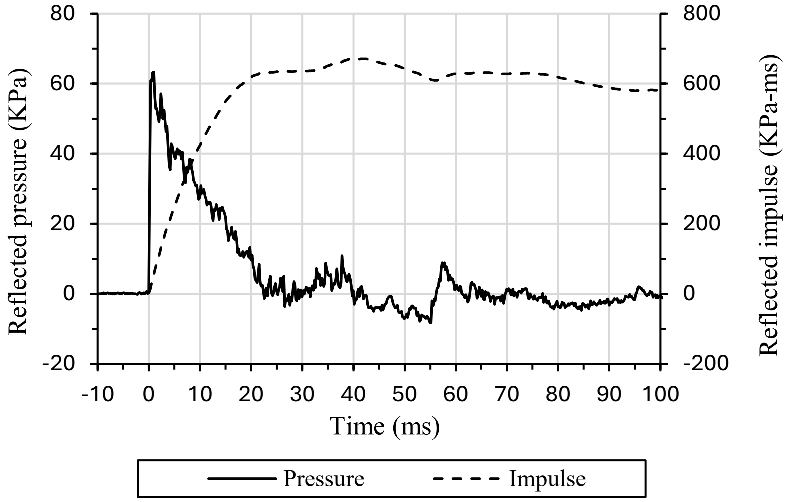

a) Pressure and impulse

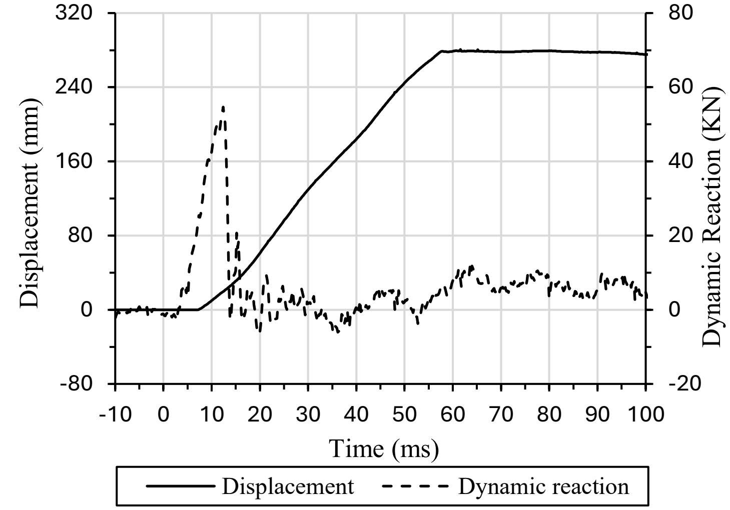

b) Displacement and reaction

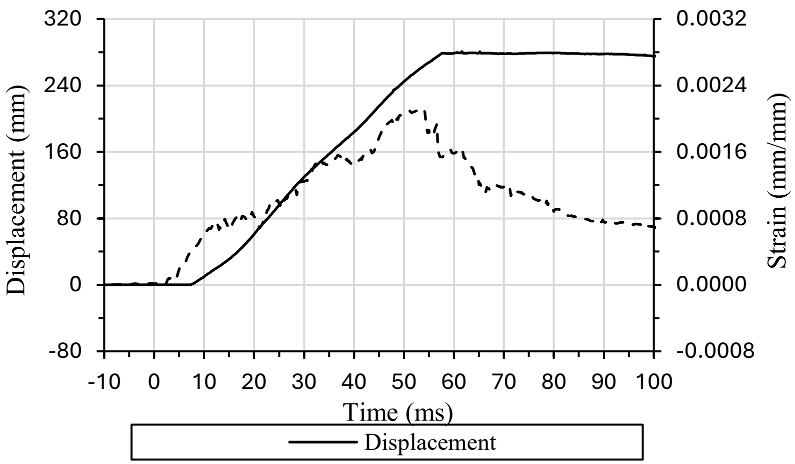

c) Displacement and strain

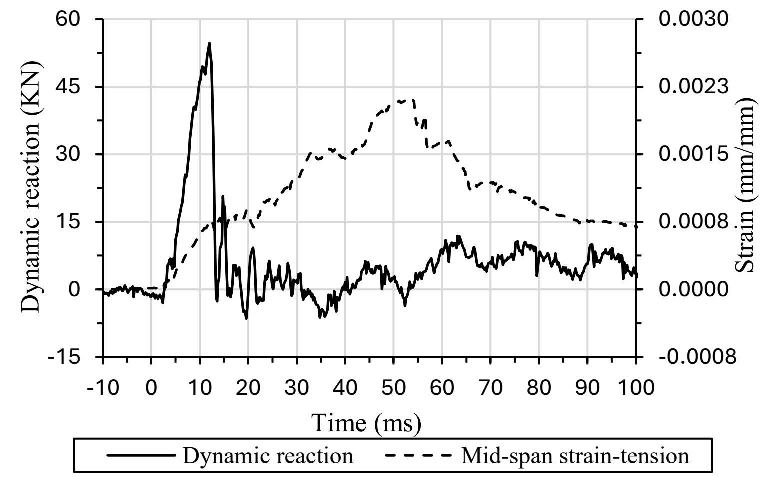

d)Dynamic reaction and strain

Figure B.6 Dynamic test results of unretrofitted glulam

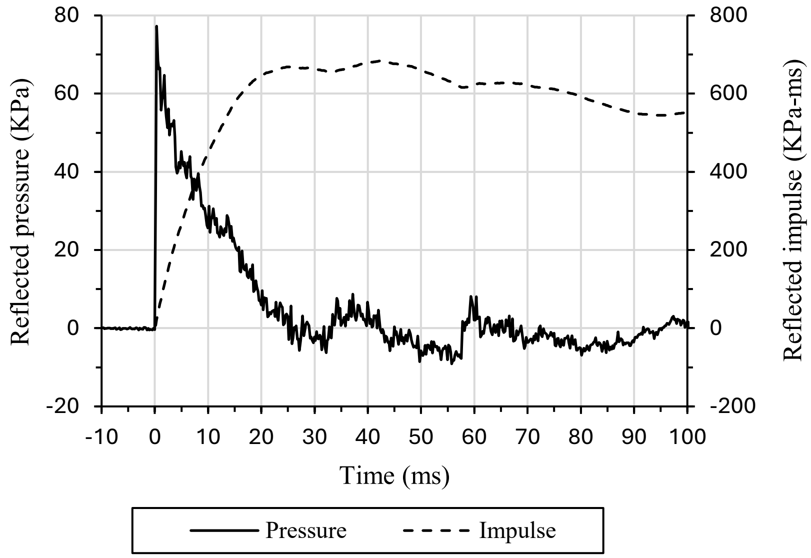

a) Pressure and impulse

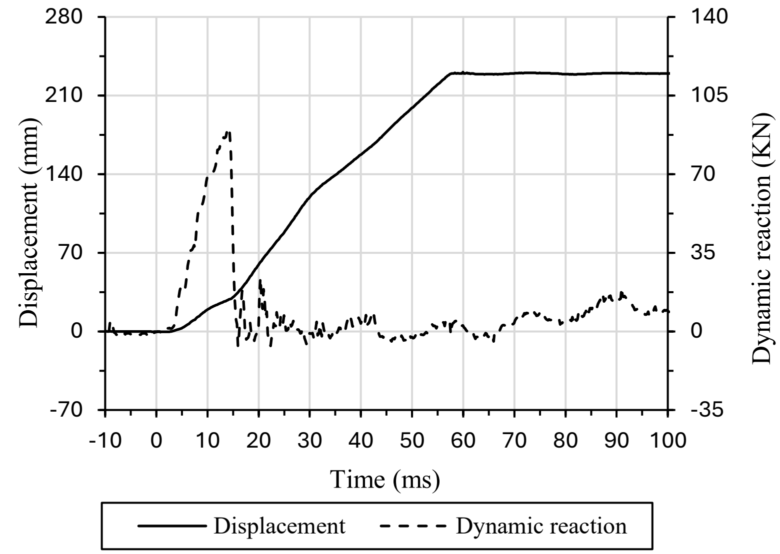

b) Displacement and reaction

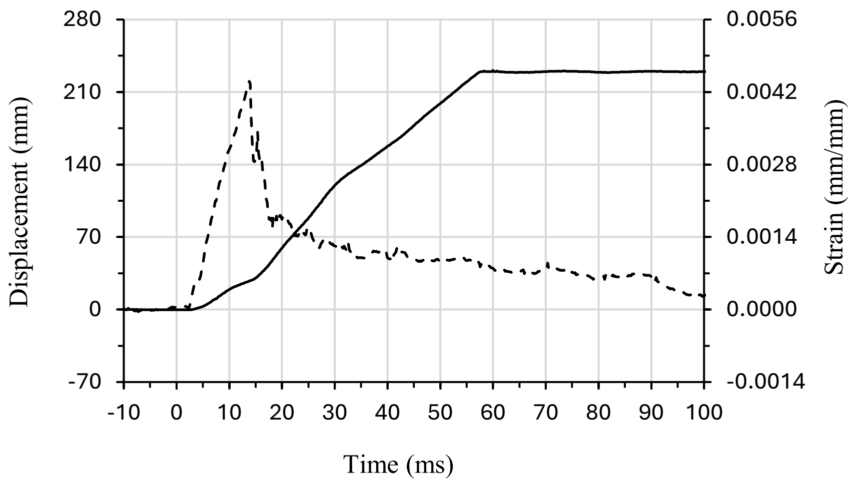

c) Displacement and strain

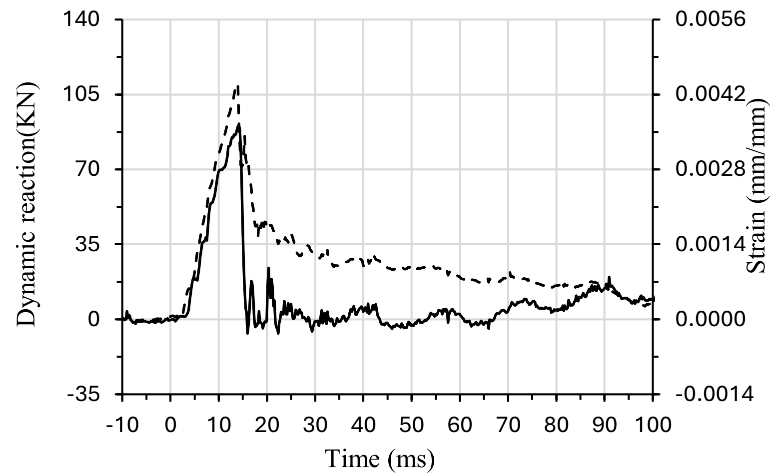

d) Dynamic reaction and strain

Figure B.7 Dynamic test results of G-T(0)C(0)

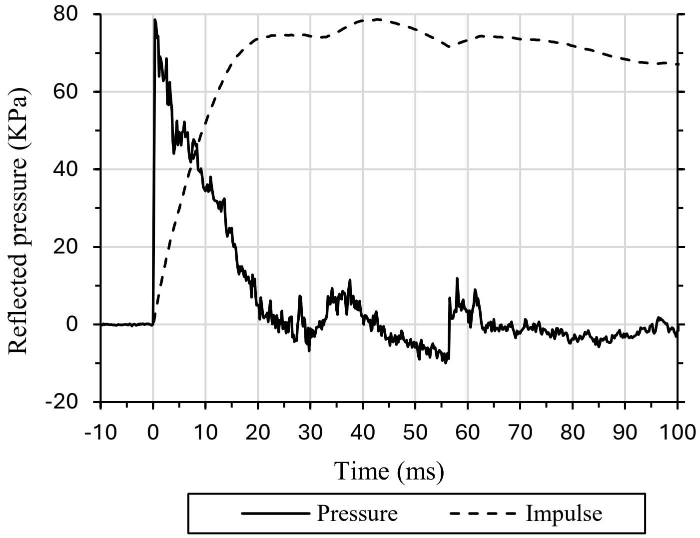

a) Pressure and impulse

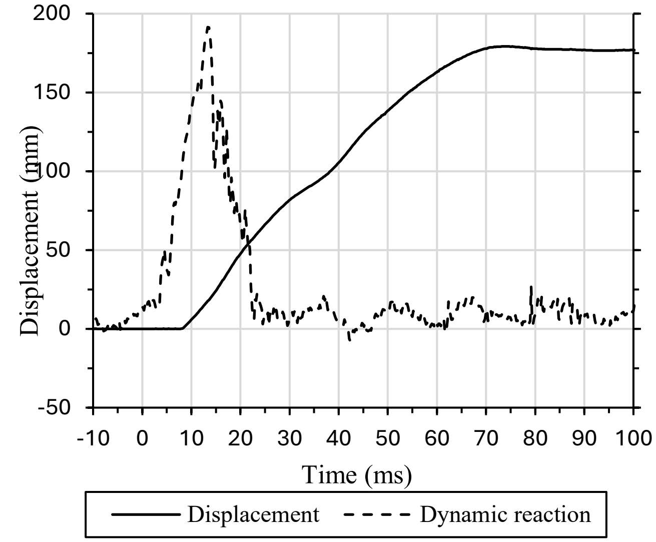

b) Displacement and reaction

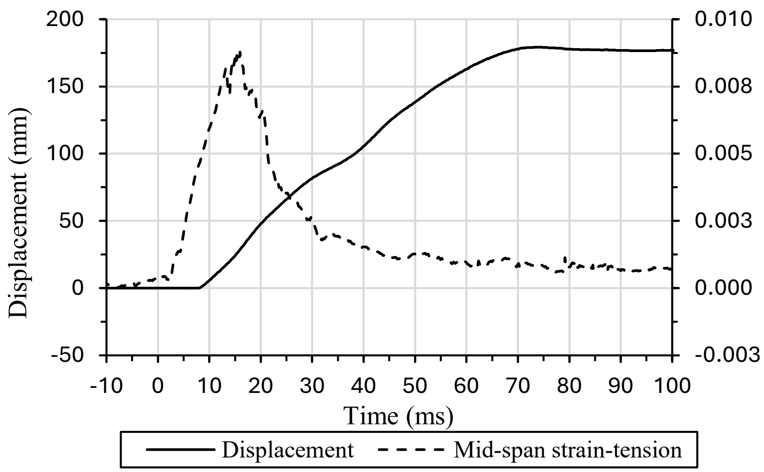

c) Displacement and strain

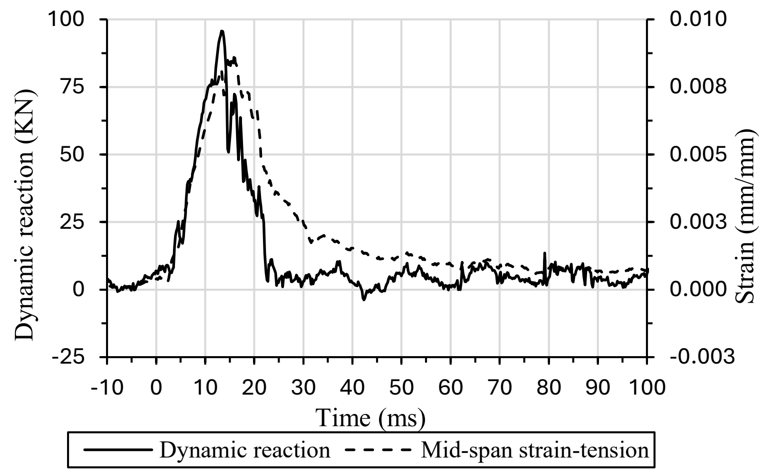

d) Dynamic reaction and strain

Figure B.8 Dynamic test results of G-T(0)C(±45)

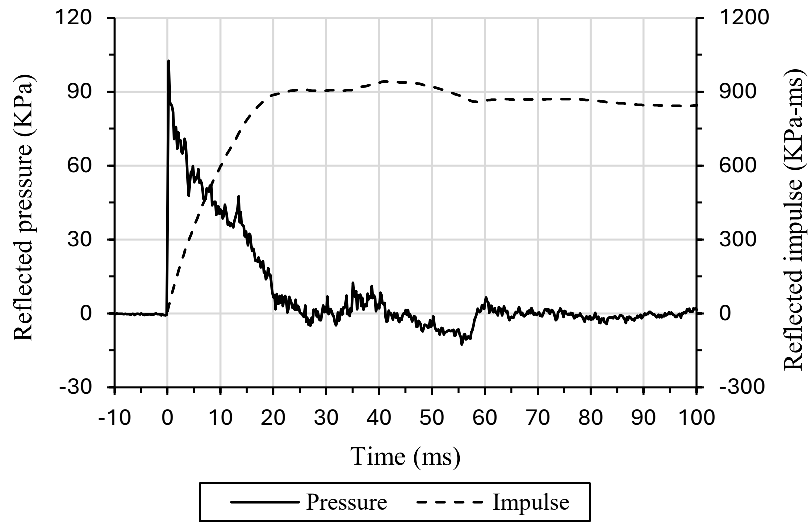

a) Pressure and impulse

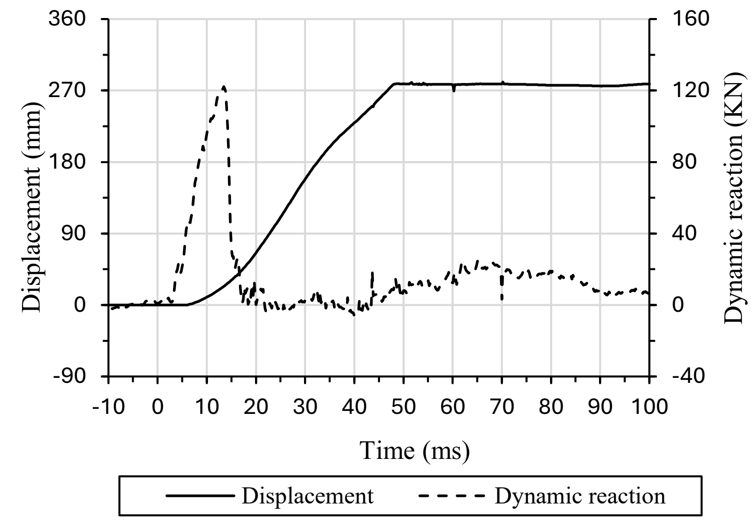

b) Displacement and reaction

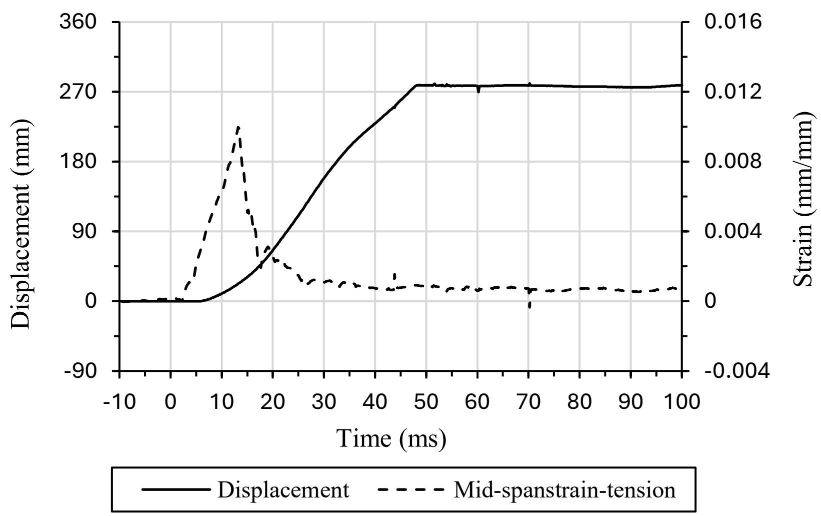

c) Displacement and strain

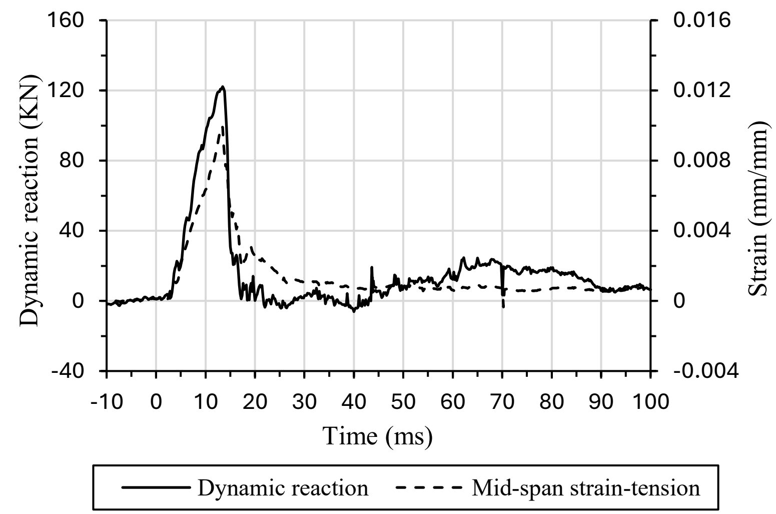

d) Dynamic reaction and strain

Figure B.9 Dynamic test results of G-T$(0)_2$C(±45)

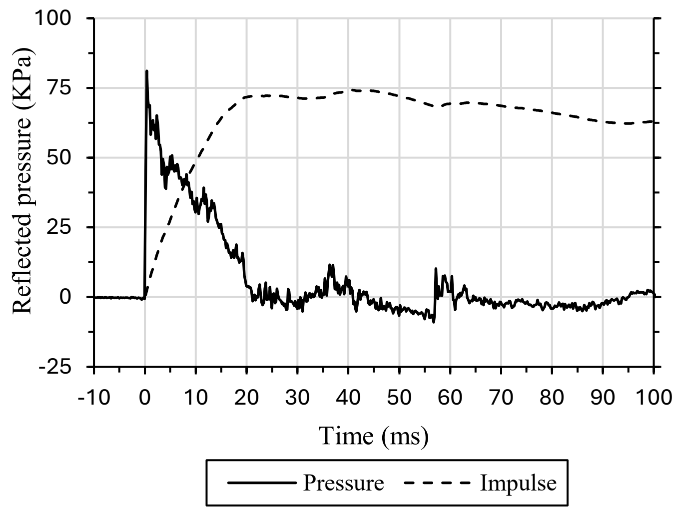

a) Pressure and impulse

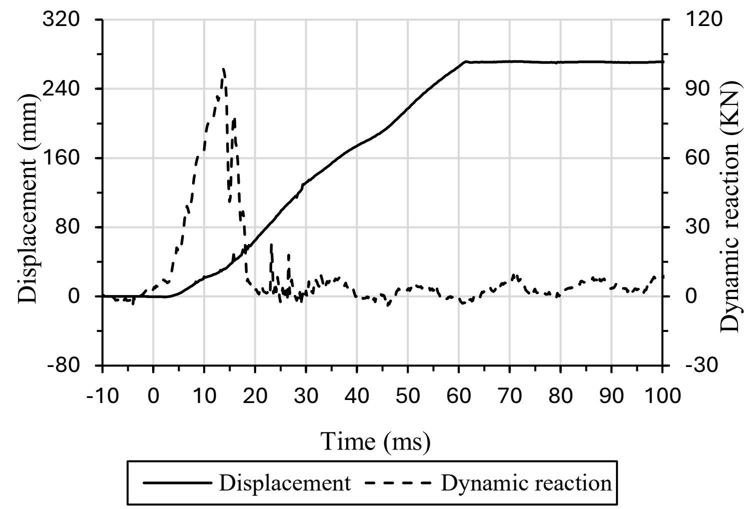

b) Displacement and reaction

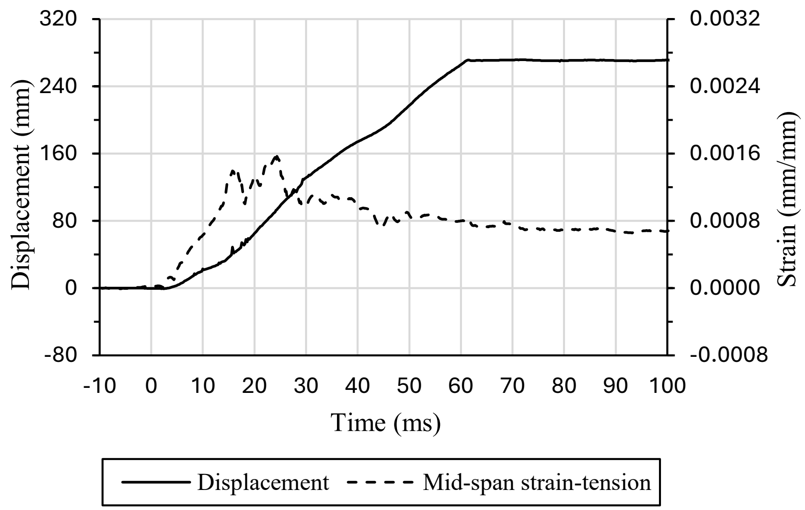

c) Displacement and strain

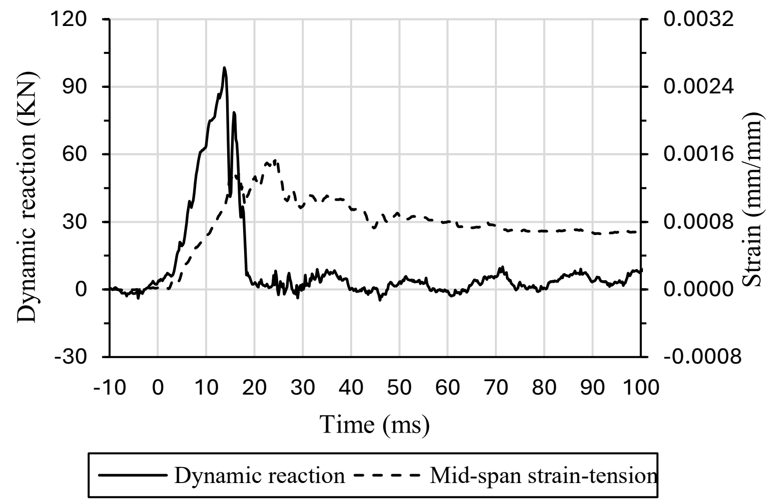

d) Dynamic reaction and strain

Figure B.10 Dynamic test results of G-T(0)U(±45)

Unretrofitted CLT CLT-T(0)C(0) (c) CLT-T(0)U(±45)

Figure B.11 Dynamic failure mode of unretrofitted CLT, CLT-T(0)C(0) and CLT-T(0)U(±45)

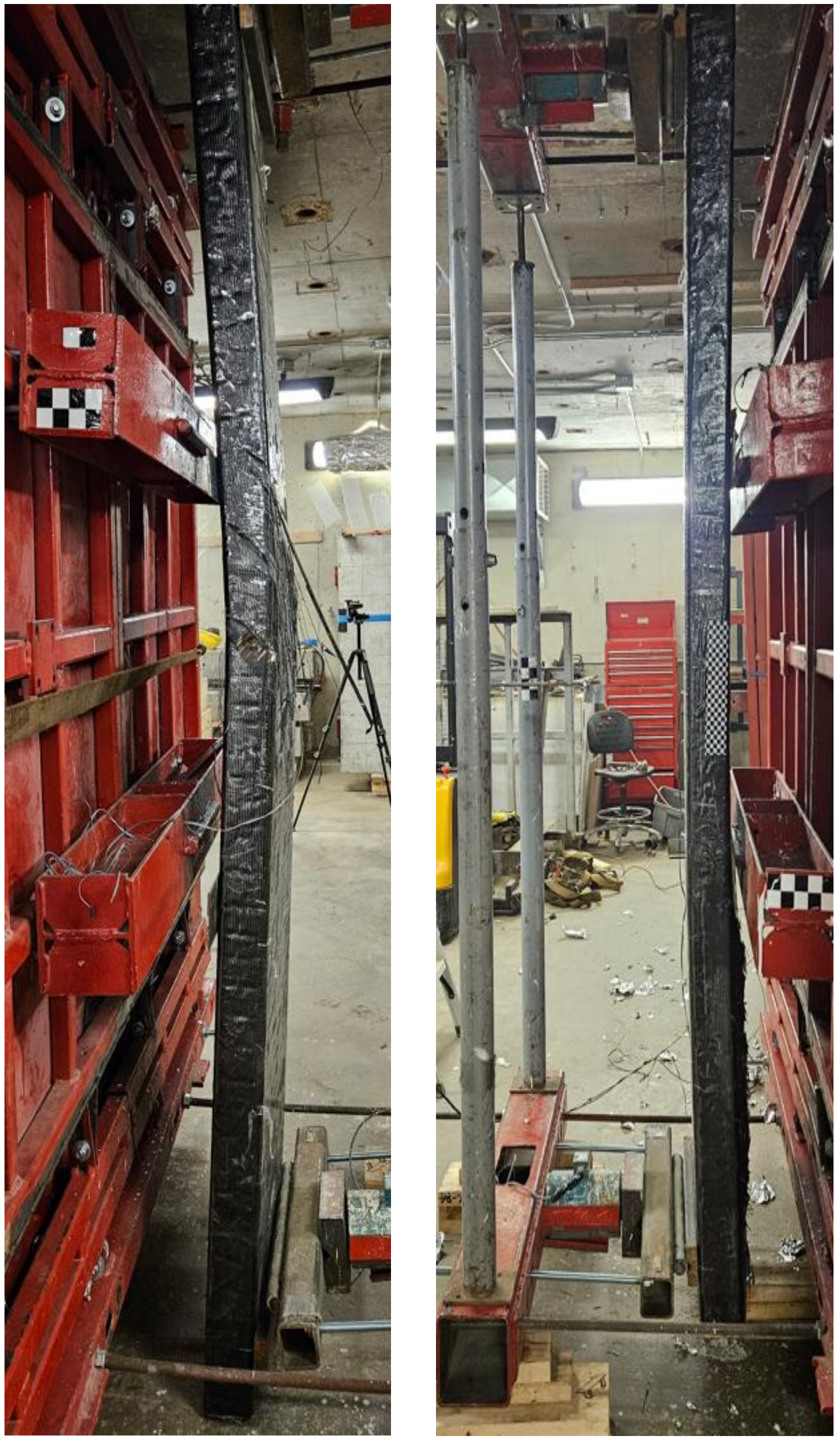

(a) CLT-T(0)C(±45) (b) CLT-T$(0)_2$C(±45)

Figure B.12 Dynamic failure mode of CCLT(0)C(±45) and CLT-T$(0)_2$C(±45)

(a) Unretrofitted glulam (b) G-T(0)C(0) (c) G-T(0)U(±45)

Figure B.13 Dynamic failure mode of unretrofitted glulam, G-T(0)C(0), and G-T(0)U(±45)

(a) G-T(0)C(±45)

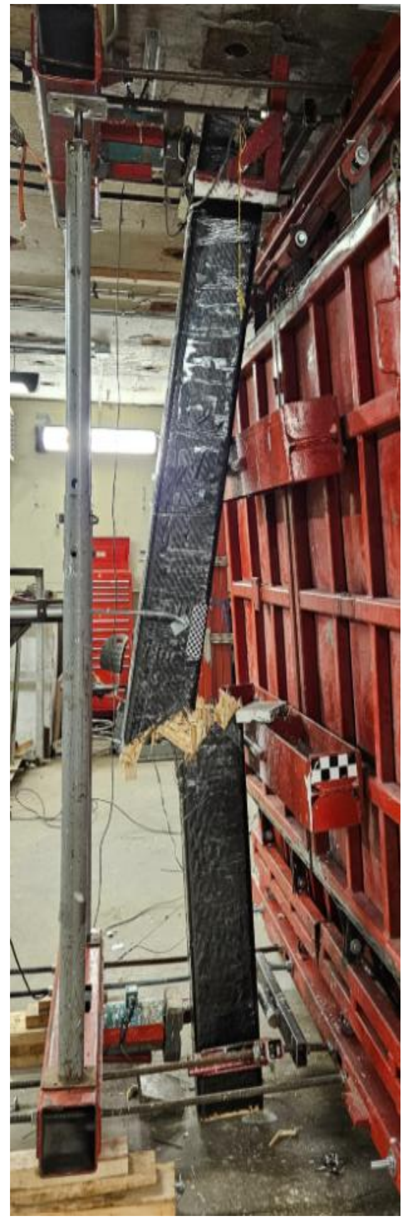

(b) G-T$(0)_2$C(±45)

Figure B.14 Dynamic failure mode of G-T(0)C(±45) and G-T$(0)_2$C(±45)

Appendix CAnalytical test results

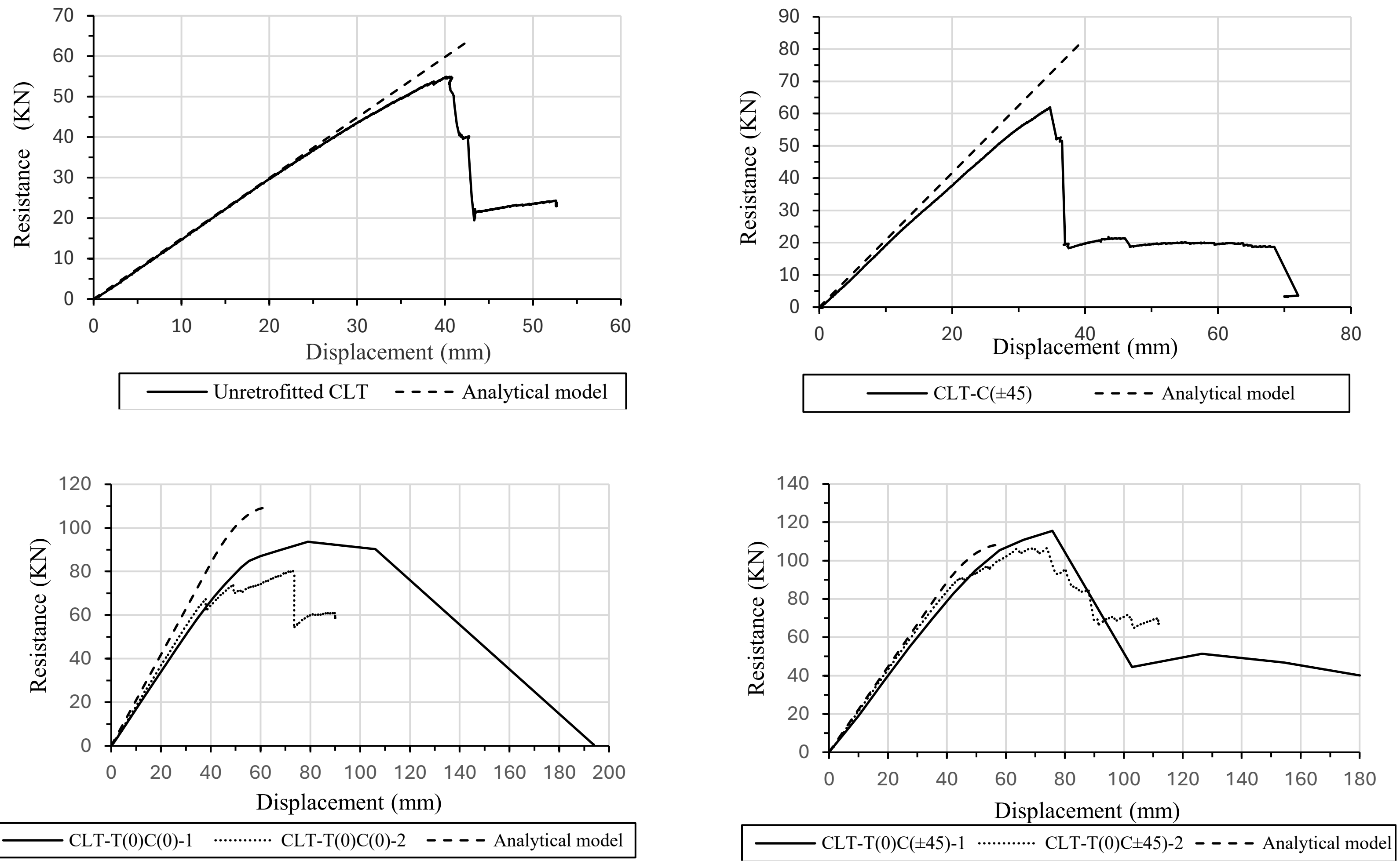

Figure C.1Resistance-displacement analytical and experimental static curve of unretrofitted CLT, CLT-C(±45), CLT-T(0)C(0) and CLT-T(0)C(±45)

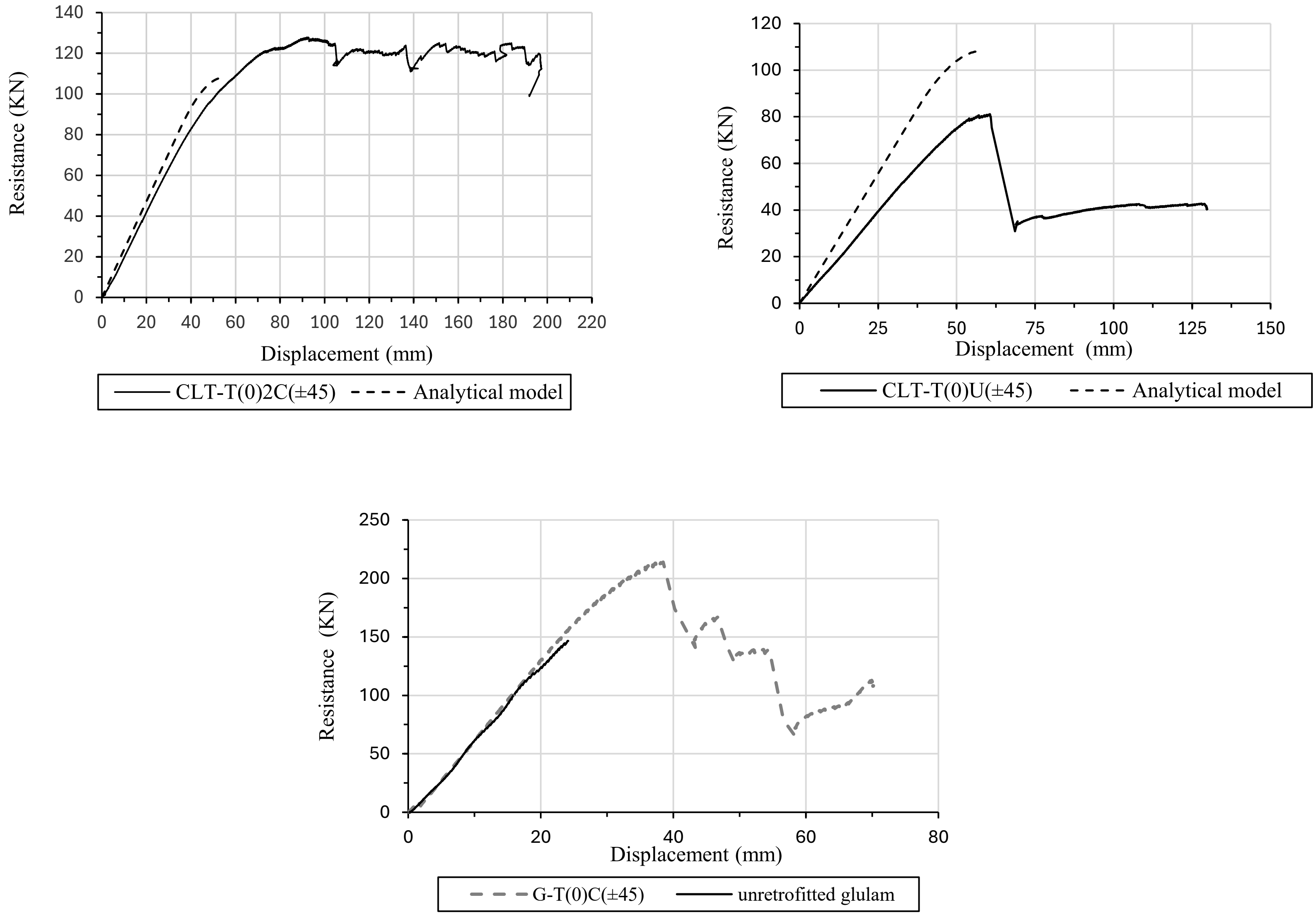

Figure C.2 Resistance-displacement analytical and experimental static curve of unretrofitted CLT, CLT-T(0)$_2$C(±45), CLT-T(0)U(±45), and unretrofitted glulam

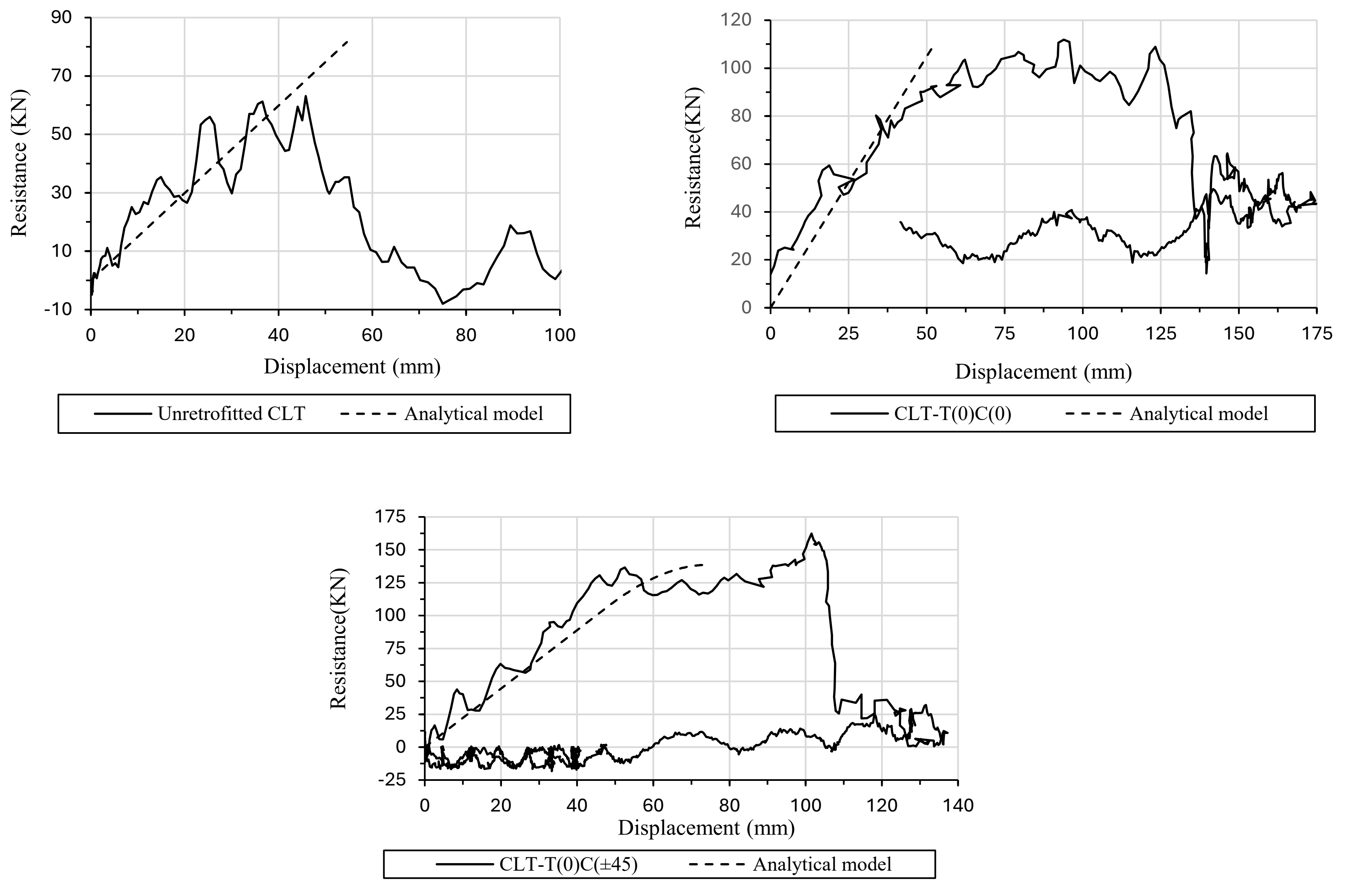

Figure C.3 Resistance-displacement analytical and experimental dynamic curve of unretrofitted CLT, CLT-T(0)C(0), and CLT-T(0)C(±45)

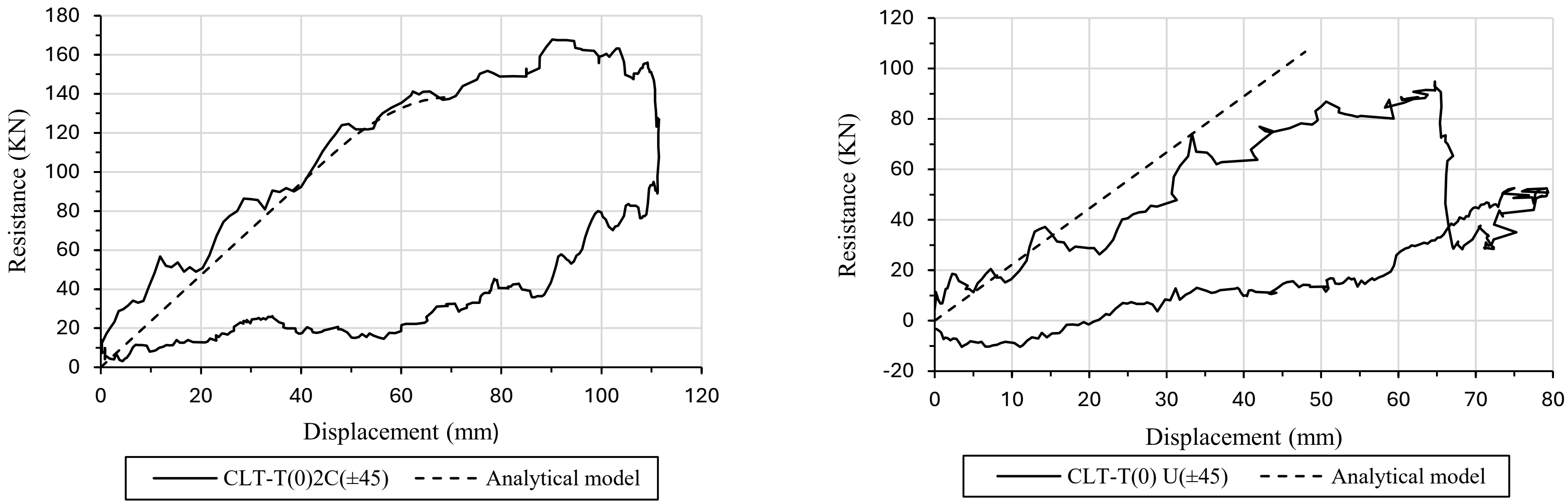

Figure C.4 Resistance-displacement analytical and experimental dynamic curve of CLT-T(0)$_2$C(±45) and CLT-T(0)U(±45)

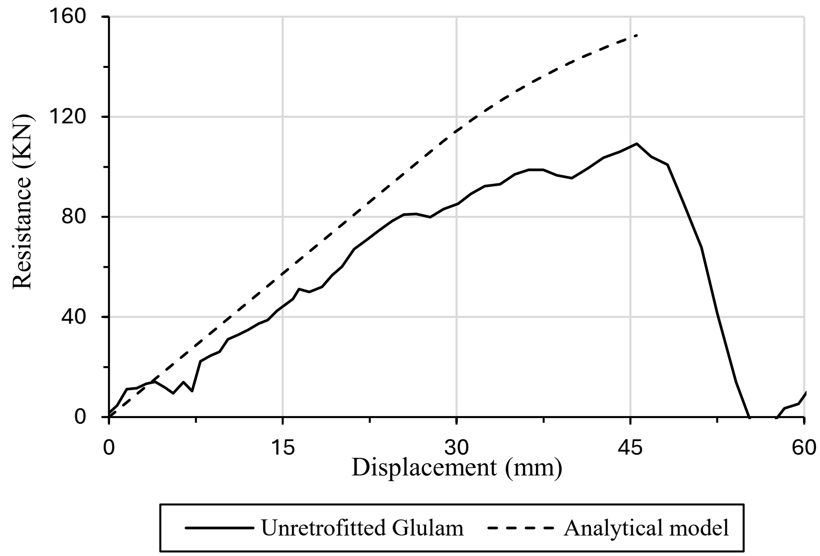

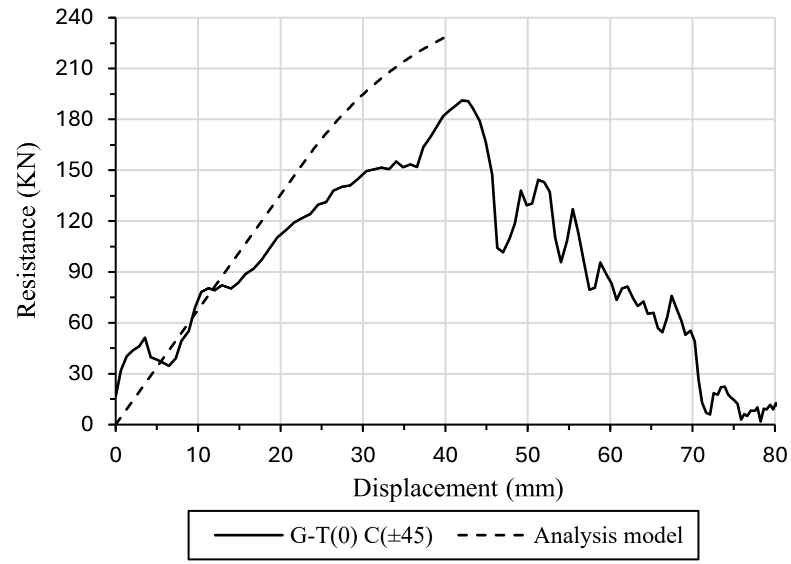

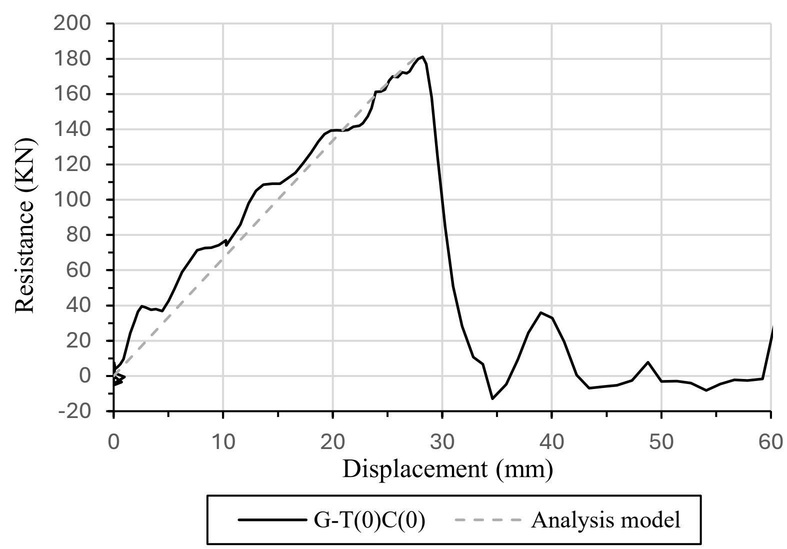

Figure C.5 Resistance-displacemnet analytical and experimental dynamic curve of unretrofitted glulam, G-T(0)C(±45), and G-T(0)C(±45)

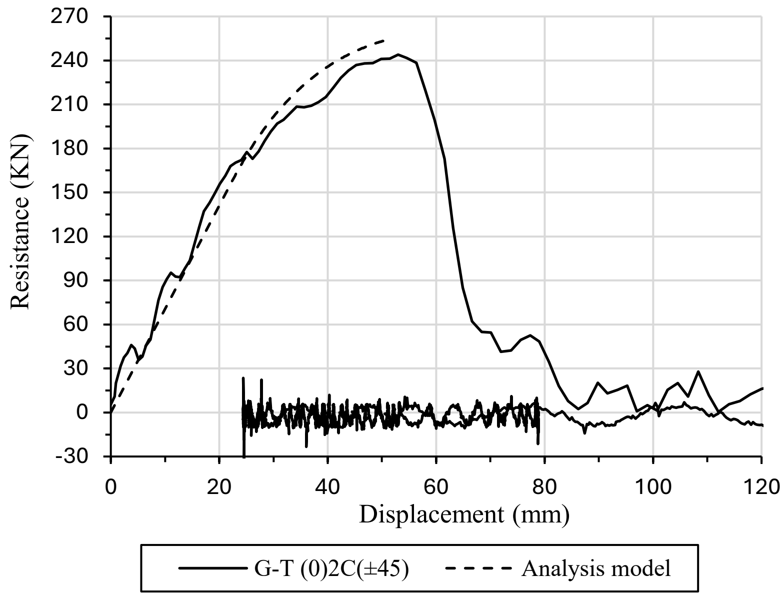

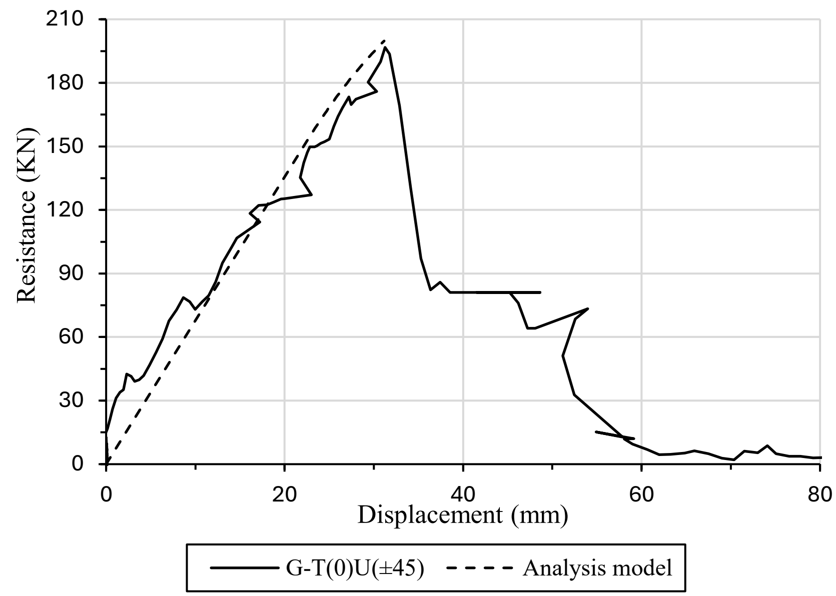

Figure C.6 Resistance-displacement analytical and experimental dynamic curve of G-T(0)$_2$C(±45) and G-T())U(±45)

Unretrofitted CLT: System mass: 344 kg

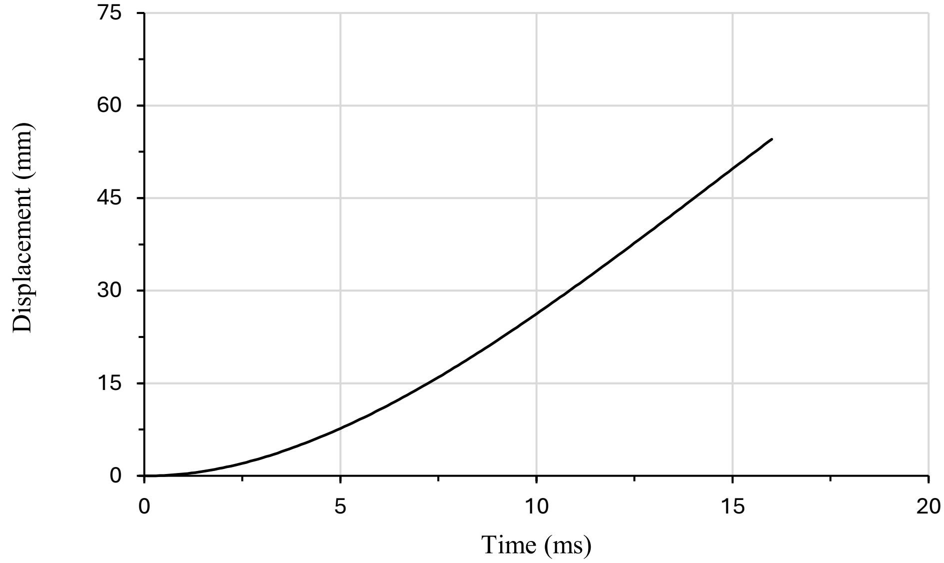

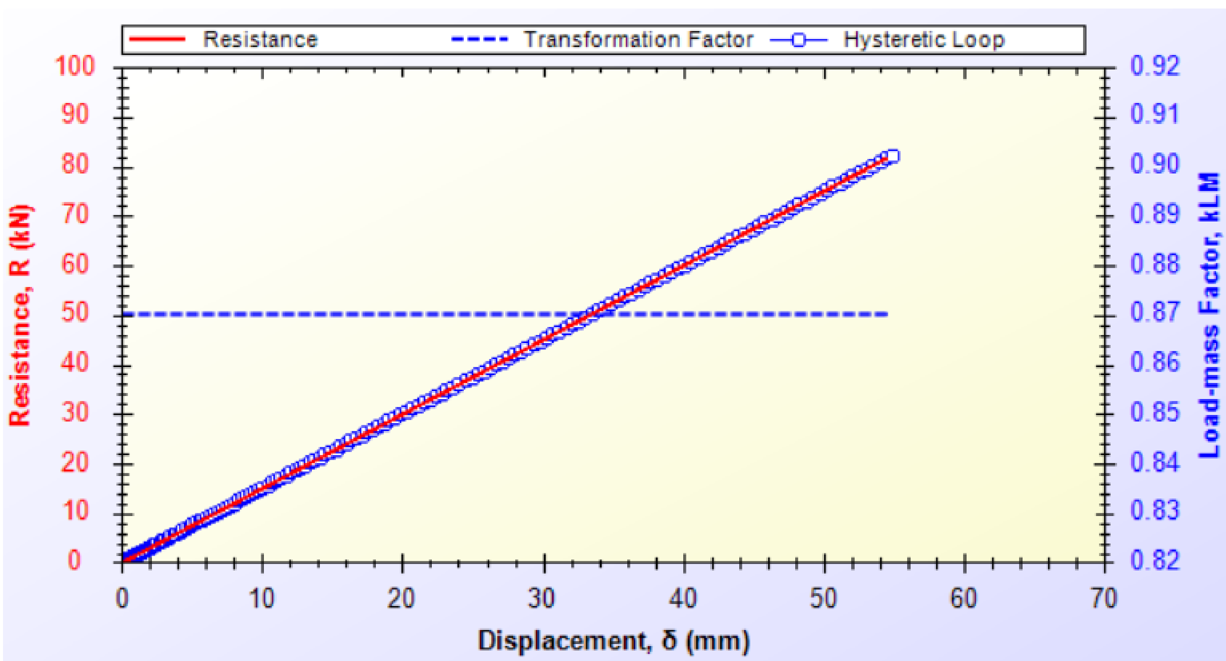

Figure C.7 Resistance and displacement time history for SDOF unretrofitted CLT

CLT-T(0)C(0): System mass 346.36 Kg

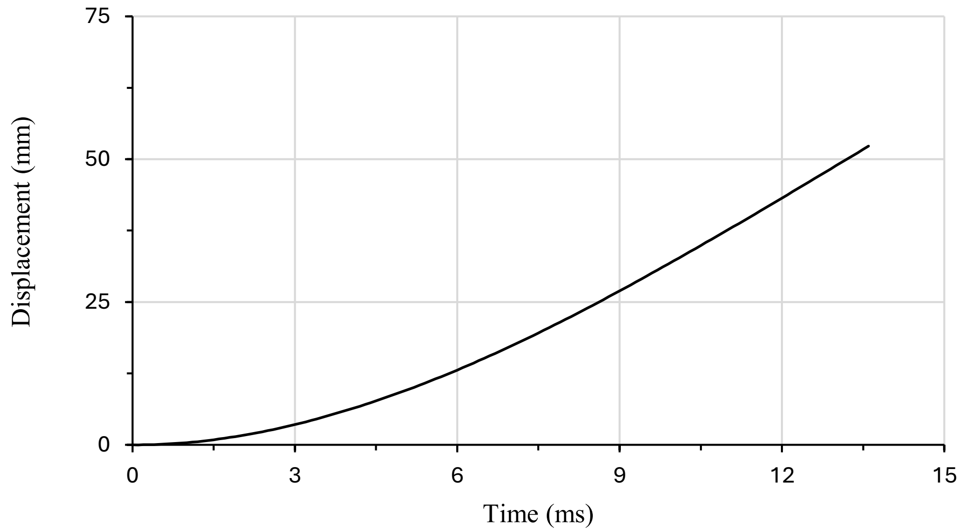

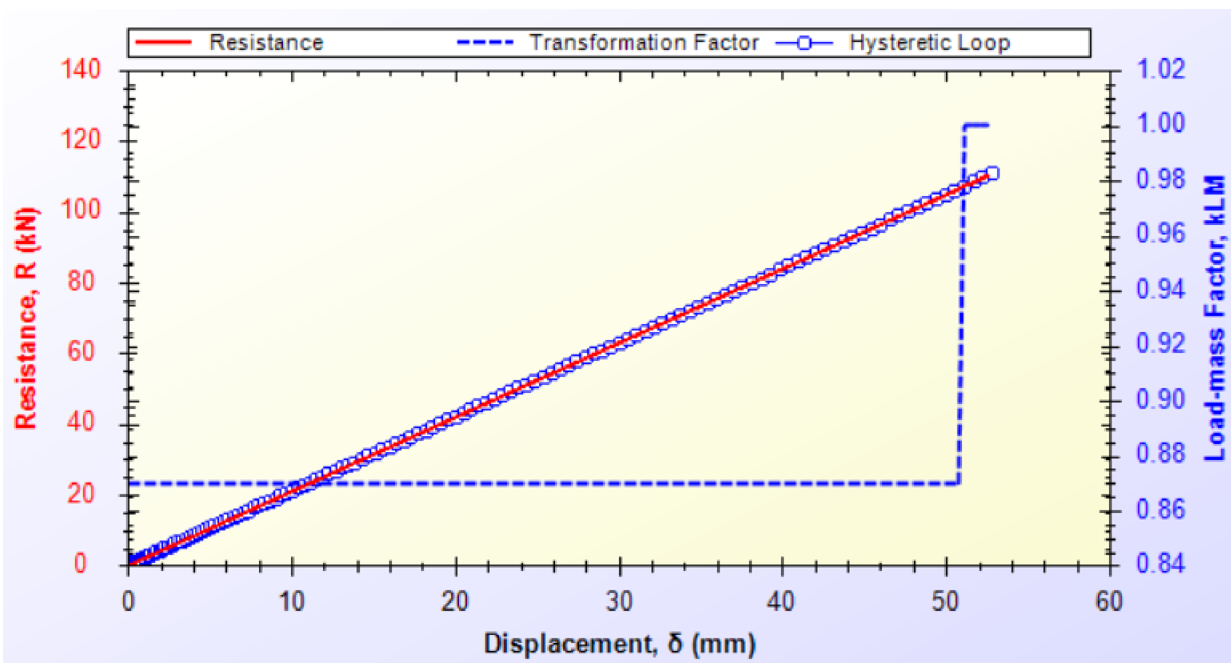

Figure C.8 Resistance and displacement time history for SDOF CLT-T(0)C(0)

CLT-T(0)C(±45): System mass 346.76 Kg

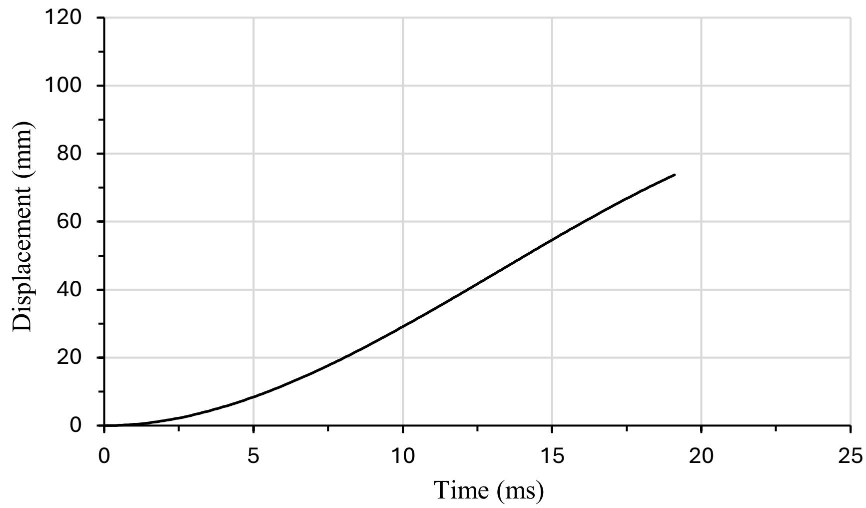

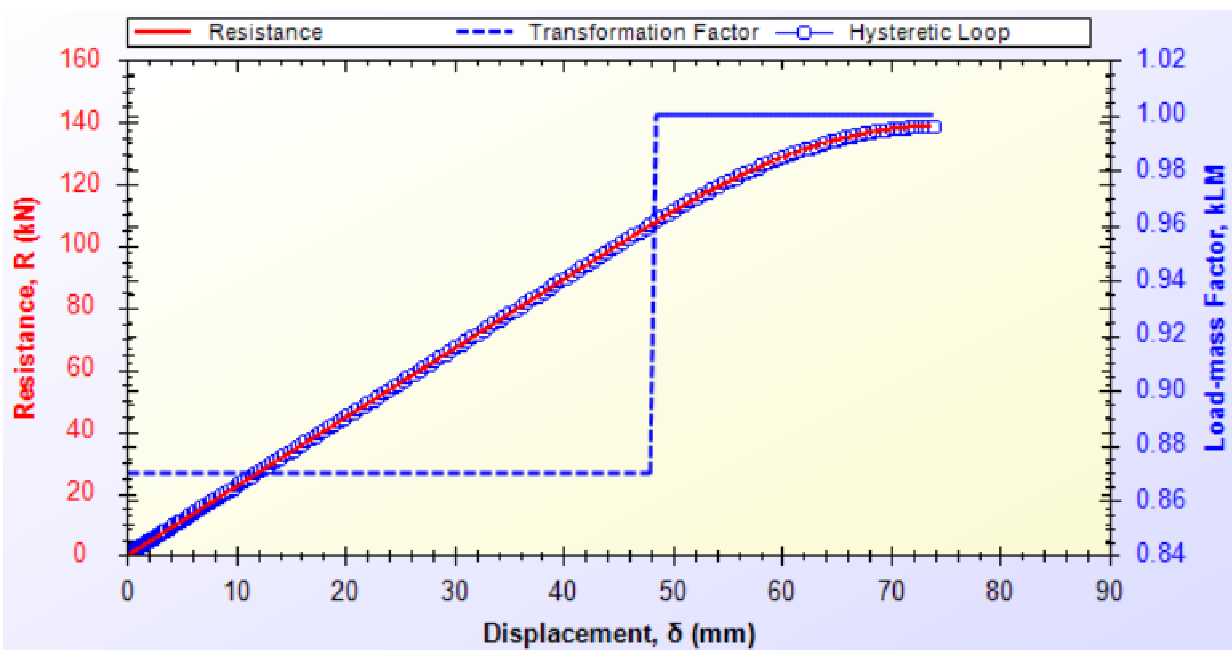

Figure C.9 Resistance and displacement time history for SDOF CLT-T(0)C(±45)

CLT-T(0)$_2$C(±45): System mass 347.66 Kg

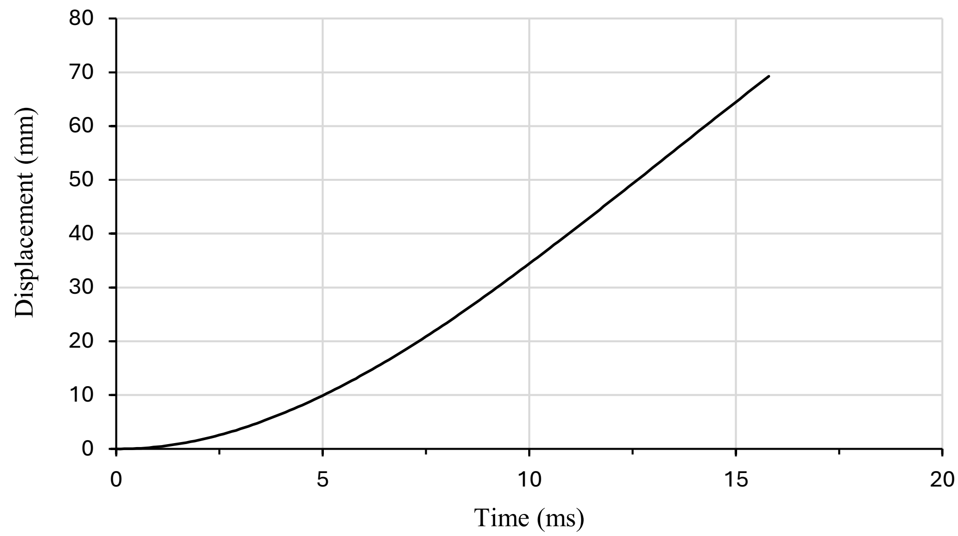

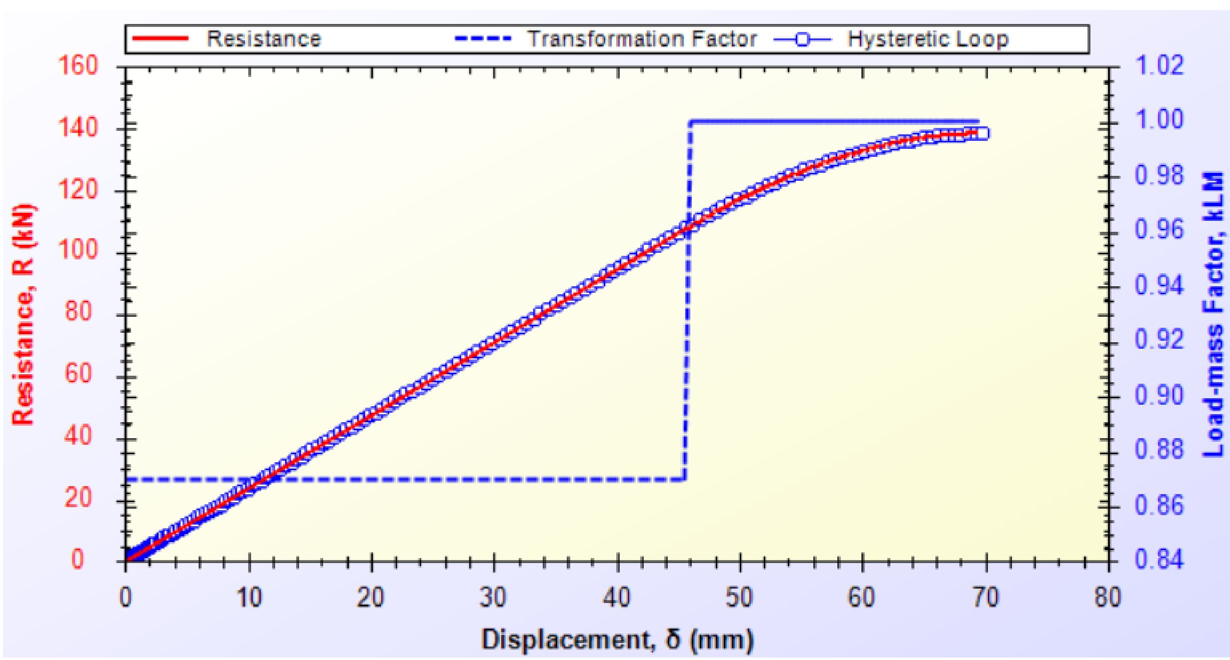

Figure C.10 Resistance and displacement time history for SDOF CLT-T(0)$_2$C(±45)

CLT-T (0) U (±45): System mass 345 Kg

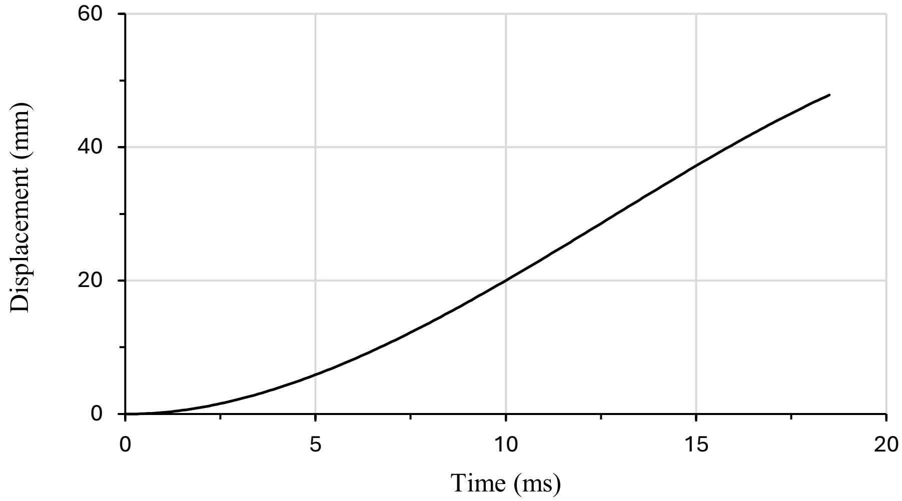

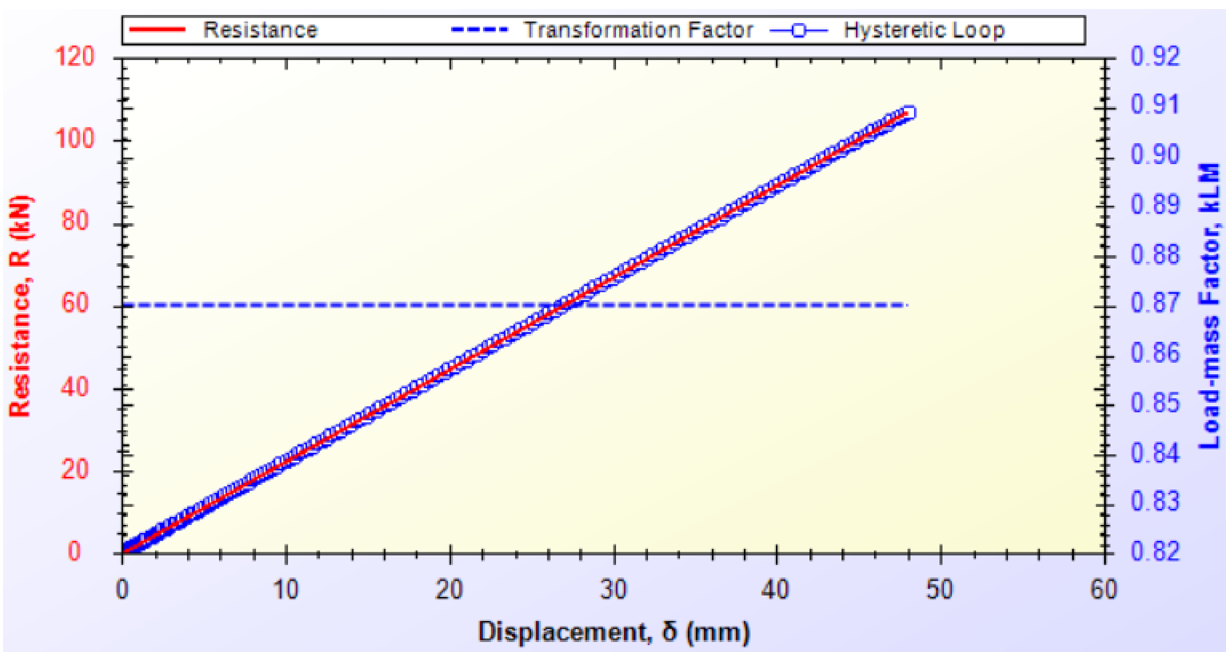

Figure C.11 Resistance and displacement time history for SDOF CLT-T(0)U(±45)

Unretrofitted Glulam: System mass: 319 kg

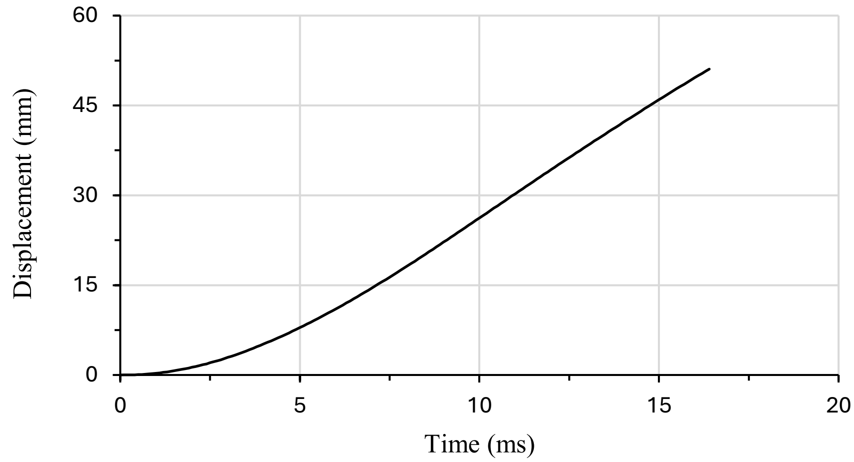

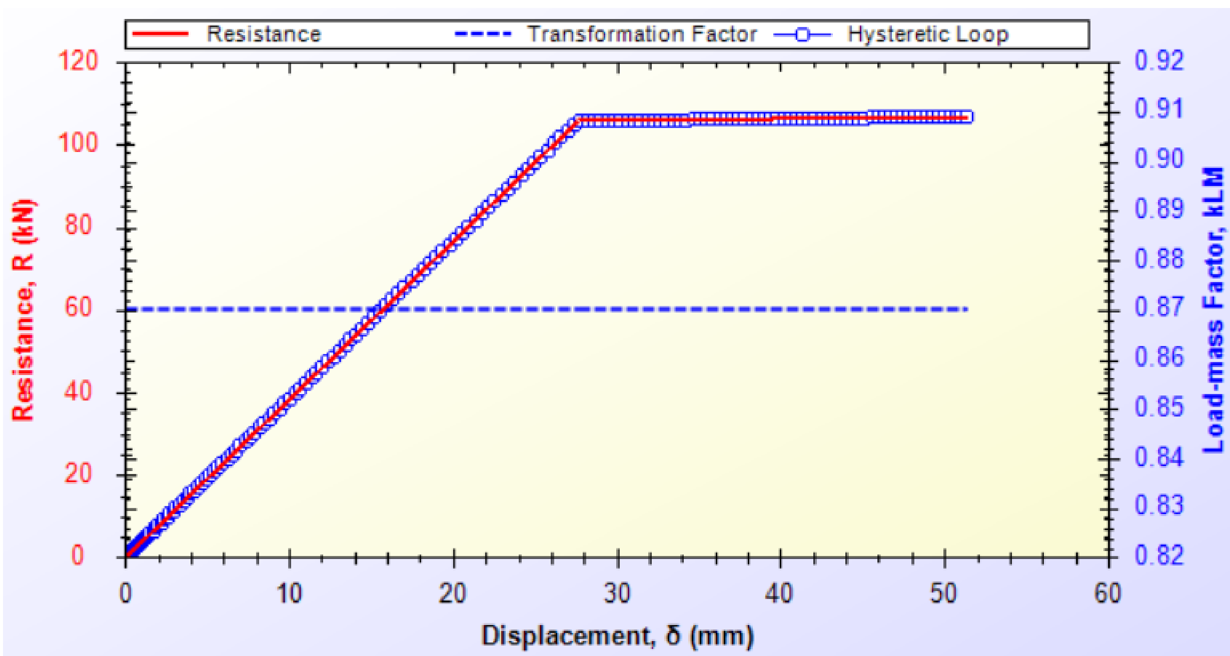

Figure C.12 Resistance and displacement time history for SDOF Glulam

G-T(0)C(0): System mass 324.66 Kg

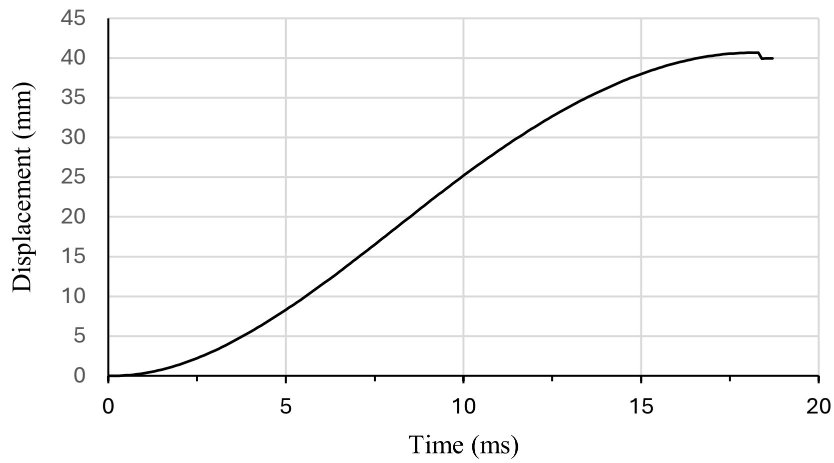

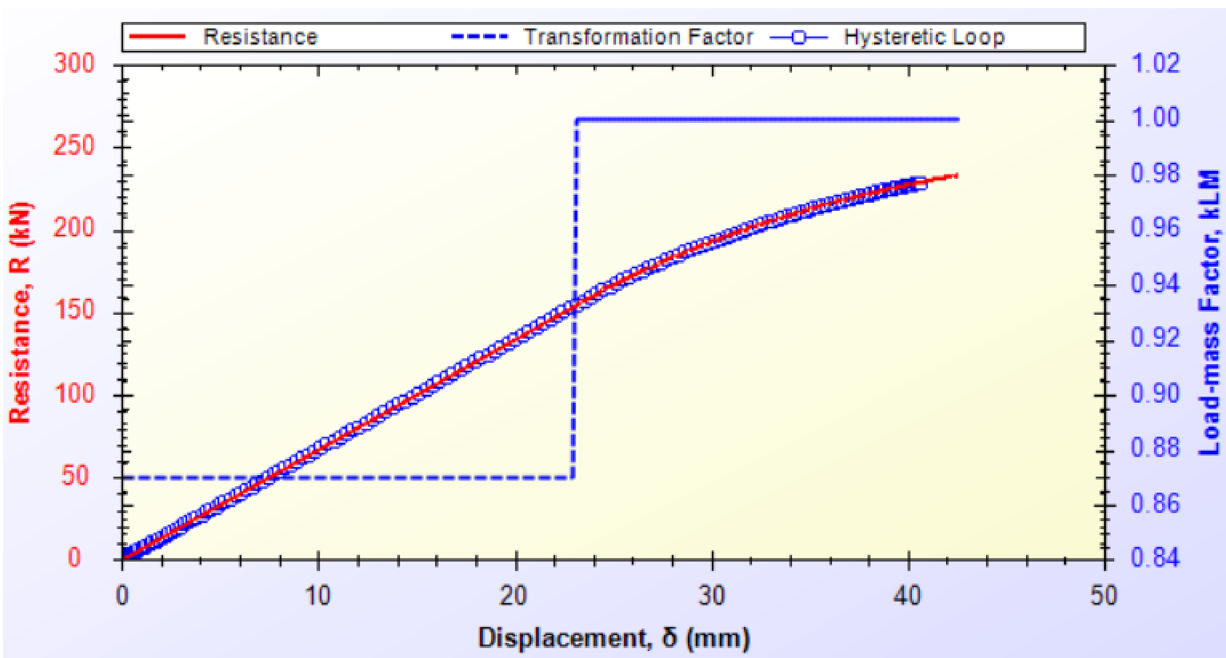

Figure C.13 Resistance-displacement time history for SDOF G-T(0)C(0)

G-T(0)C(±45): System mass 325 Kg

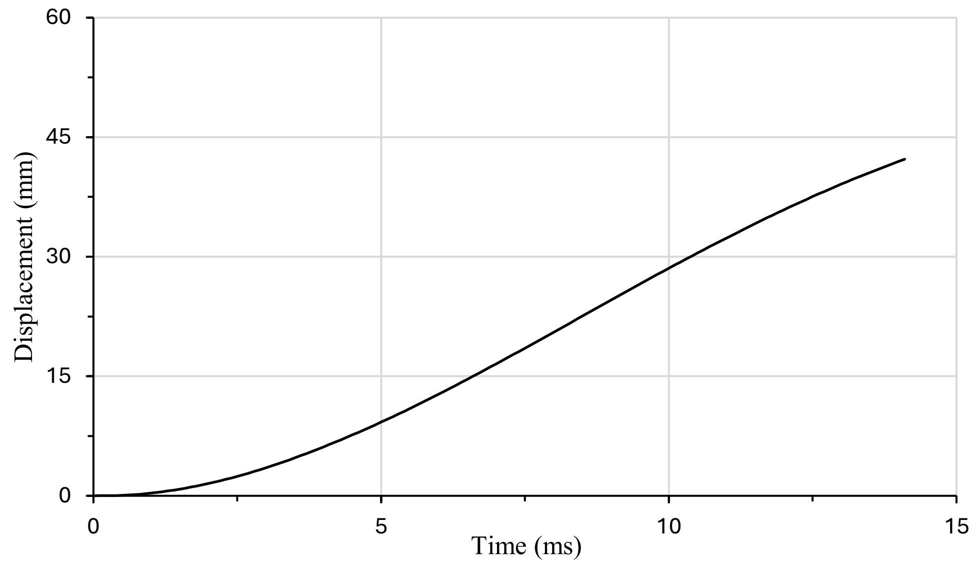

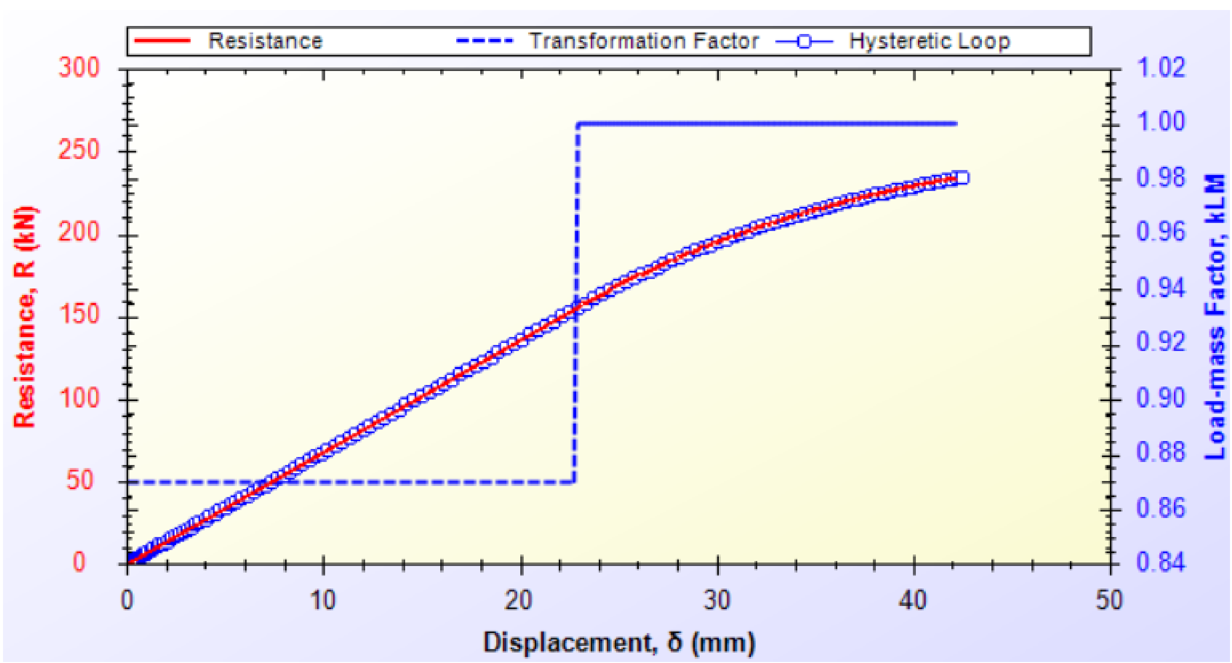

Figure C.14 Resistance and displacement time history for SDOF G-T(0)C(±45)

G-T(0)$_2$C(±45): System mass 347.66 Kg

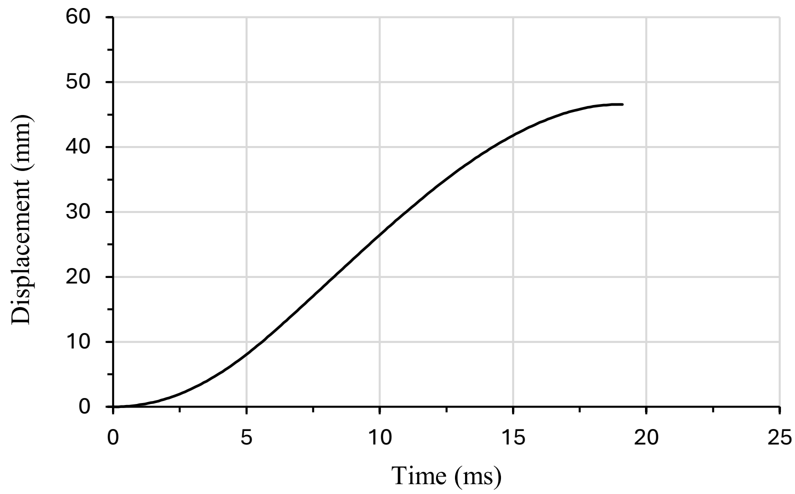

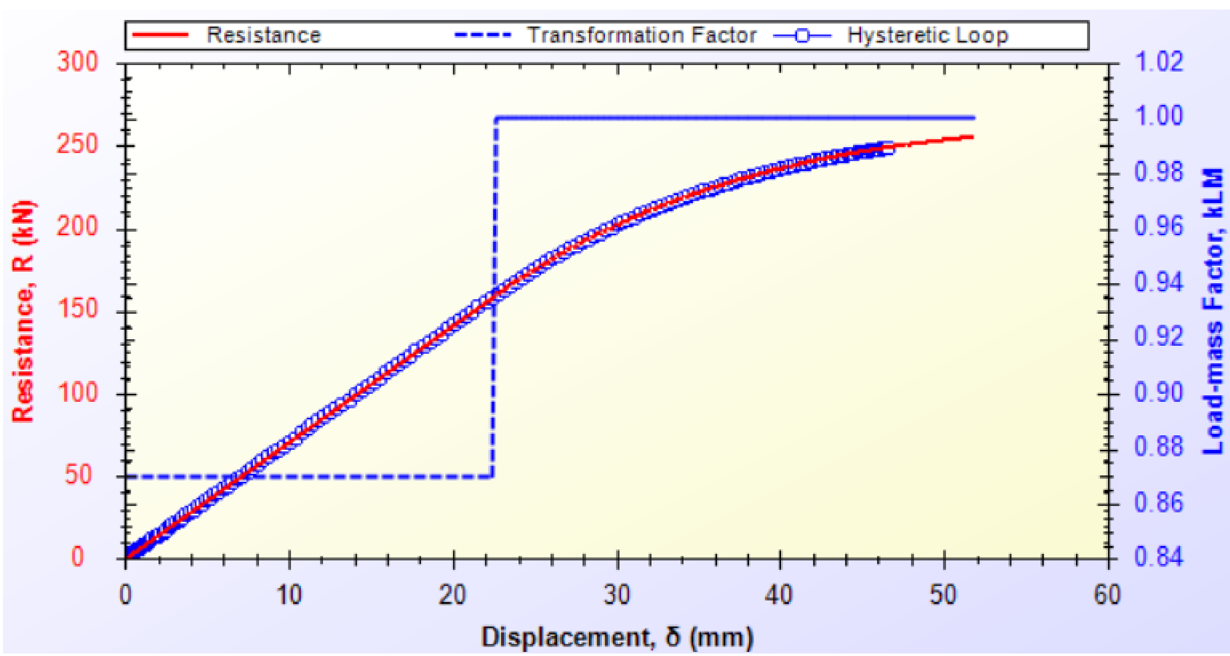

Figure C.15 Resistance displacement time history for SDOF G-T(0)2C(±45)

G-T (0) U (±45): System mass 324.72 Kg

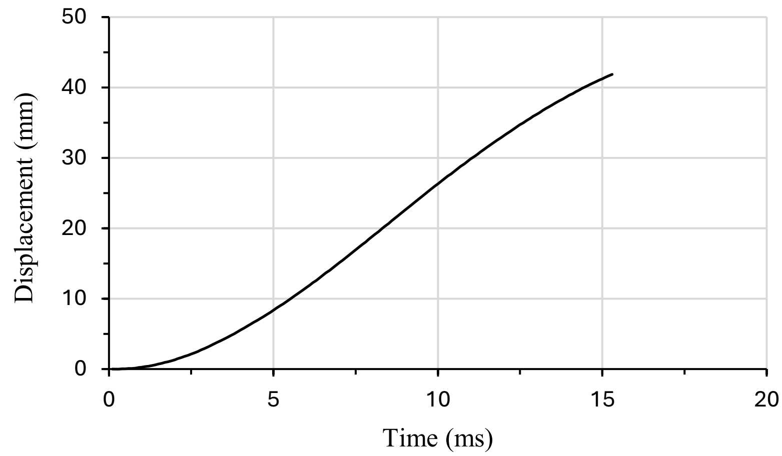

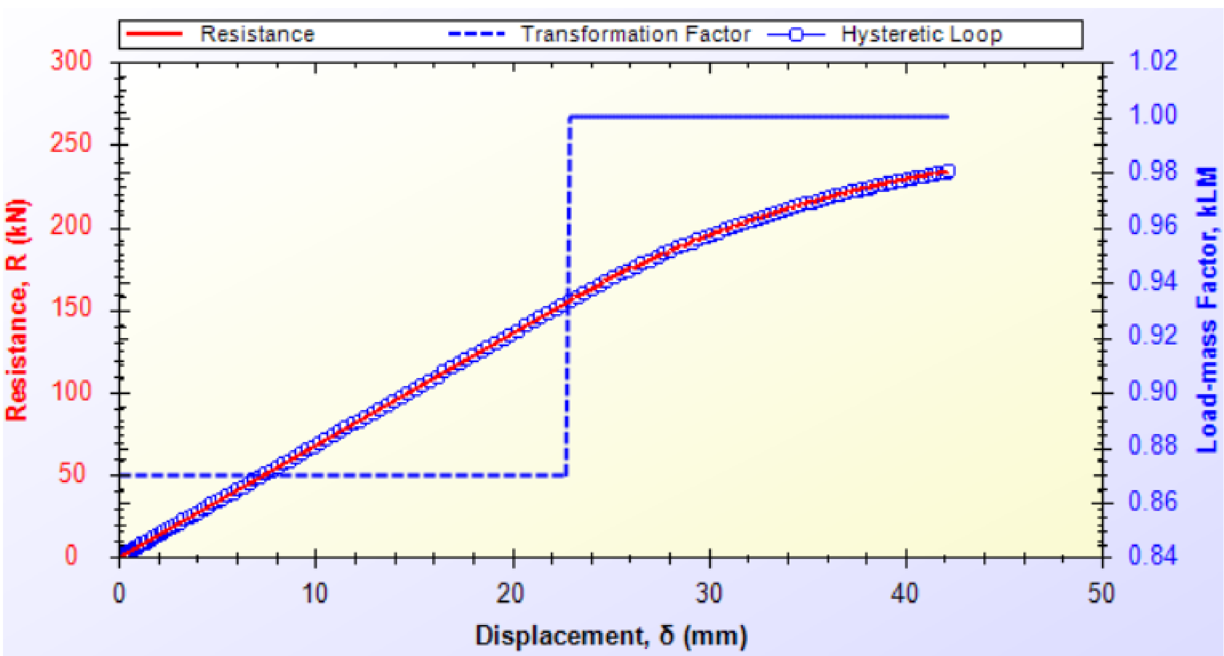

Figure C.16 Resistance and displacement time history for SDOF G-T(0)U(±45)